University of Stavanger

FACULTY OF SCIENCE AND TECHNOLOGY

MASTER'S THESIS

Study programme/specialization: Petroleum Engineering/ D&W	Spring/ ~~Autumn~~ semester, 2020 Open / ~~Confidential~~
Author: Abazar Al-Barakat	
Supervisor(s): Dmitry Shogin	
Title of master's thesis: Assessing the Reliability of Physical Non-Newtonian Fluid Models for Saline FLOPAAM Polymer Solutions.	
Credits: 30	
Keywords: C-FENE-P Salinity Polymer PTT Material Function Shear-flow	Number of pages: 170 Stavanger, July/2020 date/year

Abstract

Experiments were conducted to investigate the impact of salt (NaCl) on rheological properties of specifically FLOPAAM 5115 VHM and FLOPAAM 3630-S polymers. These polymers were dissolved in brines of various salinity levels ranging from 0 to 20 g/l of NaCl. The experiments were comprised of steady shear ramping, start-up and cessation tests using advanced rheometer with a cone and plate tool. Apparent viscosity and shear stresses were recorded at various step shear rates.

The data obtained from these tests were graphically presented and analyzed. Additionally, the scope of this theses was to investigate the reliability of physical non-Newtonian fluid models and their capability to predict the behavior of complex fluids. The models involved in this work are LPTT, EPTT, FENE-P and C-FENE-P. These models were fitted against the experimental data for qualitative and quantitative analysis.

Results of the experiment showed that the salt has a stabilizing effect on the polymers' viscosity as well as a dampening effect on shear stress growth and a greater decay of shear stress for the cessation test. These effects amplifies with increasing salt content. Furthermore, the data fitting showed interesting results, especially for the C-FENE-P dumbbell model. As it has proven itself capable of predicting viscosity of saline solution very well, something which cannot be said for shear stress, which has shown to be sensitive to the approach used for the applying such models.

Acknowledgement

I would like to express my sincere gratitude and appreciation towards my supervisor Phd. Dmitry Shogin for being humble and sharing of his extremely valuable knowledge, guidance, and time. Even during this difficult time with the novel Covid-19 virus.

I would also like to offer my appreciation to Kim Andre Vosse Vorland for orienting me on the use of laboratory equipment.

Last but not least, my appreciation is extended to Phd. Mesfin Belayneh Agonafir for being accessible and helping, who kept a positive spirit at the laboratory.

Table of Content

List of figures

List of Tables

1. Introduction

Majority of the oil produced today come from mature oil fields (SNF, 2012; Surguchev et al., 2005). Improving oil recovery has been a concern for oil companies and authorities for decades, as nearly 2×10^{12} barrels of conventional oil and 5×10^{12} barrels of heavy oil remain in reservoirs worldwide after conventional recovery methods have been exhausted. At the same time, the industry is experiencing a steady decline in new discoveries to replace mature reserves. Hence, it is critical to exploit these fields by increasing the recovery factors to face the increasing energy demand by encompassing new enhanced oil recovery (EOR) methods.

Water flooding as an improved oil recovery (IOR) method has been applied for many years (Needham and Doe, 1987; SNF, 2012). But it is generally known that oil and water are immiscible fluids. Hence, neither of them can properly displace the other from an oil reservoir, as there will always remain residual oil saturations that cannot be displaced. With polymer flooding, which is a water-soluble substance added to the water to be flooded. Which has been commercially applied for more than 40 years. It has shown low risk and can be applied to a wide range of reservoir conditions. This substance increases the fluid viscosity and contributes in reducing the effective permeability to water in the flooded zones. However, the polymer flooding does not reduce the residual oil saturation, but impacts oil production efficiency and the recovery factor. Water injected into the reservoirs, will by physical law follow the path of least resistance. Reservoirs containing oil with higher viscosity than the injected fluid will cause a fingering effect where the flooded water will flow through the oil, resulting in lower sweep efficiency. Thus, the benefit of polymer is the capability to minimize such fingering effects. But polymeric fluids are rheologically complex, thus it is important to identify its properties and develop models that can predict their behavior.

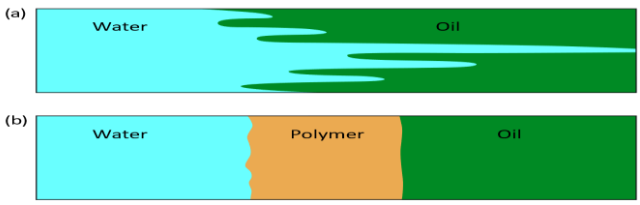

Figure 1 (a) illustrating the fingering effect of by flooding water without polymer and (b) illustrates polymer flooding (NPD, 2020) .

2. Objectives

The objectives of this thesis are as following:

- Investigate the impact of salinity on polymer material functions based on measured data from steady shear ramping, start-up and cessation measurements.

- Assess the reliability of physical non-Newtonian fluid models for saline polymer solutions by data fitting.

3. Polymers

Polymer is a molecular structure comprising of many smaller molecular units, it is also referred to as a macromolecule (Muralisrinivasan, 2015). These smaller units which can be identical in chemical structure are known as monomers. They have a unique molecular architecture such as molar mass, composition, and chain structure. Polymers originates either from natural (biological) or synthetical processes. The key factor distinguishing the natural polymer from the synthetic ones is the structural network, as the first mentioned can consist of larger quantity of monomers. Polymers dissolved in solvents are noticeably from a rheological perspective considered viscoelastic, as it can show elastic and viscous characteristics. And they are classified based on the following criteria:

- Chemical nature of monomers
- Molecular structure of polymers
- Polymer chain growth mechanism
- Type of polymerization process

3.1.1 Chemical Nature of Monomers

Monomers can contain reactive groups of hydroxyl and carboxyl amines, that are either bifunctional or multifunctional (Muralisrinivasan, 2015). These groups can undergo condensation polymerization reactions.

Furthermore, monomers containing one or more double bonds are capable of forming polymers by converting these bonds to saturated linkages.

3.1.2 Molecular Structure of Polymers

Polymers consist of different structural units, chain structure and are classified accordingly (Muralisrinivasan, 2015). There are homopolymers where there is a repetitive linkage of monomers in the polymer chain. And copolymers where there is more than one type of

monomers, such as biopolymers, terpolymers and multipolymers. These polymers can have different chain structure such as,

- Linear polymers
- Branched polymers
- Comb-like polymers
- Star-like polymers
- Cyclic polymers
- Dendrimer polymers

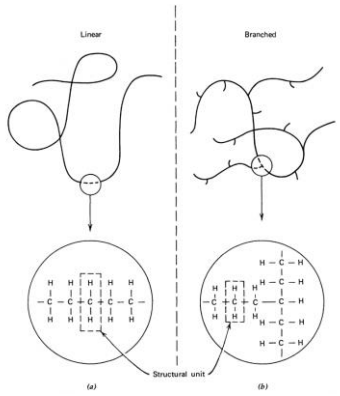

Figure 2 Illustration of linear(a) and branched(b) polymers (Bird et al., 1987).

3.1.3 Polymer Chain Growth Mechanisms

There are two growth mechanisms of chains in polymers during production, step-growth polymerizations and chain polymerizations, and polymers are classified based on these mechanisms.

Type of Polymerization Process:

The reactions in which monomers combine is defined as polymerization. The polymerization processes are dictated by a set of parameters such as flow as the material is transported and meet at different points. Pressure and temperature are among them as well.

Polymerization can occur by addition of monomers, ionic, or free-radical processes.

3.2 Polyacrylamide Polymers

Polymers of the type polyacrylamide (PAM) are the most used polymers in the petroleum industry for EOR purposes (Wever et al., 2011). It gives thickening effects for aqueous solutions. By thickening it is meant as increase in solution's viscosity. PAM's are mainly made of high molecular weight. These polymers are classified as VHM's, which stands for very high molecular weight and can reach values more than $10^6\ g/mol$. PAM comes in many different chemical structures and researchers have zealously attempted to modify these structures for improved properties, such as shear resistance, brine compatibility and temperature stability.

3.2.1 Partially Hydrolyzed Polyacrylamide (HPAM)

HPAM is a copolymer of PAM and PAA (poly acrylic acid) combined by hydrolysis of PAM or by copolymerization of sodium acrylate and acrylamide. Factors influencing the viscosity of HPAM's are solution temperature, molecular weight, solvent quality, and degree of hydrolyzation. For optimal HPAM's it is necessary for the acrylamide monomers to be hydrolyzed for a degree of minimum of 25 %. The reasoning behind this is assumed to be related to the salinity of the polyelectrolyte solution. As electrostatic charges cause repulsion between the coils, the polymeric chains stretch which provides us with the thickening effect of the polymer. But it is important to notice that increased hydrolyzation increases the salinity sensitivity. This reduces the effect of the electrostatic repulsions, thus minimizing the thickening of the solution.

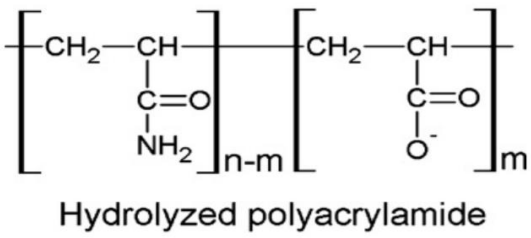

Figure 3 Chemical structure of an HPAM polymer.

HPAM's can tolerate high mechanical forces and is less degradable to bacterial attacks which is why it is favorized for EOR operations. A broadly known fact about polymers is that they are characterized as a non-Newtonian due to their shear-rate dependency. Such polymers commonly show shear thinning effects in viscometric measurements, this basically means that the apparent viscosity decreases with increasing shear rate. But when applying to real life reservoir flooding, the polymers' apparent viscosity can possibly experience shear-thickening which is the opposite of shear-thinning. This phenomenon takes place as the shear rate reaches a critical rate where polymer chains coil and these coils entangle. This effect has been observed during experiments conducted by (Ait-Kadi et al., 1987), which is likely to only behave in this way for high-molecular weight polymer solutions. The critical shear rate is dictated by the previous mentioned factors. And this rate decreases with increasing degree of hydrolyzation. And increases with increasing polymer concentration.

3.3 Polymeric Flow Phenomena

3.3.1 Shear Dependent Viscosity

A polymeric fluid is non-Newtonian due its viscosity's dependency on shear-rate (Bird et al., 1987). Newtonian fluids have the following characteristics (Deshpande et al., 2010):

- Viscosity independent of shear rate
- Viscosity independent of time of shear at a constant shear rate
- The normal stress differences are zero
- Viscosities measured by different types of deformations are proportional to each other.

Any fluid with characteristics violating the above-mentioned points, are considered non-Newtonian. One can easily demonstrate this by conducting a simple tube flow experiment (Bird et al., 1987). Using two identical vertical tubes with their bottom open end covered by a plate one of which is filled with a polymeric fluid and the other with a Newtonian fluid. Due to the very low shear rate exerted on these liquids in this experiment one must consider liquids with the same viscosity.

By removing the covering plate and allowing gravity to take its effect on the liquid samples one can observe that the polymeric liquid flows out of the tube much rapidly compared to the Newtonian liquid. This confirms the polymeric liquid's shear thinning characteristics and by shear thinning is meant that the viscosity decreases when shear-rate increases. Such liquids are also known as pseudoplastics. This is due to the gradual breakdown of the viscosity under stress.

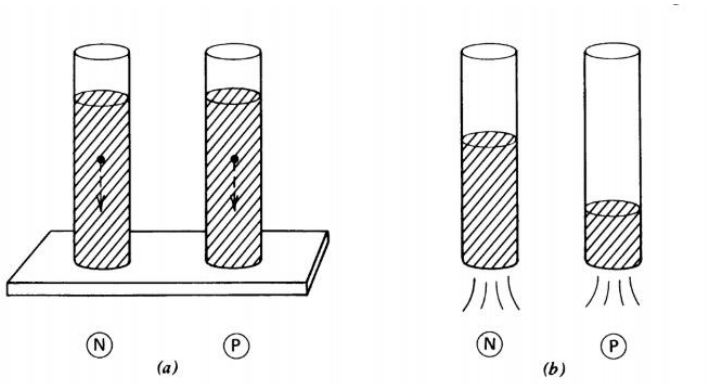

Figure 4 An Illustration of the tube flow experiment with(a) and without(b) the cover plate (Bird et al., 1987).

3.3.2 Normal Stress Effects

When discussing polymer liquids, one must consider normal stresses (Bird et al., 1987). These stresses are exerted under shear flow by the act of stretching and aligning of polymer molecules. This triggers thermal motion that makes the polymer behave as a spring that oscillates when released after extension. It yields additional tension along the streamlines. To showcase the validity of this theory, simple experiments can be conducted.

3.3.2.1 Weissenberg Rod Climbing Effect

Polymers are famous for the fascinating the rod climbing phenomenon, where the liquids start to ‘’climb’’ the rod under continuous rotation (Bird et al., 1987; Deshpande et al., 2010). This is the opposite to vortexes generated in Newtonian fluids. This is called the Weissenberg effect and is exhibited due to a normal stress difference. The liquid is stirred, and circular streamlines are created generating normal forces acting inwards and upwards on the liquid that are greater than the centrifugal- and gravitational forces. The figure below illustrates this effect.

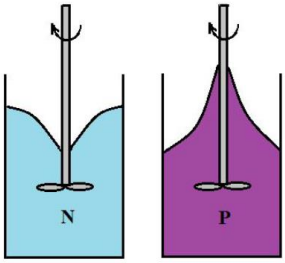

Figure 5 Comparison between Newtonian fluid(N) and Polymer fluid(P) on rotation, N generates vortex and P generates rod climbing.

There are several other methods to illustrate normal stress effects, such as the quelle effect which is an experiment that recreates a similar liquid ‘’rod climbing’’ behavior seen in the previous mentioned experiment (Bird et al., 1987). In this experiment the rod is replaced by a magnet to stir the liquid with the help of an actuator, and a bulge on the surface can be observed.

3.3.2.2 Extrudate Swell Effect

When a flow polymer solution ejects from a capillary or a die, it takes a signature formation where the diameter of the flow widens as the liquid travels further away from the capillary (Bird et al., 1987; Deshpande et al., 2010). This diameter expansion can reach up to four times its capillary diameter, and this behavior is called extrudate swelling. This cannot be easily observed for Newtonian fluids where diameter change is minimal. Such phenomenon is argued to be related to the normal stress difference induces by shear flow in the capillary. As additional tension is exerted along the streamlines of the polymer liquid creating contraction along its axis and expansion radially, due to the extra tension being unsupported. This is not the only argument for why polymers behave in this way, others have argued that viscous heating contributes to the swelling where the liquid is heated near capillary walls while the temperature in the center is lower. There exist several other explanations, but they are just theories and are yet to be proven. The extrudate swelling is illustrated in the figure below.

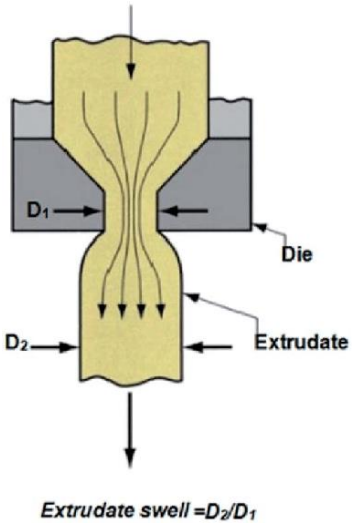

Figure 6 An illustration of the swell effect as the fluid exits the capillary (Yousfi et al., 2018).

3.3.3 Elastic Recoil/Memory Effects

Polymers as described previously can take on a conglomeratic formation when in equilibrium state and thus having the ability to be stretched when applying stress. It will react by snapping back as the forces applied to it are released giving it an elastic tendency also known as elastic recoil (Bird et al., 1987; Deshpande et al., 2010). This could easily be demonstrated with a simple experiment, by pouring a polymer liquid into a beaker. The fluid column can then literally be cut into two sections using a scissor. The upper section will then experience elastic recoil by pulling itself back into the bottle. As illustrated in the figure below.

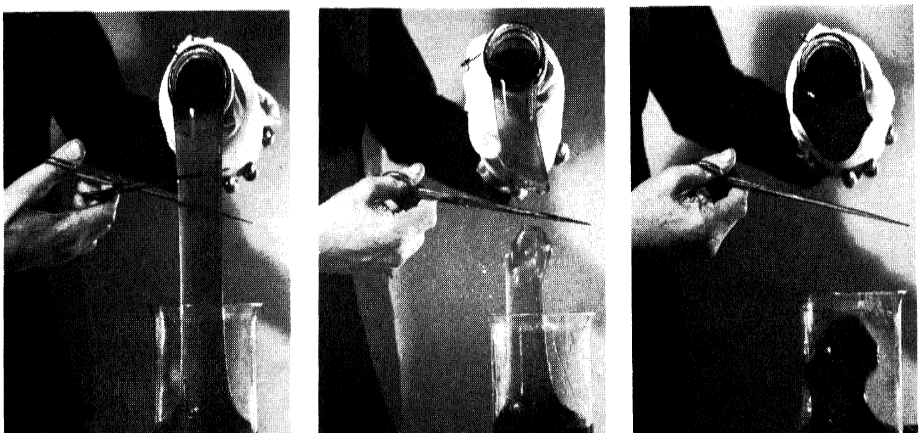

Figure 7 Images illustrating the memory effects of polymers. The polymer fluid snaps back immediately as it is cut using a scissor (Bird et al., 1987).

4. Mathematical Introduction

In this chapter mathematical theories that will be introduced are considered fundamental to the understanding of fluid dynamics. Physical quantities will be used with their respective notations to describe these mathematical formulations; thus, the following sections are added for the purpose of clarification:

- Scalar

  A scalar is described in a physical matter as a quantity comprising of a single element of a number field such as a real number.

  The following notation will be expressed when referring to a scalar:

  (…) Quantity inside round brackets is a scalar.
  And normal Latin font will be used.

- Vector

  A vector is a mathematical representation of a physical quantity that has magnitude and direction. It assigns a number to each direction.

  The following notation will be expressed when referring to a vector:

  […] Quantity inside square brackets is a vector.
  And bold face Latin font will be used.

- Tensor

  Tensor is a physical quantity that assigns a number to an ordered pair of vectors.

  The following notation will be expressed when referring to a tensor:

  {…} Quantity inside curly brackets is a tensor.
  And bold face Greek font will be used.

4.1 The Navier-Stokes Equation

The widely known Navier-Stokes equations are applied in many sectors of engineering, and commonly in fluid dynamics as it can describe fluid motion in complex flows (Bird et al., 1987). The derivation of this fundamental equation is based on the laws of conservation of mass, momentum, and energy.

Fluid dynamics is a very complex subject and laws of conservation helps us better understand fluid behavior and solve the problems it presents (Bird et al., 1987). Before getting into the specifics of the derivation of the Navier-Stokes equation, let's put things into context. Considering a volume V and its surface S, we will assume in the coming sections that a fluid will flow through an arbitrary fixed region of this volume with a velocity, $\boldsymbol{v}$. Furthermore, an infinitesimal surface element, dS, will act as the surface of such region from which a normal unit vector, $\boldsymbol{n}$, will point outwards, representing flow direction. For illustration see figure below. Thus, volumetric- and mass flow will take the following form, $(\boldsymbol{n} \cdot \boldsymbol{v})\mathrm{d}S$ and $(\boldsymbol{n} \cdot \rho\boldsymbol{v})\mathrm{d}S$, respectively. Where ρ is defined as the density of the fluid.

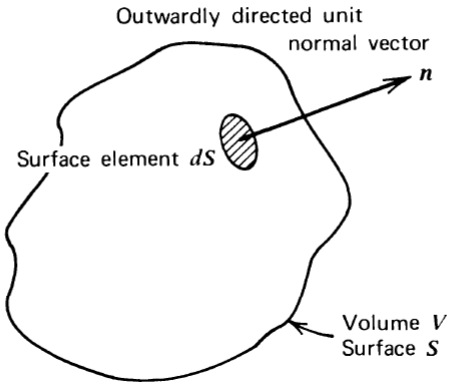

Figure 8 Arbitrary control volume, fixed in space, over which mass, momentum and energy balances are made (Bird et al., 1987).

4.1.1 Conservation of Mass

The law of mass balance states that influx into a fixed volume equals outflux and hence, we have a conservation of mass (Bird et al., 1987; Deshpande et al., 2010).

$$\begin{pmatrix}\text{Rate of mass}\\ \text{accumulation}\end{pmatrix} = \begin{pmatrix}\text{Rate of mass}\\ \text{IN}\end{pmatrix} - \begin{pmatrix}\text{Rate of mass}\\ \text{OUT}\end{pmatrix} \tag{1}$$

Now, let us take a closer look at the derivation of this law by assigning volumetric outflux across a local dS with positive sign and influx with a negative sign.

Based on conservation of mass law, the total fluid mass within V can only increase if net influx manifests. Taking the following mathematical form,

$$\frac{\mathrm{d}}{\mathrm{d}t}\int_V \rho \,\mathrm{d}V = -\int_S (\boldsymbol{n}\cdot\rho\boldsymbol{v})\mathrm{d}S \tag{2}$$

By transforming the surface integral into a volume integral using Gauss's divergence theorem gives,

$$\frac{d}{\mathrm{d}t}\int_V \rho \,\mathrm{d}V = -\int_V (\boldsymbol{\nabla}\cdot\rho\boldsymbol{v})\mathrm{d}V \tag{3}$$

Furthermore, V being fixed allows us to rearrange and bring the time derivative into the integral and hence, we obtain:

$$\int_V \left[\frac{\partial\rho}{\partial t} + (\boldsymbol{\nabla}\cdot\rho\boldsymbol{v})\right] = 0 \tag{4}$$

This gives an integral of an arbitrary volume, which allows us to set to zero, yielding:

$$\frac{\partial \rho}{\partial t} = -(\boldsymbol{\nabla} \cdot \rho \boldsymbol{v}) \tag{5}$$

Equation 5 is known as the equation of continuity. This shows that mass is conserved. For liquids it is assumed to be incompressible. Thus, Eq. 5 can be further simplified to,

$$\boldsymbol{\nabla} \cdot \boldsymbol{v} = 0 \tag{6}$$

4.1.2 Conservation of Momentum

Momentum in fluid dynamics is defined as the quantity of motion of the moving fluid and measured as the product of its mass and velocity making it a vector quantity and is a consequence of Newton's second law of motion (Bird et al., 1987; Deshpande et al., 2010). Momentum of a fluid should not only be considered as a bulk, but rather on a molecular level as well, the motion and interactions within a fluid contributes to the momentum as whole. With regards to momentum we also have the conservation of momentum law which states that the total momentum of a fluid within V will increase because of a net influx of momentum across the bounding surface due to bulk flow and molecular motion and the gravitational force acting on the fluid.

This can be mathematically illustrated in the following:

$$\frac{\mathrm{d}}{\mathrm{d}t}\int_V \rho \boldsymbol{v}\, \mathrm{d}V = -\int_S [\boldsymbol{n} \cdot \rho \boldsymbol{v}\boldsymbol{v}]\mathrm{d}S - \int_S [\boldsymbol{n} \cdot \boldsymbol{\pi}]\mathrm{d}S + \int_V \rho \boldsymbol{g}\, \mathrm{d}V \tag{7}$$

Where $\boldsymbol{g}$ is the standard acceleration due to gravitational force.

By applying Gauss divergence theorem, we obtain:

$$\int_V \frac{\partial}{\partial t} \rho \boldsymbol{v}\, \mathrm{d}V = -\int_V [\boldsymbol{\nabla} \cdot \rho \boldsymbol{v}\boldsymbol{v}] \mathrm{d}V - \int_V [\boldsymbol{\nabla} \cdot \boldsymbol{\pi}] \mathrm{d}V + \int_V \rho \boldsymbol{g}\, \mathrm{d}V \tag{8}$$

This can be further simplified as V is arbitrary and by this, we have obtained the equation of motion.

$$\frac{\partial}{\partial t} \rho \boldsymbol{v} = -[\boldsymbol{\nabla} \cdot \rho \boldsymbol{v}\boldsymbol{v}] - [\boldsymbol{\nabla} \cdot \boldsymbol{\pi}] + \rho \boldsymbol{g} \tag{9}$$

4.2 The Stress tensor and Constitutive Equations

The π used in the previous sections is the total stress tensor and describes the state of stress applied at any point of a body (Bird et al., 1987; Deshpande et al., 2010; Garrido, 2007). It is related to the total stress tensor **σ** used in other scientific disciplines which is defined as $\boldsymbol{\pi}_{-n}\, dS = \boldsymbol{\pi}_n\, dS = [\boldsymbol{\sigma} \cdot \boldsymbol{n}]$ dS and can be rewritten as $\boldsymbol{\pi} = -\boldsymbol{\sigma}^T$, where T stands for transpose. This yields a stress tensor π with a negative sign and different order of indices and is assumed to be symmetrical.

The stress tensor can be decomposed of nine components (Fig. 8) and can be expressed as,

$$\boldsymbol{\tau}_{ij} = \begin{bmatrix} \tau_{xx} & \tau_{xy} & \tau_{xz} \\ \tau_{xy} & \tau_{yy} & \tau_{yz} \\ \tau_{xz} & \tau_{yz} & \tau_{zz} \end{bmatrix} \tag{10}$$

Where, π_{ij} is the force per unit area in *j* direction acting on the face of a cubic element and whose normal vector points in the *i* direction, as illustrated in the figure below. The normal stresses in such a tensor will be the components where $i = j$, while components where $i \neq j$ are the shear stresses. The symmetry obtained from a tensor benefits us in reducing the number of unknown components from nine to six.

The total stress tensor describes effects of deformation on an element and can be defined in a formula as,

$$\boldsymbol{\pi} = P\boldsymbol{\delta} + \boldsymbol{\tau} \tag{11}$$

Where, $\boldsymbol{\pi}$ is total stress tensor, P is the thermodynamic pressure, $\boldsymbol{\delta}$ is the unit tensor and $\boldsymbol{\tau}$ is an extra anisotropic stress tensor. Here $\boldsymbol{\tau}$ is part a of the total stress tensor and is associated with the viscosity of the respective fluid. In an equation where the value of the $\boldsymbol{\tau}$ is specified is called the constitutive equation.

Whereas $\boldsymbol{\tau}$ for Newtonian fluids can be written in the following form,

$$\boldsymbol{\tau} = -\mu\{\boldsymbol{\nabla v} + \boldsymbol{\nabla v}^T\} + (\frac{2}{3}\mu - k)(\boldsymbol{\nabla} \cdot \boldsymbol{v})\boldsymbol{\delta} \tag{12}$$

Where, μ is the shear viscosity constant and k the dilatational viscosity. For monoatomic gases $k = \frac{2}{3}\mu$ for monoatomic gases thus the last term vanishes, whereas for incompressible fluids $\boldsymbol{\nabla} \cdot \boldsymbol{v} = 0$. Thus, $\boldsymbol{\tau}$ can be further simplified to,

$$\boldsymbol{\tau} = -\mu\{\boldsymbol{\nabla v} + \boldsymbol{\nabla v}^T\} = -\mu\dot{\gamma} \tag{13}$$

Where $\dot{\gamma} = -\mu\{\boldsymbol{\nabla v} + \boldsymbol{\nabla v}^T\}$, is the rate of strain tensor or rate of deformation tensor. By this we can obtain the Navier stokes equation for incompressible Newtonian fluids,

$$\rho\left[\frac{\partial \boldsymbol{v}}{\partial t} + \boldsymbol{v} \cdot \boldsymbol{\nabla v}\right] + \boldsymbol{\nabla} p - \mu\boldsymbol{\nabla}^2\boldsymbol{v} - \rho\boldsymbol{g} = 0 \tag{14}$$

Newton assumed the simplest form: that $\boldsymbol{\tau}$ is linear in velocity gradients and proposed the most general case, Eq. (12). This equation was tested experimentally, and it was found to hold for the fluids known at that time. Later, it was proven not to hold for some complex fluids; these got the name non-Newtonian in contrast to those obeying the Newton's relation (Newtonian).

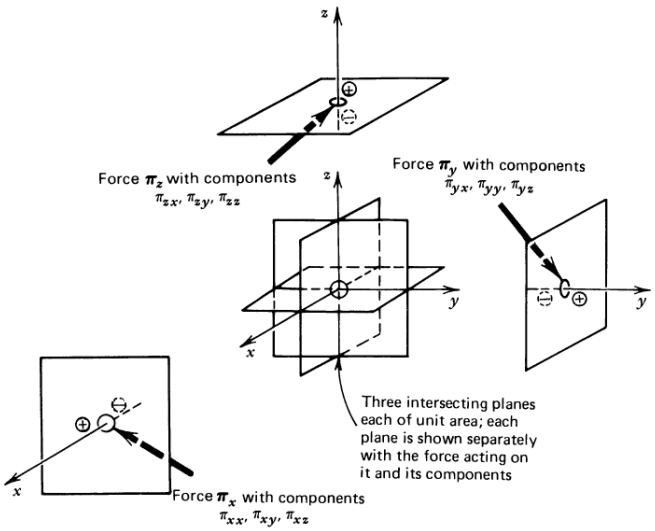

Figure 9 Sketch showing the components of stress tensor pi with their respective signs and indices (Bird et al., 1987).

5. Material Functions

The previous sections showcased how the simple Newtonian laws of viscosity are only applicable for Newtonian fluids, which are only dependable on two material constants: the density, ρ and viscosity, μ (Bird et al., 1987). These constants can be simply obtained from experimental measurements. And as we approach more complex fluids, we face the limitation of these models as they cannot accurately describe non-Newtonian fluids. Thus, we need to seek experimental methods to define material functions of such fluids, but this is rather complicated as we do not know what other property or properties are needed to be measured. From isothermal experiments conducted on a Newtonian fluid we obtain a single material constant which is the viscosity, μ. As for polymeric fluids it is the contrary, experiments yield several material functions which are functions of kinematic parameters that are used to characterize the behavior of fluids that depend on a set of parameters like shear rate, frequency, time, etc. Therefore, scientist have introduced us to a new set of advanced models to predict non-Newtonian behavior to a certain degree. The functions obtained from these experiments will help us in determining the constants in these specific non-Newtonian constitutive equations. But before we discuss these models, it is important to fully understand the different flow types as these will govern the material functions, we obtain. The two common types of flows used to characterize polymer liquids are shear and shear free flows which will be presented in the next sections with their respective velocity and stress fields.

5.1 Shear Flow

Shear flow can be described as layers of liquid that slide relative to one another without mixing. This type of flow can easily occur for flow between two parallel plates. As the upper plate moves, it drags the upper layer of liquid with it and so on, while the bottom plate remains static, see Fig. 9.

We have three directions that are perpendicular to each other at any local point in such flow.

- The direction of flow.
- The direction in which velocity changes.
- The neutral direction, which equals zero.

Furthermore, a simple shear flow has a velocity field,

$$v_x = \dot{\gamma}_{yx} y; \qquad v_y = 0; \qquad v_z = 0; \tag{15}$$

Where the velocity gradient, $\dot{\gamma}_{yx}$ can be a function of time. The shear rate is the absolute value of $\dot{\gamma}_{yx}$. It is important to differentiate between steady and unsteady shear flow, where the first mentioned is independent of time due to constant shear rate, and obviously making unsteady shear flow time dependent as the shear rate changes.

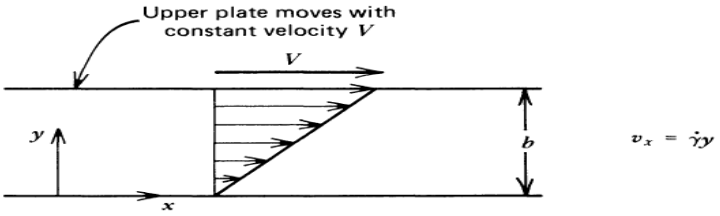

Figure 10 An illustration of steady shear flow (Bird et al., 1987).

5.1.1 Stress Tensor for Shear Flow

Newtonian fluids during shear flow yield zero stress in all components of the stress tensor, except the shear stress, τ_{yx} (Bird et al., 1987). As for non-Newtonian that is not valid, we must assume that all six independent components of the stress tensor have a non-zero value. By further assuming that the fluid is isotropic and the stresses in the fluid depends only on the flow field, one can express the total stress tensor in following form,

$$\pi = P\delta + \tau = \begin{bmatrix} P + \tau_{xx} & \tau_{yx} & 0 \\ \tau_{yx} & P + \tau_{yx} & 0 \\ 0 & 0 & P + \tau_{zz} \end{bmatrix} \tag{16}$$

Something to notice is that the pressure and the normal stress contribution in on surfaces from experimental measurements using common equipment is considered impossible to separate when evaluating an incompressible fluid. This means that the only quantities that are of interest on an experimental level are the shear stress and the two normal stress differences, as given below.

Shear stress:	τ_{yx}
First normal stress difference:	$\tau_{xx} - \tau_{yy}$
Second normal stress difference:	$\tau_{yy} - \tau_{zz}$

These are the three main experimentally accessible quantities in simple shear flow.

5.1.2 Material Functions of Steady Shear Flow

There is no time dependency in steady shear flow (Bird et al., 1987). And as stated previously with such flow we assume that the stress tensor only depends on the flow field, meaning that the stresses are shear rate, $\dot{\gamma}$ dependent. This results in a viscosity for non-Newtonian fluids also being shear-rate dependent viscosity, η. This gives us the following material functions:

$$\tau_{yx} = -\eta(\dot{\gamma})\dot{\gamma}_{yx} \tag{17}$$

$$\tau_{xx} - \tau_{yy} = -\Psi_1(\dot{\gamma})\dot{\gamma}_{yx}^2 \tag{18}$$

$$\tau_{yy} - \tau_{zz} = -\Psi_2(\dot{\gamma})\dot{\gamma}_{yx}^2 \tag{19}$$

The shear-rate dependent viscosity, $\eta(\dot{\gamma})$ is considered to be similar to the Newtonian viscosity. Where, $\eta(\dot{\gamma}) = \mu = \text{constant}$. Whereas the functions Ψ_1 and ψ_2 are the coefficients of the first and second order normal stresses. All these three functions are known as viscometric functions.

Plotted data of $\eta(\dot{\gamma})$ from experiments brough forward by Bird et al., 1987, shows that the shear stress is proportional to shear rate at lower $\dot{\gamma}$. And that the viscosity moves towards a constant viscosity, η_0 which is the zero-shear-rate viscosity also known as the lower-Newtonian region, and this was the case for all three polymer solutions evaluated in this experiment. Something else to notice was that the viscosity would decrease when increasing the shear rate. This phenomenon is called shear-thinning and is common for majority of polymers which is the main property of interest for engineering applications. This will later be investigated further with self-produced experimental data in the analysis chapter.

When plotting log η versus log $\dot{\gamma}$, one can observe a linear region of the viscosity versus shear rate curve at high rates can last through a large interval of decreasing viscometric viscosity. The findings based on the experimental data showcase that region of linearity, the slope which can be identified as the power-law region is set to be between -0.4 to -0.9 for typical polymer liquids. Furthermore, the plots also indicate a proportionality between the molecular weight distribution of the polymer and the shear rate range of which viscosity transit from constant viscosity and the power-law region. This means that an increase in polymer weight will increase the rapidness of the transition and shifts to the linear region at lower shear rates. It is also observable that the viscosity starts to reach the infinite-shear-rate-viscosity, η_∞ also known as the upper-Newtonian region. This means that the viscosity is less and less dependent on shear rate at higher rates. Due to high probability for degradation of the polymer at high shear rates, makes measurement of η_∞ less likely. While the temperature effects, does not seem to prevent the viscosity's dependence on the shear rate, but rather provides different starting-point of the zero-shear-rate-viscosity at a variety of temperatur

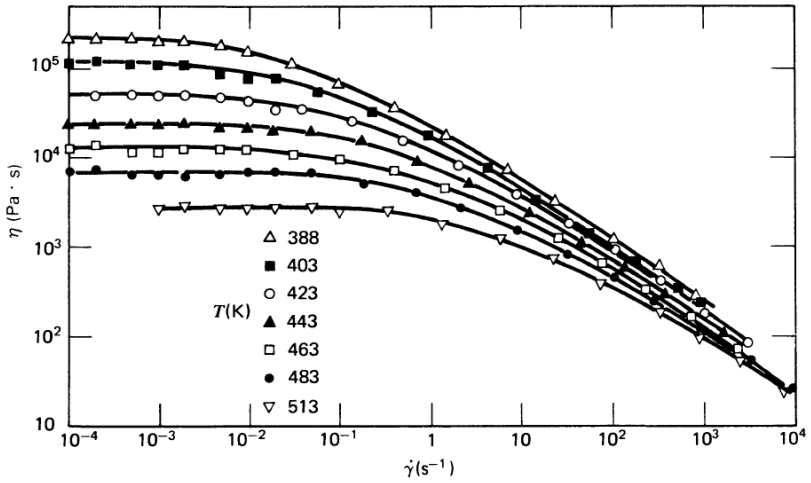

Figure 11 LogLogPlot of apparent viscosity η versus shear rate $\dot{\gamma}$ of a polymer melt at several temperatures (Bird et al., 1987).

As for first and second order normal stress coefficients they seem to have commonalities with viscosity behavior under similar circumstances. However, the plots also show that the rate of decline of Ψ_1 with $\dot{\gamma}$ is greater than η with $\dot{\gamma}$. The power-law region of ψ_1 can fall by factor of 10^6. Furthermore, as the $\dot{\gamma}$ approaches zero we obtain a first normal stress difference to be proportional to $\dot{\gamma}^2$, meaning that ψ_1 moves towards a constant zero-shear-rate first normal stress coefficient, $\Psi_{1.0}$. The Ψ_1 and Ψ_2 share the same characteristic of a large power-law region, but differ in some points, as it only counts for about 10% of Ψ_1 magnitude in addition to its negative sign. But other than that, there is not sufficient knowledge about Ψ_2.

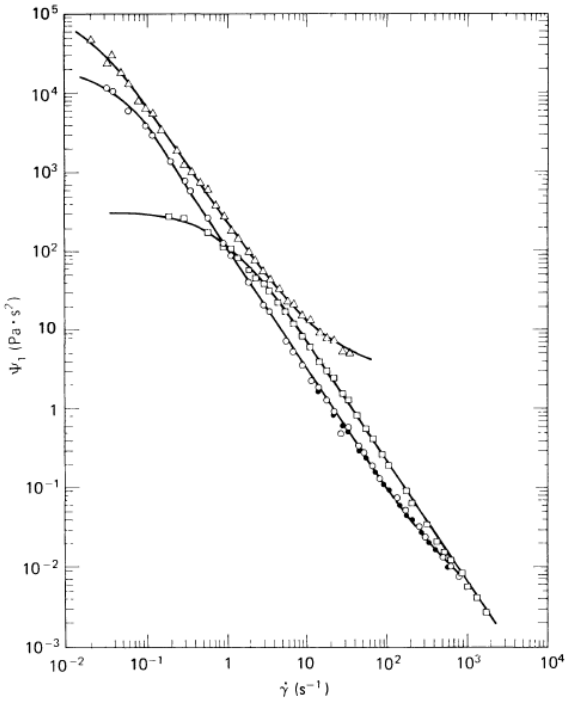

Figure 12 LogLog plot of Ψ_1 versus $\dot{\gamma}$ (Bird et al., 1987).

5.1.3 Material Functions of Unsteady Shear Flow

Unsteady shear flow is the contrary of steady shear flow, meaning that it is time dependent. But they have in common the three measurable stress quantities:

- The shear stresses
- Two normal stress differences

The material functions of these quantities will have similar η, Ψ_1 and Ψ_2, but will in such flow depend on time or frequency in addition to shear rate. There is large variety of types of experimental shear flow used in rheology. For the purpose of this thesis start-up and cessation of shear flow have been chosen for further description in the next sections.

5.2 Start-up of Steady Shear Flow

Start-up of steady shear flow is an experimental method with a purpose to investigate the shear stress that fluids are exposed to until it reaches the desired steady state (Bird et al., 1987). Starting up steady shear flow of a polymer liquid yields gradual growth in shear stress from its resting zero-shear stress. Before it reaches the steady state, it goes through a transient region of shear stress build up. The transient properties of this experiment can be measured using a cone and plate rheological instrument. Fig. 12 illustrates the start-up of steady shear flow.

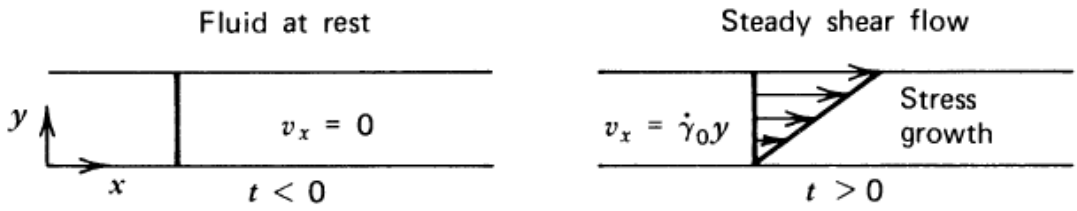

Figure 13 An illustration of start-up of steady shear flow (Bird et al., 1987).

It is assumed that the fluid is at rest at all times prior to the initiation of the flow, at time, $t = 0$ and a constant velocity gradient, $\dot{\gamma}_0$ for times, $t \geq 0$. This experiment enables us to measure the material functions η^+, Ψ_1^+ and Ψ_2^+ which are functions of both time, t and shear rate, $\dot{\gamma}_0$ and the plus sign indicates validity for positive times, $t \geq 0$. These functions equal μ, 0 and 0, respectively for a Newtonian fluid. All three functions are analogous to η, Ψ_1 and Ψ_2, respectively. And with the contributions of these functions we can describe the transient shear stress and normal stress differences by inserting them into the following defining equations,

$$\tau_{yx} = -\eta^+(t, \dot{\gamma}_0)\dot{\gamma}_0 \tag{20}$$

$$\tau_{xx} - \tau_{yy} = -\Psi_1^+(t, \dot{\gamma}_0)\,\dot{\gamma}_0^2 \tag{21}$$

$$\tau_{yy} - \tau_{zz} = -\Psi_2^+(t, \dot{\gamma}_0)\,\dot{\gamma}_0^2 \tag{22}$$

When plotting the ratio $\frac{\eta^+(t,\dot{\gamma}_0)}{\eta(\dot{\gamma})}$ versus time, t it is expected a minimal shear stress overshoot at lower shear rates and at the lowest it is monotone to the steady state. It is important to keep in mind that the lower the shear rate is the more time is required to reach a steady state. The behavior at high shear rates is different from what is seen at lower shear rates, as η^+ will exit the linear viscoelastic trend, reach the peak of the overshoot and then reach the steady state after one or more oscillations about $\eta(\dot{\gamma})$. The figure below illustrates this behavior.

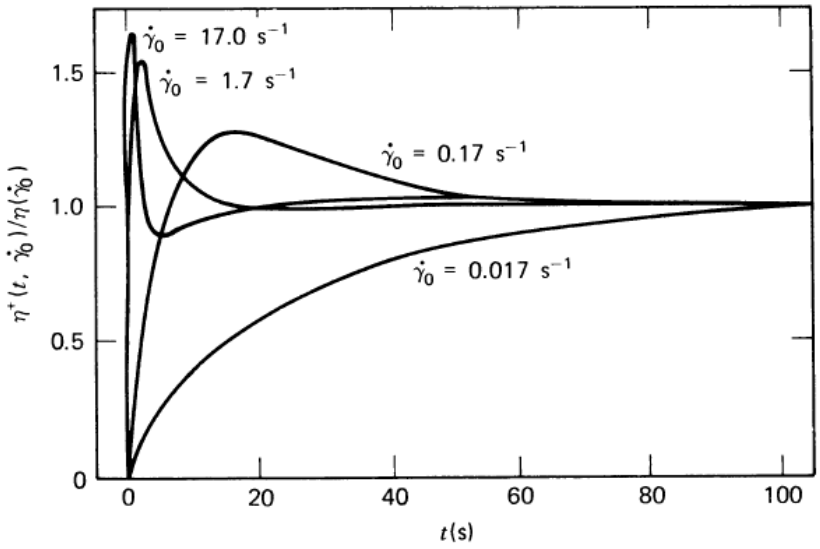

Figure 14 Shear stress growth plot for different shear rates (Bird et al., 1987).

This figure also reflects that the time needed for η^+ to exit the linear viscoelastic trend is reduced with increased shear rate in such a way that shear strain is constant where non-linear effects are first detected. Furthermore, the first normal stress difference has a similar dependence on $\dot{\gamma}_0$ as shear stress.

5.3 Cessation of Steady Shear Flow

The cessation experiment is the opposite of the start-up experiment described in the previous section (Bird et al., 1987). It is an experimental method of which a cone and plate instrument can be used to measure the relaxation properties of a fluid undergoing steady shear flow that stops abruptly by command at a reference time, $t = 0$. That means the time for $\dot{\gamma}_0$ to drop to zero will be $t \geq 0$.

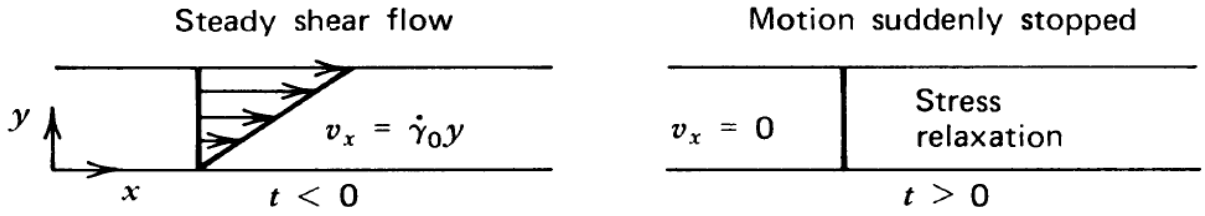

Figure 15 An illustration of relaxation of steady shear flow (Bird et al., 1987).

At $\dot{\gamma}_0 = 0$ the shear stress is then simply zero after some time is passed. But to describe that path to zero shear stress, new material functions of relaxation are introduced as the following η^-, Ψ_1^- and Ψ_2^- similar to the viscometric functions. They are time and shear rate dependent, analogously to the start-up material functions. Whereas the negative sign refers to validity for negative times, t. For Newtonian fluids, $\eta^- = 0$ at $t > 0$. While ψ_1^- and ψ_2^- both equals zero. By these functions we obtain the following defining equations,

$$\tau_{yx} = -\eta^-(t, \dot{\gamma}_0)\dot{\gamma}_0 \tag{22}$$

$$\tau_{xx} - \tau_{yy} = -\psi_1^-(t, \dot{\gamma}_0)\,\dot{\gamma}_0^2 \tag{23}$$

$$\tau_{yy} - \tau_{zz} = -\psi_2^-(t, \dot{\gamma}_0)\,\dot{\gamma}_0^2 \tag{24}$$

Experimentally, it is expected for steady shear flows at high rates to relax more rapidly than at low shear rates. But common for all non-Newtonian fluids is that they relax monotonically, as they do not read negative shear stresses. The figure below illustrates this behavior quite well.

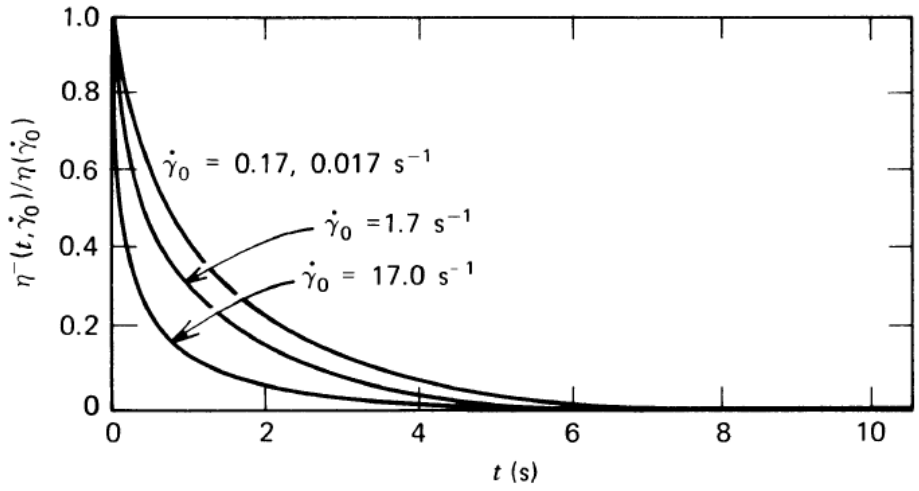

Figure 16 Plot showing relaxation of shear stress for different shear rates (Bird et al., 1987).

This experiment also points out that the first normal stress difference experiences a reactive delay like the start-up experiment. Whereas in this case the measurements are expected to show a more rapid relaxation of shear stress compared to first normal stress difference.

6. Generalized Newtonian Fluid Model

The generalized Newtonian fluid is based on the simple constitutive equation with minor changes (Bird et al., 1987). Its capable of describing shear rate dependent viscosity which enables it to become applicable for not only Newtonian fluids, but non-Newtonian fluids as well. For this reason, it is widely used for engineering purposes. But of course, it has its limitations of incapability to describe normal stress effects and time-dependent elastic effects. The modified constitutive equation has taken following form,

$$\tau = -\eta(\dot{\gamma})\dot{\gamma} \tag{25}$$

The notations have been defined in previous sections.

However, the limitations mentioned above are some of the reasons to pursue more reliable modified Newtonian models, thus the power law model and the Carreau-Yasuda model are to be introduced in the next sections.

6.1 The Power-Law Model

The power law model is one of the most used models for rheological purposes (Bird et al., 1987). After all it is a generalization of the Newtonian fluid model. The power law region mentioned previously and that is often observable on viscosity versus shear rate plots are based on the following model,

$$\eta = m\dot{\gamma}^{n-1} \tag{26}$$

This model was first introduced by Oswald and de Waele where they added two new temperature sensitive parameters, m which is the consistency index and n the power-law index.

These parameters add the benefit of flexibility to apply the model for non-Newtonian fluids as well. If $n < 1$ then the fluid is shear thinning, while $n > 1$ is shear thickening, if $n = 1$ and $m = \mu$ then obviously we have a Newtonian fluid. However, this model has its limitations, as it is incapable of sufficiently describing viscosity at low shear rates. There is also no indication of any relationship between these parameters and the molecular weight and concentration.

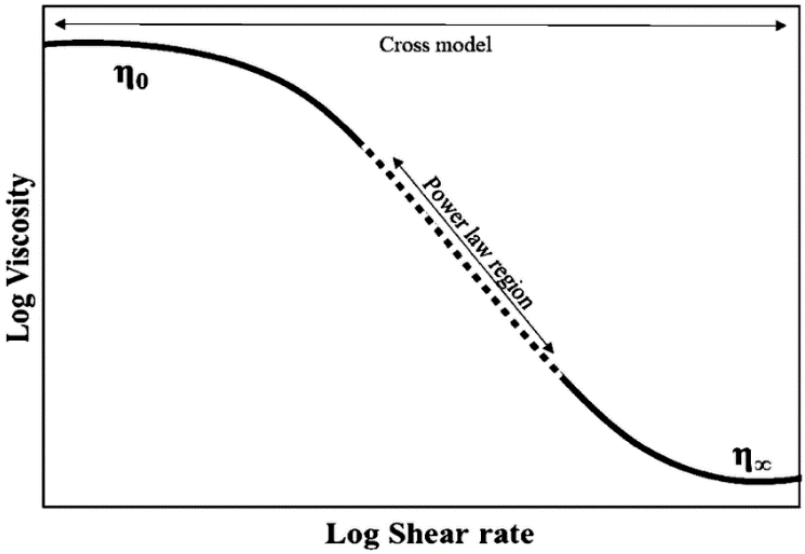

Figure 17 An idealized flow curve showing the power law region, zero shear and infinite shear viscosity regions (Yah, 2018).

6.2 Carreau-Yasuda Model

The Carreau-Yasuda Model is a generalization of the Newtonian fluid model and is based on five parameters(Andrade et al., 2007). The model is defined by the following equation,

$$\eta = \eta_\infty + (\eta_0 - \eta_\infty)[1 + (\lambda\dot{\gamma})^a]^{\frac{n-1}{a}} \tag{27}$$

Where, λ is the time constant, a is a dimensionless parameter describing transition region between zero shear rate region and power law region.

The Carreau-Yasuda model includes additional parameters, which make it more capable of describing the variation of viscosity, η with shear rate, $\dot{\gamma}$ at a higher accuracy when comparing to the power law model.

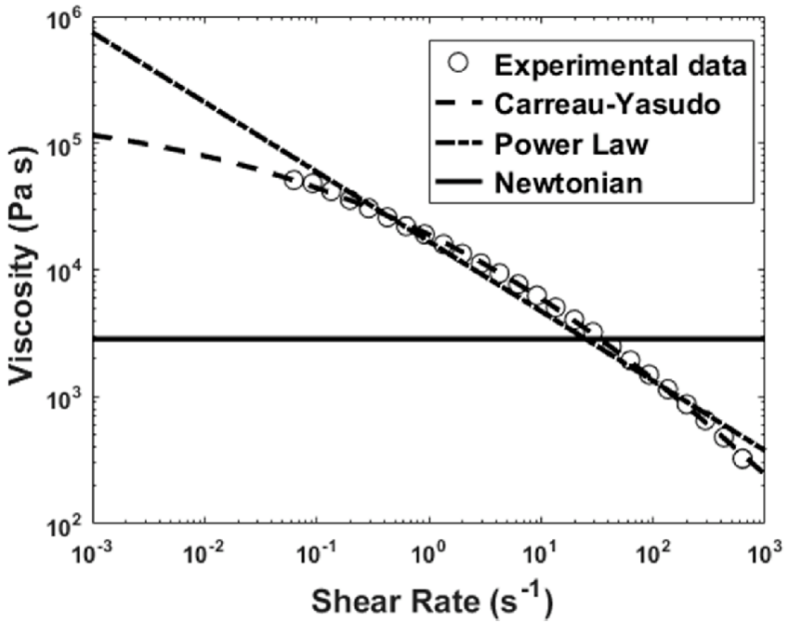

Figure 18 Shear viscosity curve fitting using Generalized Newtonian Fluid models (Wang and Smith, 2018).

7. Physical Non-Newtonian Fluid Models

Moving on, polymer molecules will be considered as elastic dumbbells with two beads connected by a spring and are suspended by a Newtonian solvent.

7.1 Hookean Dumbbells Model

Dumbbell models are based on the idea of idealizing polymer molecules as dumbbells with beads connected by elastic connectors (Bird et al., 1987). And for the Hookean dumbbell model it differs with a Hookean spring connecting these beads, where this spring is assumed to obey Hook's law,

$$\boldsymbol{F} = H\boldsymbol{Q} \tag{28}$$

Where, $\boldsymbol{F}$ is the connector force, H is the spring constant and $\boldsymbol{Q}$ is the connector vector between beads.

The simplicity of this model brings disadvantages such that this model is considered realistic only for small deformations from equilibrium. And the model does not have an extensibility limit, meaning that the dumbbells can stretch infinitely (Shogin. 2020).

7.2 FENE Dumbbell Model

FENE which stands for Finitely Extensible Non-Linear Elastic is another bead-spring model that builds on the Hookean dumbbell model by incorporating a non-linear spring (Leschber, n.d.). In an attempt to resolve the shortcomings of the basic dumbbell model (Warner, 1972) introduced a new parameter Q_0 which defines the maximum spring extension. This gives the altered equation,

$$F = \frac{H\boldsymbol{Q}}{1 - \frac{Q^2}{Q_0^2}} \tag{29}$$

Where, Q is an extension of the connector vector and Q_0 is the maximum spring extension.

This model is assumed applicable for sufficiently dilute polymer, capable of describing the shear rate dependence of intrinsic viscosity fairly decent (Bird et al., 1980). But it cannot describe the internal motions of the polymers sufficiently, thus the model is not a good fit to display accurate curves for complex viscosities.

By dilute polymer solution it is meant that the polymer molecules will interact more with the Newtonian solvent than the polymer molecules, this gives them more room to move and expand freely. And even though this model was developed to apply an extensibility limit, we are actually unable to measure the extension of these molecules (Leschber, n.d.).

7.2.1 FENE-P Dumbbell Model

FENE-P where P stands for Peterlin is an extension of the FENE dumbbell model which its main disadvantage is that it cannot yield a closed-form constitutive equation for the polymer stress (van Heel et al., 1998). Therefore, Peterlin suggested to replace the denominator of FENE model connector force by a pre-averaged value enabling him to close the model (Deville and Gatski, 2012).

$$F = \frac{H\boldsymbol{Q}}{1 - \langle\frac{Q^2}{Q_0^2}\rangle} \tag{30}$$

There are two stress contributors in a FENE-P fluid, the contribution of the Newtonian fluids and the polymer, which is suspended in it, this gives following total stress,

$$\boldsymbol{\tau} = \boldsymbol{\tau}_s + \boldsymbol{\tau}_p \tag{31}$$

Where, $\boldsymbol{\tau}_s$ is the stress contribution of the solvent and $\boldsymbol{\tau}_p$ is the stress contribution of the polymer.

The polymer contribution to the stress tensor of the solution are reliant on firstly the ideal gas pressure nkT where n is number of dumbbells, k is the Boltzmann's constant and T the temperature (D. Shogin and Amundsen, 2020). Secondly the dimensionless nonlinearity parameter,

$$b = \frac{hQ_0^2}{kT} \tag{32}$$

And thirdly the time constant,

$$\lambda = \lambda_Q = \frac{\zeta Q_0^2}{12kT} \tag{33}$$

Where ζ is the confirmation independent coefficient of the Stoke's law.

$\boldsymbol{\tau}_p$ takes part in the following constitutive equation,

$$\frac{b}{3} Z\boldsymbol{\tau}_p + \lambda\boldsymbol{\tau}_{p(1)} - \lambda\{\boldsymbol{\tau}_p - nkT\boldsymbol{\delta}\} D_t \ln Z = -nkT\dot{\gamma} \tag{34}$$

Where, Z is the Z-factor and $\boldsymbol{\tau}_{p(1)}$ is an Oldroyd derivation of $\boldsymbol{\tau}_p$.

The model is considered highly suitable for polymer solutions (Purnode and Crochet, 1998). As it can exhibit shear-thinning while its elongational viscosity remains finite for all rates of extension.

7.2.1.1 C-FENE-P Dumbbell Model

All the previous models fail to describe behavior of polyelectrolyte solutions, as they cannot account for the electric repulsion between the mobile ions. Therefore, in an attempt to derive closed constitutive equations for such fluids, Dmitry Shogin and Amundsen (2020), proposed a new model, the C-FENE-P model where C stands for charged. D. Shogin and Amundsen (2020) describes this repulsive characteristic by defining a new term to the FENE-P connector force,

$$F = \frac{H\boldsymbol{Q}}{1 - \frac{Q^2}{Q_0^2}} + \frac{q^2}{4\pi\varepsilon_0\varepsilon}\frac{\boldsymbol{Q}}{Q^3} \tag{35}$$

Where, ε is the relative permittivity of the solvent, ε_0 is the permittivity of vacuum and q is the effective charge.

The constitutive equation yields,

$$\frac{b}{3}Z\boldsymbol{\tau}_p + \lambda\boldsymbol{\tau}_{p(1)} - \lambda\{\boldsymbol{\tau}_p - nkT\boldsymbol{\delta}\}D_t \ln Z = -nkT\dot{\gamma} \tag{36}$$

Similarly to FENE-P, we have an identical constitutive equation that differs with Z consisting of a dimensionless ratio E that can be mathematically written as,

$$E = \frac{q^2}{(4\pi\varepsilon_0\varepsilon Q_0)kT} \tag{37}$$

And the Z-factor is expressed as,

$$Z = (Z_{FENE} - 1)\mathcal{F}(Z_{FENE} - 1, E/b) \tag{38}$$

Where, Z_{FENE} is the original Z-factor of FENE-P model and $\mathcal{F}$ is a special function introduced by D. Shogin and Amundsen (2020).

The E which is specific to C-FENE-P is the intrinsic rigidity of the polyelectrolyte molecules and accounts for salt-sensitivity. Lower salinity results in higher values of E, yielding stiffer molecules.

7.3 Concentrated Solutions

Up until now only dilute fluids have been considered. Therefore, the previous mentioned models are no longer valid for concentrated polymer solutions, hence new models accounting for close-packed molecular interaction are necessary to predict fluid behavior.

7.3.1 Phan-Thien-Tanner Model

Lodge and Yamamoto introduced the network theory for polymeric fluids in the mid-nineteen hundreds (Ferrás et al., 2019; Thien and Tanner, 1977). Later on, several constitutive equations were derived based on this theory, but Phan-Thien and Tanner argued that these models do not accurately account for the rates of creation and destruction of network junctions. Therefore, Thien and Tanner (1977) developed a single-mode model that describes simple shear and elongation flows while at the same time account for creation and destruction of such networks, assuming the fluid is incompressible and isothermal. Their work resulted the following relationship,

$$Z(tr\boldsymbol{\tau})\tau + \lambda\boldsymbol{\tau}_{(1)} = \eta_0\dot{\gamma} \tag{39}$$

Where, $tr\tau$ is the trace of the stress tensor.

The model was originally introduced with the linear component,

$$Z(tr\boldsymbol{\tau}) = 1 + \frac{\varepsilon\lambda}{\eta_0} tr\boldsymbol{\tau} \tag{40}$$

Where, ε is the extensibility parameter.

Phan-Thien proceeded solely to derive a more complex version of the model by accounting for an exponential growth of certain fluid components by introducing an alternative, exponential form for Z, Eq. (41).

$$Z(tr\boldsymbol{\tau}) = e^{\frac{\varepsilon\lambda}{\eta_0} tr\boldsymbol{\tau}} \tag{41}$$

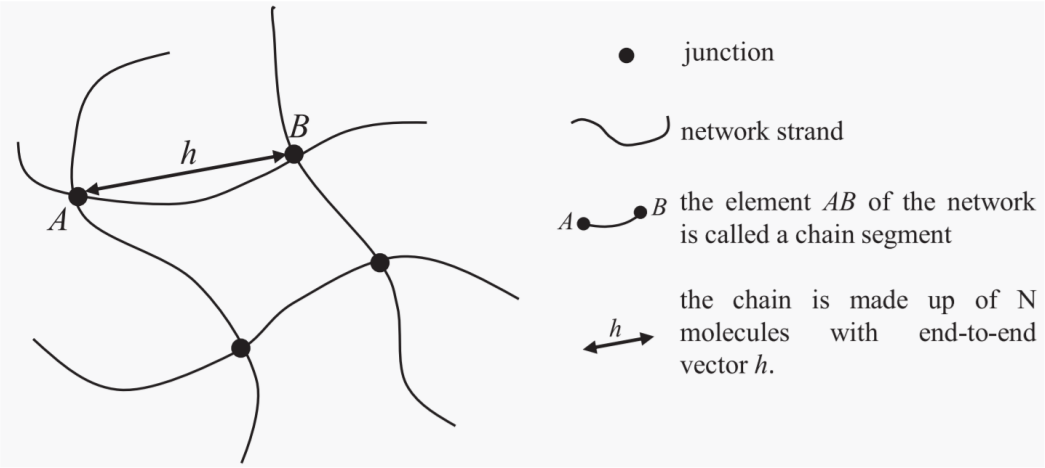

Figure 19 Lodge–Yamamoto network. The polymer liquid consists of polymer segments connected by junctions, and constantly changes its topology (Ferrás et al., 2019).

8. The Experiment

8.1 Procedure

The experiment for this thesis was conducted stepwise with the following steps:

1. First, prepare three brine solutions with predefined salinities.
2. Secondly, prepare a ‘’pure’’ solution of a specific polymer with a predefined concentration, prepared with distilled water.
3. Thirdly, prepare three additional solutions of the same polymer mixed with brines of different salinities, but maintain approximately the same polymer concentration as the ‘’pure’’ polymer solution.
4. Then reiterate step 2 and 3 for a different type of polymer.
5. Conduct steady shear ramp, start-up and relaxation measurements for a range of shear-rates using an advanced rheometer.
6. Lastly, analyze data obtained from laboratory measurements.

8.1.1 Brine Preparation

For this experiment three brines where prepared, the brines consisted of half a liter distilled water with dissolved Sodium Chloride. The brine solutions had concentrations of 5, 10 and 20 grams per liter.

Solid Sodium chloride samples were weighed to be 2.5, 5 and 10 grams for the three concentrations, respectively.

The distilled water was contained in a half liter container, and the Sodium Chloride was added to it slowly as the solution was stirred on a magnetic stirrer for thirty minutes.

Further on, to remove any solid particles the solutions were filtered through a nylon mesh, able to retain particles sizes larger than 22 μm using a vacuum pump.

This procedure was executed for all three concentrations.

Sample	Distilled water (l)	NaCl (g)	Salinity (g/l)
1	0.5	2.5	5
2	0.5	5	10
3	0.5	10	20

Table 1 Amount of distilled water (l) and NaCl (g) for three different brines.

8.1.2 Polymer Solution Preparation

Eight polymer solutions were prepared for this experiment, six of which were mixed with brines of different salinities. The polymer types selected were FLOPAAM 5115 VHM and FLOPAAM 3630-S. The desired polymer concentration was 6000 ppm for all solutions see Table. 2 and 3, to obtain an unbiased comparison for later analysis.

The polymer preparation procedure started by adding an arbitrary amount of distilled water or brine into a container, depending on if it is a saline or non-saline solution that is desired. The weight of the liquid was then measured and the amount of polymer powder to be added was calculated using formula 1, with desired concentration goal of 6000 ppm. The polymer powder was added to liquid gradually as it was mixing using Heidolf propeller mixer. The solution underwent mixing for two hours at a rate of 750 rpm.

Further on, the solution was moved over to a magnetic stirrer and was left to stir for 24 additional hours. This is to obtain a homogenous polymer hydration and remove any bubbles for optimal measurements.

Lastly, the polymers were poured into bottles and labeled with their respective specifications and stored in the refrigerator to attenuate any degradation.

FLOPAAM	3630-S	5115 VHM
Group	Standard	Acrylamide acid polymers
Anionicity	Medium to high	Medium
Molecular weight	High	Very high

Table 2 FLOPAAM parameters.

8.1.3 Concentration Determination

The following mathematical set up was used to obtain the desired concentrations of polymers:

$$Required\ mass\ of\ polymer\ (g) = \frac{c \cdot Ms \cdot 10^{-6}}{1 - c \cdot 10^{-6}} \tag{44}$$

Where, c is the desired concentration (ppm) and Ms is the measured mass of solvent (g).

$$True\ concentration\ of\ polymer\ (ppm) = \frac{Mp}{Mp + Ms} \cdot 10^{6} \tag{45}$$

Where, Mp is the measured mass of polymer (g).

Polymer	NaCl concentration (g/l)	Desired polymer concentration (ppm)	Measured mass of solvent (g)	Calculated mass of polymer (g)	Measured mass of polymer (g)	True concentration of polymer (ppm)
FLOPAAM 5115 VHM	0	6000	276.21	1.67	1.68	6045.59
	5	6000	153.97	0.93	0.93	6003.87
	10	6000	182.51	1.10	1.11	6045.09
	20	6000	199.49	1.20	1.21	6028.90

Table 3 True concentration of FLOPAAM 5115 VHM for different salinity solutions.

Polymer	NaCl concentration (g/l)	Desired polymer concentration (ppm)	Measured mass of solvent (g)	Calculated mass of polymer (g)	Measured mass of polymer (g)	True concentration of polymer (ppm)
FLOPAAM 3630-S	0	6000	182.20	1.10	1.10	6001.09
	5	6000	110.96	0.67	0.67	6001.97
	10	6000	161.52	0.97	0.98	6030.77
	20	6000	167.27	1.01	1.01	6001.90

Table 4 True concentration of FLOPAAM 3630-S for different salinity solutions.

8.1.4 Measurement Procedure

For this experiment an advanced rheometer by Anton Paar was used, namely the MCR 302. It is capable of performing high accuracy rheological measurements with several accessory systems. For the purpose of this thesis, the cone and plate measuring system were the preferable choice, due to its capability to provide constant shear rate during measurements, among other reasons.

It is obvious from the name cone and plate measuring system that it comprises of a flat circular cone and a plate, which in this case the CP-50 MS cone was selected (Mezger, 2019). The cone is of unique geometrical shape that enable us to achieve a constant shear rate. The cone is the mobile part of this system and has radius, R and cone angle, α. DIN-standards recommends remaining within the cone radius range $10\ mm \leq R \leq 100\ mm$ and $\alpha = 1°$. The plate is the stationary part of the system and is mounted onto the rheometer stand.

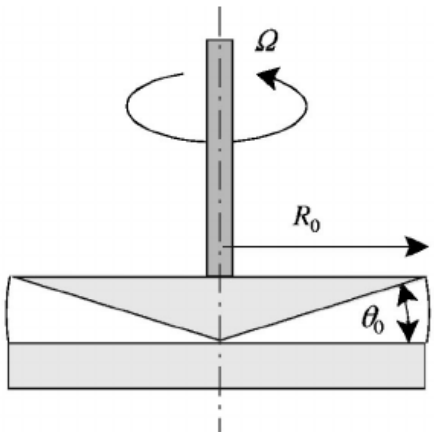

Figure 20 An illustrative diagram of the cone-and-plate system (Rothstein and Mckinley, 2001).

Before any measurements takes place, the system is turned on and initialized, and the plate is set to an arbitrary desired constant temperature. Normal force readings were calibrated to 0 N. A zero-gap run is performed and then a sample of empirical amount is added onto the stationary plate. The cone is then set to measuring position and ready to run measurements on a pre-defined program created on the rheometer software platform. The rheometer is connected to a pc that transmits the program run to the rheometer and in return receives a feed

of data. The chosen rheometer parameters for measurements were the same for all polymer solutions, this is to obtain data that is unbiased.

General rheometer parameters

Parameter	
Cone type	CP-50-1-SN30011 MS
Cone angle	$\alpha = 1°$
Plate diameter	$d = 25\ mm$
Gap between cone and plate	$a = 96\ \mu m$
Plate temperature	$T = 24\ °C$
Initial normal force	$NF = 0\ N$

Table 5 Rheometer parameters for cone CP-50-1-SN30011 MS.

8.1.4.1 Steady Shear Ramp Measurement

The steady shear ramp measurements were conducted using Anton Paar's cone and plate system with the variable measuring point duration log measuring profile, see Table. 5. The objective was to obtain viscosities of the for all salinity levels of FLOPAAM 5115 VHM and FLOPAAM 3630-S polymer solutions that are considered in this paper. Measurements took place for shear rates ranging from 0.01 upto 1000 s^{-1} for a total of 25 measuring points. Starting 60 s of measuring time and ending with 7 s for the final point. The plate temperature was preset to 24 $°C$.

Parameter		
Temperature	24 $°C$	
Range of shear rates	0.01-1000 1/s	
Measuring profile	Var. meas. pt. duration log	
Measuring points	25 pts.	
Measuring time duration	Initial: @ 0.01 1/s	60 s
	Final: @ 1000 1/s	7 s

Table 6 Parameters for steady shear ramp measurements.

8.1.4.2 Start-up and Cessation Measurement

The start-up and cessation measurements were conducted using Anton Paar's cone and plate system with the variable measuring point duration linear measuring profile, see Table. 6. The objective was to obtain shear stress growth and decay data for all salinity levels of FLOPAAM 5115 VHM and FLOPAAM 3630-S polymer solutions that are considered in this paper. Measurements took place by imposing a constant step value of shear rates 0.01, 0.1, 1, 10, 100, 1000 s^{-1} for a total of 80 measuring points for each shear rate. The shearing for shear stress growth measurement were maintained until steady state was reached. After which, the shearing was suspended, and the shear stress decay was recorded. Each measurement consumed a predefined time of 30.63 s. The plate temperature was preset to 24 $°C$.

Parameter		
Temperature	24 $°C$	
Sequence of shear rates	0.01, 0.1, 1.0, 10, 100, 1000 1/s	
Measuring profile	Var. meas. pt. duration lin	
	Interval	
	1: Start-up	2: Relaxation
Measuring points	40 pts.	40 pts.
Measuring time duration	Initial: 0.01s	Initial: 0.01 s
	Final: 0.5 s	Final: 0.5 s

Table 7 Parameters for start-up and relaxation measurements.

9. Analysis

9.1 Steady Shear Ramp Data Analysis

In this section the data obtained from the steady shear ramp measurements will be graphically presented in a set of viscosity versus shear rate plots.

For both FLOPAAM 5115 VHM and FLOPAAM 3630-S solutions it is observable from viscosity versus shear rate Fig. 21 and 22 that the lower Newtonian region have an extremely narrow shear rate range prior for transition to the power law region. This differentiates significantly from other polymer types outside the scope of this thesis. The zero-shear rate viscosity ranges for shear rates $0.010 - 0.017\ s^{-1}$ and $0.010 - 0.019\ s^{-1}$ for FLOPAAM 5115 VHM, respectively.

As for the saline solutions, do however show noticeably a tendency for the lower Newtonian region to widen with increasing salinity.

Furthermore, with the increasing salinity the polymer seems to react to this by yielding a lower zero-shear rate viscosity, see Fig. 21 and Fig. 22. The plots also show a large gap between the zero-shear rate viscosity of the non-saline solutions and their corresponding saline solutions. The gap between the curves of the saline solutions do however become narrower with increasing salinity compared to the transition from 0 g/l NaCl to 5 g/l NaCl solutions of both polymer types.

Moving to the power law region of the curves it is obvious that the polymer solutions experience a shear-thinning effect. The simple curve patterns observed of the measured data can be represented by a power law model or a Carreau-Yasuda viscosity model, this is illustrated in Fig. 74 and 75 in Appendix. A. In addition to this it is noticeable that the inclination of the power-law region for 0 g/l NaCl solutions show a steeper trend, as compared to the saline solutions. Which experiences a decline in gradient with increasing salinity. It is already known that the addition of salt has a stabilizing effect on the solutions' viscosity which reduces the shear-thinning. This of course is not only dependent on the salinity level but also the polymer concentration. As matter in fact the values of n of the power law model are -0.65, -0.62 and -0.58 for salinities 5 g/l, 10 g/l and 20 g/l NaCl of

FLOPAAM 5115 VHM, respectively. While the polymer solution FLOPAAM 5115 VHM 0 g/l NaCl has an n value -0.83. As for FLOPAAM 3630-S the behavior is similar, but the values differ showing a more pronounced inclination. For this polymer type the values of n of the power law model are -0.71 and -0.63 for salinities 5 g/l, 10 g/l and 20 g/l NaCl of FLOPAAM 3630-S. And -0.86 for FLOPAAM 3630-S 0 g/l NaCl. These values are clearly showing the stabilization effect of salt.

Considering the right end of the curves, at high shear rates the curves of the various polymer solutions seem to move towards an almost identical infinite-shear rate viscosity. The plots also show that the impact of salinity decreases with shear rate and is almost non-existent if the shear rate is very high.

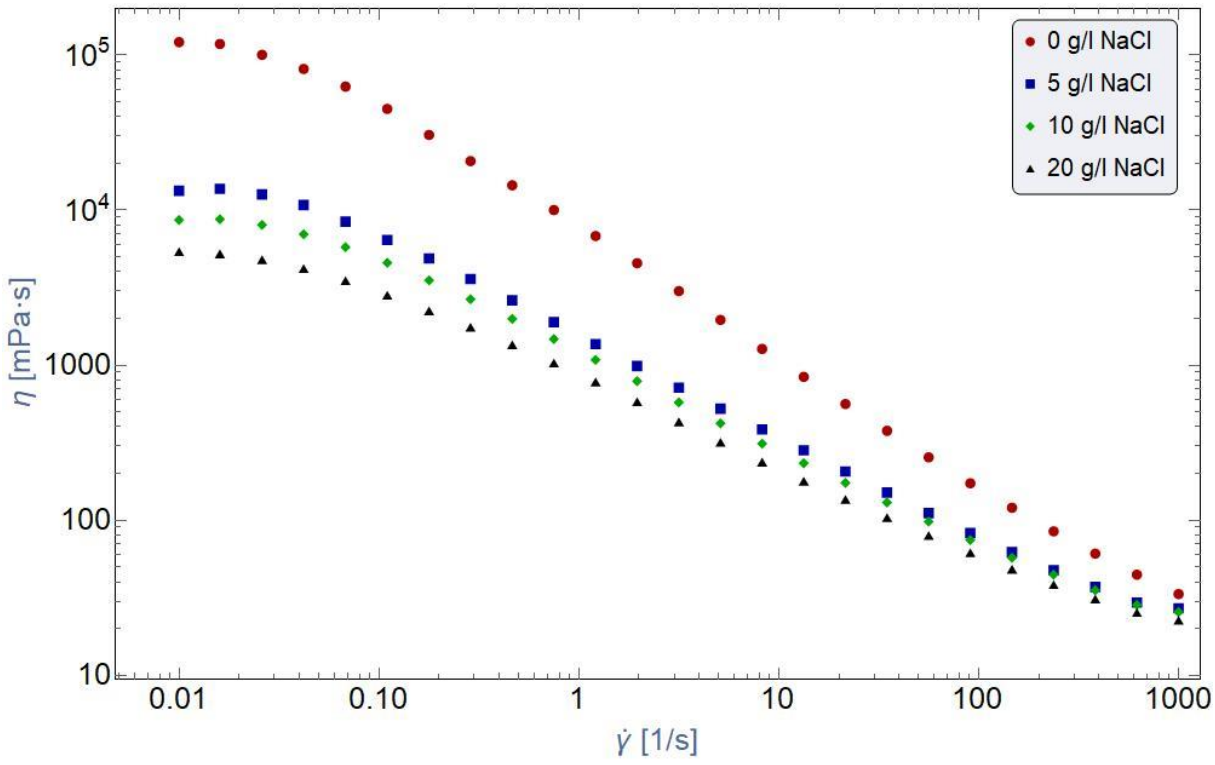

Figure 21 LogLog plot of viscosity versus shear rate for FLOPAAM 5115 VHM polymer solutions with various NaCl concentrations.

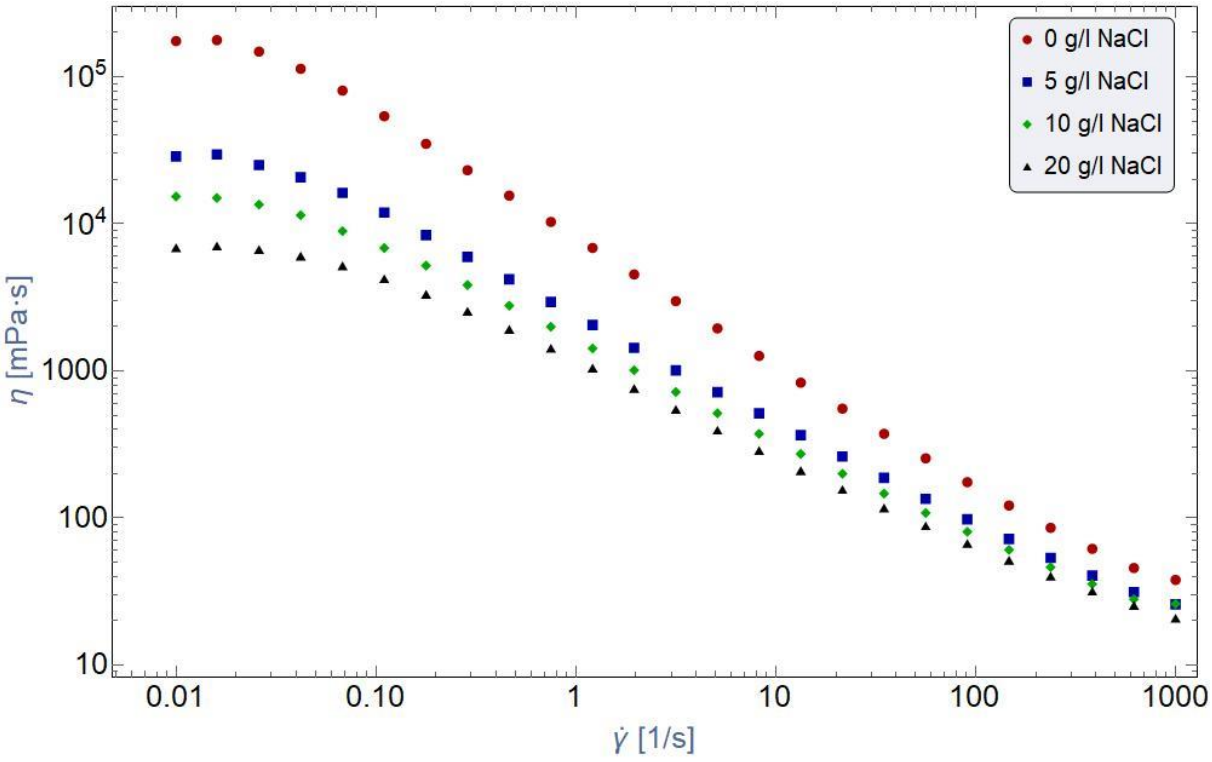

Figure 22 LogLog plot of viscosity versus shear rate for FLOPAAM 3630-S polymer solutions with various NaCl concentrations.

9.1.1 Data/Model Fitting

In the upcoming sub chapters the results of the model fitting will be discussed. The physical non-Newtonian fluid models LPTT, EPTT, FENE-P and C-FENE-P will be fitted against the measured data obtained from steady shear ramping tests. As the models use different scales, the viscosity was normalized, and the shear rate was scaled accordingly.

9.1.1.1 Full (Non-Affine) Linear PTT

For and ideal model fitting the viscosity of the measured data was normalized. The LPTT-model which was fitted against this scaled data is dependent on two parameters: ε and ξ. ξ is the affinity parameter that ranges from 0 to 1, at $\xi > 0$ the model is non-affine. These two parameters were selected manually for optimal fitting and resulted in normalized viscosity versus dimensionless shear rate plots with red dots representing the measured data and blue

line representing the model prediction. The dimensionless shear rate can be mathematically represented as $\lambda\dot{\gamma}$.

From Fig. 23 it is observable the LPTT model only predicts the first 4-5 data points. The model shows an overprediction of shear thinning for all solutions starting at $\lambda\dot{\gamma}$ values 4 and higher.

Based on the plots (Fig. 24, 25 and 26) for the saline solutions, the model predicts extreme shear-thinning. This can be explained the fact that this model has very limited applications, as the power-law index is of -2. Therefore, this is model is valid for only very weak flows (very low shear rates) and high polymer solutions. Thus, on cannot expect it to work for high shear rates for any material. And the salinity adds further a dilutive effect. Therefore, the model shows increasing shear-thinning, but the increase for 10 g/l NaCl and 20 g/l NaCl solutions is not to be considered drastic. Hence, on can state that increase in salt concentration is not significantly impactful as what was anticipated.

In conclusion, the LPTT model is unreliable for predicting polymer behavior at strong flows as expected. Therefore, it can only be applied for specific scenarios that does not include saline solutions or generally dilute or semi-dilute solutions.

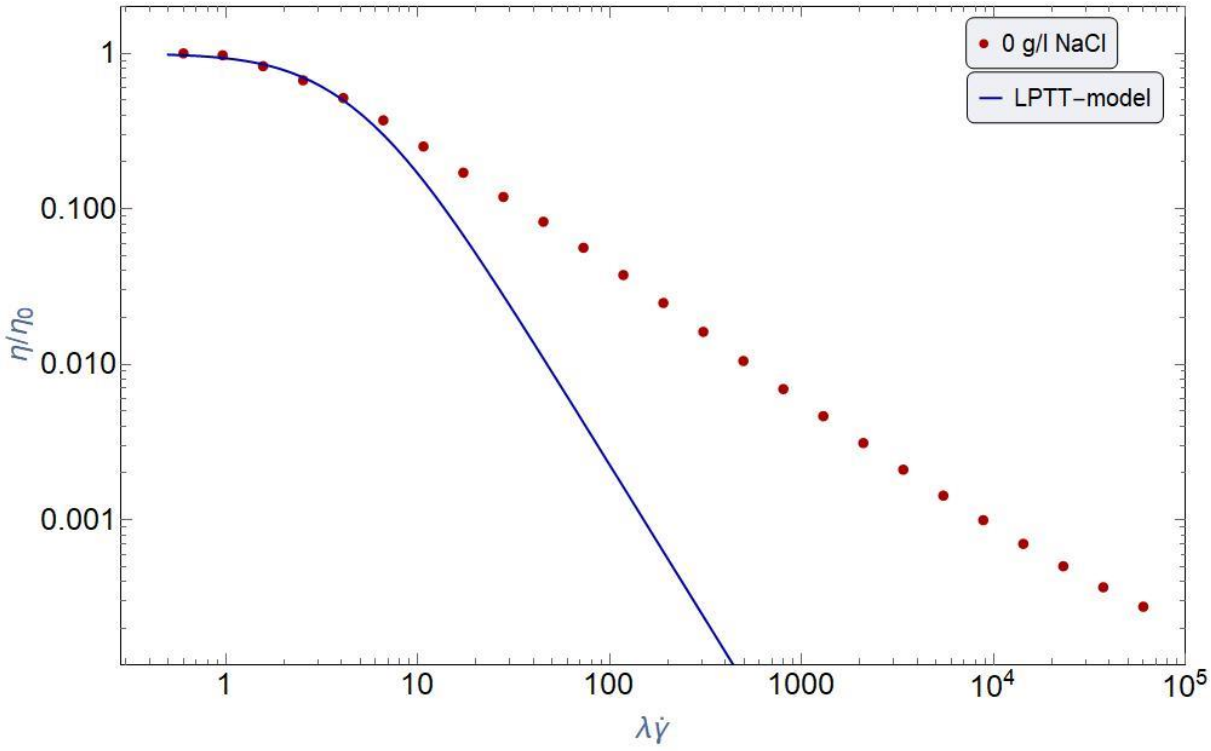

Figure 23 LogLog plot of normalized viscosity (red dots) and LPTT-model viscosity prediction (blue line) versus dimensionless shear rate for FLOPAAM 5115 VHM 0 g/l NaCl polymer solution. Fitted parameters: $\eta_0 = 121110, \varepsilon = 0.01, \xi = 0.03\ and\ \lambda = 60$.

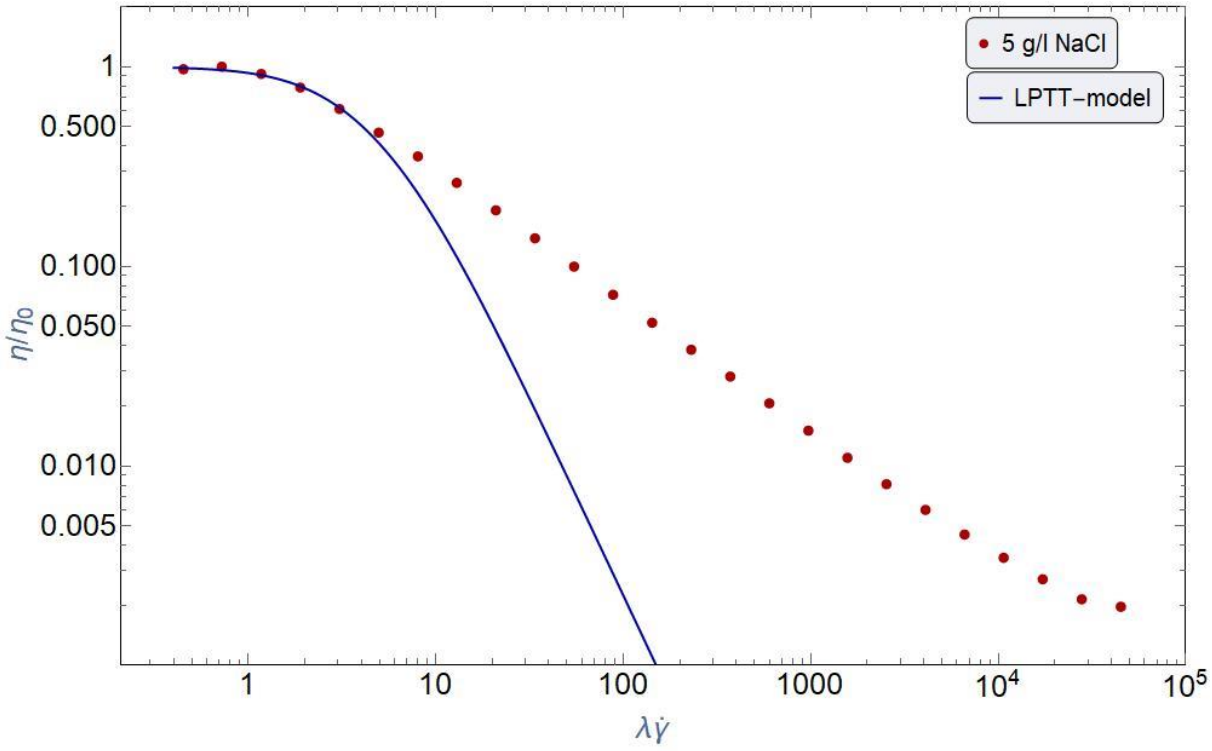

Figure 24 LogLog plot of normalized viscosity (red dots) and LPTT-model viscosity prediction (blue line) versus dimensionless shear rate for FLOPAAM 5115 VHM 5 g/l NaCl polymer solution. Fitted parameters: $\eta_0 = 13715, \varepsilon = 0.01, \xi = 0.03\ and\ \lambda = 45$.

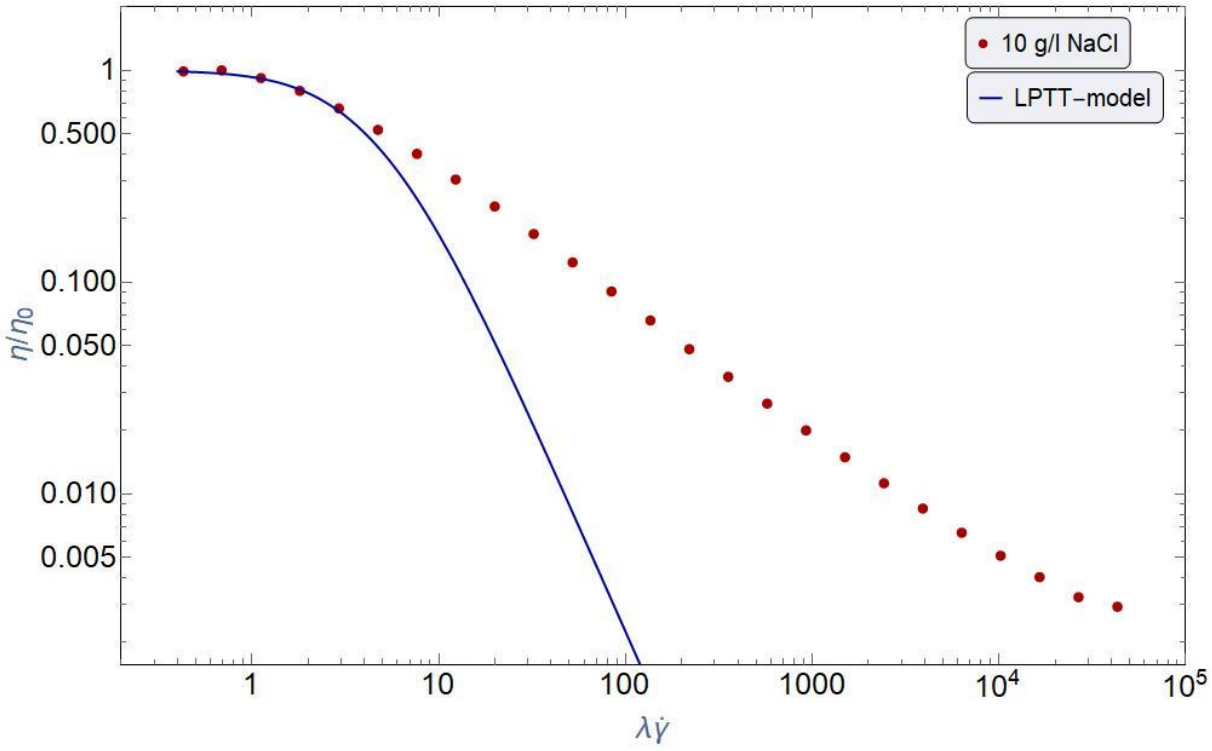

Figure 25 LogLog plot of normalized viscosity (red dots) and LPTT-model viscosity prediction (blue line) versus dimensionless shear rate for FLOPAAM 5115 VHM 10 g/l NaCl polymer solution. Fitted parameters: $\eta_0 = 8728, \varepsilon = 0.01, \xi = 0.03$ *and* $\lambda = 43$.

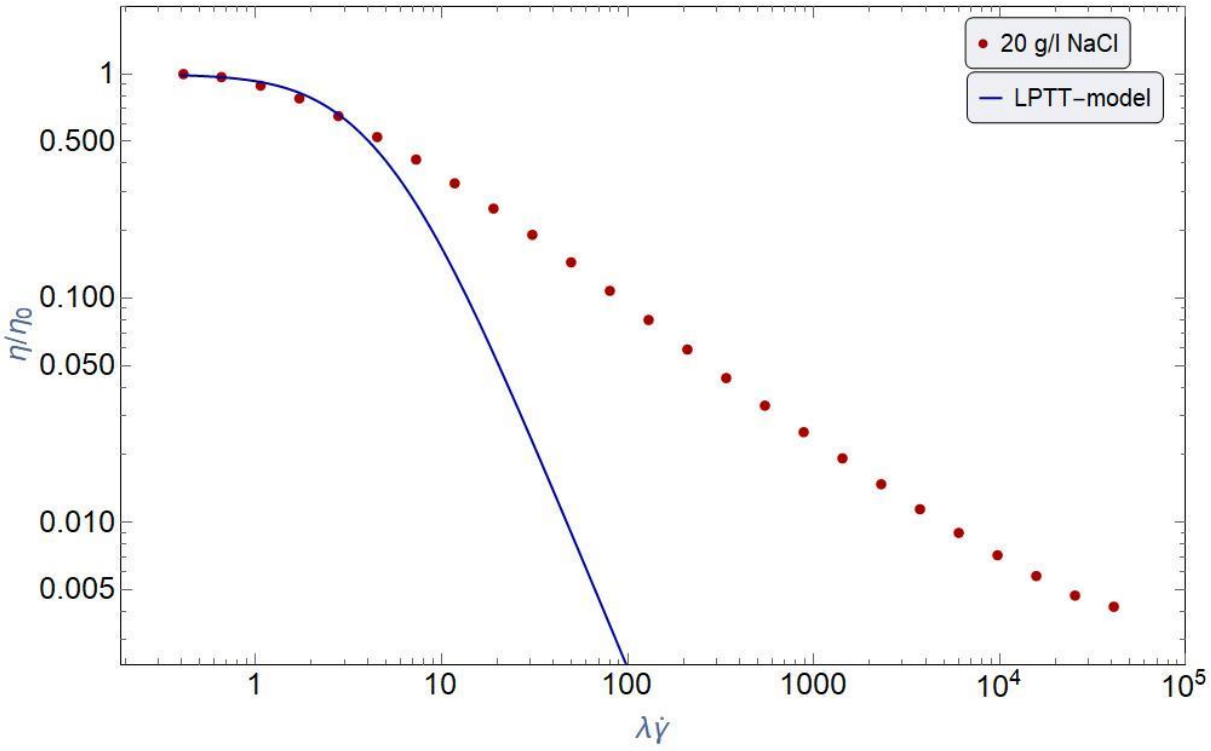

Figure 26 LogLog plot of normalized viscosity (red dots) and LPTT-model viscosity prediction (blue line) versus dimensionless shear rate for FLOPAAM 5115 VHM 20 g/l NaCl polymer solution. Fitted parameters: $\eta_0 = 5391.6, \varepsilon = 0.01, \xi = 0.03$ *and* $\lambda = 41$.

9.1.1.2 Affine Exponential PTT

The EPTT-model has only one master-curve and the model fitting resulted in normalized viscosity versus dimensionless shear rate plots with red dots representing the measured data and blue line representing the model prediction. The dimensionless shear rate can be mathematically represented as $2\sqrt{\epsilon}\lambda\dot{\gamma}$.

Fig. 27 shows almost perfect match between measured data and the EPTT-model prediction. For the 0 g/l NaCl solution we see an almost perfect alignment with the model, at least for $2\sqrt{\epsilon}\lambda\dot{\gamma}$-values ranging from low to intermediate high.

The same cannot be said for the saline solutions (Fig. 28, 29 and 30) as the model overpredicts the shear-thinning which increases with increasing salinity. In addition, the model alike LPTT does not have the ability to predict behavior of the upper-Newtonian

regions of the solutions. Furthermore, as the salinity increases, the fluid will flow more easily, and turbulence develops at lower shear rates.

This model as stated in previous chapters is an improvement of the LPTT-model which means the assumptions that it is only valid for concentrated solutions applies to the EPTT-model. And this explains the deviation in prediction for the model from the measured data for saline solutions. The explanation for the quite accurate prediction of the model for the 0 g/l NaCl lies in the exponential component incorporated in the EPTT-model.

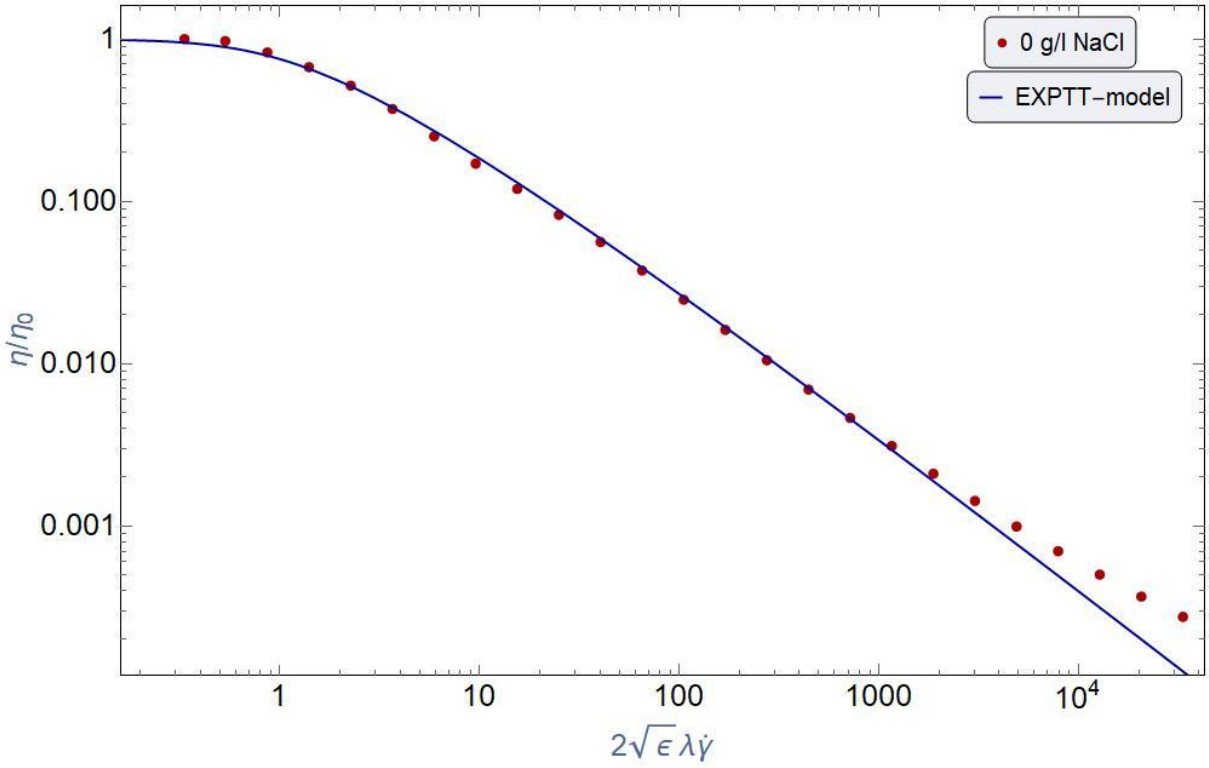

Figure 27 LogLog plot of normalized viscosity (red dots) and EPTT-model viscosity prediction (blue line) versus dimensionless shear rate for FLOPAAM 5115 VHM 0 g/l NaCl polymer solution. Fitted parameters: $\eta_0 = 121110$ and $2\sqrt{\epsilon}\lambda = 33.3$.

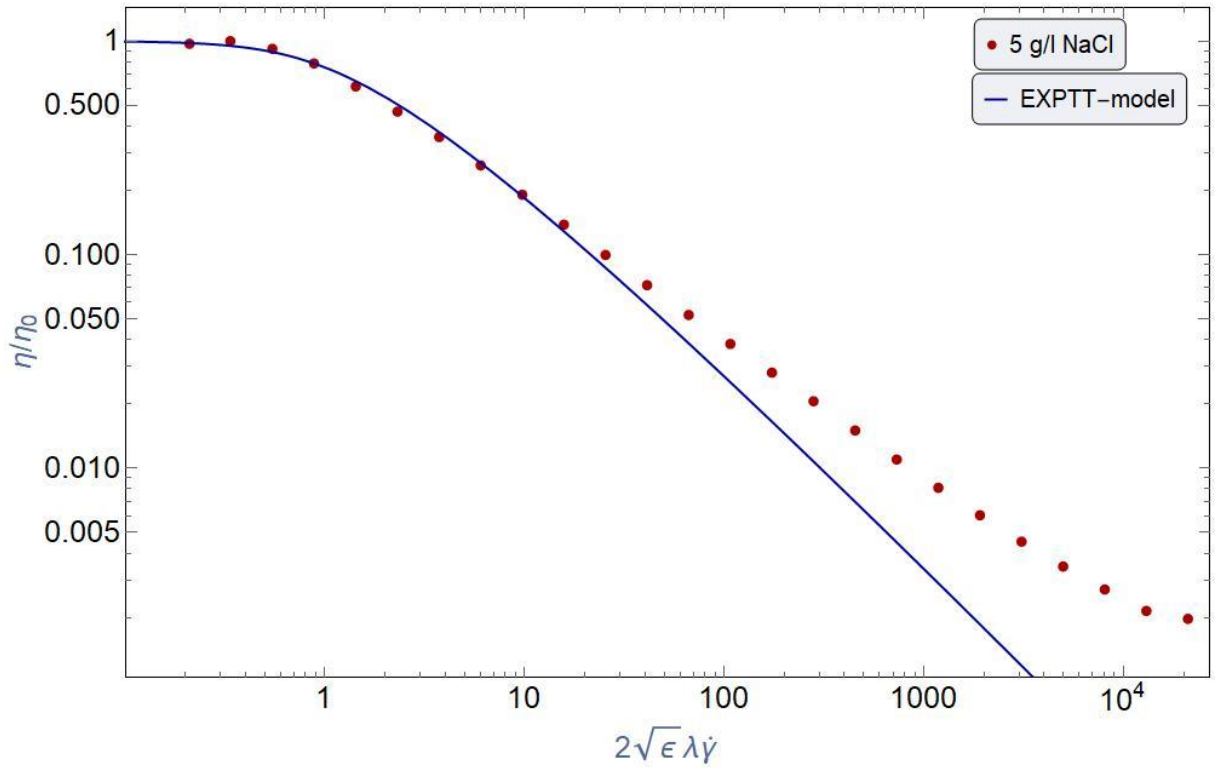

Figure 28 LogLog plot of normalized viscosity (red dots) and EPTT-model viscosity prediction (blue line) versus dimensionless shear rate for FLOPAAM 5115 VHM 5 g/l NaCl polymer solution. Fitted parameters: $\eta_0 = 13715\ and\ 2\sqrt{\epsilon}\lambda = 21$.

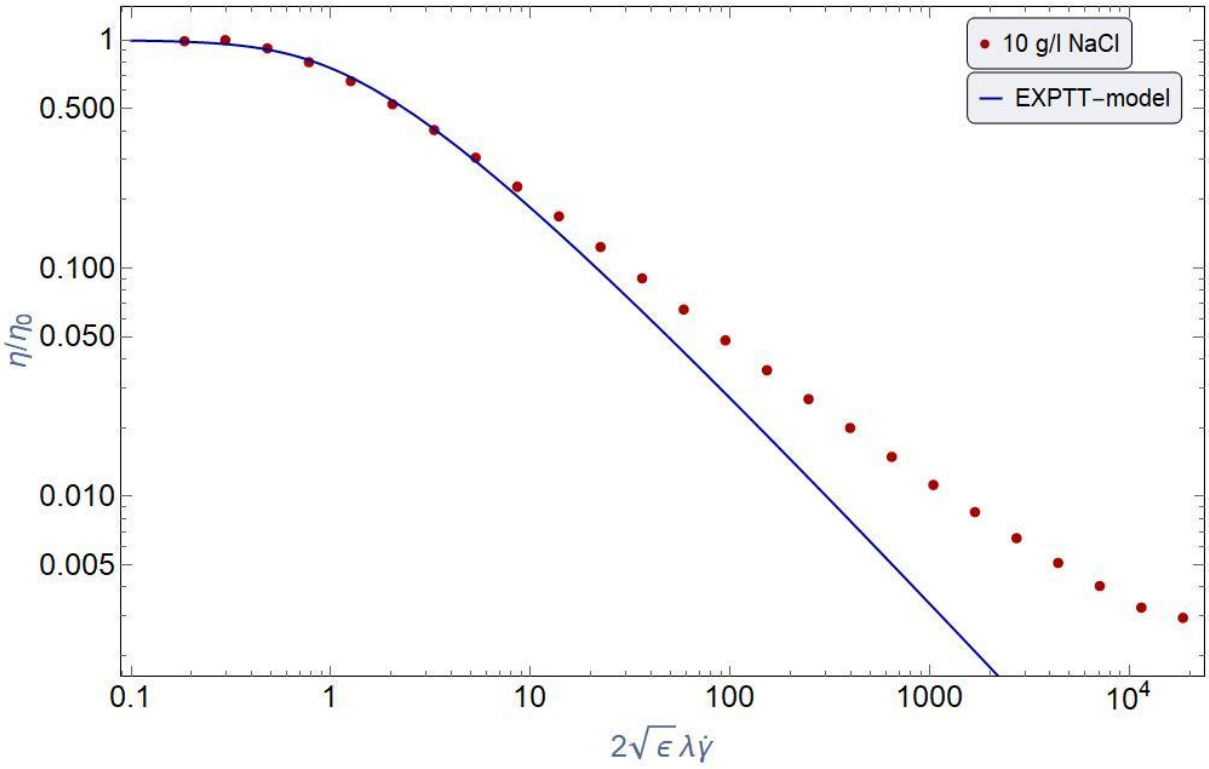

Figure 29 LogLog plot of normalized viscosity (red dots) and EPTT-model viscosity prediction (blue line) versus dimensionless shear rate for FLOPAAM 5115 VHM 10 g/l NaCl polymer solution. Fitted parameters: $\eta_0 = 8728.2\ and\ 2\sqrt{\epsilon}\lambda = 18.5$.

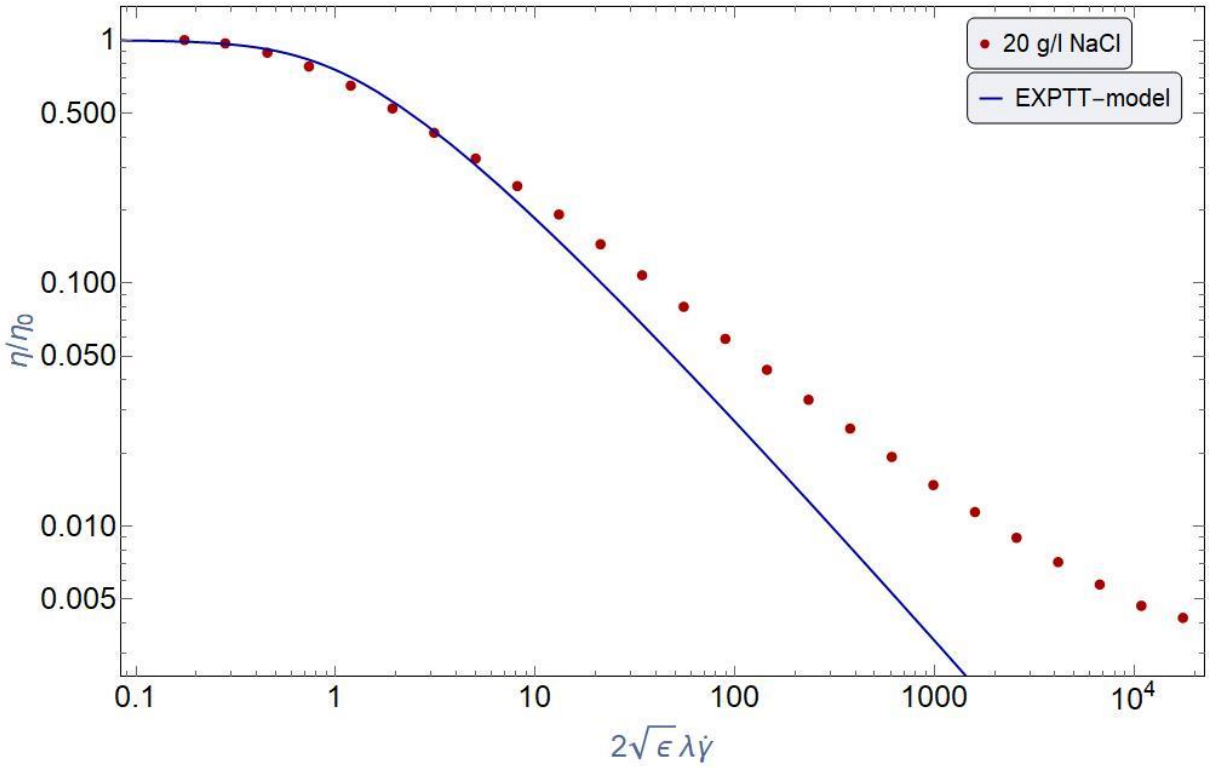

Figure 30 LogLog plot of normalized viscosity (red dots) and EPTT-model viscosity prediction (blue line) versus dimensionless shear rate for FLOPAAM 5115 VHM 20 g/l NaCl polymer solution. Fitted parameters: $\eta_0 = 5391.6\ and\ 2\sqrt{\epsilon}\lambda = 17.5$.

9.1.1.3 FENE-P Dumbbells / Affine Linear PTT

The FENE-P-model is the equivalent of LPTT up to parameter definition for steady shear flows, but is considered affine, $\xi = 0$. The model fitting resulted in normalized viscosity versus dimensionless shear rate plots with red dotted points representing the measured data and blue line representing the model prediction. The model has only one master-curve. The dimensionless shear rate can be mathematically represented as $\sqrt{3\,\epsilon/2}\,\lambda\dot{\gamma}$.

At a first glance at the FENE-P model prediction shows good prediction of shear-thinning behavior for saline solutions, this applies to both polymer types considered in this thesis, see Fig. 32, 33 and 34 below and Fig. 85, 86 and 87 in Appendix. A. Though the same cannot be said for the 0 g/l NaCl solutions (Fig. 31 and 84), as it underpredicts the shear-thinning of the polymer significantly and is only aligned with the first few measuring points due to the

polymer being a concentrated solution. This model predicts shear-thinning which asymptotically gives a power-law index of -2/3 (n=1/3). On the other hand, we see an almost perfect match for 5 g/l NaCl solution, regardless of the misalignment with last measuring points that shift away from shear-thinning behavior.

Furthermore, it seems the model is unable show predictions identical to the one of 5 g/l NaCl solution as it starts to overpredict shear-thinning for 10 and 20 g/l solutions for higher $\sqrt{3\,\epsilon/2}\,\lambda\dot{\gamma}$ values. This mismatch is due to turbulence at high shear rates.

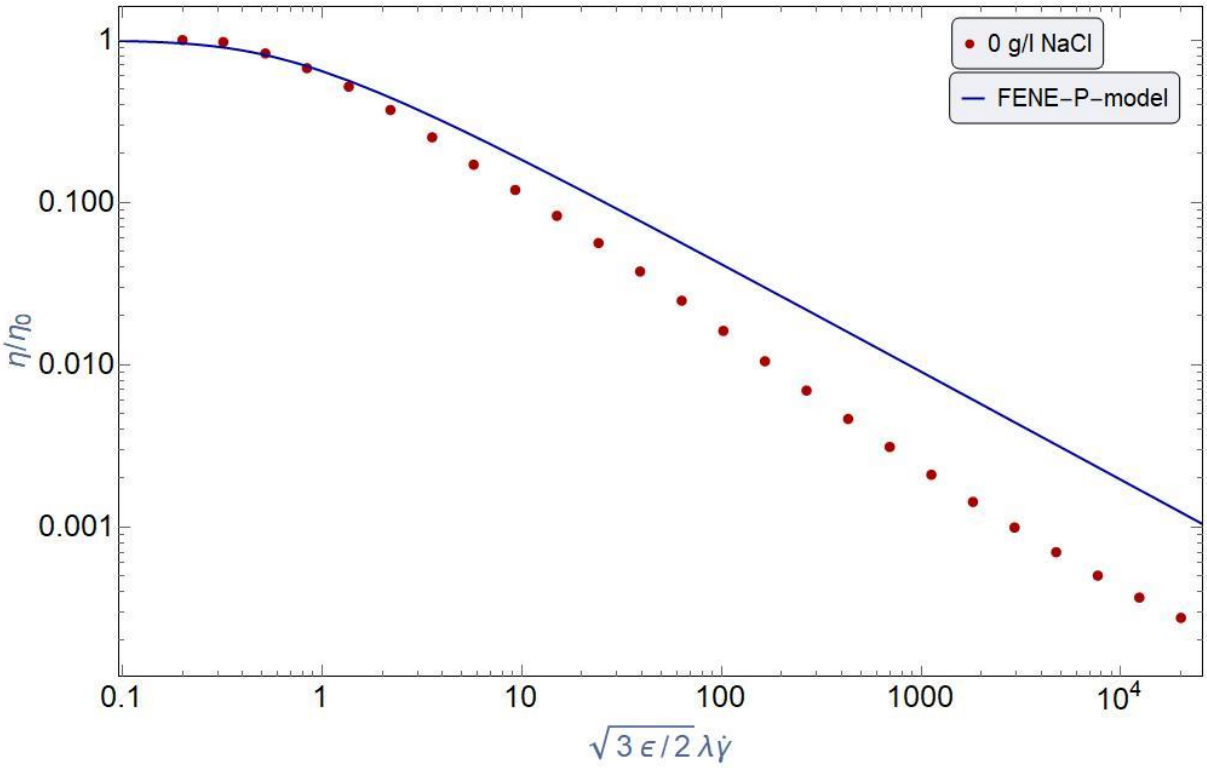

Figure 31 LogLog plot of normalized viscosity (red dots) and FENE-P-model viscosity prediction (blue line) versus dimensionless shear rate for FLOPAAM 5115 VHM 0 g/l NaCl polymer solution. Fitted parameters: $\eta_0 = 121110\ and\ \sqrt{3\,\epsilon/2}\,\lambda = 20$.

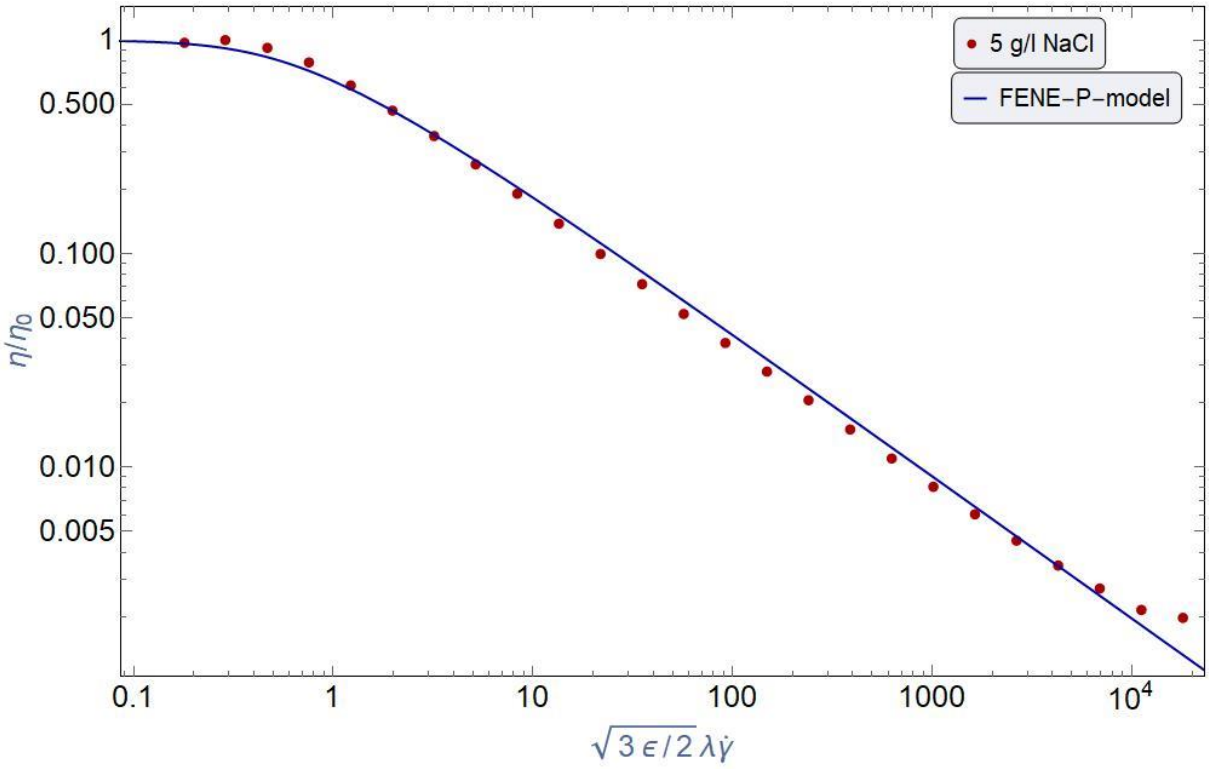

Figure 32 LogLog plot of normalized viscosity (red dots) and FENE-P-model viscosity prediction (blue line) versus dimensionless shear rate for FLOPAAM 5115 VHM 5 g/l NaCl polymer solution. Fitted parameters: $\eta_0 = 13715$ and $\sqrt{3\,\epsilon/2}\,\lambda = 18$.

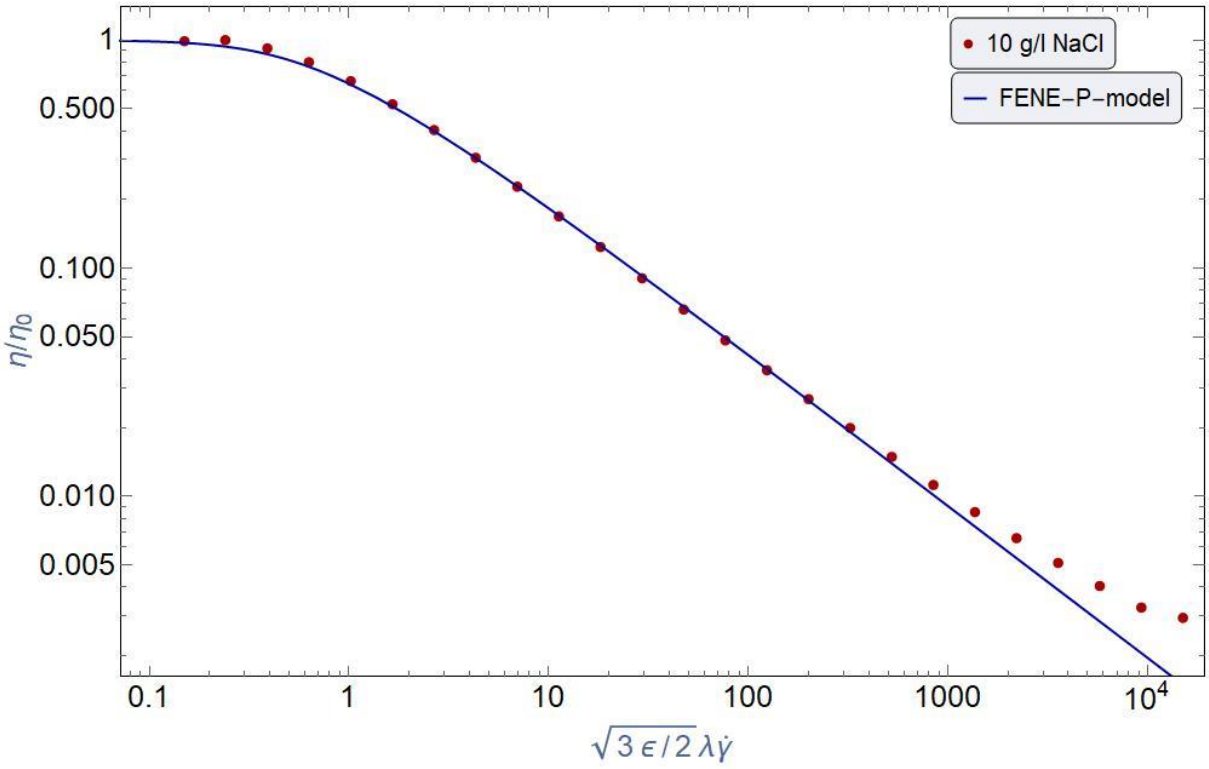

Figure 33 LogLog plot of normalized viscosity (red dots) and FENE-P-model viscosity prediction (blue line) versus dimensionless shear rate for FLOPAAM 5115 VHM 10 g/l NaCl polymer solution. Fitted parameters: $\eta_0 = 8728.2\ and\ \sqrt{3\,\epsilon/2}\,\lambda = 15$.

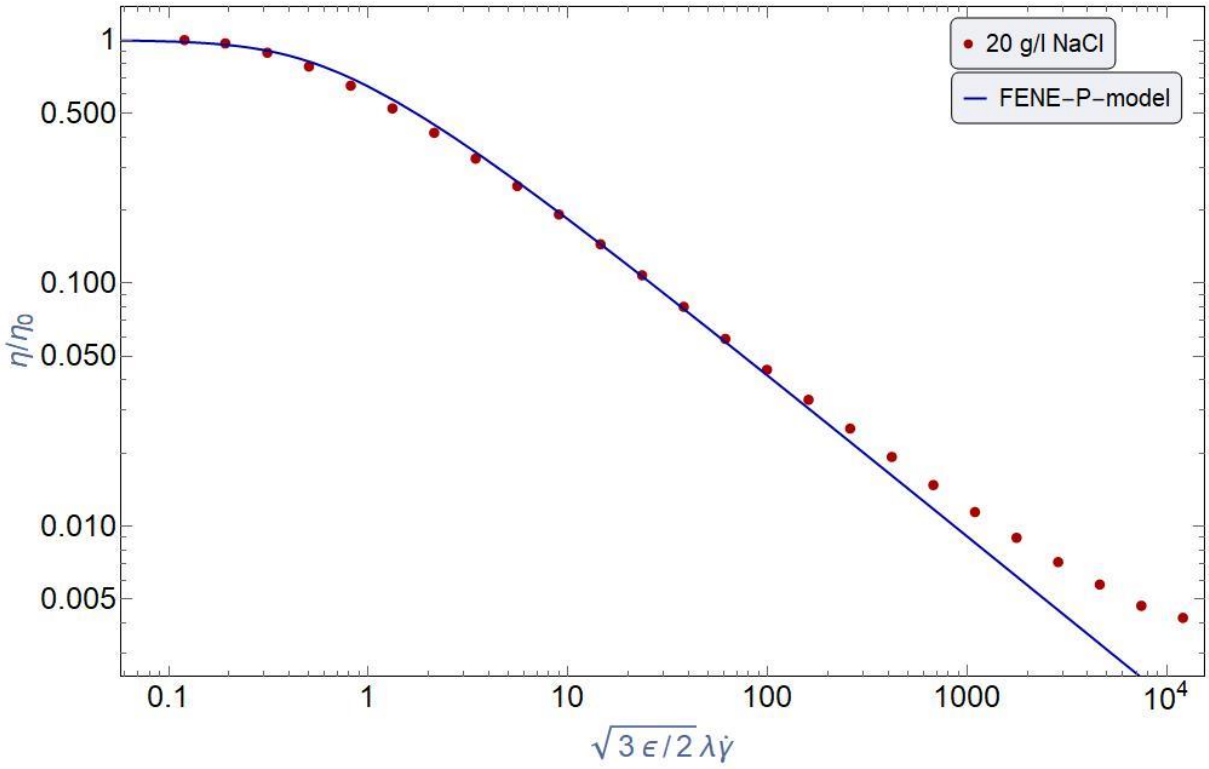

Figure 34 LogLog plot of normalized viscosity (red dots) and FENE-P-model viscosity prediction (blue line) versus dimensionless shear rate for FLOPAAM 5115 VHM 0 g/l NaCl polymer solution. Fitted parameters: $\eta_0 = 5391.6\ and\ \sqrt{3\,\epsilon/2}\,\lambda = 12$.

9.1.1.4 C-FENE-P Dumbbells

The C-FENE-P-model which was fitted against the scaled measured data which is dependent on two parameters: b and E. These two parameters were selected manually for optimal fitting and resulted in normalized viscosity versus dimensionless shear rate plots with red dotted points representing the measured data and blue line representing the model prediction. The dimensionless shear rate can be mathematically represented as $\lambda\dot{\gamma}$. A total of 8 figures have been generated, see Fig. 35, 36, 37 and 38 and Fig. 88, 89, 90 and 91 in Appendix. A.

For C-FENE-P we see a similar underprediction of shear-thinning for 0 g/l NaCl solution as was observed for the same solution for the FENE-P-model. What differs here though is that the model has been developed with the addition of the parameter E, that is supposed to

account for salt-sensitivity. In absence of salt, the polymer in this case will behave as a concentrated solution and C-FENE-P is not designed for such solutions.

As we move over to the saline solutions, we see a largely improved prediction of this model for all three salinities (5, 10 and 20 g/l NaCl). This lies in the previous mentioned parameter E, where the value is selected manually by the applier of the model.

Values of E for FLOPAAM 5115 VHM 0, 5, 10 and 20 g/l NaCl solutions were selected to be 1000, 800, 90 and 20, respectively. This complies with D. Shogin and Amundsen (2020) description of E, where lower salinity yields higher values of E. Which means the addition of salt in the solution has loosened up the polymer molecules. It shows that it is currently the best model to provide accurate prediction of saline polymer solutions.

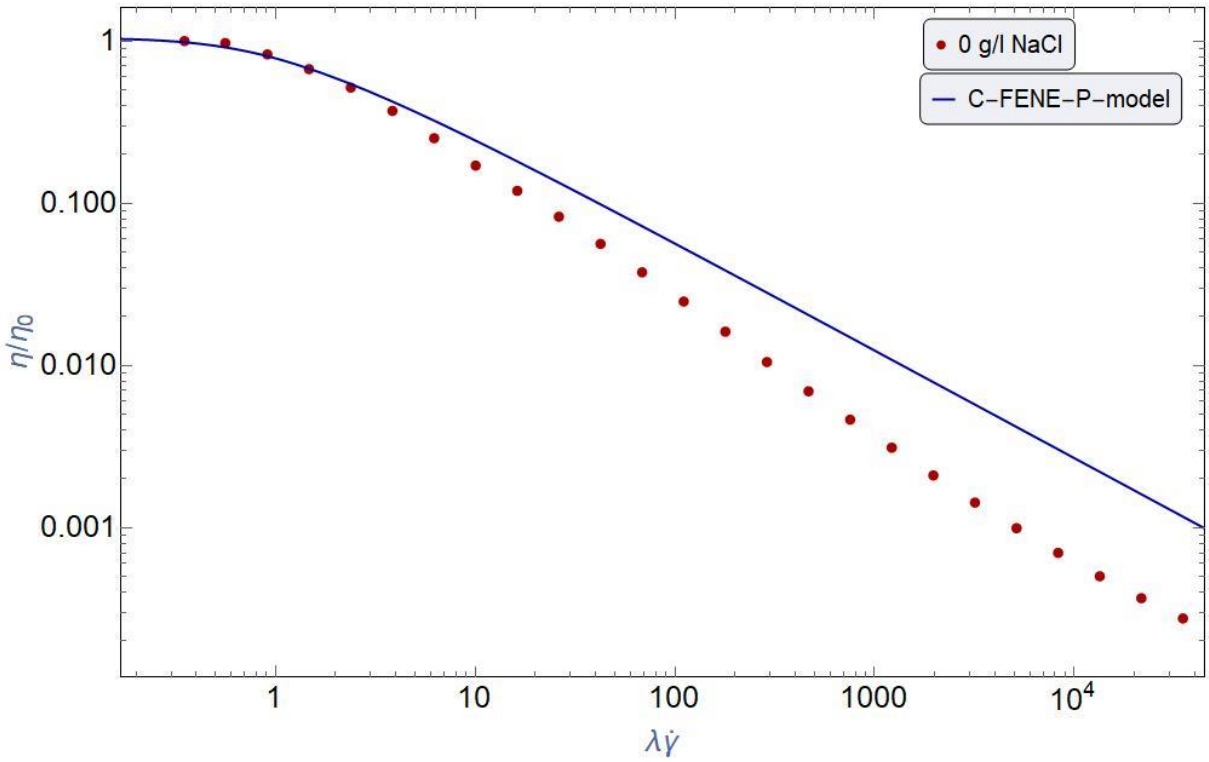

Figure 35 LogLog plot of normalized viscosity (red dots) and C-FENE-P-model viscosity prediction (blue line) versus dimensionless shear rate for FLOPAAM 5115 VHM 0 g/l NaCl polymer solution. Fitted parameters: $\eta_0 = 121110, \lambda = 35, b = 50\ and\ E = 1000$.

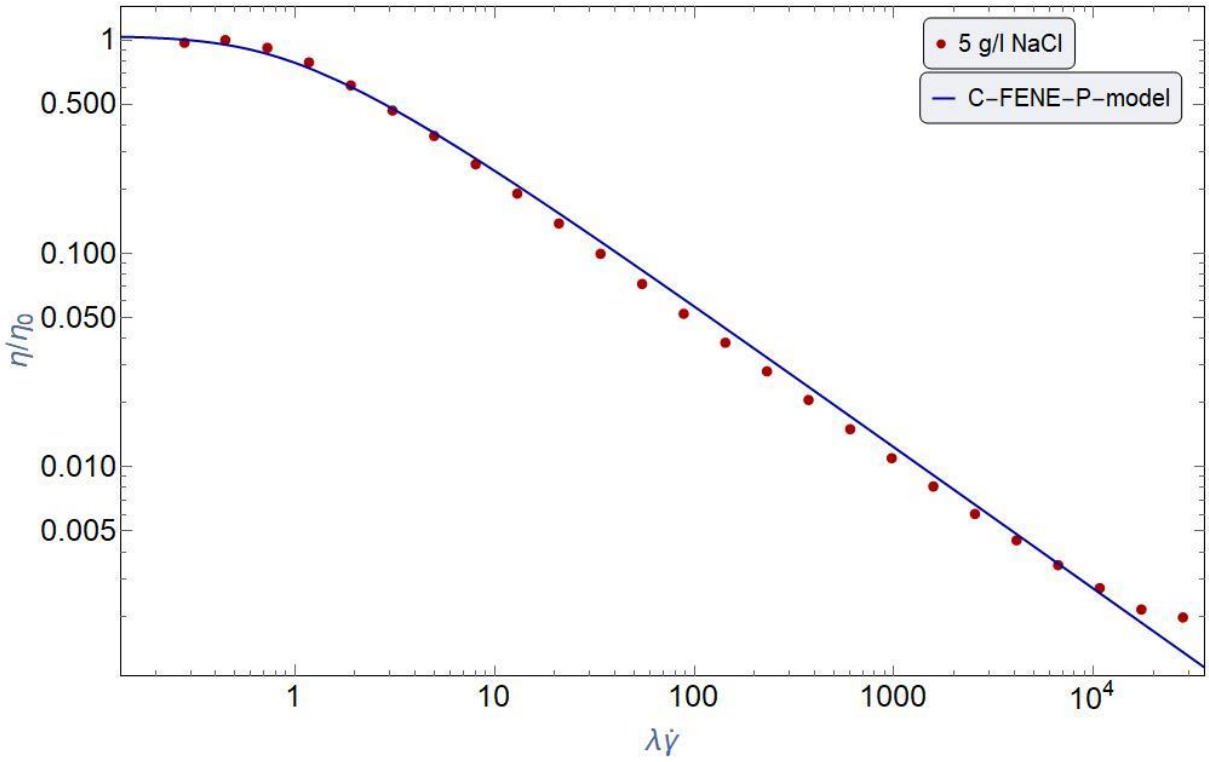

Figure 36 LogLog plot of normalized viscosity (red dots) and C-FENE-P-model viscosity prediction (blue line) versus dimensionless shear rate for FLOPAAM 5115 VHM 5 g/l NaCl polymer solution. Fitted parameters: $\eta_0 = 13715, \lambda = 35, b = 50\ and\ E = 900$.

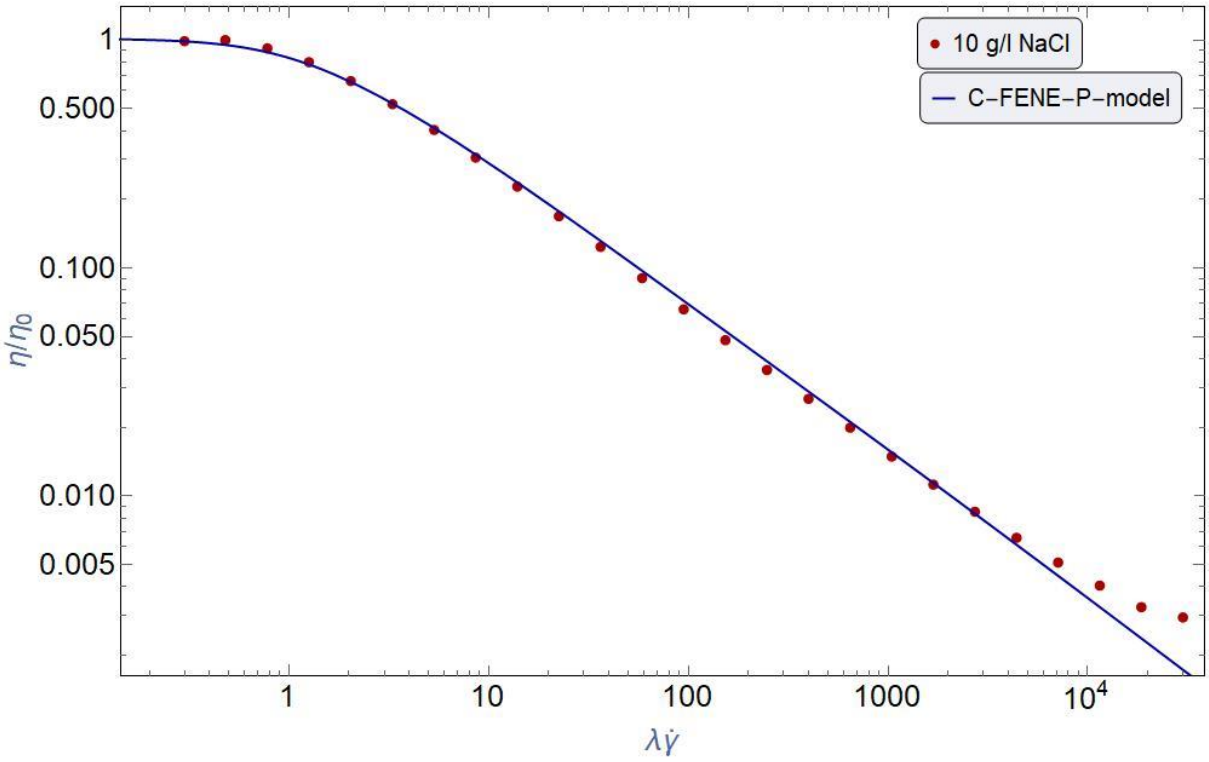

Figure 37 LogLog plot of normalized viscosity (red dots) and C-FENE-P-model viscosity prediction (blue line) versus dimensionless shear rate for FLOPAAM 5115 VHM 10 g/l NaCl polymer solution. Fitted parameters: $\eta_0 = 8728.2, \lambda = 35, b = 50\ and\ E = 90$.

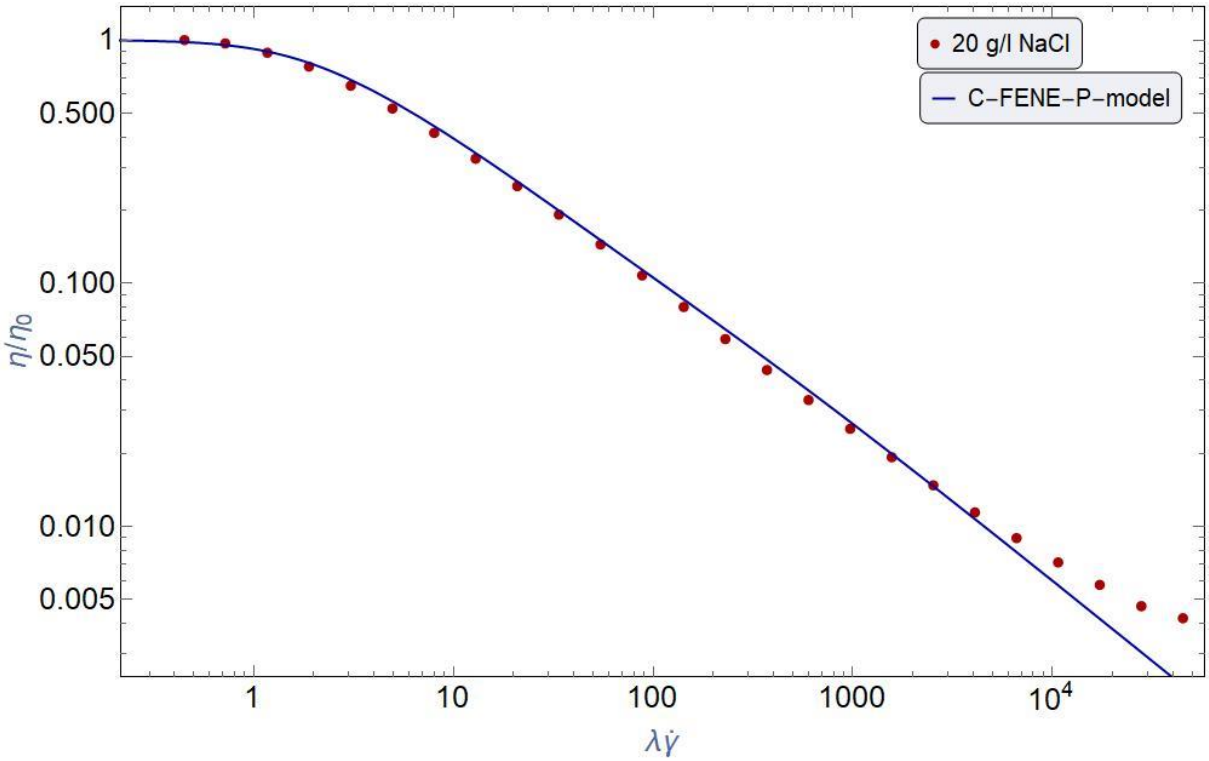

Figure 38 LogLog plot of normalized viscosity (red dots) and C-FENE-P-model viscosity prediction (blue line) versus dimensionless shear rate for FLOPAAM 5115 VHM 20 g/l NaCl polymer solution. Fitted parameters: $\eta_0 = 5391.6, \lambda = 35, b = 50\ and\ E = 20$.

9.2 Shear Stress Growth Data Analysis

In this section only the stress growth data obtained from the start-up and cessation measurements will be graphically presented in a set of normalized shear stress versus time plots. Four curves identified by 0, 5, 10 and 20 g/l NaCl for FLOPAAM 5115 VHM and FLOPAAM 3630-S are represented on a total of six figures for step shear rates $1, 10$ and $100\ s^{-1}$. Due to noise obtained in the measurements for shear rates 0.1 and $100\ s^{-1}$ have been discarded for further analysis.

From the shear stress growth versus time plots (Fig. 39, 40 and 41) for shear rate $1, 10$ and $100\ s^{-1}$ shows a sharp increase of shear stress at time $t = 0$ with an overshoot for both saline and non-saline solutions. It is observable that FLOPAAM 5115 VHM 0 g/l recorded the largest peak among its corresponding solutions, which seem to take new heights further away from the saline solutions as the step shear rate increases.

The large gap between overshoots of 5115 VHM and 5 g/l NaCl do show there is a dependency on salinity, but the gap of such overshoots between the increasing salinities shows a tendency to be less significant. As the similar gap between the curves of the several saline solutions seem to be in declining trend and will possibly overlap for large enough salinities. This is mostly observable for solutions 10 g/l and 20 g/l NaCl. This implies that the decline is not completely dependent on salinity.

Furthermore, all the solutions seem to reach steady state at the same amount of time. But they differ with overshoot amplitude, which will dictate the steepness of the slope towards steady state. The plot (Fig. 39) show the 0 g/l solutions have the highest peaks, which means they will also have the steepest inclination. No undershoot is observed past this point nor is it expected either at such low shear rate.

At the initiation of exerting the sample to shear stress in the first few seconds shows an identical shear stress growth until the curves split at $\eta^+/\eta\,(\dot{\gamma}_0)$ between 0.8 and 1.0. While solutions 10 g/l NaCl and 20 g/l NaCl have an almost identical behavior.

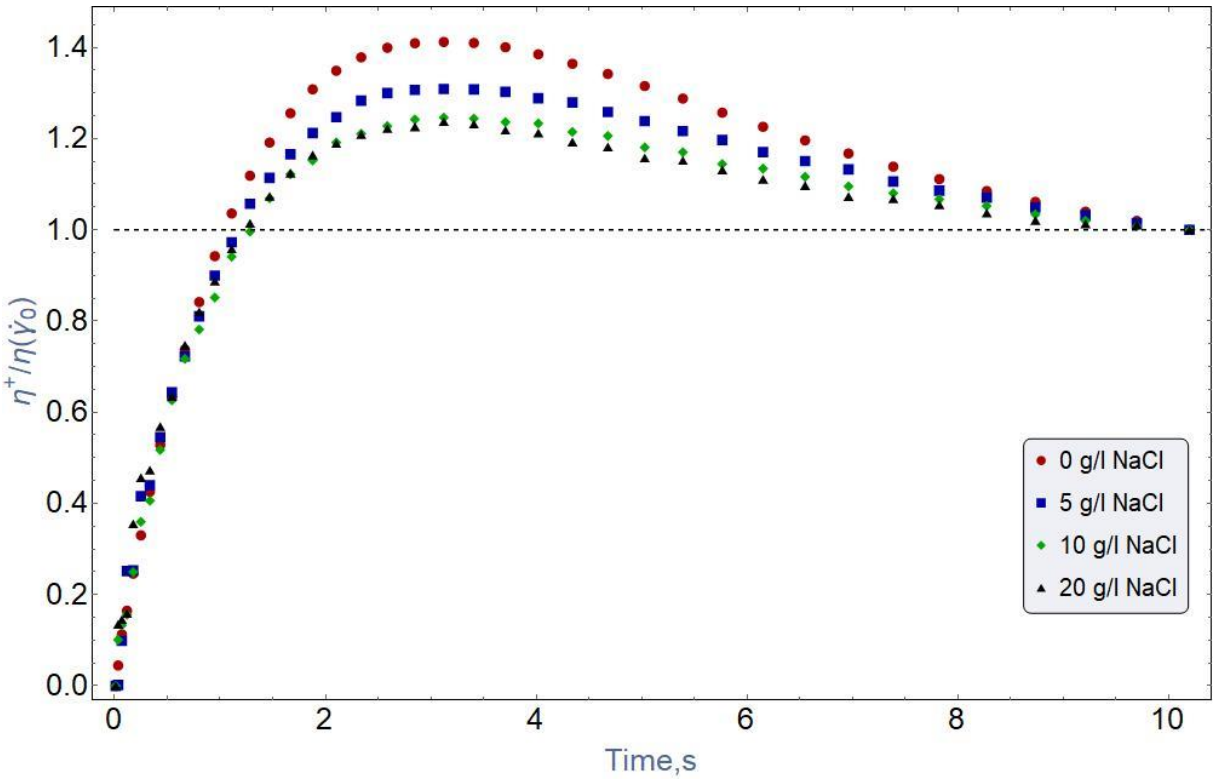

Figure 39 Normalized shear stress growth versus time for FLOPAAM 5115 VHM with various NaCl concentrations at step shear rate 1 s^{-1}.

For shear rate 10 s^{-1} things change. A much larger overshoot is observed for all solutions as seen in Fig. 40. But the most impacted by this shear rate change from 1 to 10 s^{-1} is the FLOPAAM 5115 VHM 0 g/l NaCl. It reaches a new overshoot amplitude of approximately 3 as a normalized value. This is more than doubling from the previous step shear rate 1 s^{-1} plot.

This indicates that the polymer solution has more room to stretch as compared to the saline solutions that does not experience the same dimension of shear stress growth. The salt seems to restrict this growth. But it is important to notice that the increase in salinity does not necessarily impair this growth in large significance. The plots show this restriction mostly

affecting the polymer when transitioning from non-saline to saline solvents. Thus, further increase in salt concentration has little or no impact on stress growth restriction.

It is also observable that solution 10 g/l NaCl and 20 g/l NaCl experience a minimal undershoot, whereas the solutions 0 g/l NaCl and 5 g/l NaCl does not show similar behavior. Which enables them to reach steady state more rapidly by insignificant time. And overall, with the higher shear rate a steady state is reached quicker for all solutions by more than 20% compared to shear rate $1\ s^{-1}$. And the higher the peak of overshoot and more rapid shear stress build up, the steeper slope towards steady state is obtained. However, the time that is required for the solutions to establish steady state does not seem to be dependent on salinity as all reaches that state simultaneously.

Fig. 41 which represent the step shear rate $100\ s^{-1}$ shows an overall growth in shear stress that exceed those of the previous shear rates. This is as expected.

The overshoot peak for solutions 0 g/l NaCl keeps reaching new highs, far above the closest corresponding saline solutions, the 5 g/l NaCl solution. Something interestingly different is that the plot shows a gap increase between the saline solutions as compared to 10 g/l NaCl and 20 g/l NaCl at shear rate $1\ s^{-1}$ where they were almost aligned.

The more obvious observation is that all four curves of FLOPAAM 5115 VHM solutions experience small undershoots where 20 g/l NaCl solution being the earliest to behave in such manner followed by the others incrementally. The undershoots seem to be of minimal difference between the saline solutions. The curves do not though experience any periodic or repetitive oscillations.

Moreover, they do begin to align moving towards steady state past the last undershoot. But reaches surprisingly to that state more delayed than what was observed for measurements at shear rate $10\ s^{-1}$.

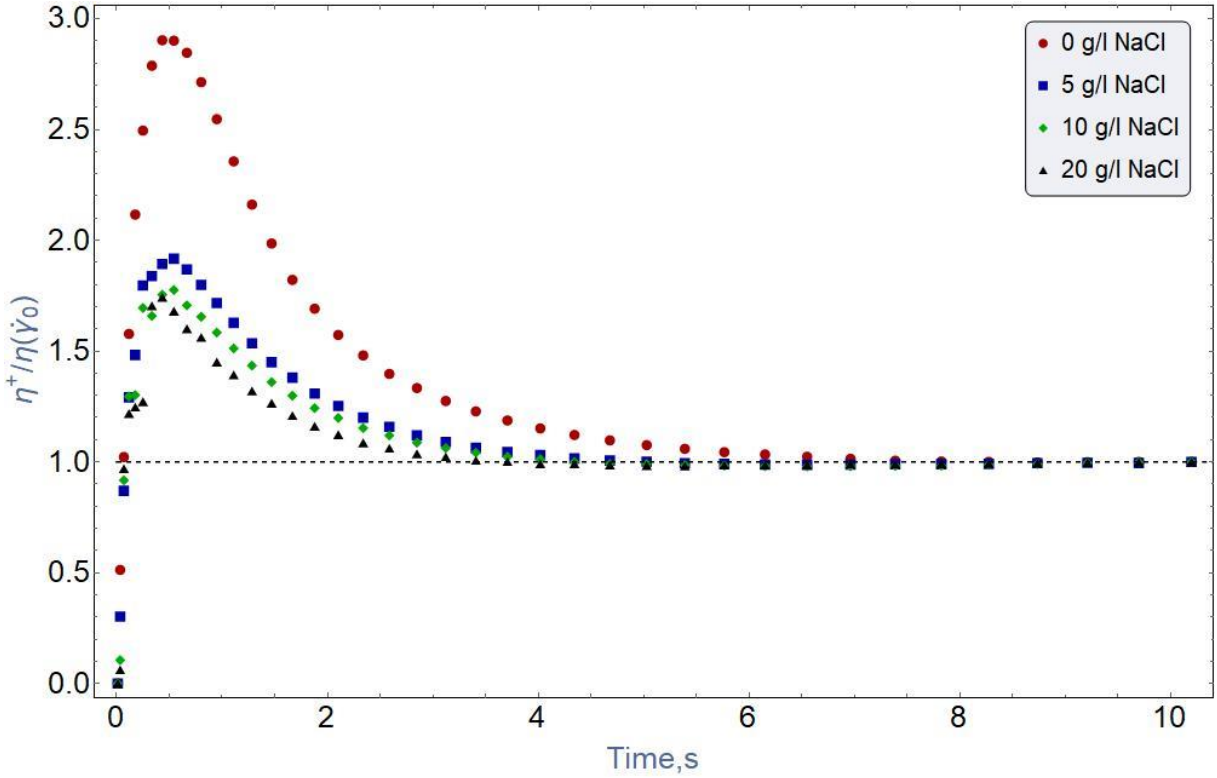

Figure 40 Normalized shear stress growth versus time for FLOPAAM 5115 VHM with various NaCl concentrations at step shear rate 10 s^{-1}.

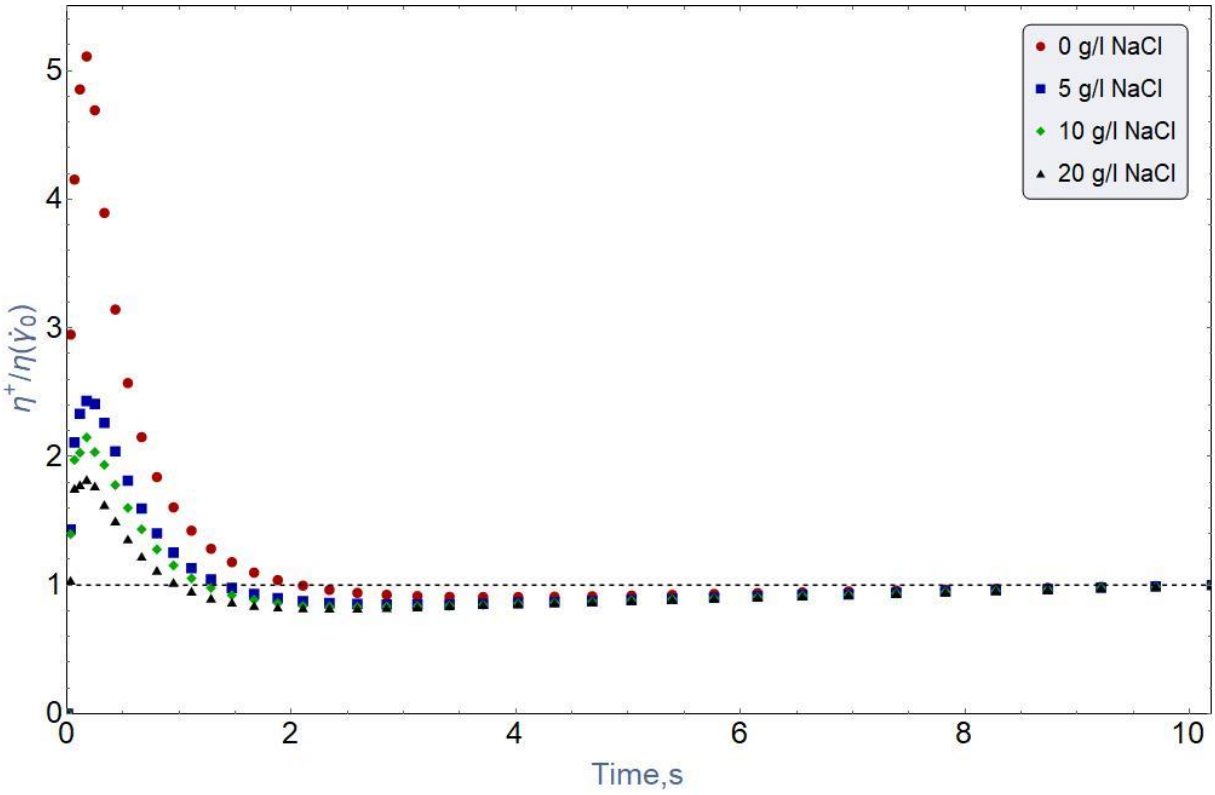

Figure 41 Normalized shear stress growth versus time for FLOPAAM 5115 VHM with various NaCl concentrations at step shear rate $100\ s^{-1}$.

9.2.1 Data/Model Fitting

In the upcoming sub chapters the results of the model fitting will be discussed. The physical non-Newtonian fluid models LPTT, EPTT, FENE-P and C-FENE-P will be fitted against the measured data obtained from the start-up of steady shear flow experiment. The models use different scales; thus, the measured data was scaled accordingly.

9.2.1.1 Affine Linear PTT

The LPTT-model was fitted against the scaled data and resulted in normalized shear stress growth versus dimensionless time plots. Seven curves for the measured data and model identified by step shear rates $1, 10$ and $100\ s^{-1}$ (or their specific Weissenberg number (Wi)) for both polymer types and each salt concentration. Thus, a total of 8 figures were generated. Where dots (red, blue, and green) represents the measured data and dashed lines (red, blue, green and black (linear viscoelastic limit)) represents the model predictions. The

dimensionless time can be mathematically presented as, $r = \frac{t}{\lambda_e}$. λ_e, which is the experimental time constant were obtained based on the exponent of the exponential region of the relaxation curves. Here the attempt was to fit both start-up and steady shear ramp data simultaneously. To better understand the definition of this parameter the reader is referred to Eq. (79) of the paper: A charged finitely extensible dumbbell model: Explaining rheology of dilute polyelectrolyte solutions (D. Shogin and Amundsen, 2020). A total of 8 figures have been generated, see Fig. 42, 43, 44 and 45 and Fig. 95, 96, 97 and 98 in Appendix. B.

The LPTT-model based on the generated plots show an extreme underprediction for the start-up of shear flow. And in addition, it does not even predict an overshoot for solution FLOPAAM 5115 VHM 0 g/l NaCl with Wi=17.544. The model only predicts a maximum shear stress growth of approximately 1.14, which is significantly less than its corresponding measured data. The model also lacks any prediction for undershoots and this goes against what measured data shows for Wi= 1566.402 curve of Fig. 42.

Furthermore, the model shows a delay in shear stress growth, which increases with decreasing Wi values and increasing salinity. This delay extremely significant, where the curve of the lowest Wi of the measured data has a much more rapid shear stress growth than what the model predicts for the curve of the second largest Wi. The only alignment between model and measured data curves is observed for Wi=156.758 curves just before reaching steady state.

As we move over to the 5 g/l NaCl solution (Fig. 43) we observe that the model prediction for all Wi curves are almost identical of Fig. 42 and provides the same behavior, but with larger time frame. In addition, it is observable that the model has an overshoot peak value limitation of which it cannot exceed. And this causes the overshoot to reach its peak and steady state significantly more rapidly than measured data for large Wi. On the other hand, with increasing salinity the model prediction for small Wi seems to get closer in predicting when measured data reaches steady state. But in general, the model shows most ideal prediction for the intermediate Wi, when it comes to the time duration for it to reach steady state.

These findings do not follow what was concluded for the affine LPTT in the steady shear ramp section, as it shows unsatisfactory fit for concentrated and saline solutions.

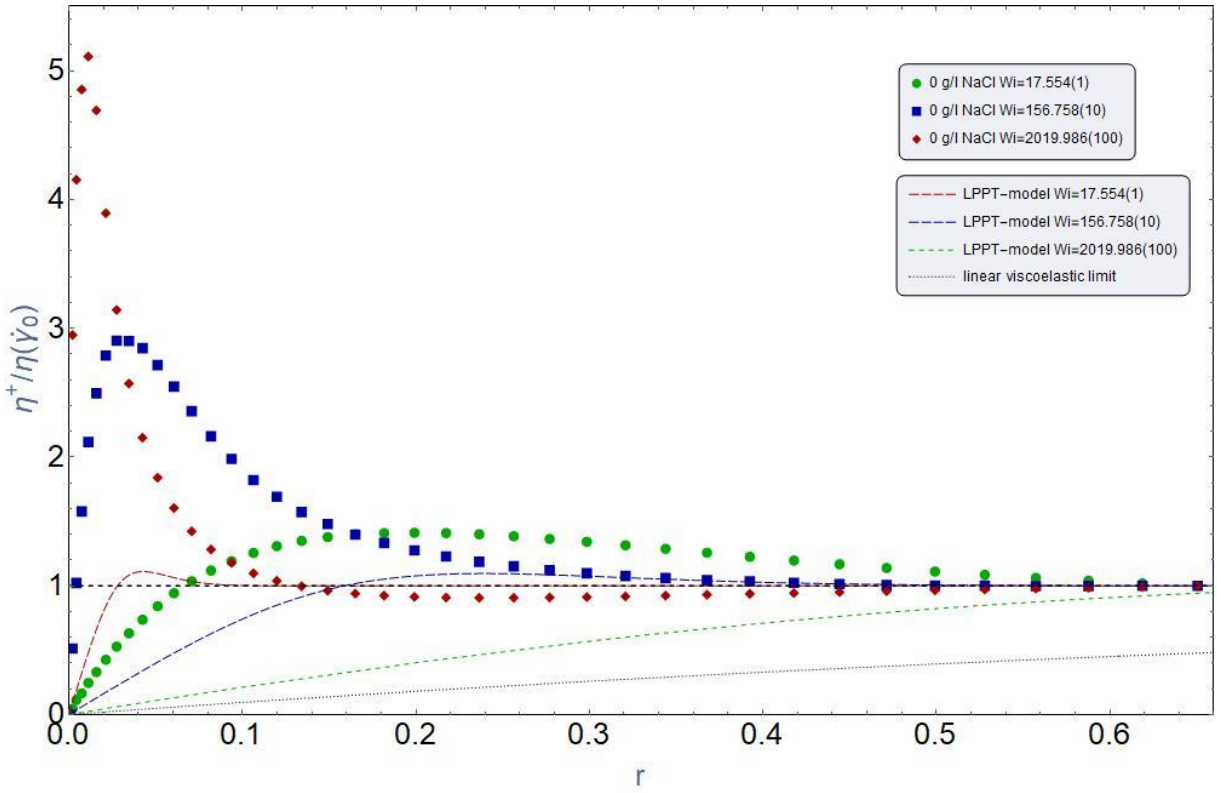

Figure 42 Normalized shear stress growth and LPTT-model prediction versus dimensionless time, r, for FLOPAAM 5115 VHM 0 g/l NaCl. Dots representing measured data and dashed lines representing model predictions for step rates (s^{-1}) 1 $(green)$, 10 $(blue)$ and 100 s^{-1}(red).

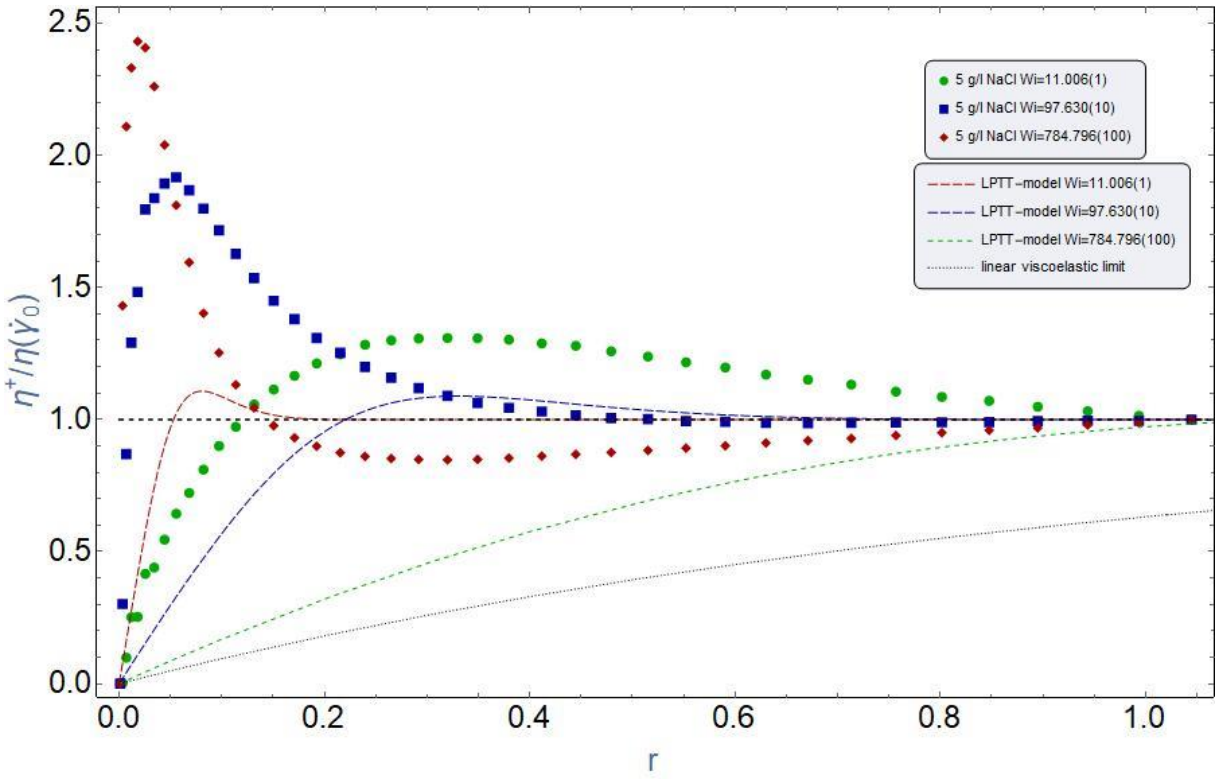

Figure 43 Normalized shear stress growth and LPTT-model prediction versus dimensionless time, r, for FLOPAAM 5115 VHM 5 g/l NaCl. Dotted points representing measured data and dashed lines representing model predictions for step rates 1 $(green)$, 10 $(blue)$ and 100 s^{-1}(red).

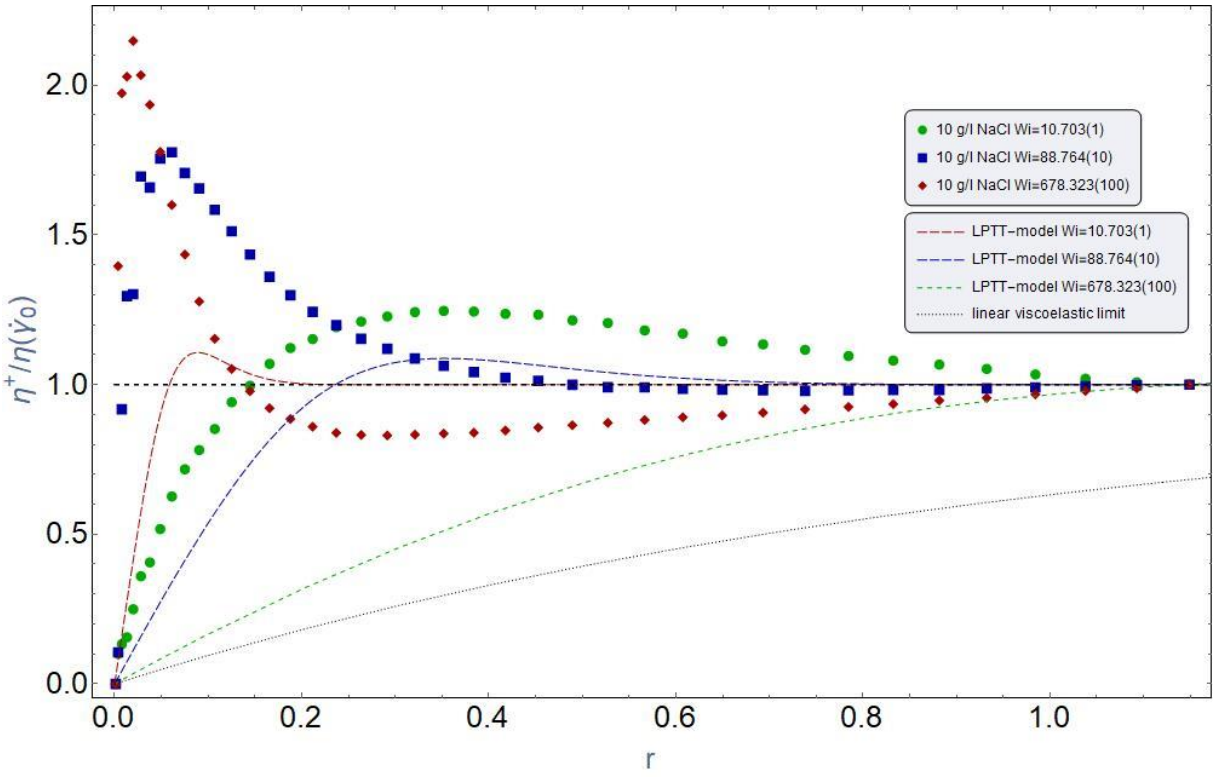

Figure 44 Normalized shear stress growth and LPTT-model prediction versus dimensionless time, r, for FLOPAAM 5115 VHM 10 g/l NaCl. Dotted points representing measured data and dashed lines representing model predictions for step rates 1 $(green)$, 10 $(blue)$ and 100 s^{-1}(red).

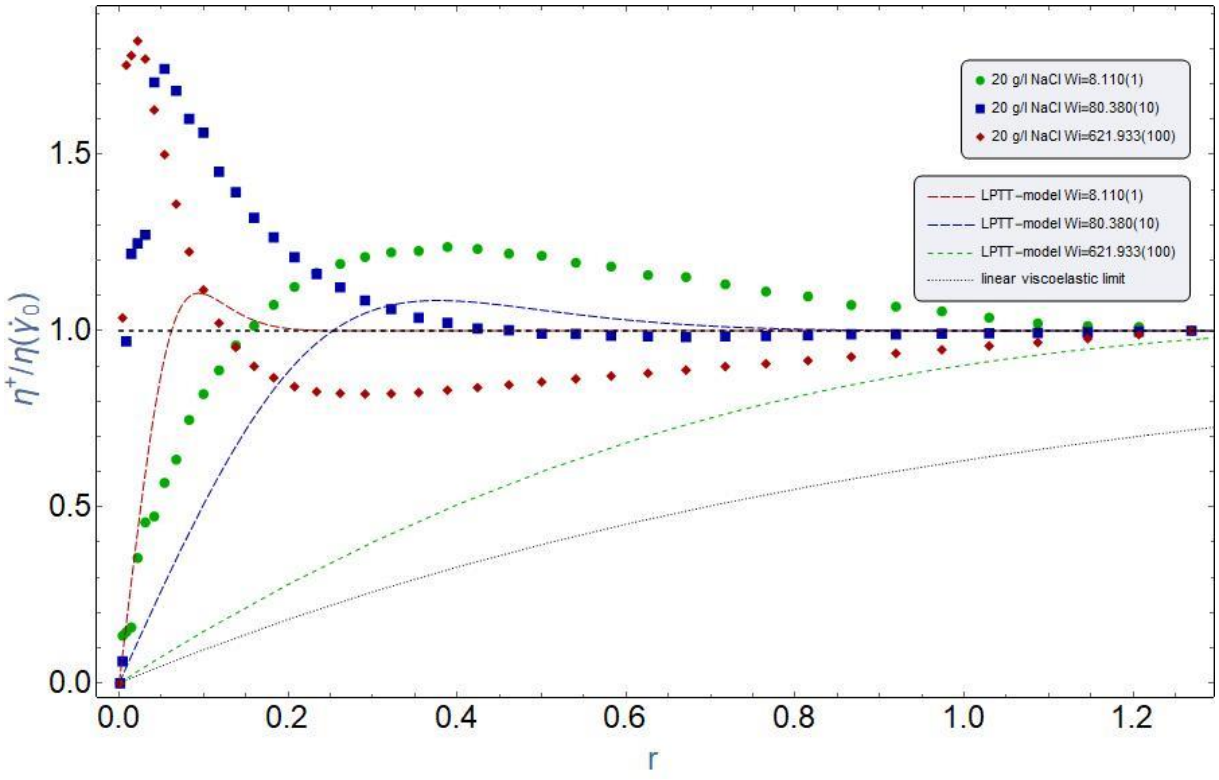

Figure 45 Normalized shear stress growth and LPTT-model prediction versus dimensionless time, r, for FLOPAAM 5115 VHM 20 g/l NaCl. Dotted points representing measured data and dashed lines representing model predictions for step rates 1 $(green)$, 10 $(blue)$ and 100 s^{-1}(red).

9.2.1.2 Affine Exponential PTT

The EPTT-model was fitted against the scaled data and resulted in normalized shear stress growth versus dimensionless time plots. Six curves for the measured data and model predictions identified by step shear rates $1, 10$ and $100\ s^{-1}$ for FLOPAAM 5115 VHM. Where dotted points (red, blue, and green) represents the measured data and dashed lines (red, blue and green) represents the model predictions. The dimensionless time is the same of LPTT, $r = \frac{t}{\lambda_e}$. A total of 16 figures have been generated, see Fig. 46, 47, 48 and 49 and Appendix. B.

In this case the EPTT shows initially at step shear rate $1\ s^{-1}$ somewhat good predictions, but it does underpredict the overshoots of shear stress growth for all step shear rates that are considered in this experiment. And this underprediction grows with increasing shear rate. But

as shown in Fig. 47, 48 and 49 the shear stress growth overshoots of measured data decrease with increasing salinity, thus the model can be a better fit for polymer solutions higher salinity levels. But it still falls short as the model predicts the polymer will reach steady state at a shorter time than what reality dictates.

For all the saline solutions an undershoot is experienced from the measured data at step shear rate $10\ s^{-1}$ of which the model is unable to predict. For step shear rate $100\ s^{-1}$ the model curve is rather un-useful due to the vast limitation of the model at high shear rates where it predicts an almost instant stress growth overshoot and steady state while measured date shear stress can grow tremendously higher.

Fig. 49 of FLOPAAM 5115 VHM 20 g/l NaCl at step shear rate $1\ s^{-1}$ shows a model curve intersecting the curve of measured data. This was not observed for FLOPAAM 3630-S 20 g/l NaCl (Appendix. B), which could indicate an anomaly in the measurement of FLOPAAM 5115 VHM 20 g/l NaCl .

In summary, the model seem to predict the initial measured data points for step shear rates $10\ s^{-1}$ and $100\ s^{-1}$ for all solutions, but is unable to reach same peak in shear stress growth as the measured data and this prevents us from knowing whether the model could predict the behavior post this peak. Overall, this model is not applicable for the polymer solutions considered in this paper, due to the polyelectrolyte nature of these polymers which causes these large overshoots. Hence, a great care must be taken when applying this model to polyelectrolytes.

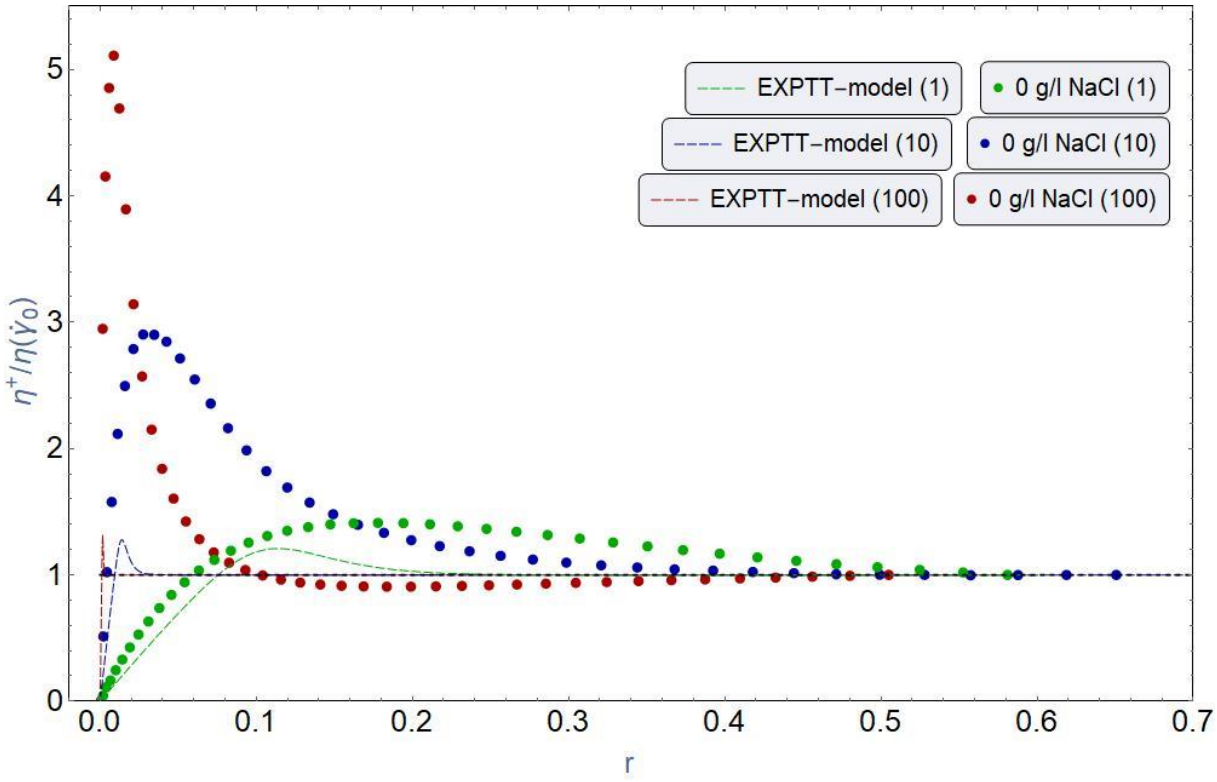

Figure 46 Normalized shear stress growth and EPTT-model prediction versus dimensionless time, r, for FLOPAAM 5115 VHM 0 g/l NaCl. Dotted points representing measured data and dashed lines representing model predictions for step shear rates 1 $(green)$, 10 $(blue)$ and 100 s^{-1}(red).

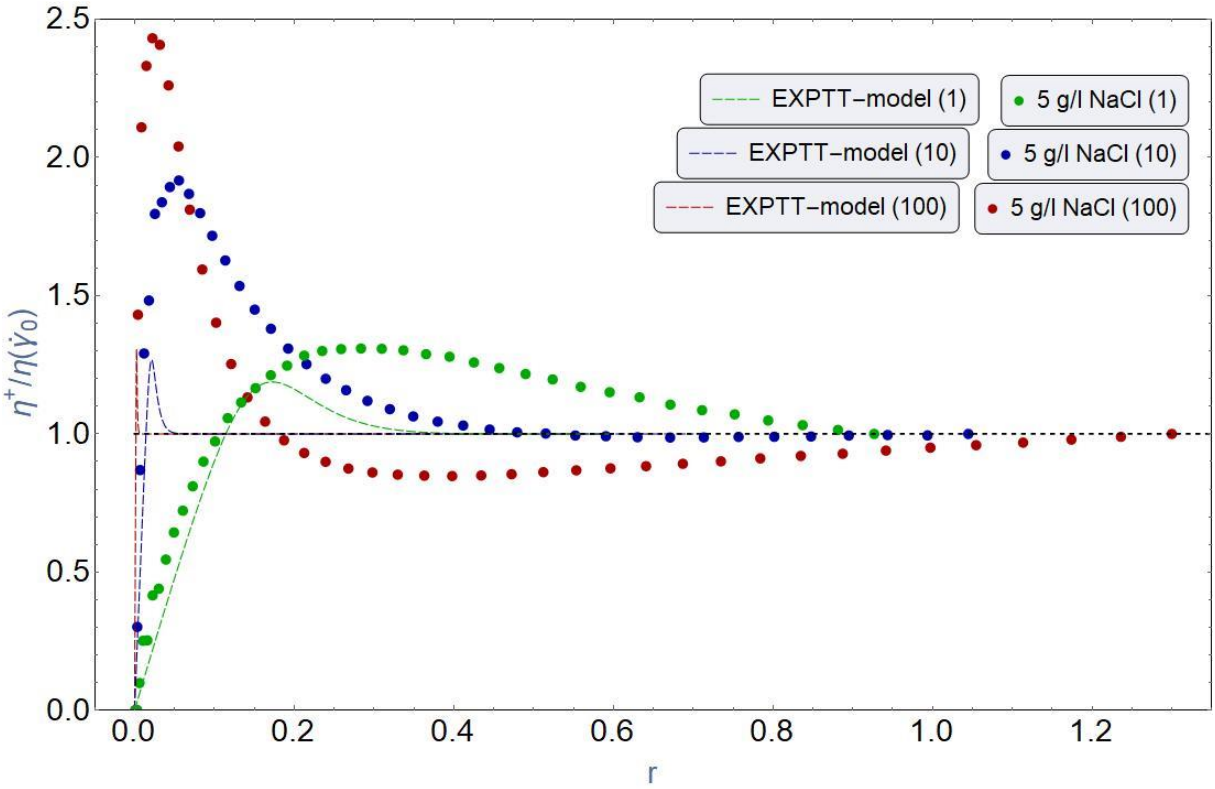

Figure 47 Normalized shear stress growth and EPTT-model prediction versus dimensionless time, r, for FLOPAAM 5115 VHM 5 g/l NaCl. Dotted points representing measured data and dashed lines representing model predictions for step shear rates 1 $(green)$, 10 $(blue)$ and 100 s^{-1}(red).

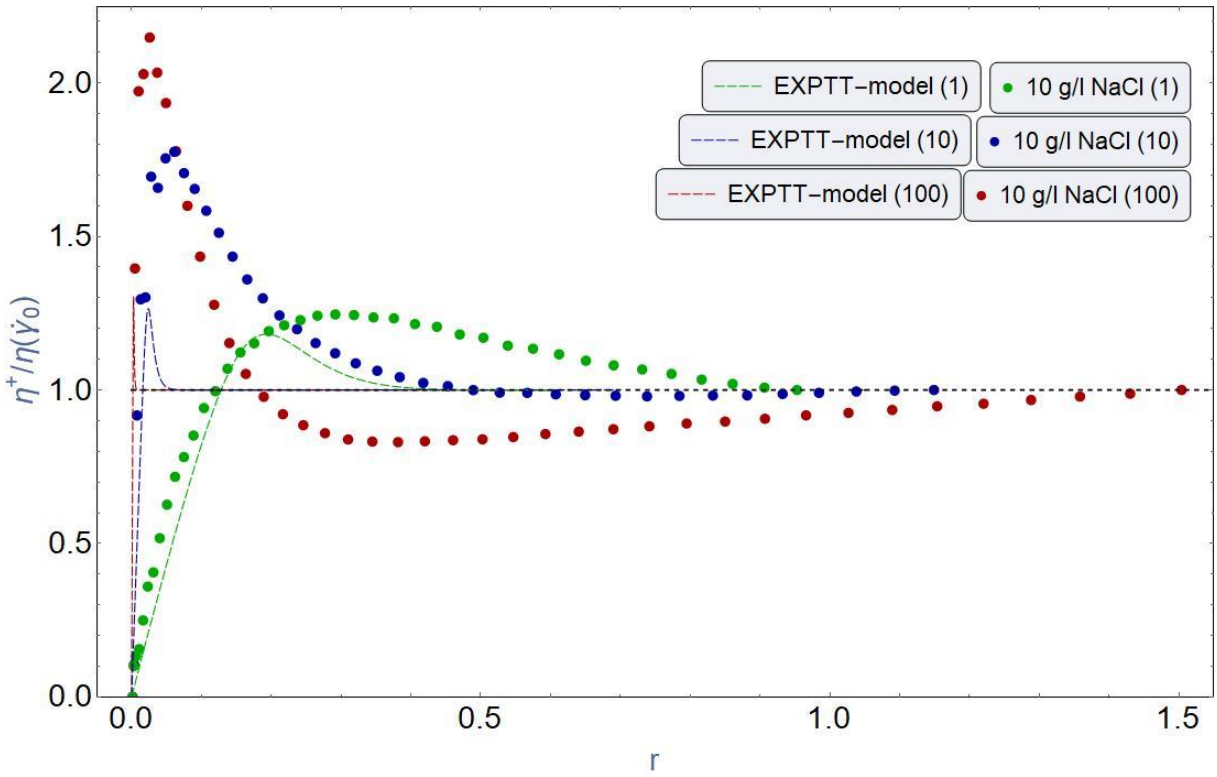

Figure 48 Normalized shear stress growth and EPTT-model prediction versus dimensionless time, r, for FLOPAAM 5115 VHM 10 g/l NaCl. Dotted points representing measured data and dashed lines representing model predictions for step shear rates 1 $(green)$, 10 $(blue)$ and 100 s^{-1}(red).

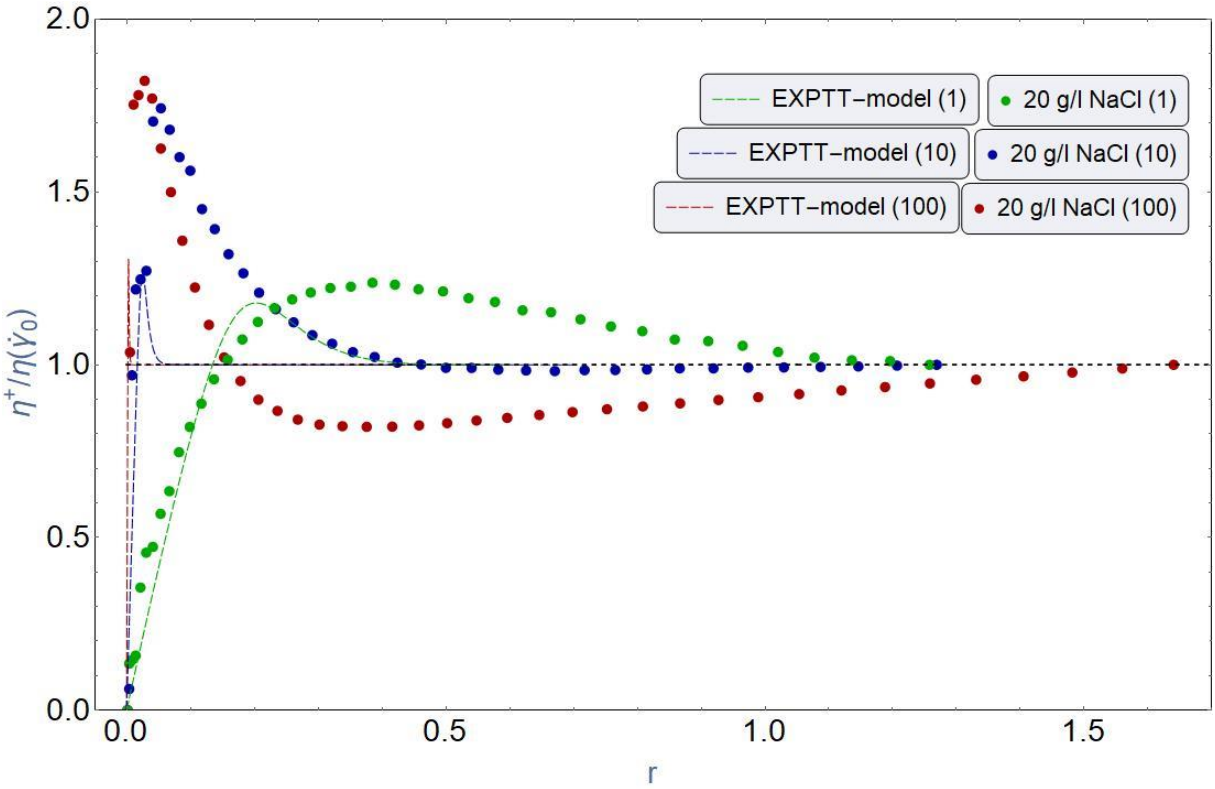

Figure 49 Normalized shear stress growth and EPTT-model prediction versus dimensionless time, r, for FLOPAAM 5115 VHM 20 g/l NaCl. Dotted points representing measured data and dashed lines representing model predictions for step rates 1 $(green)$, 10 $(blue)$ and 100 s^{-1}(red).

9.2.1.3 FENE-P Dumbbells

The FENE-P-model is the affine equivalent of LPTT-model when the polymer solution undergoes steady flow, but that is not the case for transient flow that occurs during start-up of shear flow. The model was fitted against the scaled data and resulted in normalized shear stress growth versus dimensionless time plots. The figures show curves of measured data and model prediction at step shear rates $1, 10$ and $100\ s^{-1}$ for both polymer types and each salt concentration. The dimensionless time is different than that of LPTT and EPTT and is mathematically defined as, $r = \frac{t}{\lambda}$.

Based on Fig. 50, 51, 52, 53 and 54 it is seen that FENE-P-model for start-up of steady shear flow shows invalid results. The model fails harshly to describe all solutions considered in this

paper. And this is strictly due to the negative b, which is based on λ_e that is obtained from the slope of relaxation data. The model dictates that b must always be positive for it to be applicable. In addition, b is expected to be a relatively large number, a number greater than 10. But with a large b, the λ_e should be significantly smaller than λ_Q. The results obtained from this experiment does not abide by this as λ_e is only slightly smaller. The reader is referred to paper: A charged finitely extensible dumbbell model: Explaining rheology of dilute polyelectrolyte solutions (D. Shogin and Amundsen, 2020) for a better understanding of this concept.

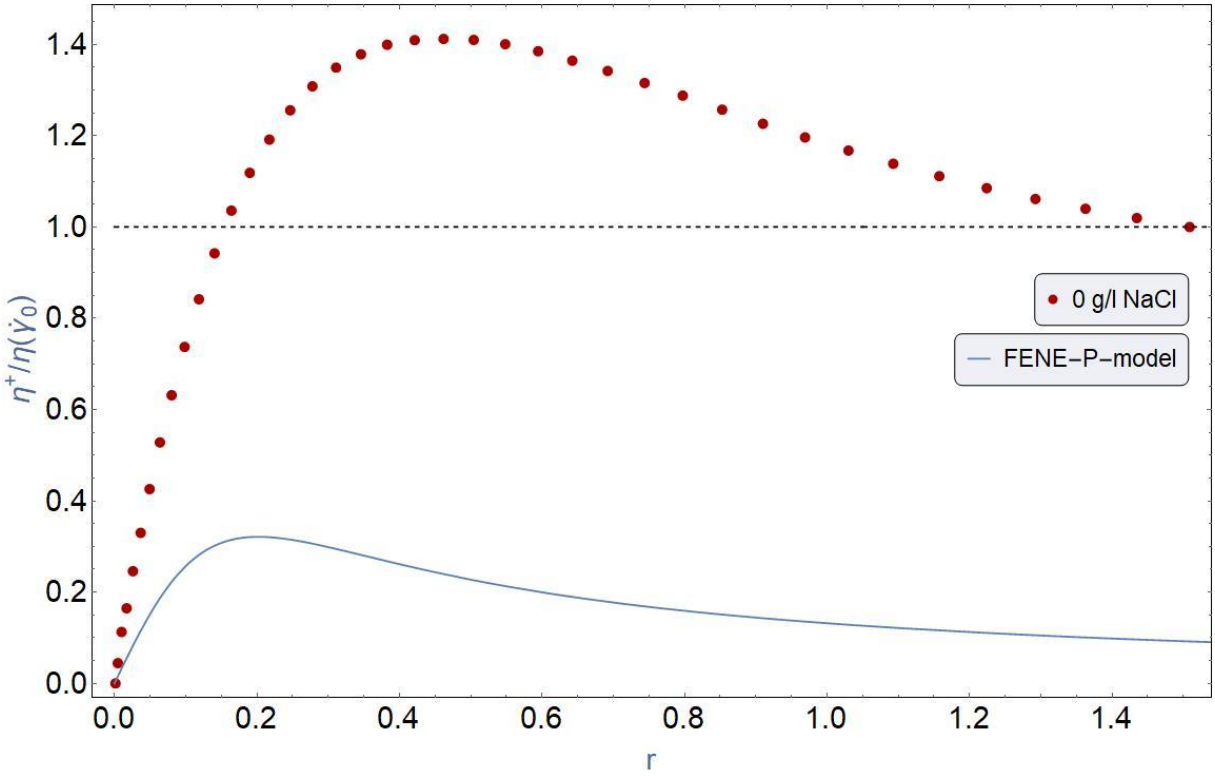

Figure 50 Normalized shear stress growth (red dots) and FENE-P-model prediction (blue line) prediction versus dimensionless time, r, for FLOPAAM 5115 VHM 0 g/l NaCl. Dotted points representing measured data and dashed lines representing model predictions for step rate 1 s^{-1}.

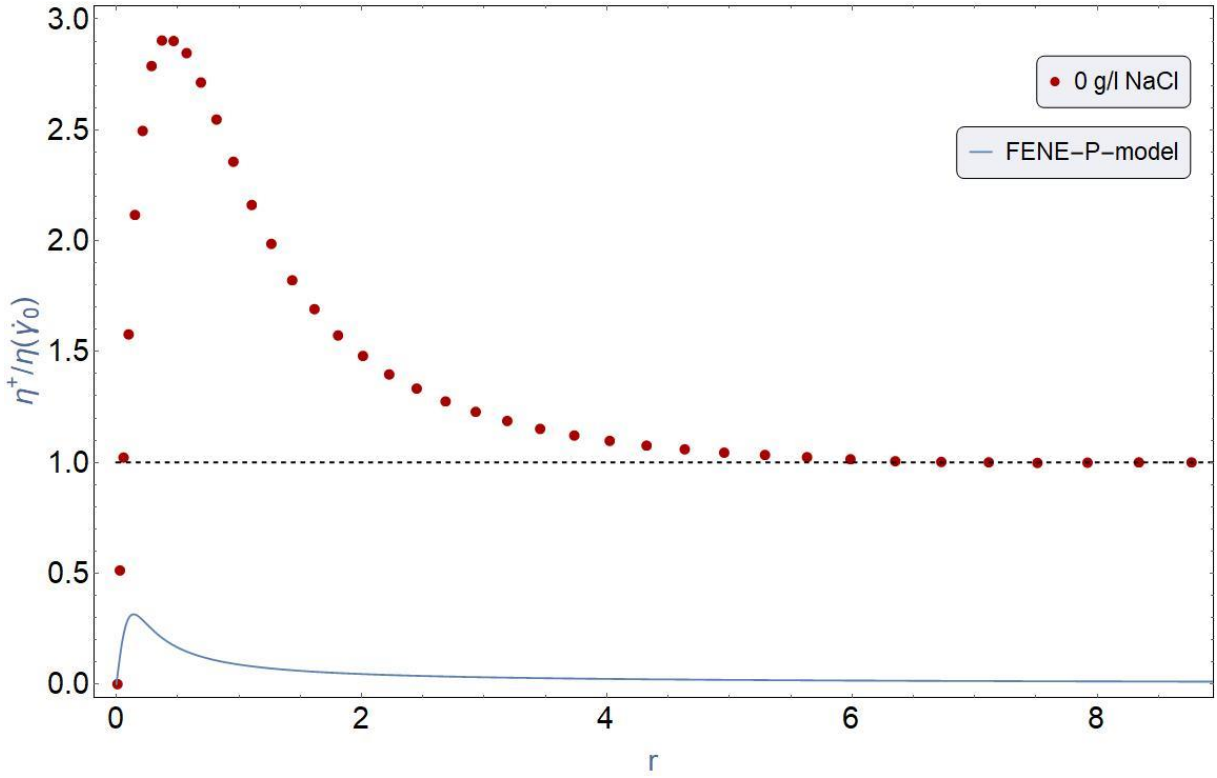

Figure 51 Normalized shear stress growth (red dots) and FENE-P-model prediction (blue line) versus dimensionless time, r, for FLOPAAM 5115 VHM 0 g/l NaCl. Dotted points representing measured data and dashed lines representing model predictions for step rate 10 s^{-1}.

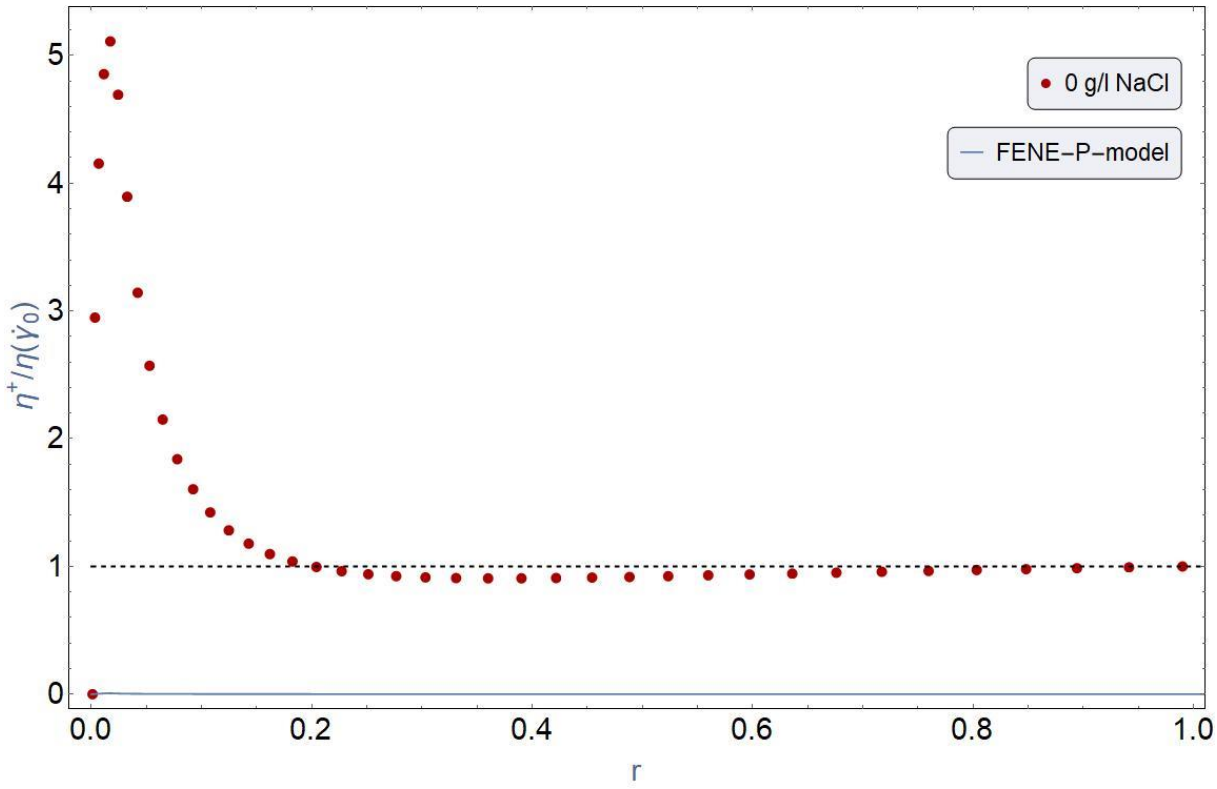

Figure 52 Normalized shear stress growth (red dots) and FENE-P-model prediction (blue line) prediction versus dimensionless time, r, for FLOPAAM 5115 VHM 0 g/l NaCl. Dotted points representing measured data and dashed lines representing model predictions for step rate 100 s^{-1}.

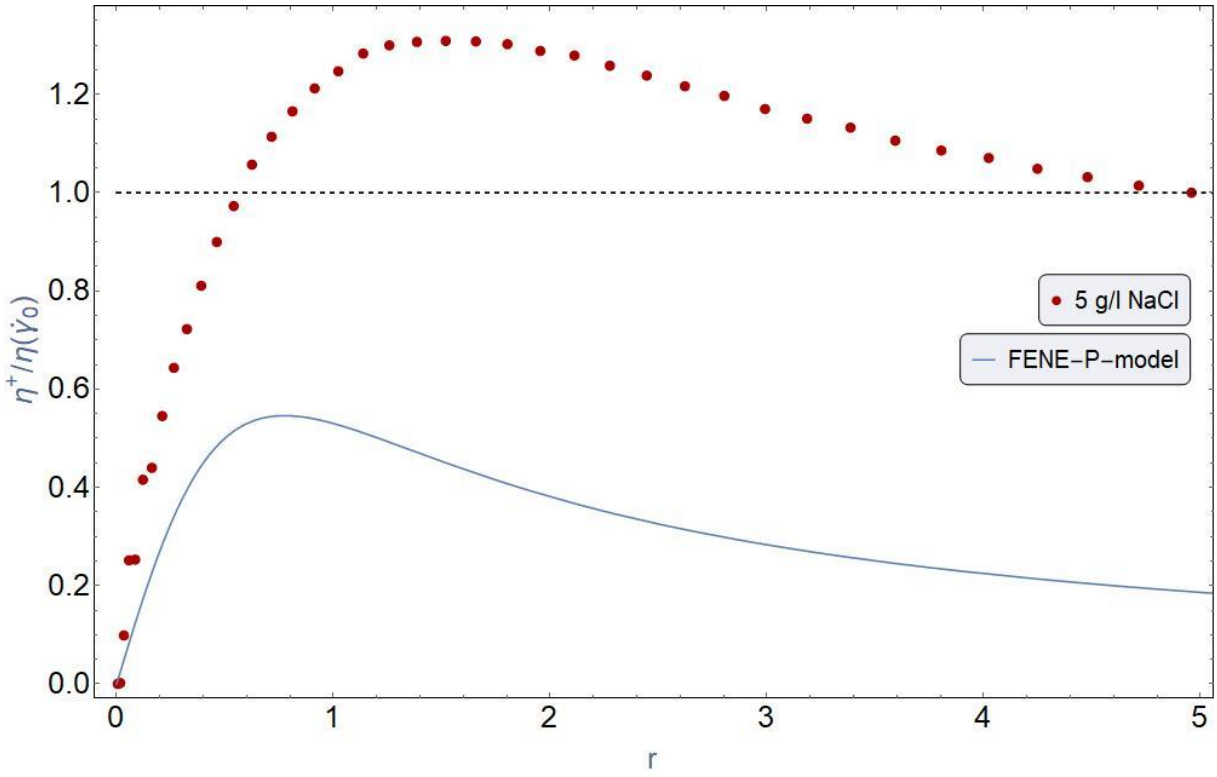

Figure 53 Normalized shear stress growth (red dots) and FENE-P-model prediction (blue line) versus dimensionless time, r, for FLOPAAM 5115 VHM 5 g/l NaCl. Dotted points representing measured data and dashed lines representing model predictions for step rate 1 s^{-1}.

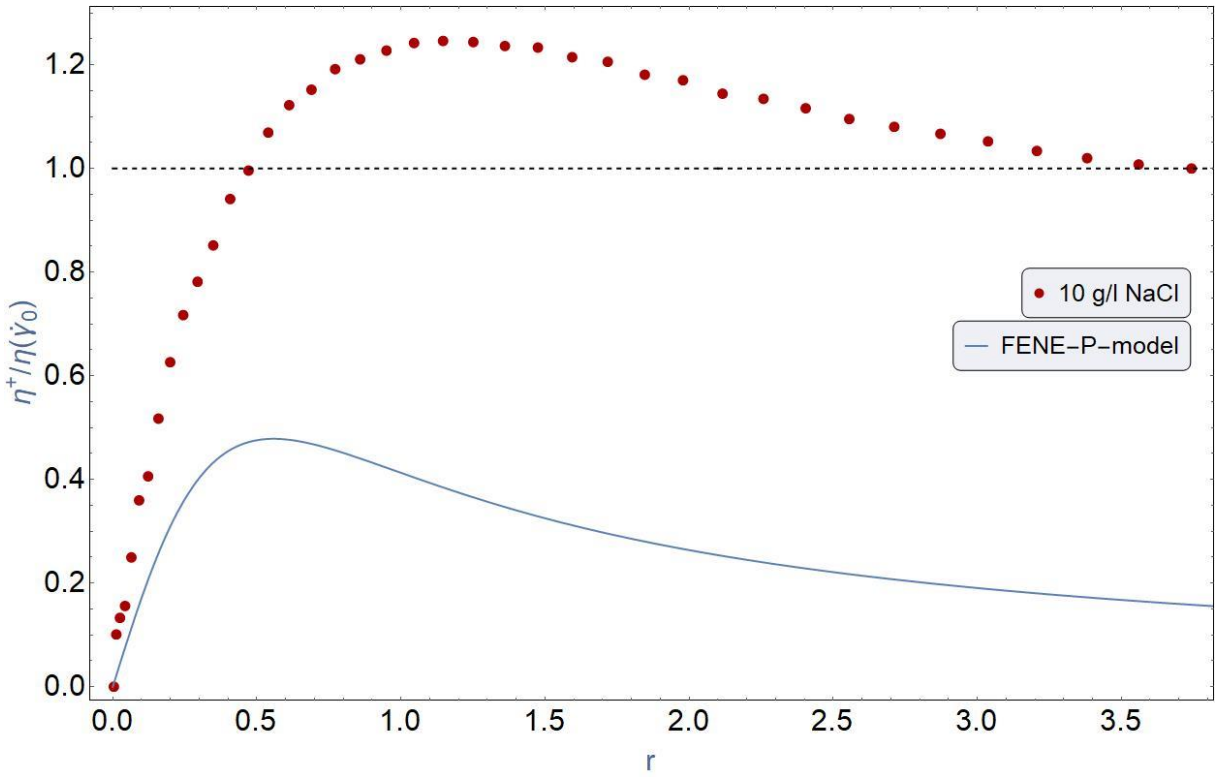

Figure 54 Normalized shear stress growth (red dots) and FENE-P-model prediction (blue line) versus dimensionless time, r, for FLOPAAM 5115 VHM 10 g/l NaCl. Dotted points representing measured data and dashed lines representing model predictions for step rate 1 s^{-1}.

9.2.1.4 C-FENE-P Dumbbells

The C-FENE-P-model was fitted against the scaled data and resulted in normalized shear stress growth versus dimensionless time plots. The model is dependent on several parameters, such as λ_e, b, and E. λ_e was obtained based in the slope of the relaxation data, and b was selected manually while λ were previously obtained from the C-FENE-P data fitting of steady shear ramping test data in section 8.1.1.4. These three parameters were then used to calculate E. Same dimensionless time, r, of FENE-P is used for this model.

The plots (Fig. 55, 56, 57, 58, 59, 60, 61 and 62) show that the C-FENE-P-model can predict large overshoots, but it is obvious that the model shows significant over-prediction. It is observable that with increasing shear rate the overshoot becomes larger, which goes in hand with how these polymer solutions behave. However, the increase in overshoot for measured data is insignificant, while the model predicts almost 4 times and 26 that of measured data at

step shear rate $10\ s^{-1}$ and $100\ s^{-1}$, respectively. The over-prediction is possibly a consequence of the model being single mode.

At $1\ s^{-1}$ we can see the model and measured data arrive steady state at approximately same time. But this trend starts to deviate at higher shear rates, where the model predicts quicker arrival to steady state.

Furthermore, it is obvious from the plots (Fig. 58, 59, 60 and 61) that the prediction of the model somewhat improves with increasing salinity. Though is still insufficient but indicates the possibility of a critical salinity level of which the model can provide almost perfect predictions. That hypothesis stands for investigation. In addition, the model shows quicker arrival to steady state with increasing salinity.

The main factor that differentiates this model from FENE-P is of course the inclusion of parameter E, but also the approach of obtaining the value of b. This parameter was obtained by calculation for FENE-P, while in this case we have the freedom to select it manually to fit the measured data more accurately. b is positive by definition, the reader is referred to Eq. (2) of the paper: A charged finitely extensible dumbbell model: Explaining rheology of dilute polyelectrolyte solutions (D. Shogin and Amundsen, 2020). By this approach one can always select a positive b and prevent the model from failing in application for these specific polymer solutions as illustrated in the model fitting of FENE-P in the previous section.

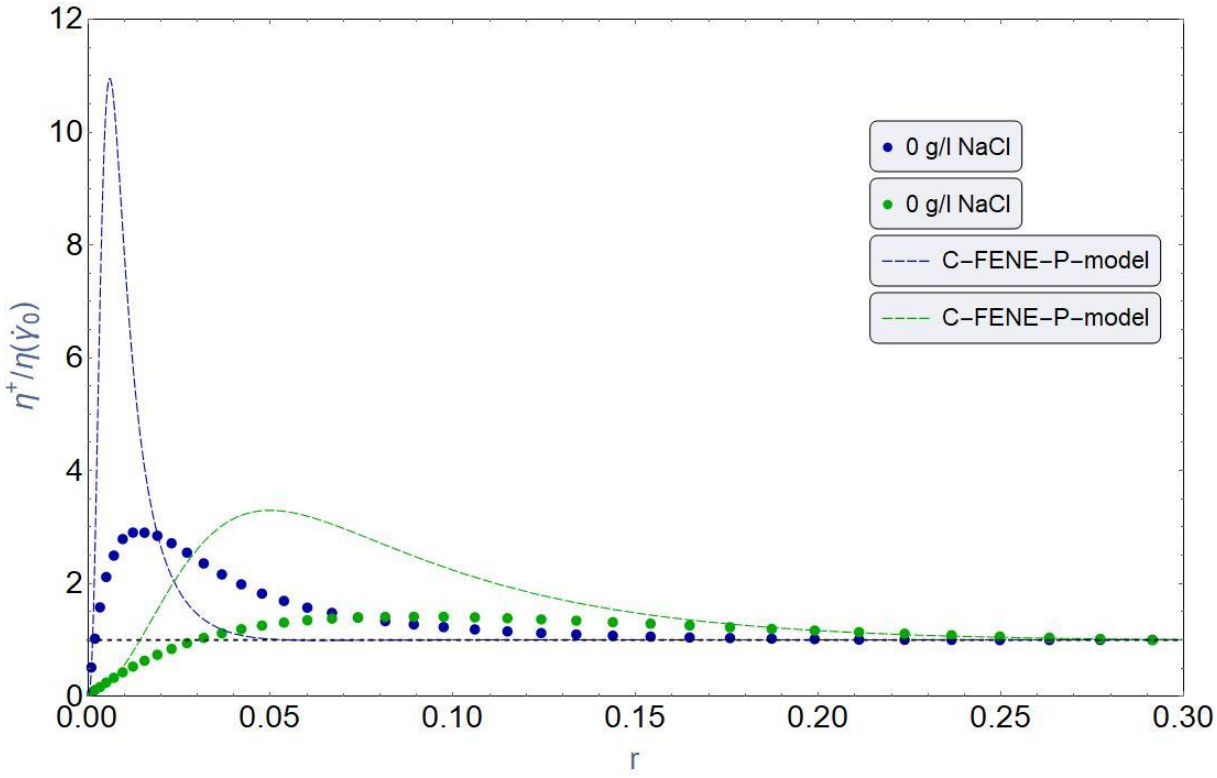

Figure 55 Normalized shear stress growth (dots) and FENE-P-model prediction (dashed lines) versus dimensionless time, r, for FLOPAAM 5115 VHM 0 g/l NaCl. Dotted points representing measured data and dashed lines representing model predictions for step shear rates $1\ and\ 10\ s^{-1}$. Fitted parameters: $b = 1000\ and\ \lambda = 35$

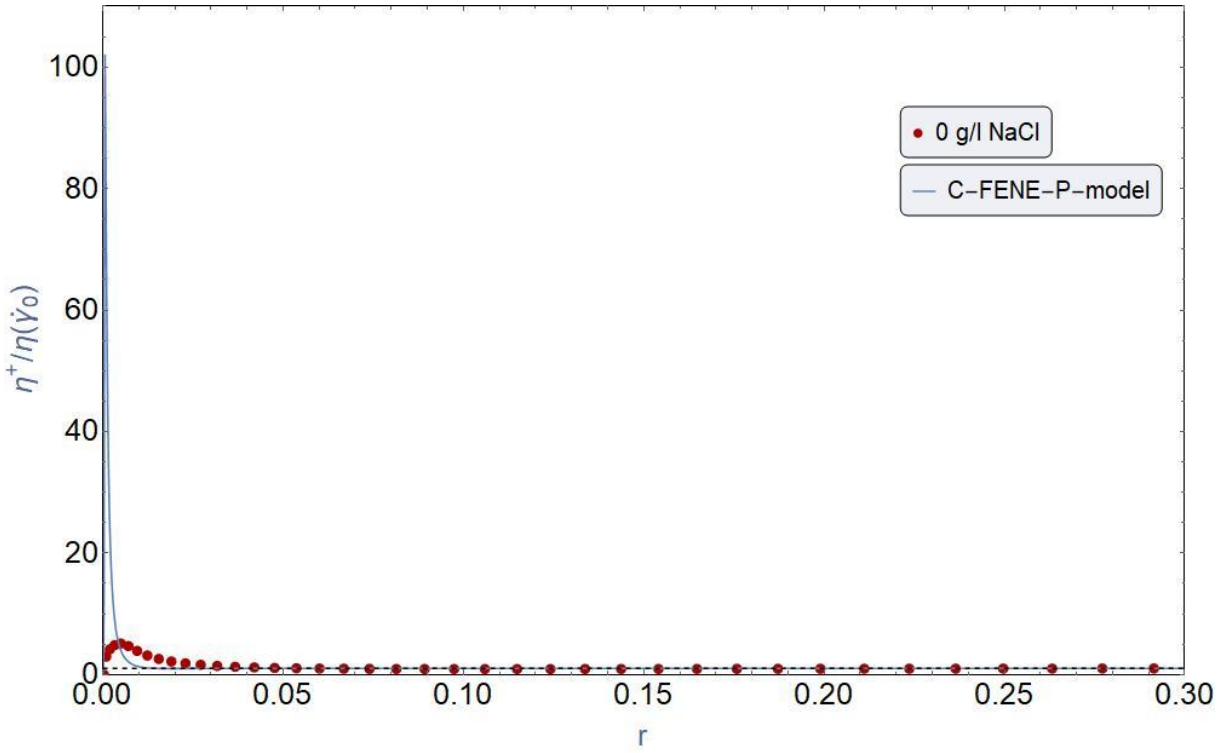

Figure 56 Normalized shear stress growth (red dots) and FENE-P-model prediction (blue line) versus dimensionless time, r, for FLOPAAM 5115 VHM 0 g/l NaCl. Dotted points representing measured data and dashed lines representing model predictions for step rate $100\ s^{-1}$. Fitted parameters: $b = 1000\ and\ \lambda = 35$

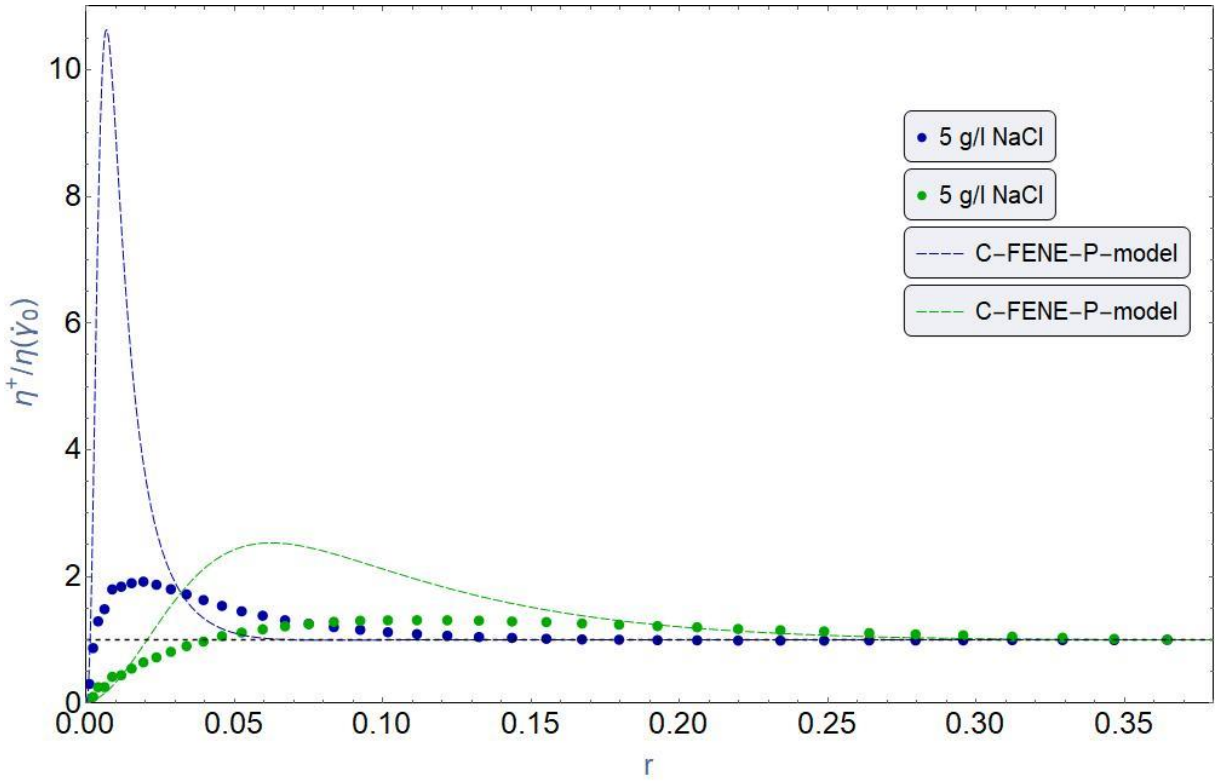

Figure 57 Normalized shear stress growth (dots) and FENE-P-model prediction (dashed lines) versus dimensionless time, r, for FLOPAAM 5115 VHM 5 g/l NaCl. Red dots representing measured data and dashed lines representing model predictions for step shear rates $1\ and\ 10\ s^{-1}$. Fitted parameters: $b = 1000\ and\ \lambda = 35$

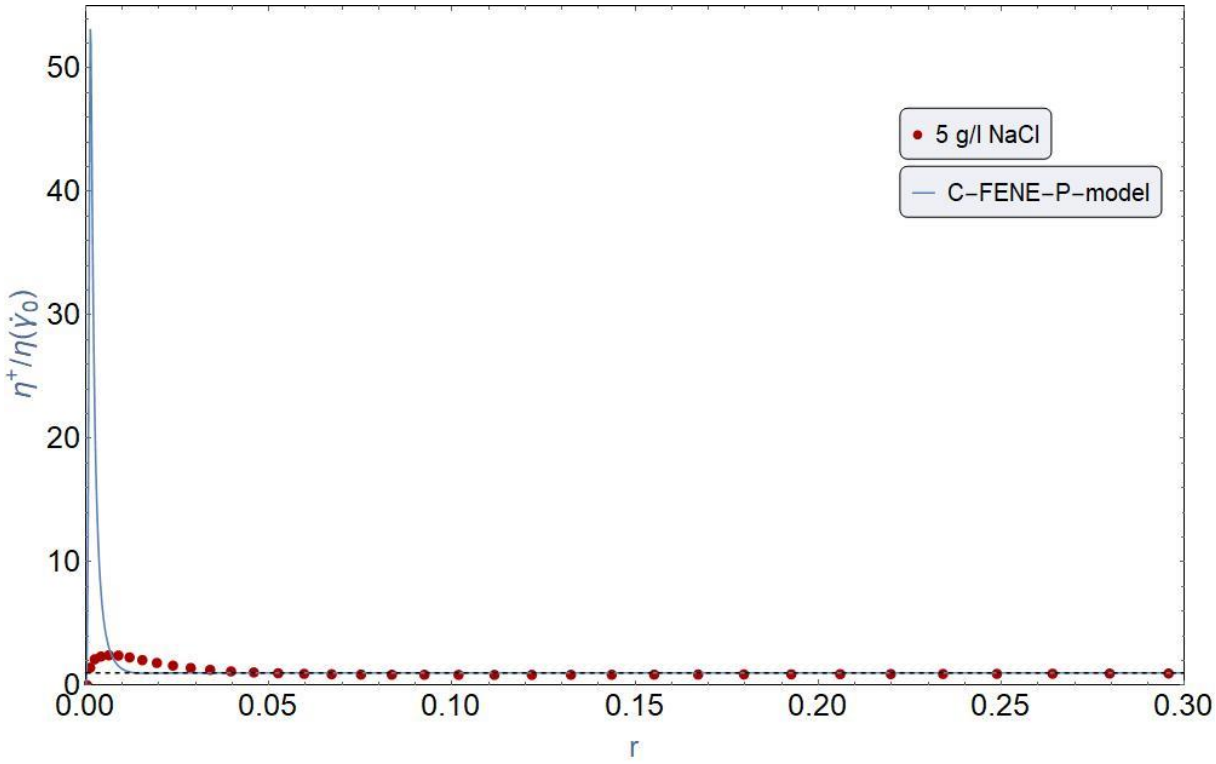

Figure 58 Normalized shear stress growth (red dots) and FENE-P-model prediction (blue line) versus dimensionless time, r, for FLOPAAM 5115 VHM 5 g/l NaCl. Red dots representing measured data and dashed lines representing model predictions for step shear rate $100\ s^{-1}$. Fitted parameters: $b = 1000\ and\ \lambda = 35$

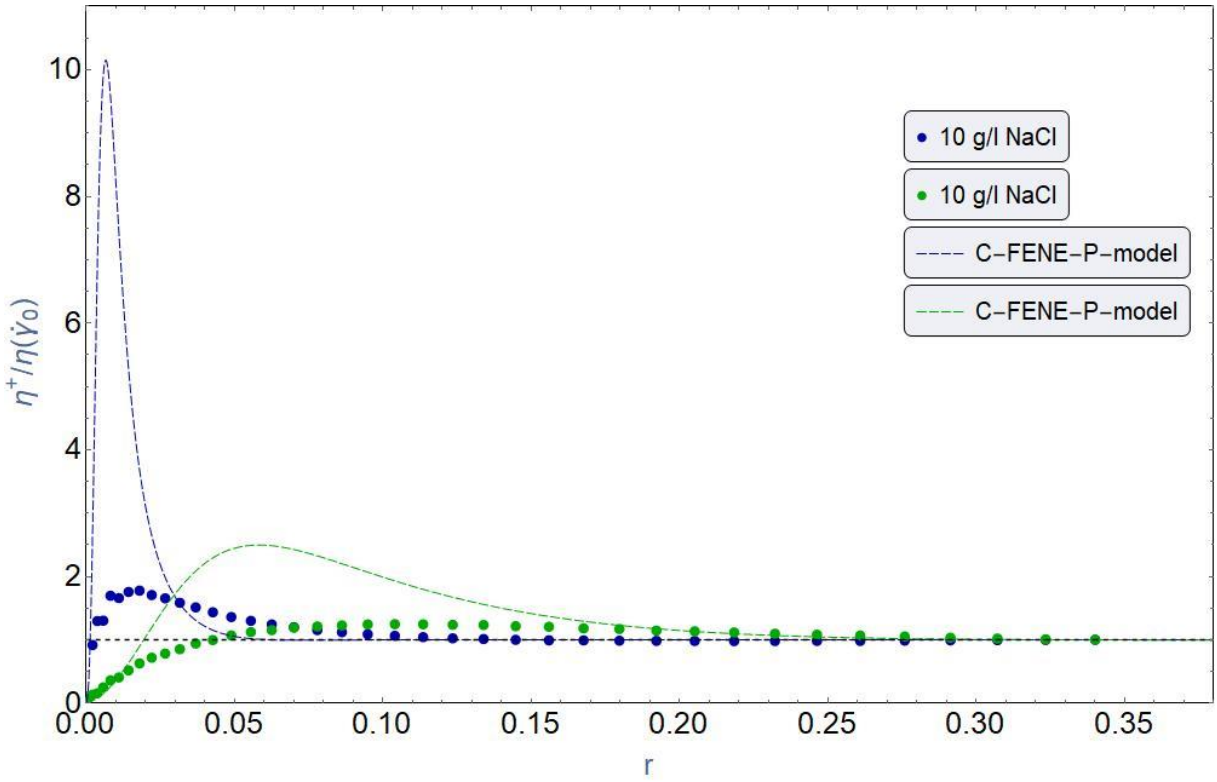

Figure 59 Normalized shear stress growth (dots) and FENE-P-model prediction (dashed lines) versus dimensionless time, r, for FLOPAAM 5115 VHM 10 g/l NaCl. Dotted points representing measured data and dashed lines representing model predictions for step shear rates $1\ and\ 10\ s^{-1}$. Fitted parameters: $b = 1000\ and\ \lambda = 35$

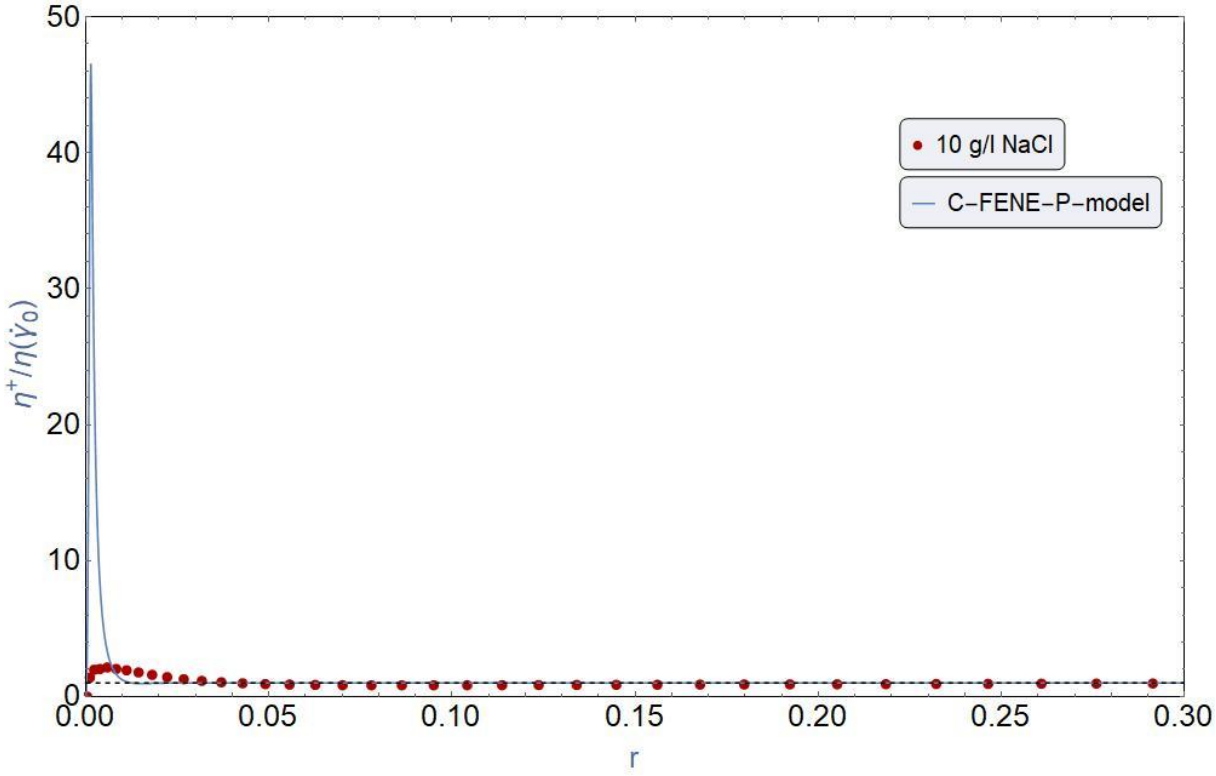

Figure 60 Normalized shear stress growth (red dots) and FENE-P-model prediction (blue line) versus dimensionless time, r, for FLOPAAM 5115 VHM 10 g/l NaCl. Red dots representing measured data and dashed lines representing model predictions for step shear rate 100 s^{-1}. Fitted parameters: $b = 1000$ and $\lambda = 35$.

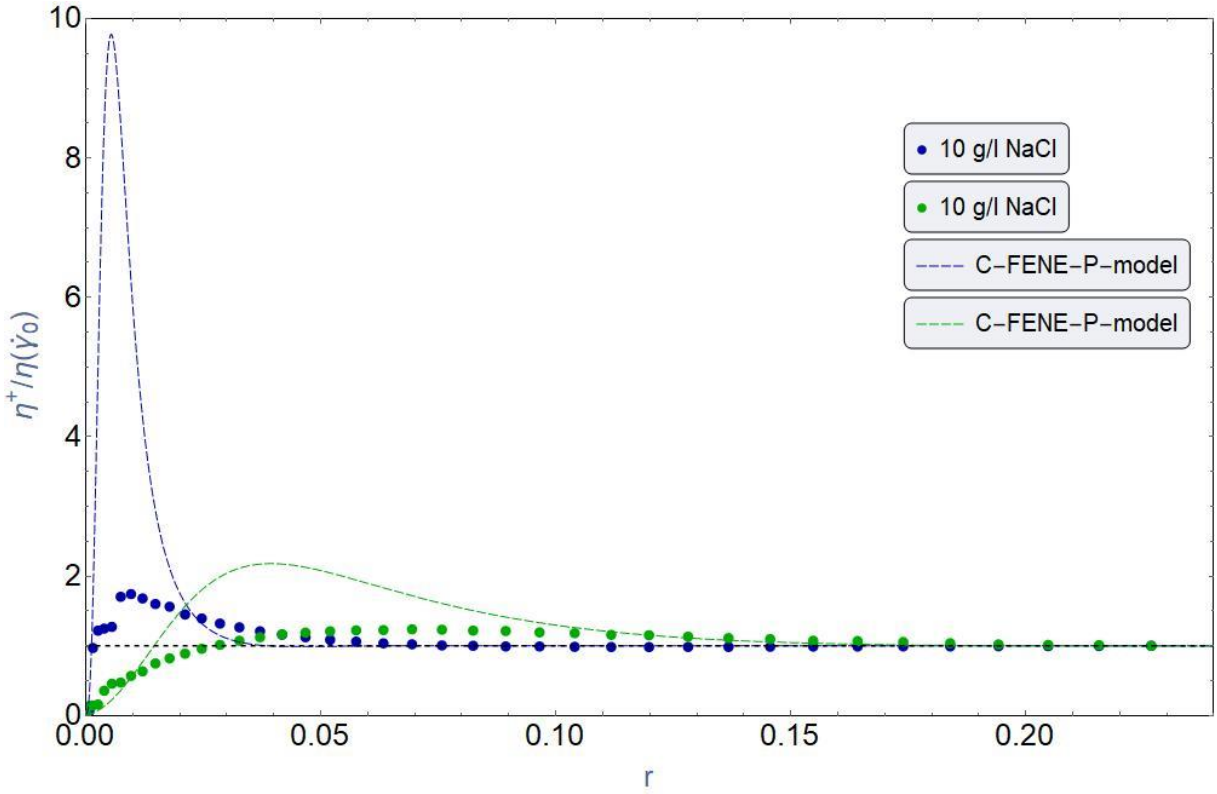

Figure 61 Normalized shear stress growth (dots) and FENE-P-model prediction (dashed lines) versus dimensionless time, r, for FLOPAAM 5115 VHM 20 g/l NaCl. Dotted points representing measured data and dashed lines representing model predictions for step shear rates $1\ and\ 10\ s^{-1}$. Fitted parameters: $b = 1000\ and\ \lambda = 35$.

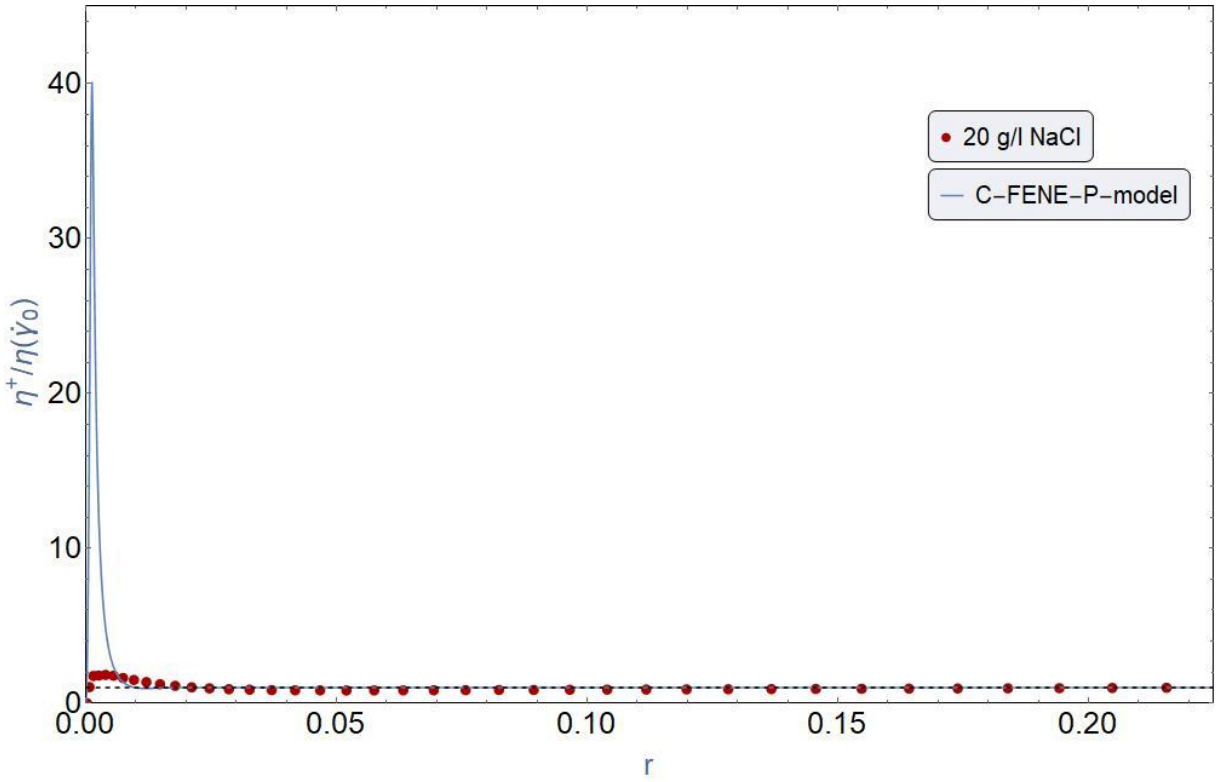

Figure 62 Normalized shear stress growth (red dots) and FENE-P-model prediction (blue line) versus dimensionless time, r, for FLOPAAM 5115 VHM 20 g/l NaCl. Red dots representing measured data and dashed lines representing model predictions for step shear rate $100\ s^{-1}$. Fitted parameters: $b = 1000\ and\ \lambda = 35$.

9.3 Shear Stress Decay Data Analysis

In this section the shear stress decay data obtained from the start-up and cessation measurements will be graphically presented in a set of normalized shear stress versus time plots. Four curves identified by 0, 5, 10 and 20 g/l NaCl for FLOPAAM 5115 VHM and FLOPAAM 3630-S are represented on a total of six figures for step shear rates $1, 10$ and $100\ s^{-1}$.

From the Fig. 63, 64 and 65 it is initially observable that there is an overall immediate stress relief after halting the shearing. The plots show a significant leap in shear stress decay, most significantly for the saline solutions. They seem to be somewhat indifferent in this leap, until they split to take their own path. Solution 20 g/l NaCl shows the sharpest shear stress decay curves, followed by solution 10 g/l NaCl.

The curves show a more stable pattern after a certain time and the relaxation trend takes a milder downward trend. The relaxation curve of 0 g/l NaCl solution show a more flatter trend relative to the saline solutions.

Furthermore, solution 5 g/l NaCl and 10 g/l NaCl seem to be uncertainly proportional to each other. While the 20 g/l NaCl solution takes a more inclined trend. These observations are in compliance with the exponent values of the exponential region of the trend lines. Where the 0 g/l NaCl solution has a less severe slope of -0.57. And the 5 g/l NaCl and 10 g/l NaCl solutions have slope values -0.091 and -0.093, respectively. By this we can almost confirm the proportionality. While the 20 g/l NaCl solution has the slope value -0.123, which showcases the deviate behavior possibly due to the higher salinity.

As the shear rate prior to the relaxation initiation is increased to $10\ s^{-1}$, shows us a more severe curviness during initial phase of stress relaxation and a more rapid movement towards stabilization. At the second measuring point of Fig. 64 shows that the 0 g/l NaCl solution is the only solution to not exceed 90% relaxation. In addition to this it is observable that the curve is shifting closer to the saline solutions. It is also taking a more inclined trend. Yet it is not proportional to the curves of the saline solutions, even though the plots might imply that. Because the obtained slope value of 0 g/l NaCl solution is -0.064, while 5 g/l NaCl, 10 g/l NaCl and 20 g/l NaCl solutions have slope values $-0.10, -0.11$ and -0.12, respectively. But these values also indicate that curve of 10 g/l NaCl solution is somewhat shifting out of proportionality with the 5 g/l NaCl solution as observed for shear rate $1\ s^{-1}$.

For shear rate $100\ s^{-1}$a more rapid relaxation is seen where even 0 g/l NaCl solution exceed 90% relaxation. Which shows a larger leap in relaxation, minimizing the gap between its curve and the saline solutions even further. But overall, we see closer movement towards 100% relaxation in significantly less time. However, a full relaxation is not obtainable for this experiment due to the limited time as it would theoretically take infinite time to reach that state.

Furthermore, the slope of the linear zone does not seem to flatten out, rather incline further for the saline solutions. While the 0 g/l NaCl solution experiences a setback with the slope value -0.05. This does not give us a clear pattern for the 0 g/l NaCl solution and the effect of shear rate on relaxation. But for the rest of the solutions that contain salt could indicate there is a relationship between salinity and relaxation.

Moreover, the 10 g/l NaCl solution is continuously shifting closer towards the 20 g/l NaCl solution. This could indicate that relaxation from high enough shear rate can possibly form an independency from salinity.

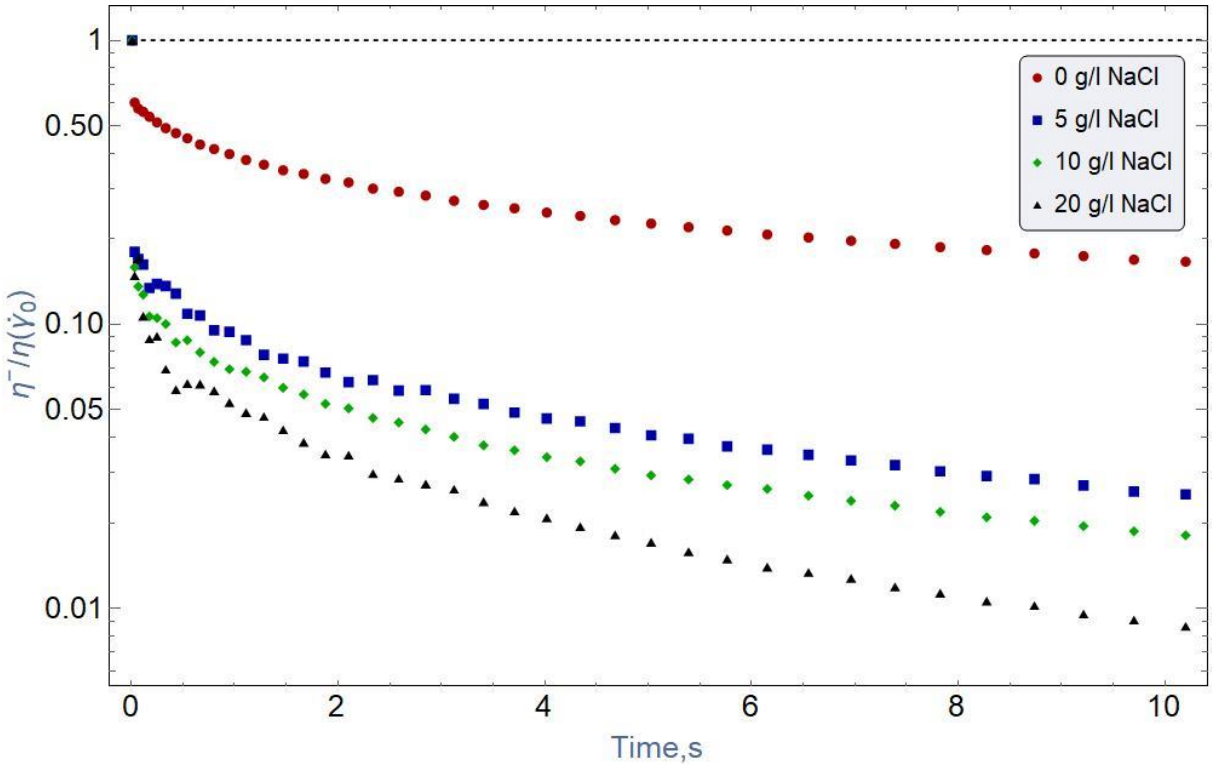

Figure 63 Normalized shear stress decay versus time for FLOPAAM 5115 VHM with various NaCl concentrations at step shear rate 1 s^{-1}.

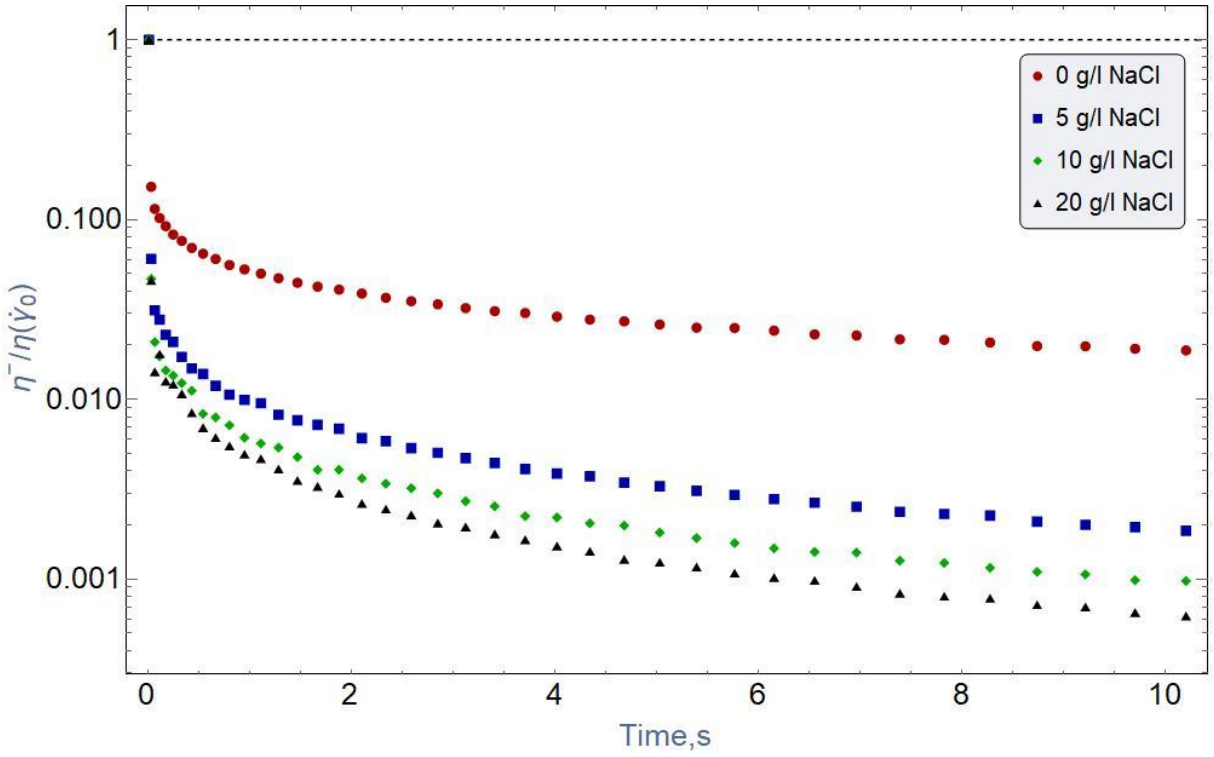

Figure 64 Normalized shear stress decay versus time for FLOPAAM 5115 VHM with various NaCl concentrations at step shear rate 10 s^{-1}.

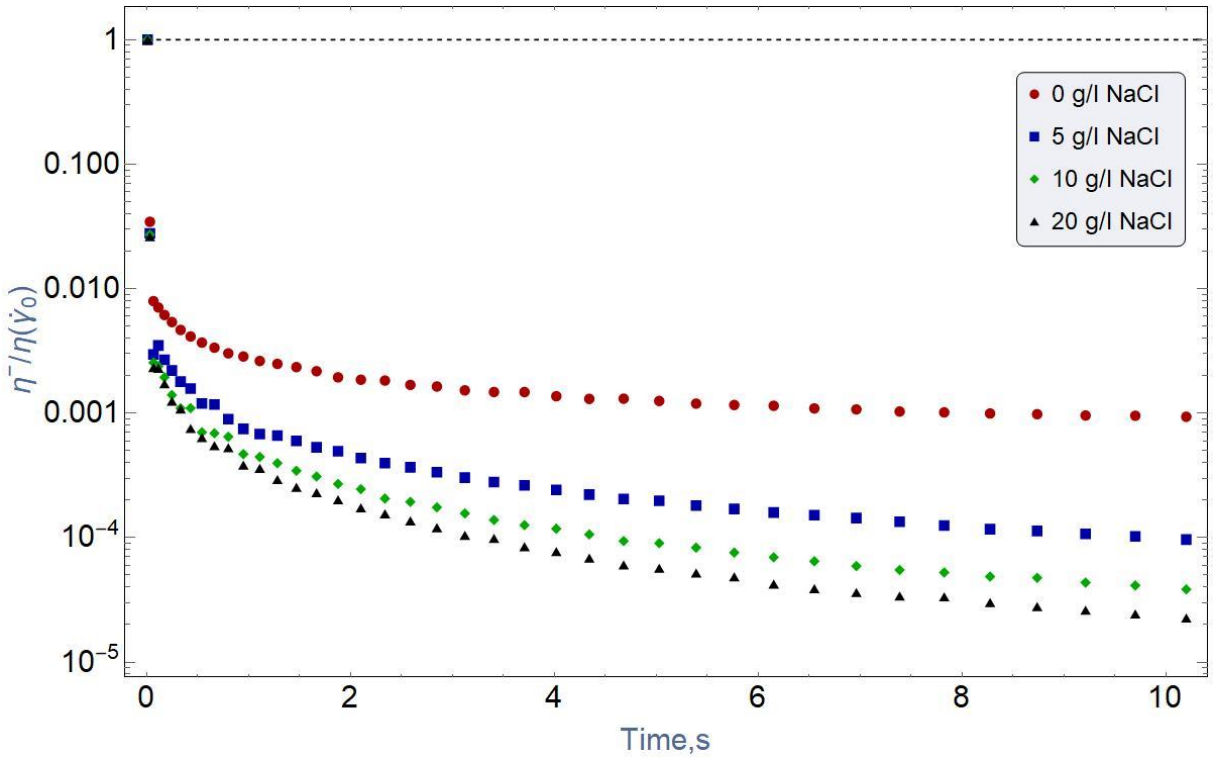

Figure 65 Normalized shear stress decay versus time for FLOPAAM 5115 VHM with various NaCl concentrations at step shear rate 100 s^{-1}.

9.3.1 Data/Model Fitting

In the upcoming sub chapters the results of the model fitting will be discussed. The physical non-Newtonian fluid models LPTT and EPTT will be fitted against the measured data obtained from the cessation of steady shear flow experiment. As the models use different scales, the measured data was scaled accordingly.

9.3.1.1 Affine Linear PTT

The LPTT-model was fitted against the scaled data and resulted in normalized shear stress decay versus dimensionless time plots. Seven curves for the measured data and model identified by step shear rates $1, 10$ and $100\ s^{-1}$ (or their specific Weissenberg number (Wi)) for both polymer types and each salt concentration. Thus, a total of 8 figures were generated. Where dotted points (red, blue, and green) represents the measured data and dashed lines (red, blue, green and black (linear viscoelastic limit)) represents the model predictions. A total of 8 figures have been generated for both FLOPAAM 5115 VHM and FLOPAAM 3630-S, see Fig. 66, 67, 68 and 69 and Appendix. C.

The LPTT-model show horrible predictions for relaxation of the experimented polymers. And this is something that was already expected based on the results of steady shear ramping and steady shear flow start-up diagrams from previous sections.

For FLOPAAM 5115 VHM 0 g/l NaCl solution, it seems that the model curve that is closest in predicting the relaxation of that particular solution is the curve at high Wi, namely curve of Wi=2019.986. Which do fail to predict the initial leap in shear stress relaxation. It does later on start to trend closer to the curve of measured data of the corresponding solution but does not align with it at all.

Furthermore, the addition of salt seen for the saline solutions show even worse model predictions. As the increase in salinity increases the rate of relaxation. Minor changes are observable for the model curves, but not in the same dimension as the curves of the measured data. This shows how model completely fail to account for any impact of salinity on the

polymer solution. The same patterns are observable for the FLOPAAM 3630-S solutions, with minor differences due to the chemical structure of the polymer itself.

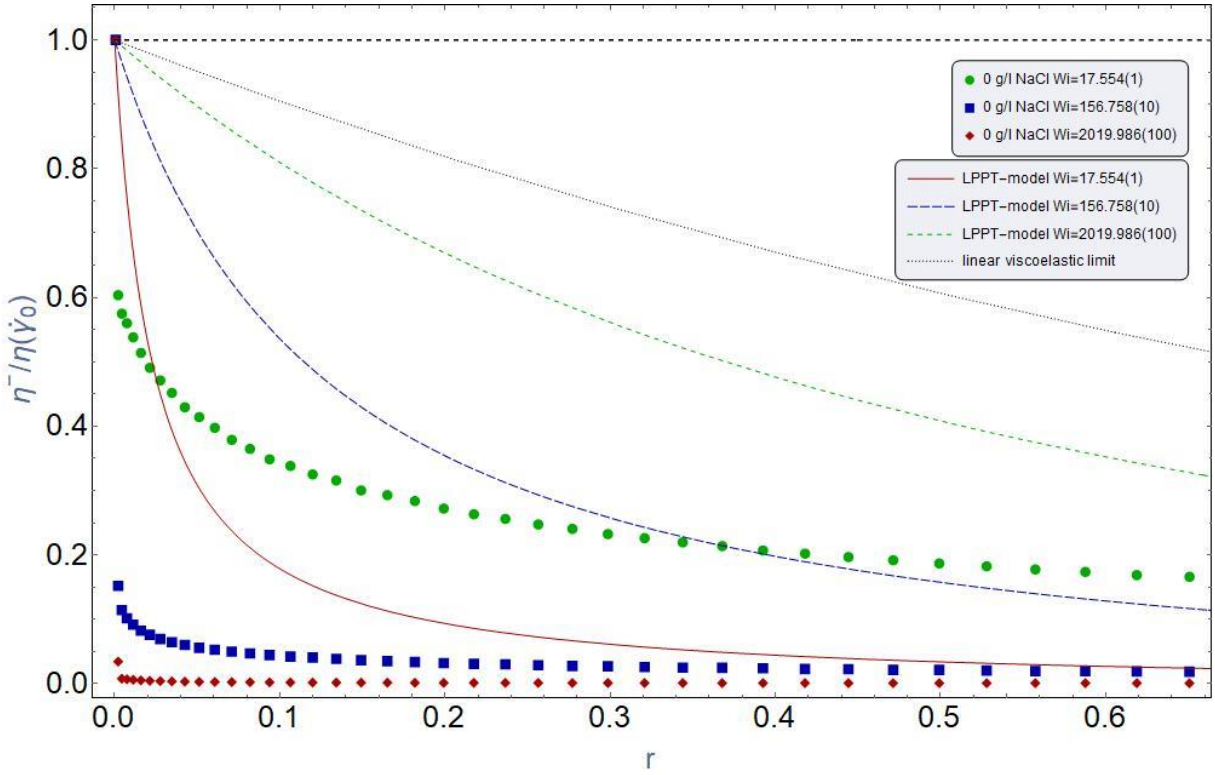

Figure 66 Normalized shear stress growth and LPTT-model prediction versus dimensionless time, r, for FLOPAAM 5115 VHM 0 g/l NaCl. Dots representing measured data and dashed lines representing model predictions for step shear rates 1 $(green)$, 10 $(blue)$ and 100 s^{-1}(red). Fitted parameters: $\epsilon = 0.01$.

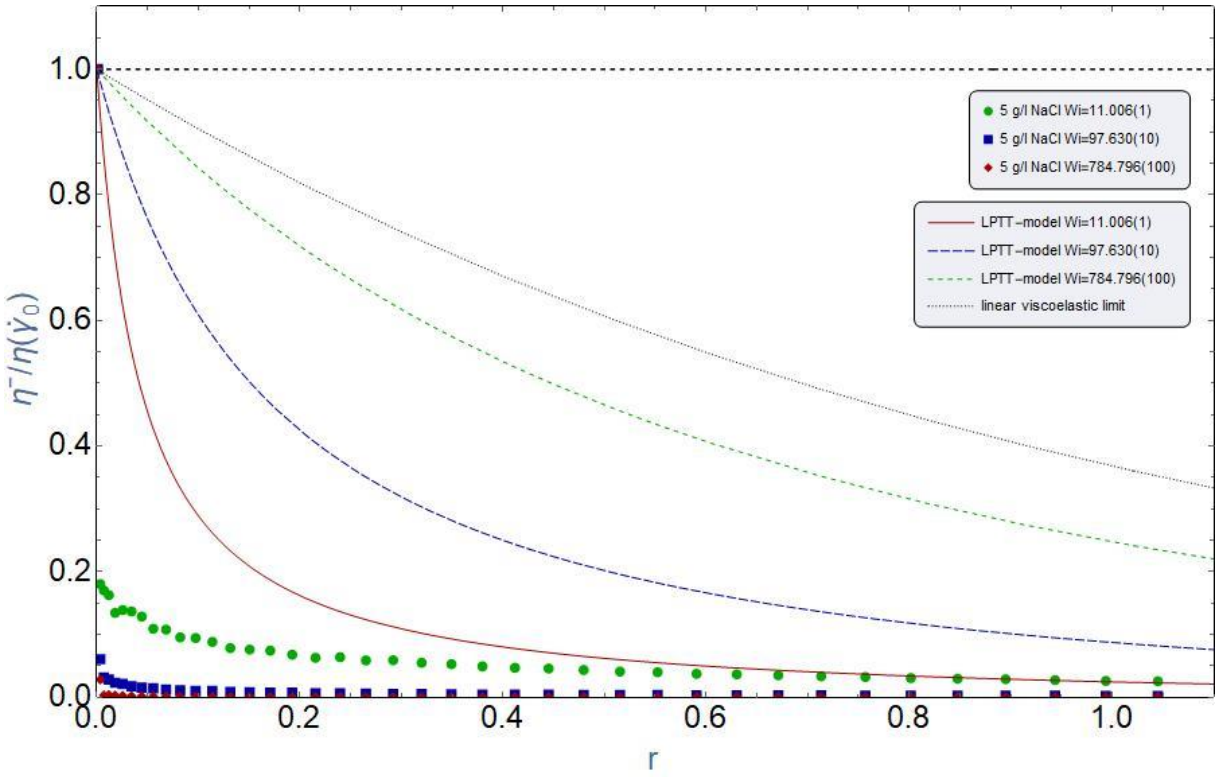

Figure 67 Normalized shear stress growth and LPTT-model prediction versus dimensionless time, r, for FLOPAAM 5115 VHM 5 g/l NaCl. Dotted points representing measured data and dashed lines representing model predictions for step shear rates 1 $(green)$, 10 $(blue)$ and 100 s^{-1}(red). Fitted parameters: $\epsilon = 0.01$.

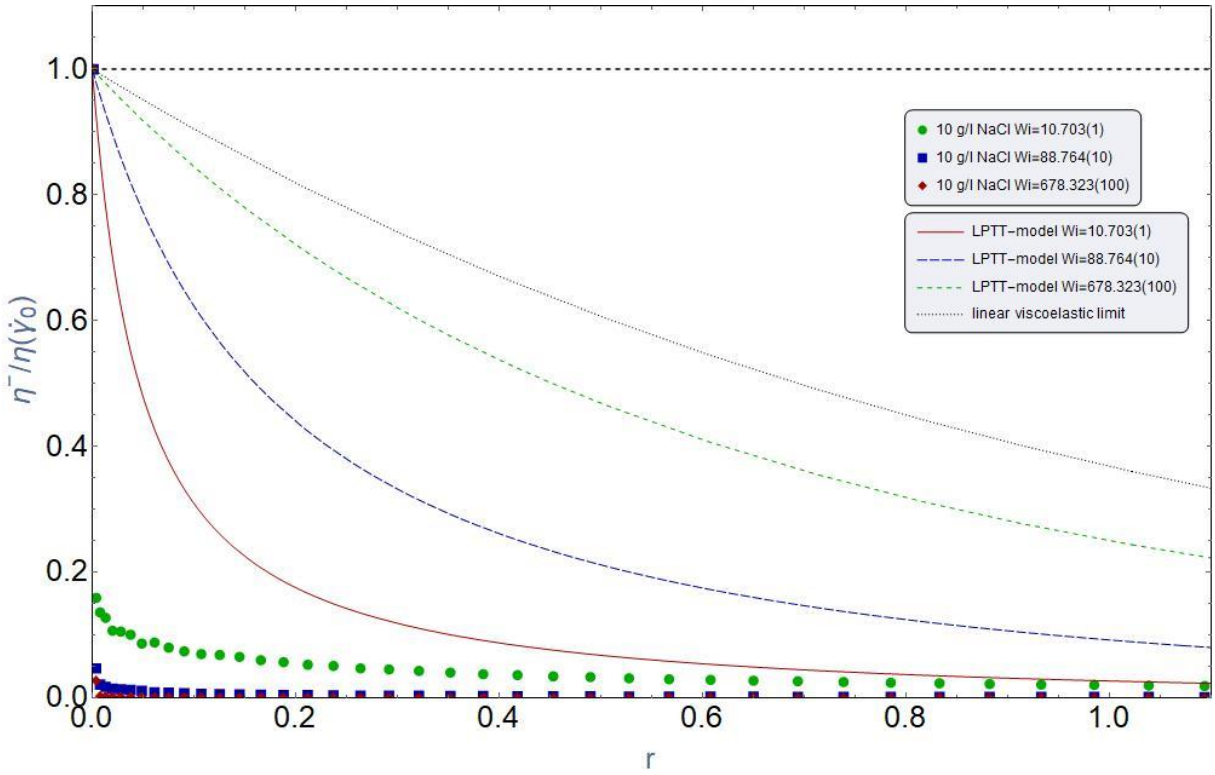

Figure 68 Normalized shear stress growth and LPTT-model prediction versus dimensionless time, r, for FLOPAAM 5115 VHM 10 g/l NaCl. Dots representing measured data and dashed lines representing model predictions for step shear rates 1 $(green), 10$ $(blue)$ and 100 s^{-1}(red). Fitted parameters: $\epsilon =$ 0.01.

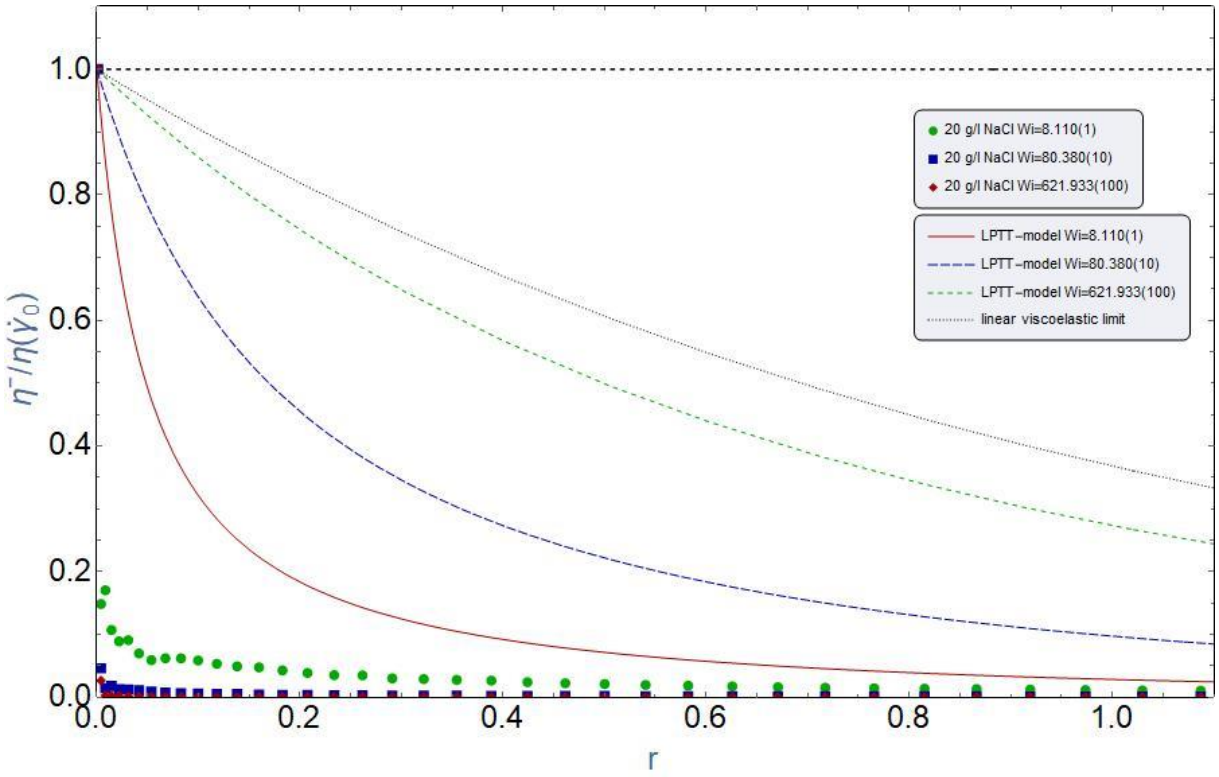

Figure 69 Normalized shear stress growth and EPTT-model prediction versus dimensionless time, r, for FLOPAAM 5115 VHM 20 g/l NaCl. Dots representing measured data and dashed lines representing model predictions for step shear rates 1 $(green), 10$ $(blue)$ and 100 s^{-1}(red). Fitted parameters: $\epsilon = 0.01$.

9.3.1.2 Affine Exponential PTT

The EPTT-model was fitted against the scaled data and resulted in normalized shear stress decay versus dimensionless time plots. Six curves for the measured data and model predictions identified by step shear rates $1, 10$ and $100\ s^{-1}$ for FLOPAAM 5115 VHM. Where dotted points (red, blue, and green) represents the measured data and dashed lines (red, blue and green) represents the model predictions. A total of 16 figures have been generated, see Fig. 70, 71, 72 and 73 and Appendix. C.

The EPTT-model as expected do show improvement in predicting shear stress relaxation over the LPTT-model, but it is still insufficient. Again, the model's most ideal curve is seen for FLOPAAM 5115 VHM 0 g/l NaCl solution as it acts less dilute than the saline solutions, yet it underpredicts the relaxation significantly.

In the case for step shear rate $1\ s^{-1}$ the model show a more severe relaxation at later times than what shown for measured data, but seem to later on correct itself as the reference shear rate is increased to 10 and $100\ s^{-1}$ as seen on Fig. 69. The same behavior is also observable for FLOPAAM 3630-S 0 g/l NaCl solution. However, the model worsens its prediction at such high reference shear rates by which gap between model curve and measured data enlarges further. Where the shear stress of polymer solution is relieved by a factor of 10^{-2}, the model predicts it by a factor of 10^{-1}.

The unproportional curve pattern seen for FLOPAAM 5115 VHM 0 g/l NaCl at shear rate $1\ s^{-1}$ is not observed for any of the saline solutions. However, as the salinity increases the gap between model curve and measured data widens further.

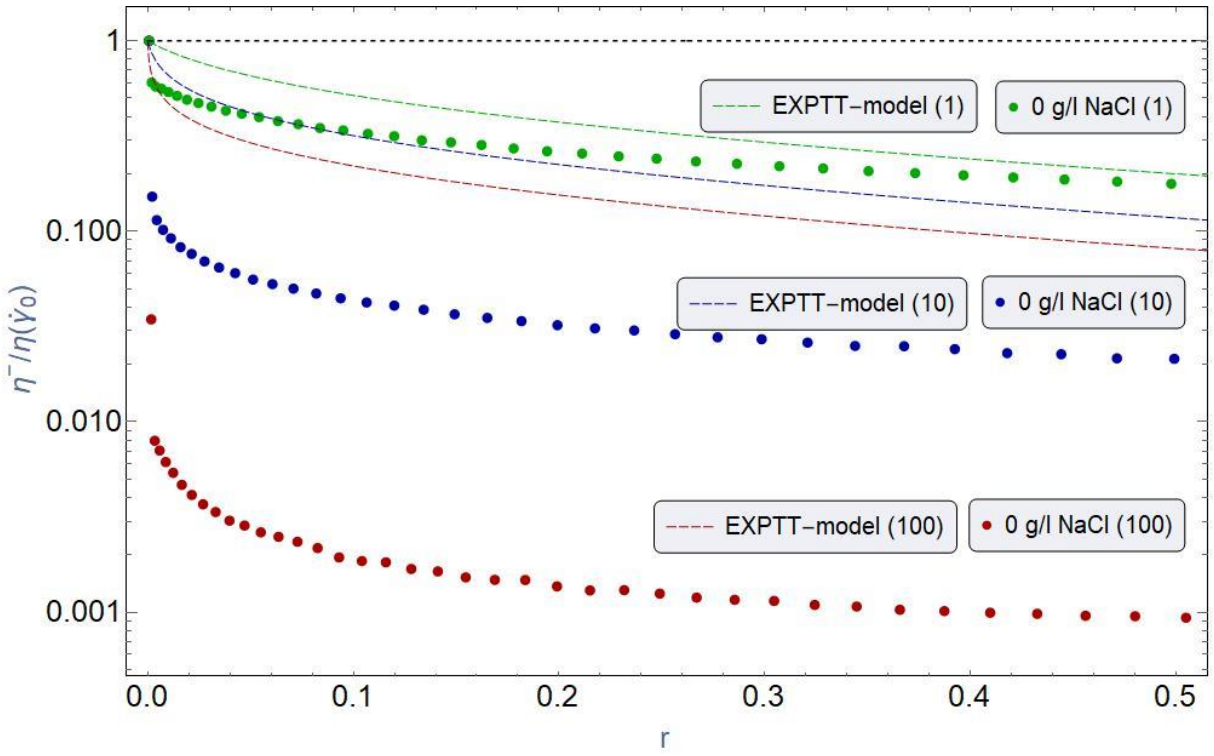

Figure 70 Normalized shear stress growth and EPTT-model prediction versus dimensionless time, r, for FLOPAAM 5115 VHM 0 g/l NaCl. Dotted points representing measured data and dashed lines representing model predictions for step rates 1 $(green)$, 10 $(blue)$ and 100 s^{-1}(red).

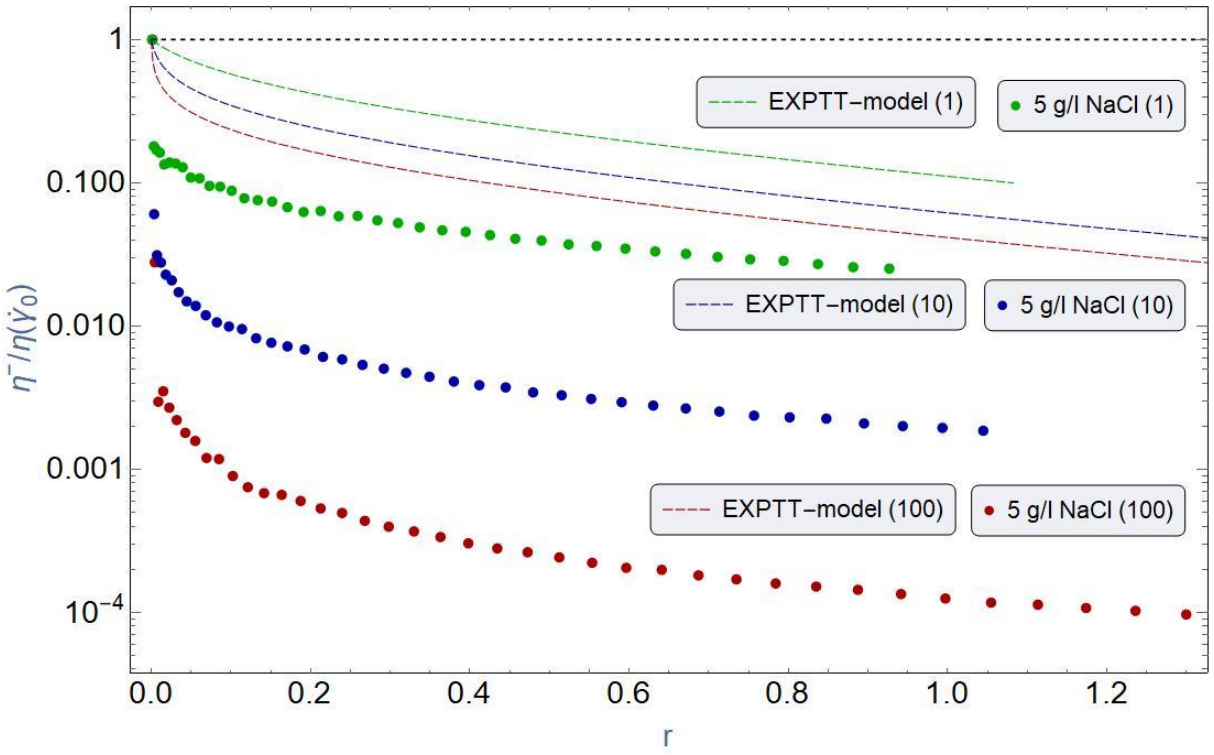

Figure 71 Normalized shear stress growth and EPTT-model prediction versus dimensionless time, r, for FLOPAAM 5115 VHM 5 g/l NaCl. Dotted points representing measured data and dashed lines representing model predictions for step rates 1 $(green)$, 10 $(blue)$ and 100 s^{-1}(red).

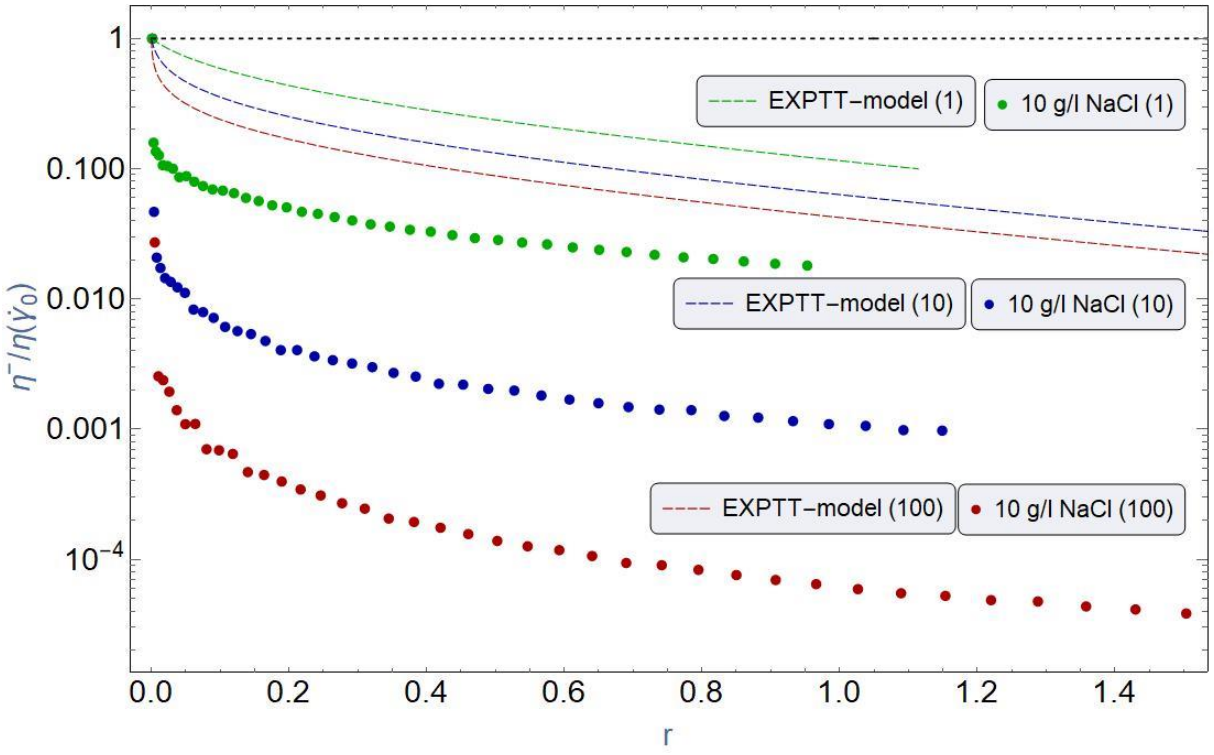

Figure 72 Normalized shear stress growth and EPTT-model prediction versus dimensionless time, r, for FLOPAAM 5115 VHM 10 g/l NaCl. Dotted points representing measured data and dashed lines representing model predictions for step rates 1 $(green)$, 10 $(blue)$ and 100 s^{-1}(red).

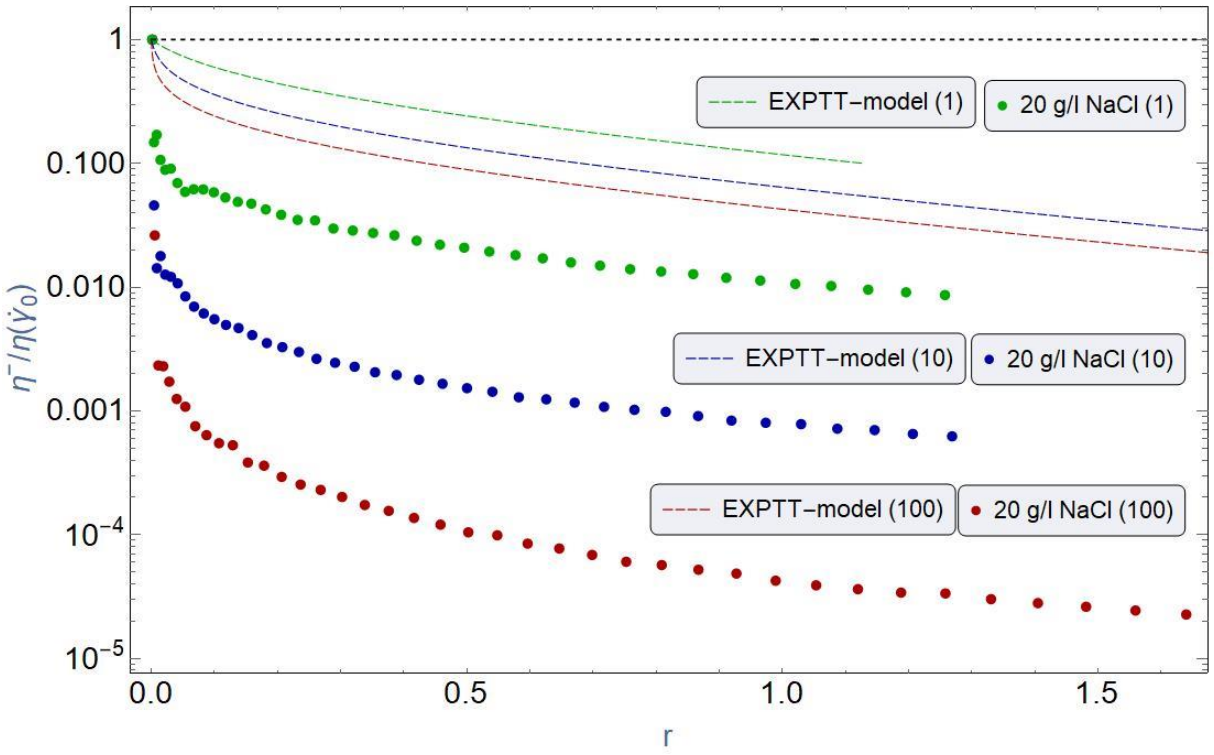

Figure 73 Normalized shear stress growth and EPTT-model prediction versus dimensionless time, r, for FLOPAAM 5115 VHM 20 g/l NaCl. Dotted points representing measured data and dashed lines representing model predictions for step rates 1 $(green)$, 10 $(blue)$ and 100 s^{-1}(red).

Conclusions

The objectives of this work were to attempt to achieve a better understanding of the impact of salt addition on the material functions of specific FLOPAAM polymers, both quantitively and qualitatively based on the experiments conducted. Several papers of similar work have been published, but quantitative analysis of physical non-Newtonian fluid models when applied to EOR polymers remains scarce. This work was not intended to provide such extensive analysis, but rather a contribution in the work to fully understand their performance, mainly the C-FENE-P-model as it is a relatively new model that supposedly have the capability to account for salt-sensitivity. This quantitative analysis of C-FENE-P can be considered a first time ever, as we are unaware of such work being made previously. Based on the analysis made in the prior chapters the following have been concluded.

The addition of NaCl has certainly a stabilizing effect on the apparent viscosity of FLOPAAM's. As the measured data recorded lower viscosities and a larger impairment of shear-thinning behavior with increasing salinity. But this is not as significant as going from 0 to 5 g/l NaCl, therefore the increase of salt content has a declining impact on the magnitude of further impairment.

Furthermore, the shear stress growth has shown to be a non-monotonic function of salinity level. Salt content contributes with a dampening effect on the shear stress growth overshoot amplitude most significantly at high step shear rates. This is due to the dilutive effect of salt. However, the time consumed in establishing steady state does not show the same dependency, as all the solutions arrive simultaneously regardless of salt concentration. In addition, the measured data has shown a similar correlation of salinity and the declining impact of salinity level on the overshoot amplitudes, as discovered for the apparent viscosity.

Regarding shear stress decay curves, the exponent values of the exponential region of show a clear dependency on salinity and step shear rate, whereas the zero-salinity solution shows a contradicting trend.

The LPTT-model is by theory applicable for only concentrated polymer solutions undergoing weak flow, but surprisingly failed to predict the relative viscosity for the ~ 6000 ppm 0 g/l NaCl solutions by showing a significant over-prediction in relative viscosity, which means this model has its own scale for what is considered as concentrated. Thus, naturally the model will fail for saline solutions as well. It is recommended for further work to investigate the concentration range to define what is considered as concentrated by this model. From this it is unsurprising that the model cannot predict the relative shear stress growth and decay, as it has an overshoot peak limitation of 1.14 scaled value, which is insufficient to predict shear stress growth and it cannot keep up with the impact of salinity regarding the shear stress decay.

The EXPPT-model, however, is a somewhat good fit for concentrated solutions, but breaks down for saline solutions, this applies to viscosity, shear stress growth and decay.

The FENE-P-model is meant to be applicable for dilute polymer solutions, which is agreeable upon as it is under-predictive of shear-thinning for concentrated solutions and almost perfect for low salinity solutions undergoing shear flow. However, it fails to a certain degree as the shear rate ramps up to higher levels when applied for high salt concentrated solutions. Additionally, FENE-P-model for start-up of steady shear flow has the limitation to depend b values being positive to be applicable and fails whenever the opposite is obtained.

C-FENE-P on the other hand, covers most of the areas the FENE-P model fails in. It is capable of predicting shear-thinning behavior quite well, but still has the shortcomings FENE-P experienced with concentrated solutions. The benefit of this model is not only the incorporation of E, but the ability to bypass the obstacle of determining b by calculative measures and instead select it manually to maintain a positive value. Yet, resolving this issue does not resolve the overprediction of this model for shear stress growth. Therefore, one can state this model is unreliable for shear stress growth. This approach is imperfect, as it provides high level of uncertainty, but nonetheless this is considered an improvisation as it would demand extensive experiments to obtain additional parameters to determine b and E more precisely.

Lastly, it is important to notice that these models are highly sensitive to several parameters and different experiments can performed to determine them for improved model accuracy, but also the approach of applying these models will have a significance on the end results and might be line between the model failing or not. As most of these models are reliant on λ_e, the approach selected in this work for obtaining these values were based on the exponent of the exponential region of the cessation experiment, in this case the last five measurement points, which are prone to noise. This approach was found to not yield satisfactory fits for transient flows as the data from which λ_e was calculated involve very low stresses, which yields large uncertainty. Therefore, this particular method of fitting the models is questionable. Hence, the second recommendation for further work is to attempt to validate this theory.

Bibliography

Ait-Kadi, A., Carreau, P.J., Chauveteau, G., 1987. Rheological Properties of Partially Hydrolyzed Polyacrylamide Solutions. J. Rheol. 31, 537–561. https://doi.org/10.1122/1.549959

Andrade, L.C.F., Petronílio, J.A., Maneschy, C.E. de A., Cruz, D.O. de A., 2007. The carreau-yasuda fluids: a skin friction equation for turbulent flow in pipes and kolmogorov dissipative scales. J. Braz. Soc. Mech. Sci. Eng. 29. https://doi.org/10.1590/S1678-58782007000200005

Bird, R.B., Armstrong, R.C., Hassager, O., 1987. Dynamics of polymeric liquids. Vol. 1, 2nd Ed. : Fluid mechanics. John Wiley and Sons Inc.,New York, NY, United States.

Bird, R.B., Dotson, P.J., Johnson, N.L., 1980. Polymer solution rheology based on a finitely extensible bead—spring chain model. J. Non-Newton. Fluid Mech. 7, 213–235. https://doi.org/10.1016/0377-0257(80)85007-5

Deshpande, A., Murali Krishnan, J., Kumar, P.B., Deshpande, A.P., Krishnan, J.M., 2010. Rheology of Complex Fluids. New York, NY: Springer, New York, NY. https://doi.org/10.1007/978-1-4419-6494-6

Deville, M., Gatski, T., 2012. Mathematical Modeling for Complex Fluids and Flows, Mathematical Modeling for Complex Fluids and Flows. https://doi.org/10.1007/978-3-642-25295-2

Ferrás, L.L., Morgado, M.L., Rebelo, M., McKinley, G.H., Afonso, A.M., 2019. A generalised Phan–Thien—Tanner model. J. Non-Newton. Fluid Mech. 269, 88–99. https://doi.org/10.1016/j.jnnfm.2019.06.001

Garrido, V.H.R., 2007. Molecular Structure and Constitutive Modelling of Polymer Melts, Schriftenreihe Kunststoff-Forschung. Univ.-Verlag der TU Berlin.

Leschber, A., n.d. Finitely Extensible Nonlinear Elastic Model Notes 8.

Mezger, T.G., 2019. The Rheology Handbook: 4th Edition. Vincentz Network, Hannover, Germany. https://doi.org/10.1515/9783748600367

Muralisrinivasan, N.S., 2015. Basics of polymers : fabrication and processing technology, Plastics and Polymers Collection. Momentum Press, New York, NY.

Needham, R.B., Doe, P.H., 1987. Polymer Flooding Review. SPE-17140-PA 39, 1503–1507. https://doi.org/10.2118/17140-PA

NPD, 2020. A brief description of EOR methods. [WWW Document]. URL https://www.npd.no/en/facts/publications/reports2/resource-report/resource-report-2017/technical-potential/avanserte-utvinningsmetoder-eor/a-brief-description-of-eor-methods/

Purnode, B., Crochet, M.J., 1998. Polymer solution characterization with the FENE-P model. J. Non-Newton. Fluid Mech. 77, 1–20. https://doi.org/10.1016/S0377-0257(97)00096-7

Rothstein, J., Mckinley, G., 2001. Non-isothermal modification of purely elastic flow instabilities in torsional flows of polymeric fluids. Phys. Fluids 13. https://doi.org/10.1063/1.1338540

Shogin, Dmitry, Amundsen, P., 2020. A charged finitely extensible dumbbell model: explaining rheology of dilute polyelectrolyte solutions.

Shogin, D., Amundsen, P.A., 2020. A charged finitely extensible dumbbell model: Explaining rheology of dilute polyelectrolyte solutions. Phys. Fluids 32, 063101. https://doi.org/10.1063/5.0008321

SNF, 2012. Enhancing Polymer Flooding Performance 30 Years of Experience in EOR.

Surguchev, L., Manrique, E., Alvarado, V., 2005. Improved Oil Recovery: Status And Opportunities, in: WPC-18-0886. Presented at the 18th World Petroleum Congress, World Petroleum Congress, WPC, p. 17.

Thien, N.P., Tanner, R.I., 1977. A new constitutive equation derived from network theory. J. Non-Newton. Fluid Mech. 2, 353–365. https://doi.org/10.1016/0377-0257(77)80021-9

van Heel, A.P.G., Hulsen, M.A., van den Brule, B.H.A.A., 1998. On the selection of parameters in the FENE-P model. J. Non-Newton. Fluid Mech. 75, 253–271. https://doi.org/10.1016/S0377-0257(97)00060-8

Wang, Z., Smith, D., 2018. Rheology Effects on Predicted Fiber Orientation and Elastic Properties in Large Scale Polymer Composite Additive Manufacturing. J. Compos. Sci. 2, 10. https://doi.org/10.3390/jcs2010010

Warner, H.R., 1972. Kinetic Theory and Rheology of Dilute Suspensions of Finitely Extendible Dumbbells. Ind. Eng. Chem. Fundam. 11, 379–387. https://doi.org/10.1021/i160043a017

Wever, D.A.Z., Picchioni, F., Broekhuis, A.A., 2011. Polymers for enhanced oil recovery: A paradigm for structure–property relationship in aqueous solution. Prog. Polym. Sci. 36, 1558–1628. https://doi.org/10.1016/j.progpolymsci.2011.05.006

Yah, C.S., 2018. A study of the flow behavior of prevulcanised natural rubber latex/singlewalled carbon nanotubes (SWCNT) blends using rotational viscometry and power law model.

Appendix. A

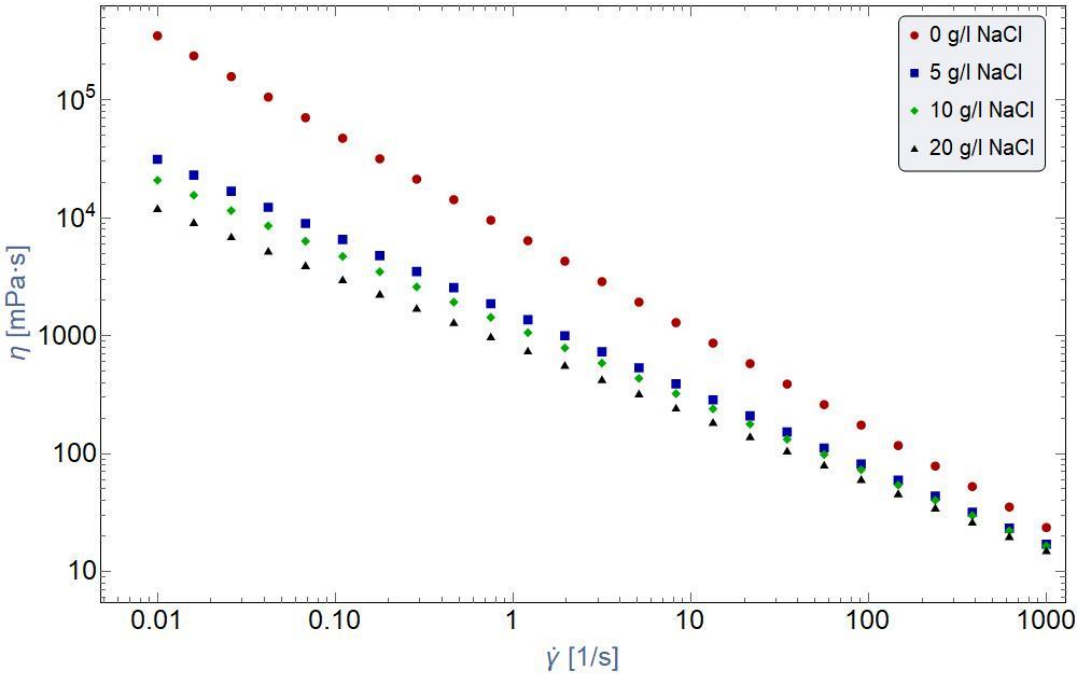

Figure 74 Power-law plot of viscosity versus shear rate for FLOPAAM 5115 VHM with various salinity level.

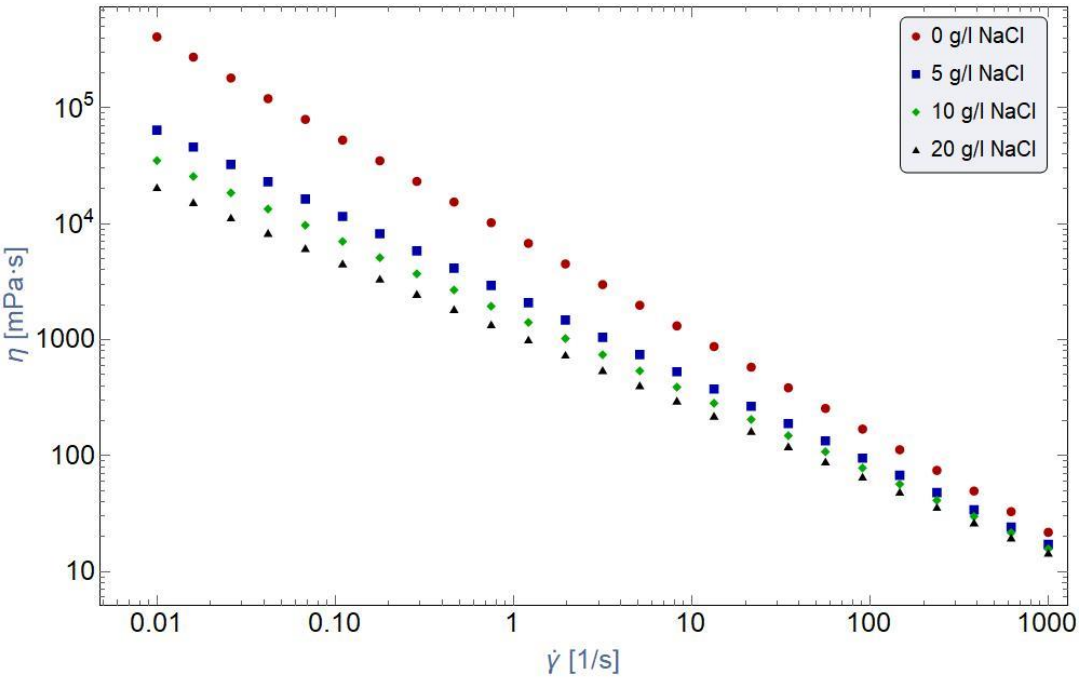

Figure 75 Power-law plot of viscosity versus shear rate for FLOPAAM 3630-S with various salinity level.

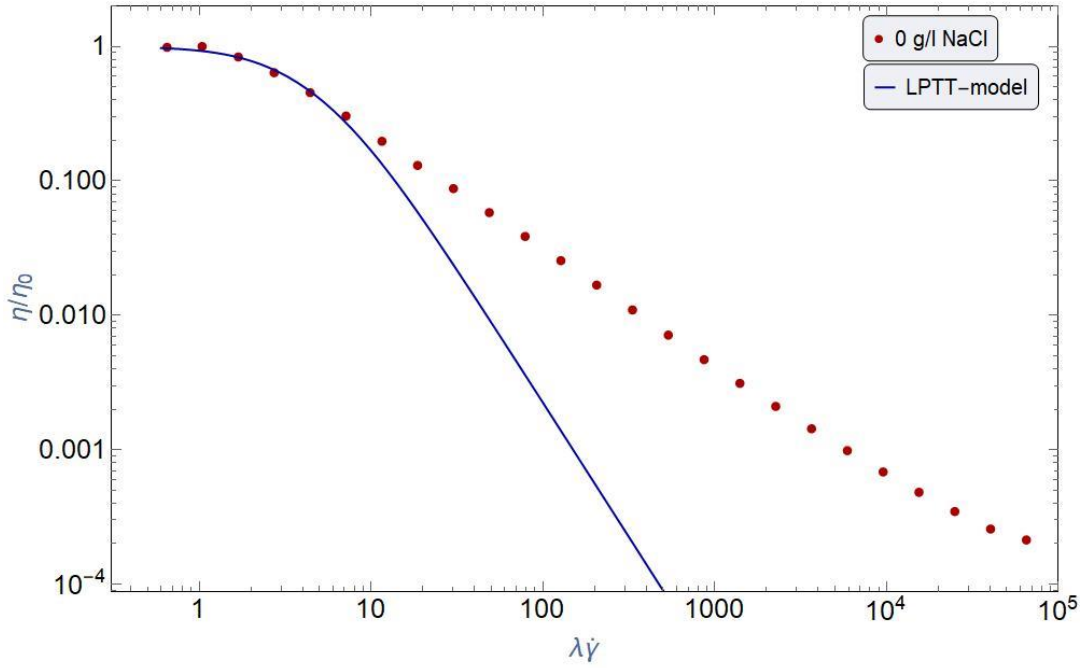

Figure 76 LogLog plot of normalized viscosity (red dots) and LPTT-model viscosity prediction (blue line) versus dimensionless shear rate for FLOPAAM 3630-S 0 g/l NaCl polymer solution.

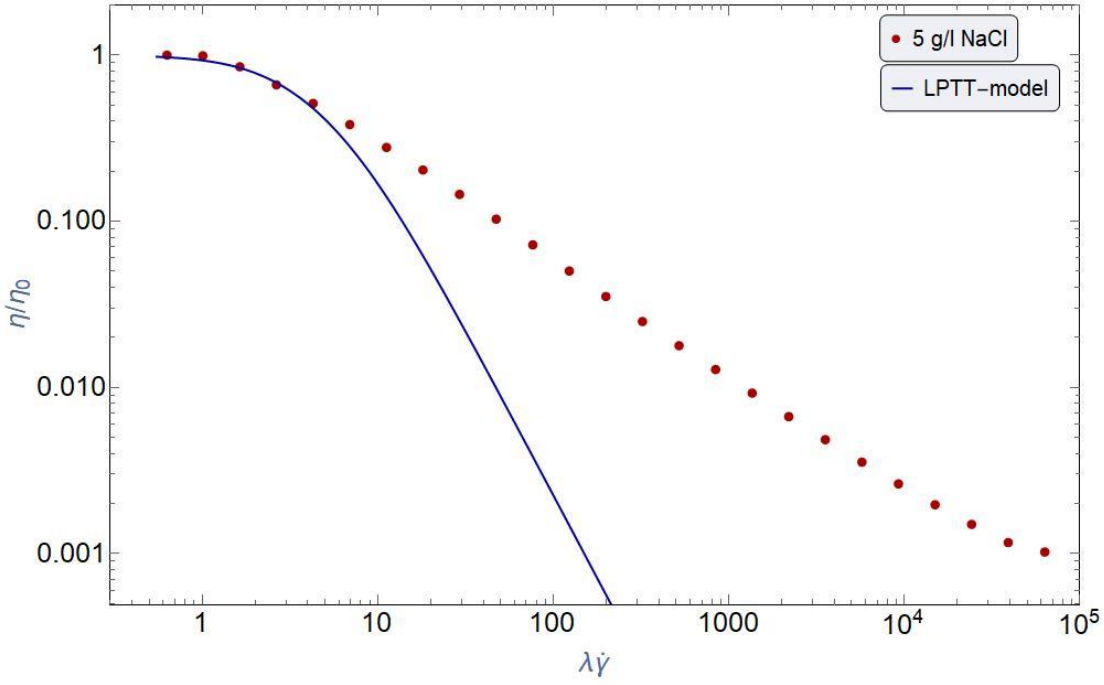

Figure 77 LogLog plot of normalized viscosity (red dots) and LPTT-model viscosity prediction (blue line) versus dimensionless shear rate for FLOPAAM 3630-S 5 g/l NaCl polymer solution.

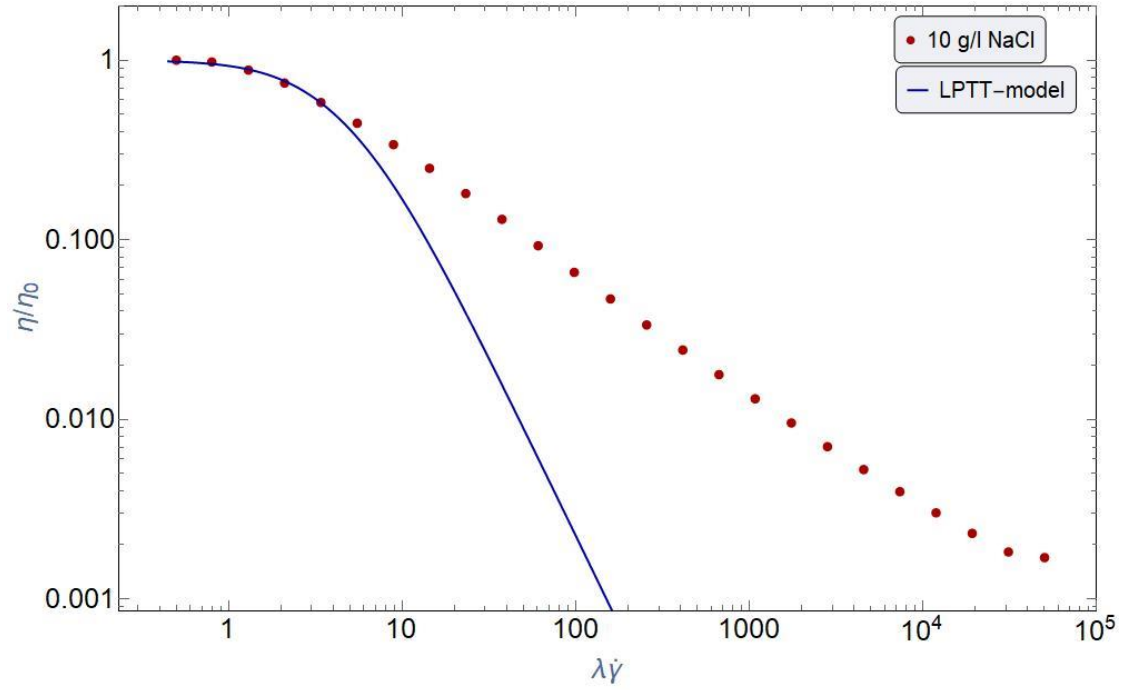

Figure 78 LogLog plot of normalized viscosity (red dots) and LPTT-model viscosity prediction (blue line) versus dimensionless shear rate for FLOPAAM 3630-S 10 g/l NaCl polymer solution.

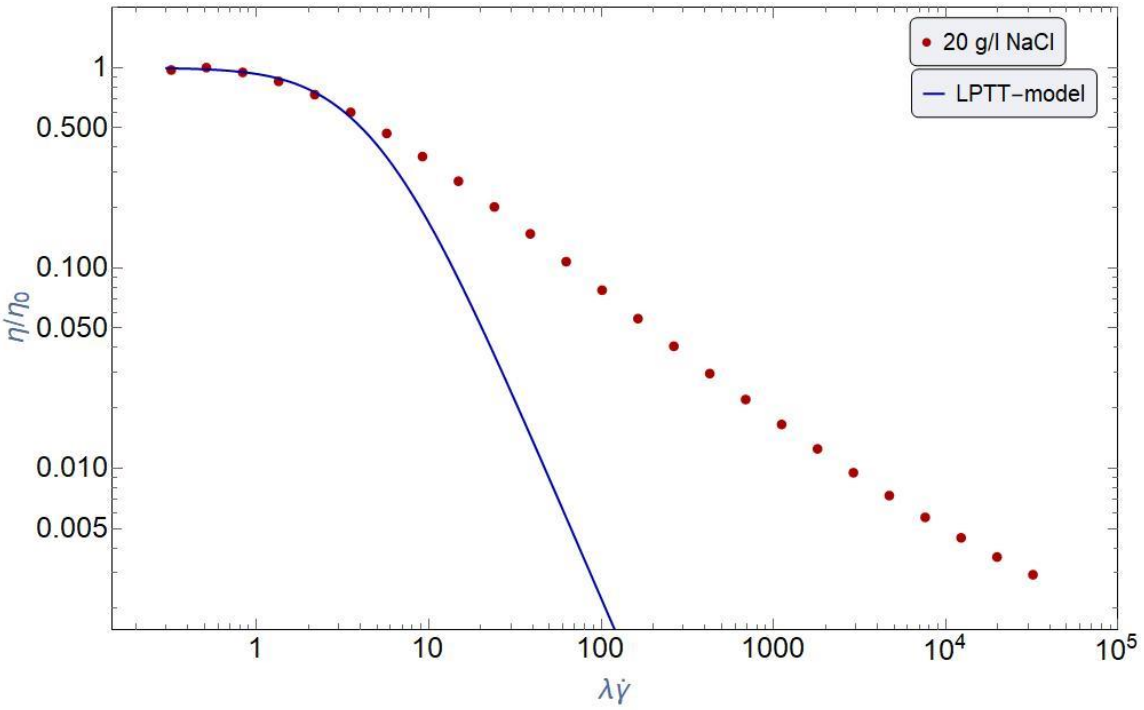

Figure 79 LogLog plot of normalized viscosity (red dots) and LPTT-model viscosity prediction (blue line) versus dimensionless shear rate for FLOPAAM 3630-S 20 g/l NaCl polymer solution.

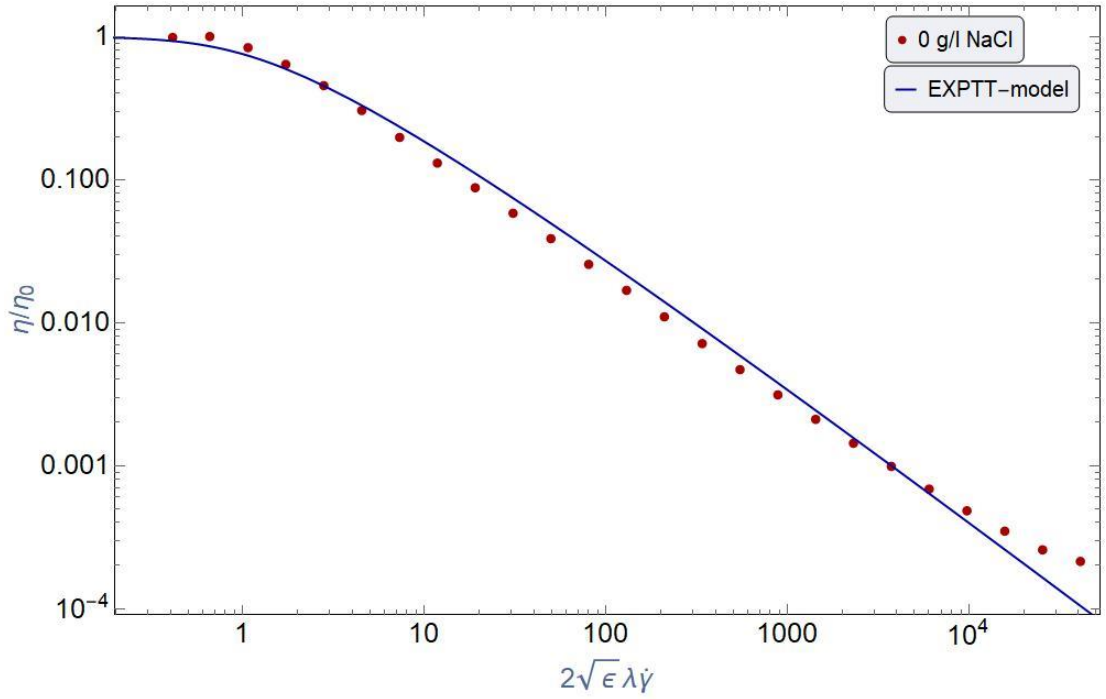

Figure 80 LogLog plot of normalized viscosity (red dots) and EPTT-model viscosity prediction (blue line) versus dimensionless shear rate for FLOPAAM 3630-S 0 g/l NaCl polymer solution.

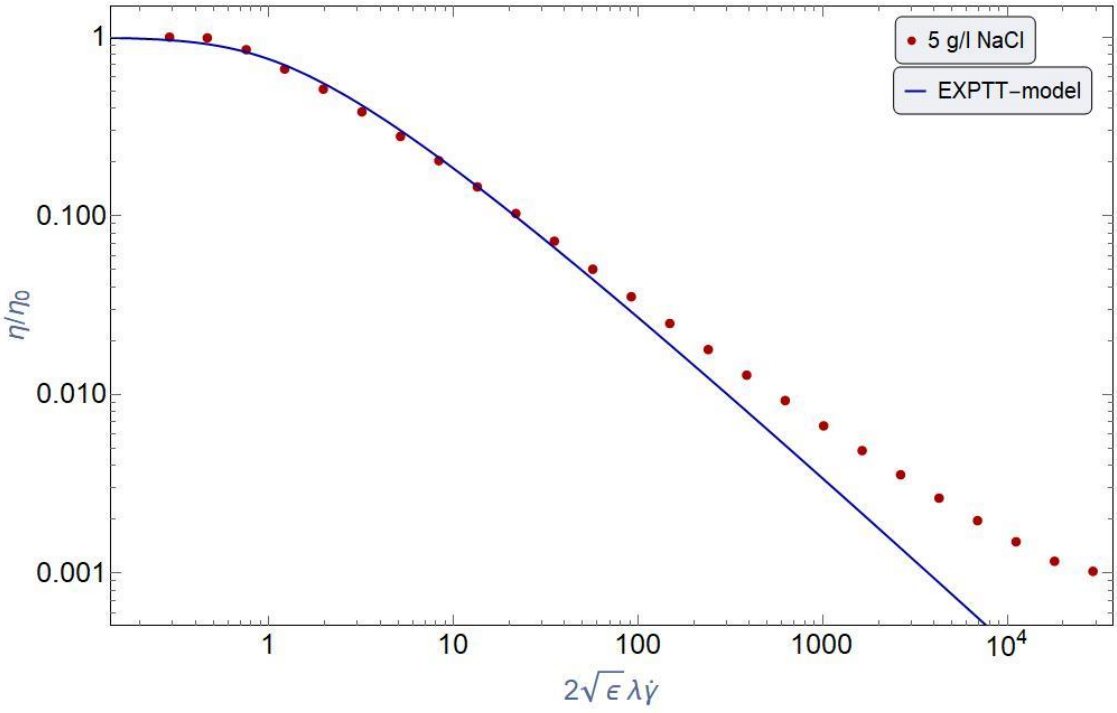

Figure 81 LogLog plot of normalized viscosity (red dots) and EPTT-model viscosity prediction (blue line) versus dimensionless shear rate for FLOPAAM 3630-S 5 g/l NaCl polymer solution.

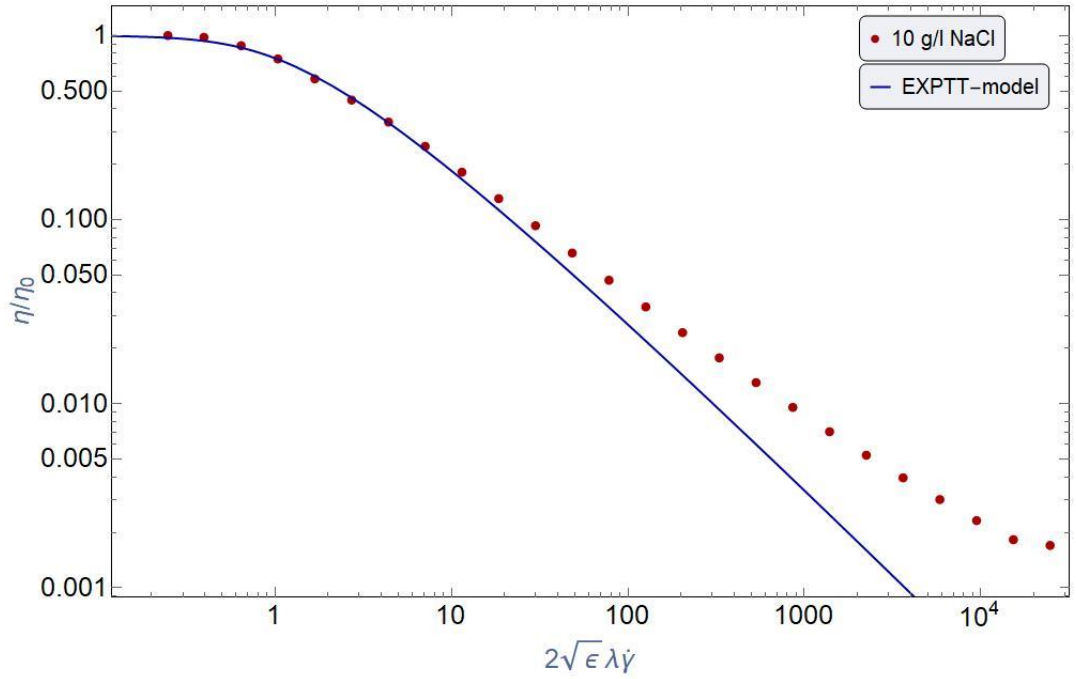

Figure 82 LogLog plot of normalized viscosity (red dots) and EPTT-model viscosity prediction (blue line) versus dimensionless shear rate for FLOPAAM 3630-S 10 g/l NaCl polymer solution.

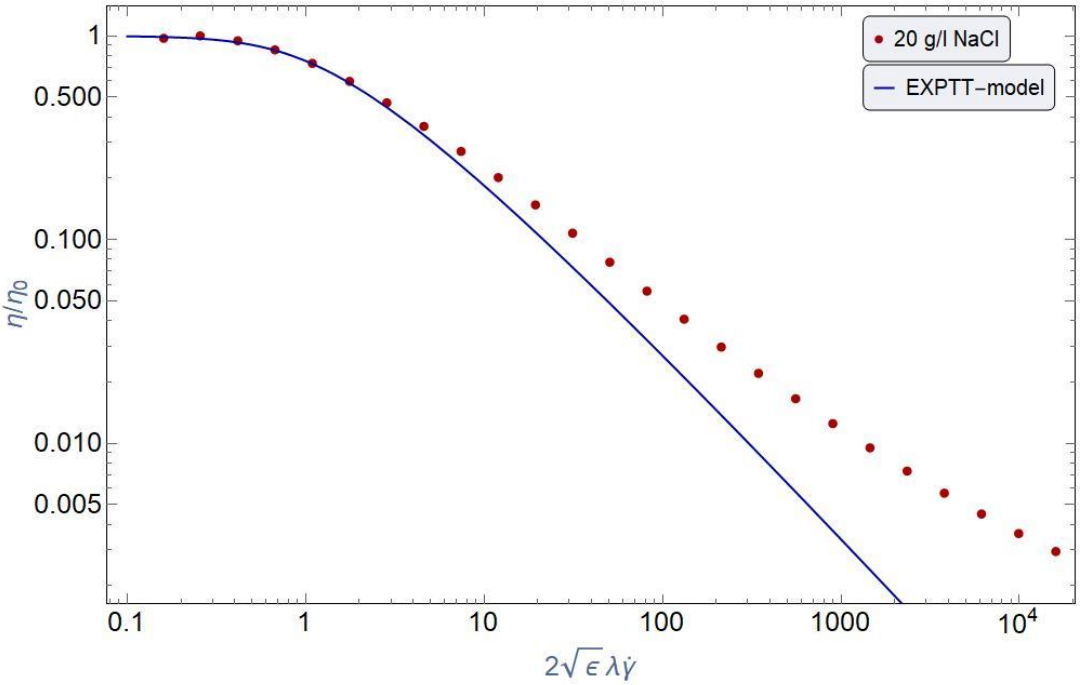

Figure 83 LogLog plot of normalized viscosity (red dots) and EPTT-model viscosity prediction (blue line) versus dimensionless shear rate for FLOPAAM 3630-S 20 g/l NaCl polymer solution.

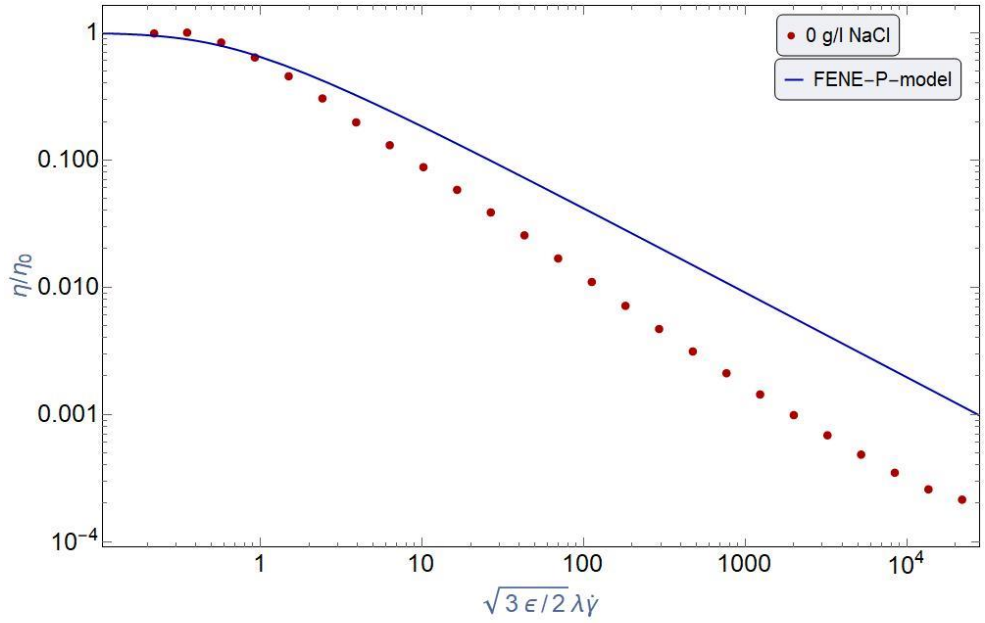

Figure 84 LogLog plot of normalized viscosity (red dots) and FENE-P-model viscosity prediction (blue line) versus dimensionless shear rate for FLOPAAM 3630-S 0 g/l NaCl polymer solution.

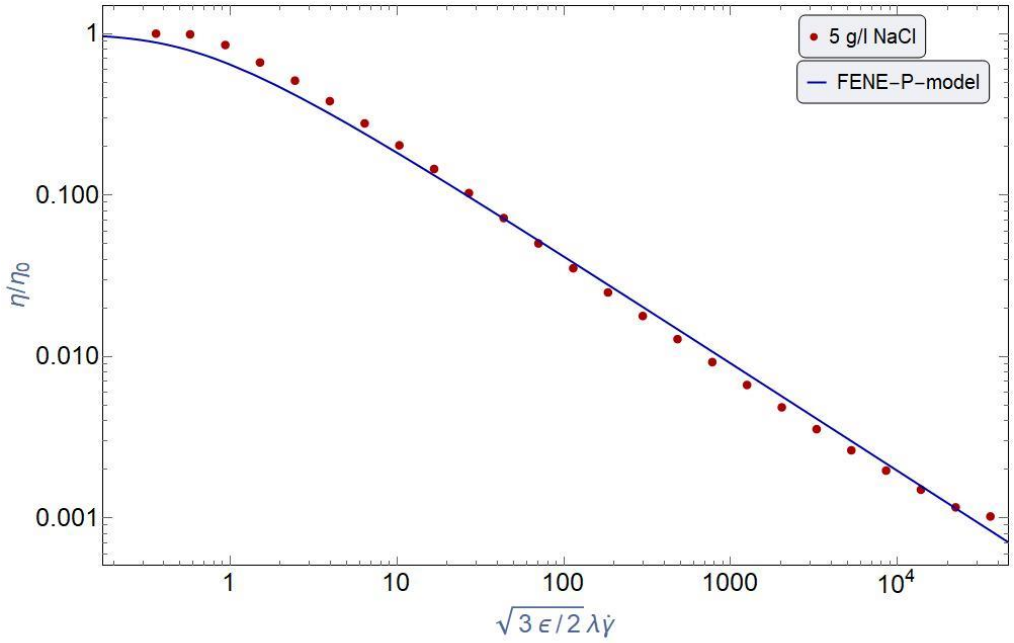

Figure 85 LogLog plot of normalized viscosity (red dots) and FENE-P-model viscosity prediction (blue line) versus dimensionless shear rate for FLOPAAM 3630-S 5 g/l NaCl polymer solution.

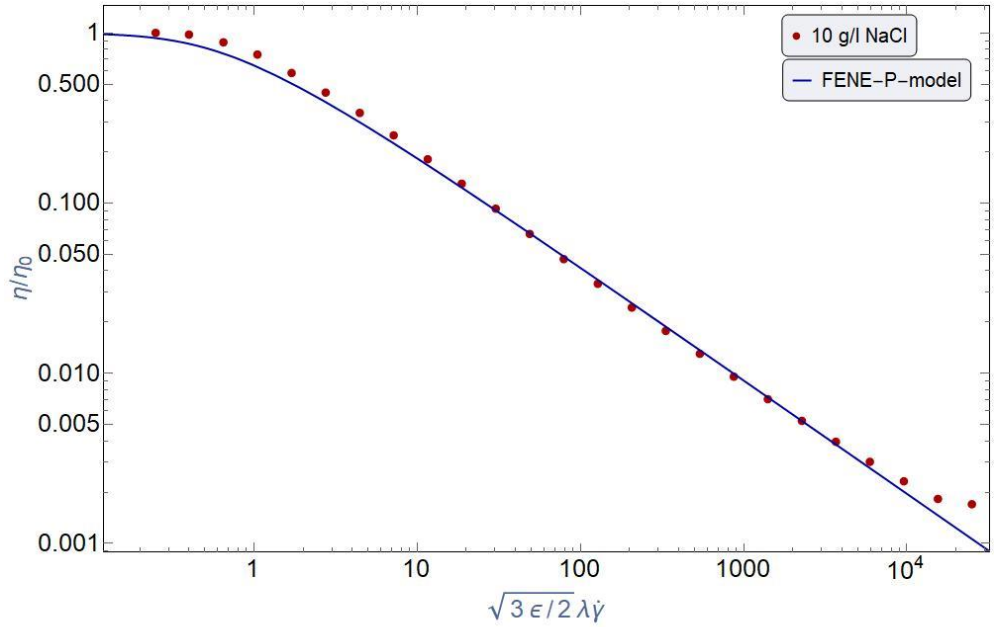

Figure 86 LogLog plot of normalized viscosity (red dots) and FENE-P-model viscosity prediction (blue line) versus dimensionless shear rate for FLOPAAM 3630-S 10 g/l NaCl polymer solution.

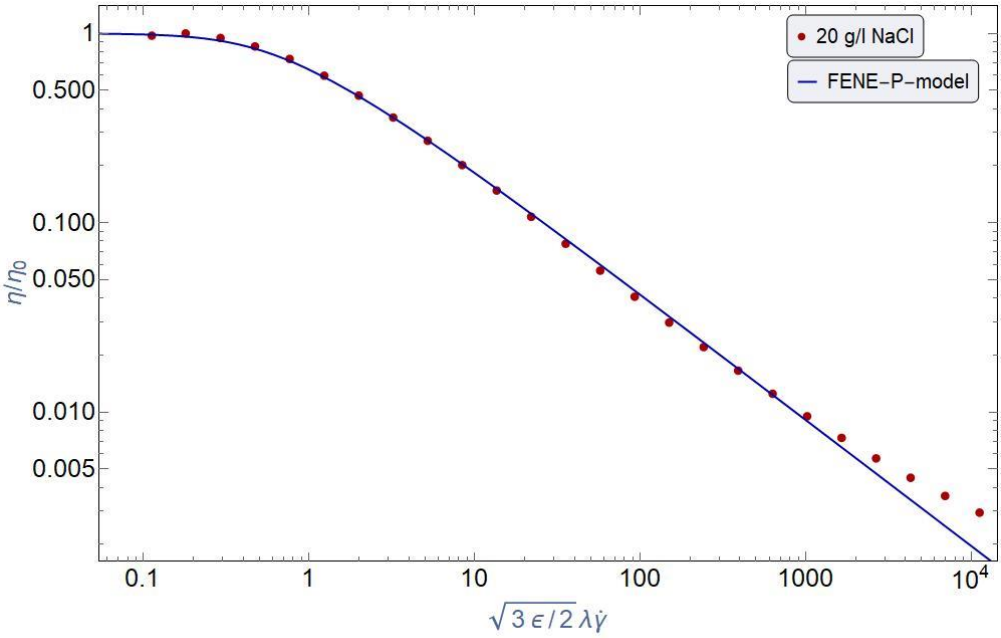

Figure 87 LogLog plot of normalized viscosity (red dots) and FENE-P-model viscosity prediction (blue line) versus dimensionless shear rate for FLOPAAM 3630-S 20 g/l NaCl polymer solution.

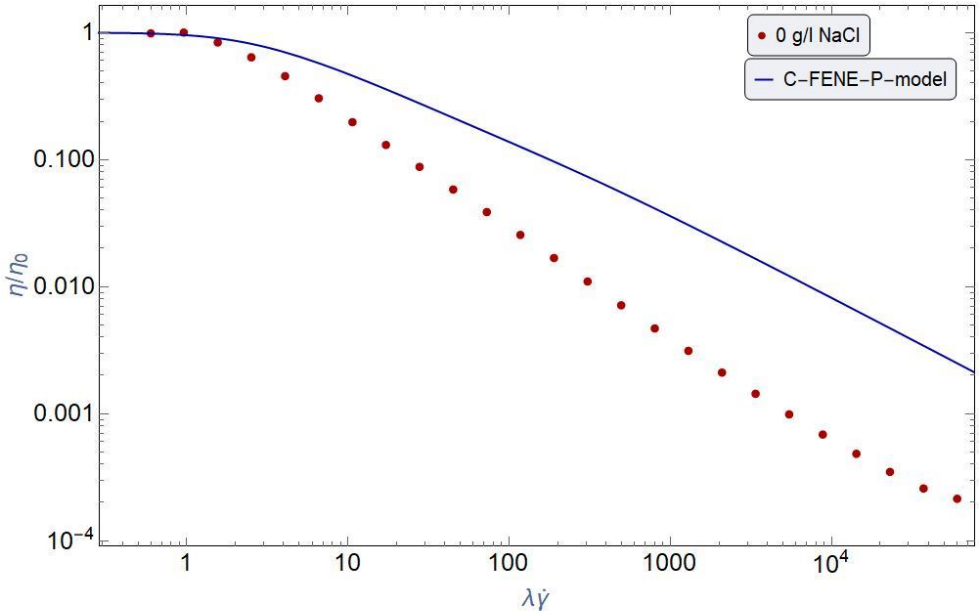

Figure 88 LogLog plot of normalized viscosity (red dots) and C-FENE-P-model viscosity prediction (blue line) versus dimensionless shear rate for FLOPAAM 3630-S 0 g/l NaCl polymer solution.

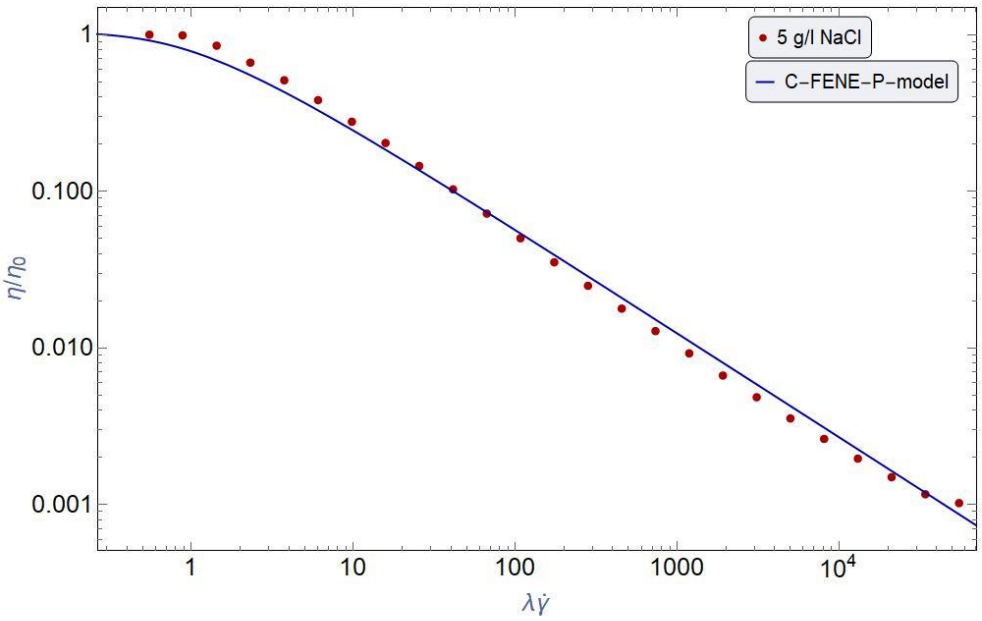

Figure 89 LogLog plot of normalized viscosity (red dots) and C-FENE-P-model viscosity prediction (blue line) versus dimensionless shear rate for FLOPAAM 3630-S 5 g/l NaCl polymer solution.

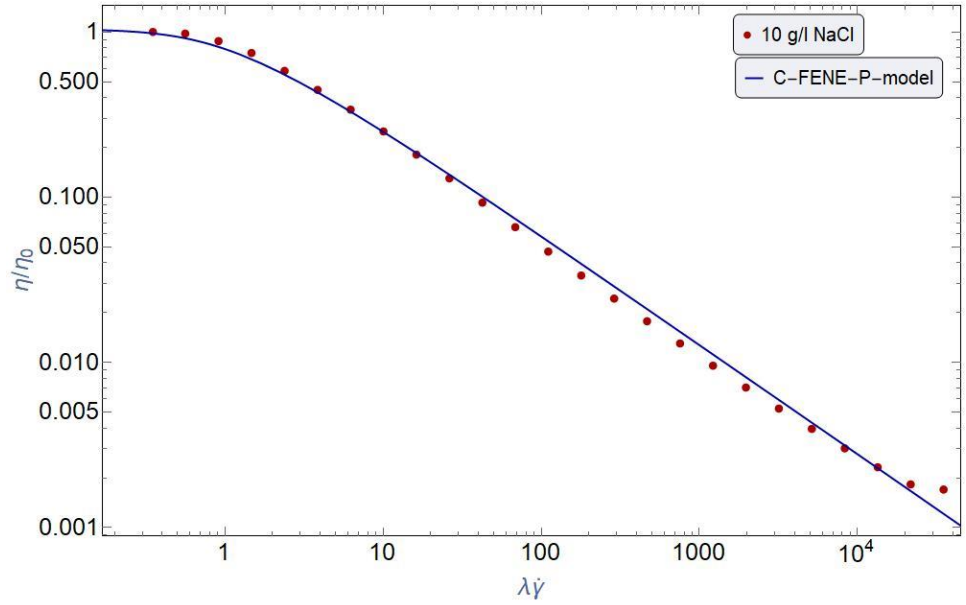

Figure 90 LogLog plot of normalized viscosity (red dots) and C-FENE-P-model viscosity prediction (blue line) versus dimensionless shear rate for FLOPAAM 3630-S 10 g/l NaCl polymer solution.

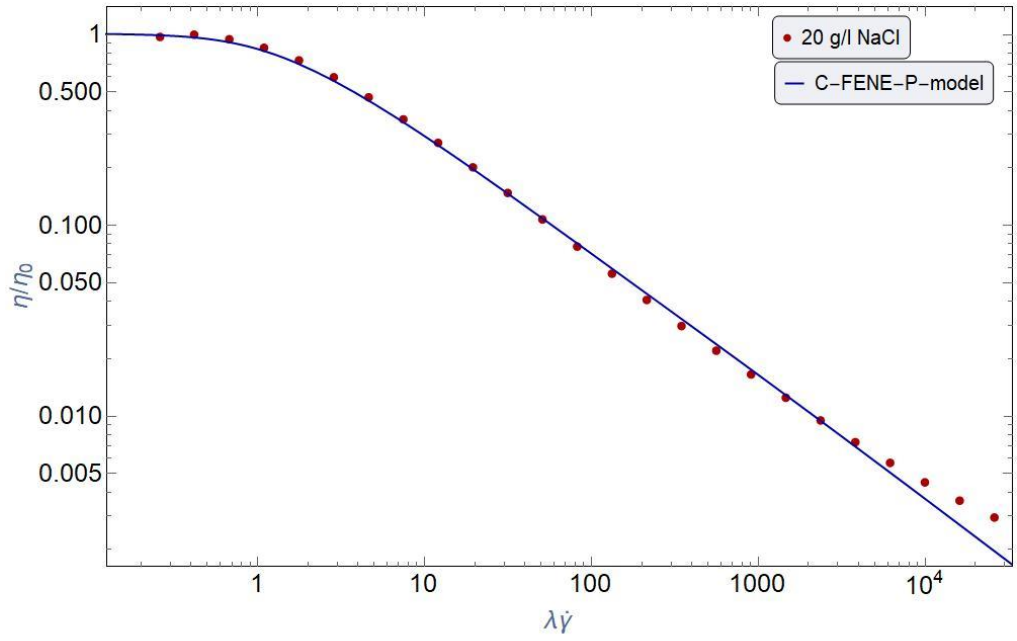

Figure 91 LogLog plot of normalized viscosity (red dots) and C-FENE-P-model viscosity prediction (blue line) versus dimensionless shear rate for FLOPAAM 3630-S 20 g/l NaCl polymer solution.

Appendix. B

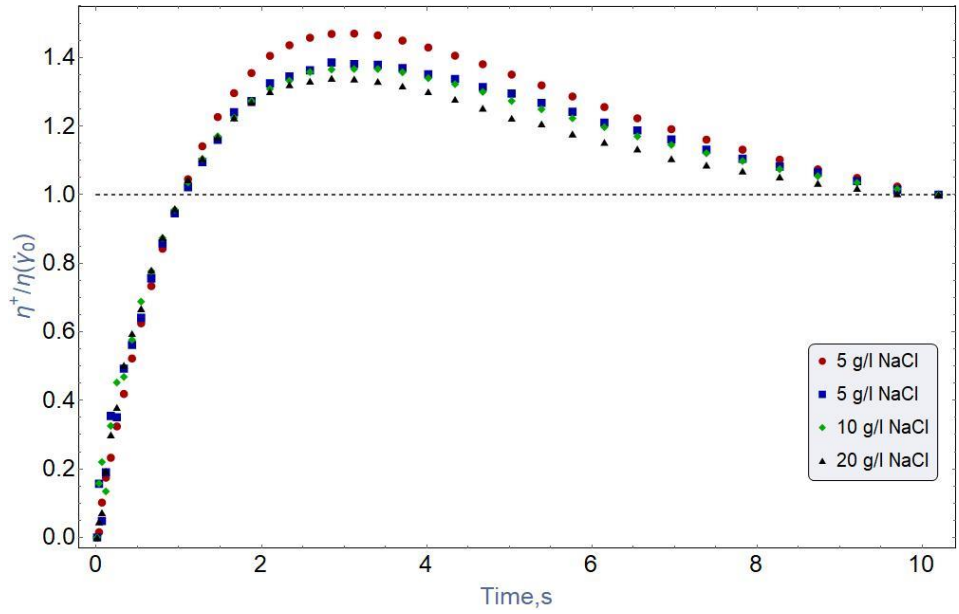

Figure 92 Normalized shear stress growth versus time for FLOPAAM 3630-S with various NaCl concentrations at step shear rate 1 s^{-1}.

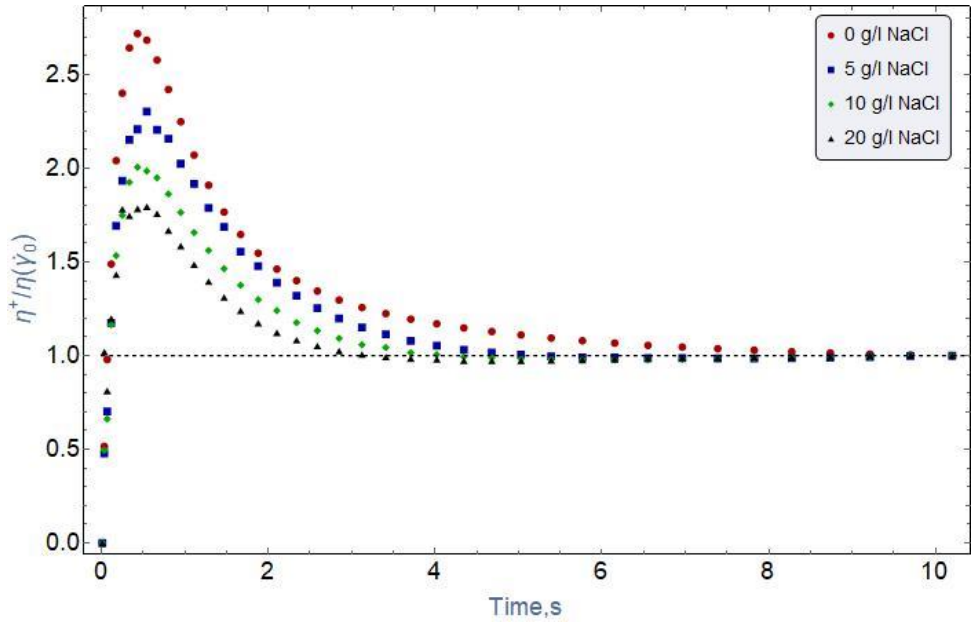

Figure 93 Normalized shear stress growth versus time for FLOPAAM 3630-S with various NaCl concentrations at step shear rate 10 s^{-1}.

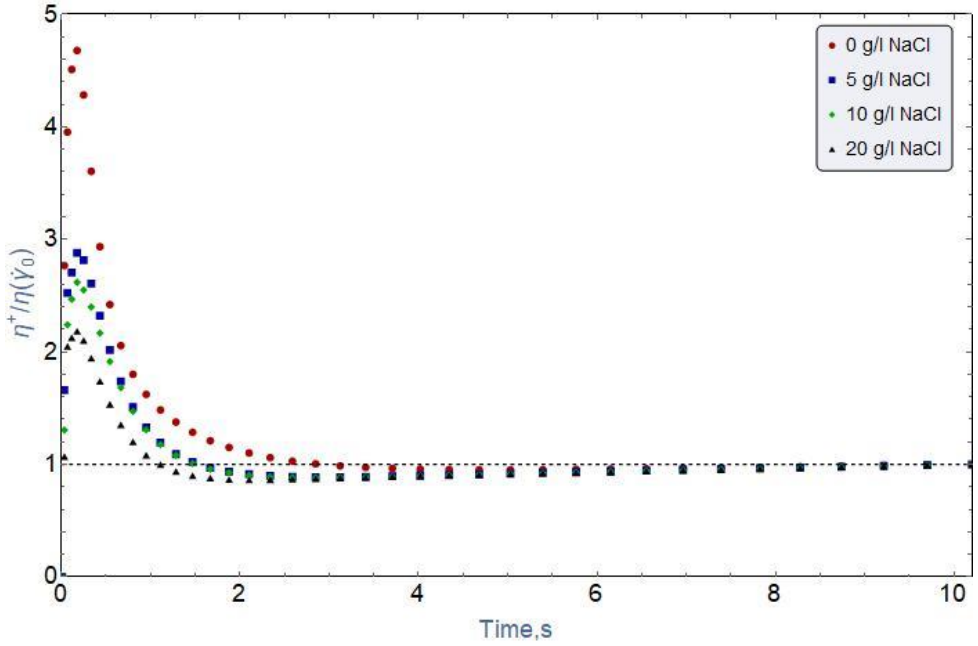

Figure 94 Normalized shear stress growth versus time for FLOPAAM 3630-S with various NaCl concentrations at step shear rate 100 s^{-1}.

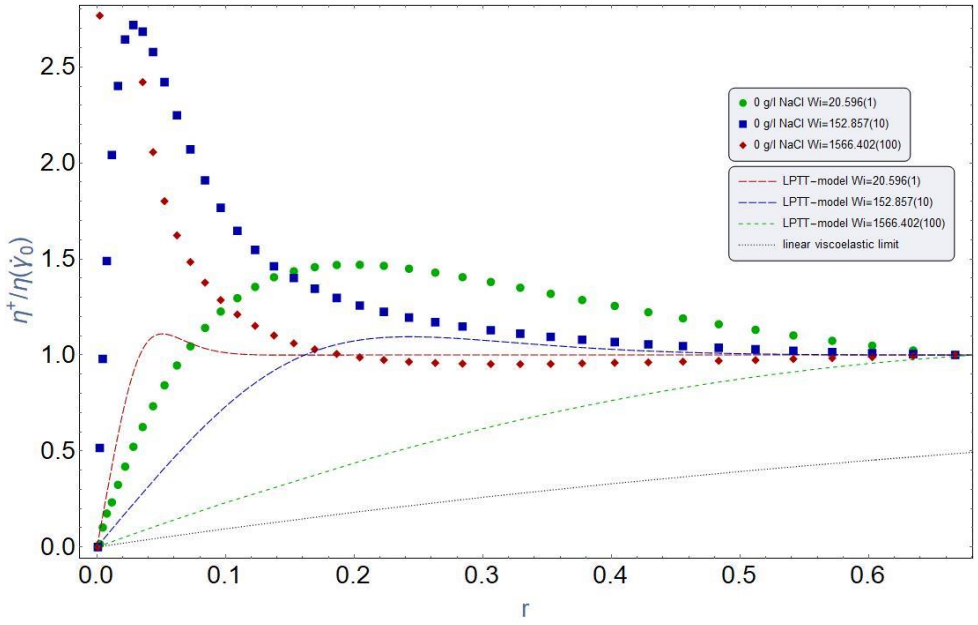

Figure 95 Normalized shear stress growth and LPTT-model prediction versus dimensionless time, r, for FLOPAAM 3630-S 0 g/l NaCl. Dots representing measured data and dashed lines representing model predictions for step rates (s^{-1}) 1 $(green)$, 10 $(blue)$ and 100 s^{-1}(red).

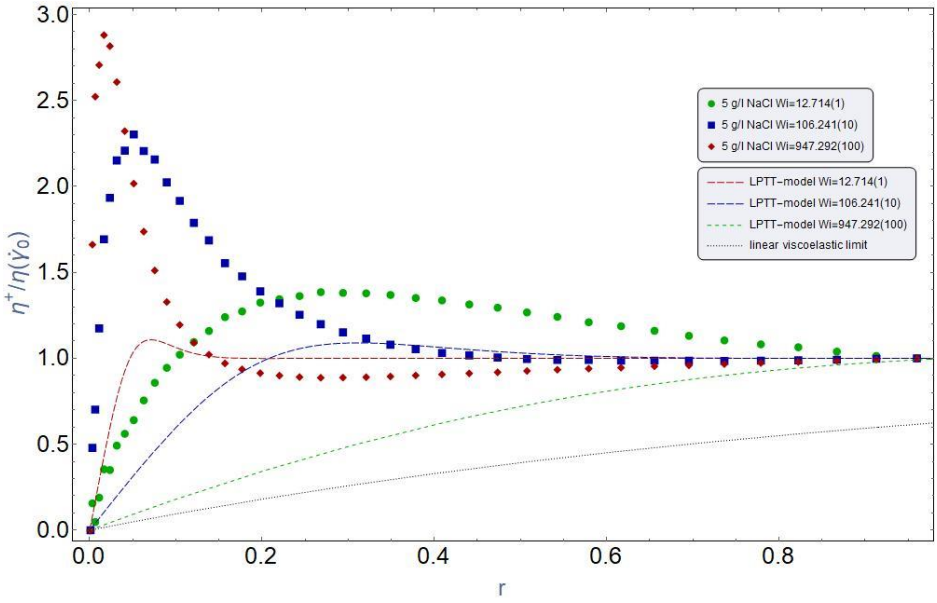

Figure 96 Normalized shear stress growth and LPTT-model prediction versus dimensionless time, r, for FLOPAAM 3630-S 5 g/l NaCl. Dots representing measured data and dashed lines representing model predictions for step rates (s^{-1}) 1 ($green$), 10 ($blue$) and 100 s^{-1}(red).

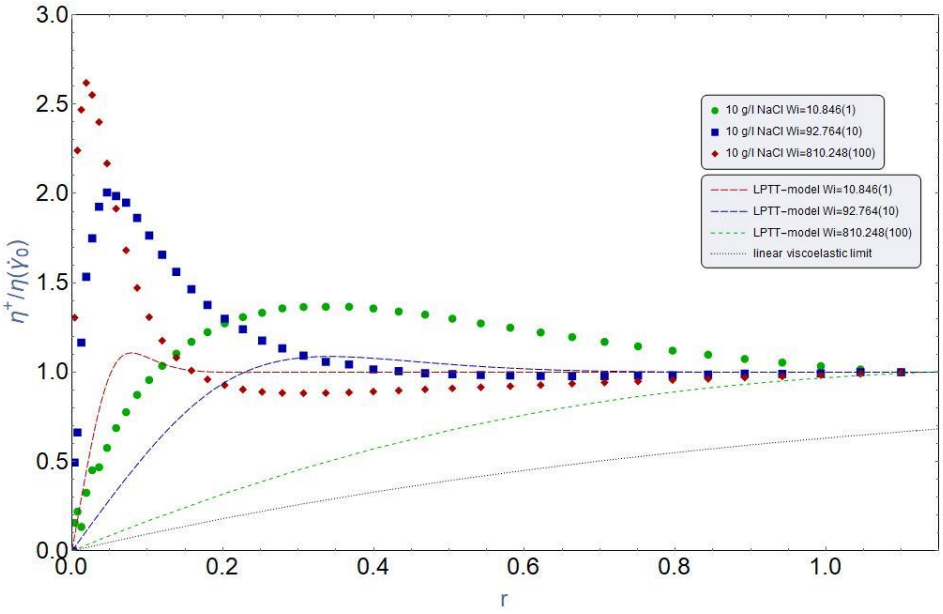

Figure 97 Normalized shear stress growth and LPTT-model prediction versus dimensionless time, r, for FLOPAAM 3630-S 10 g/l NaCl. Dots representing measured data and dashed lines representing model predictions for step rates (s^{-1}) 1 ($green$), 10 ($blue$) and 100 s^{-1}(red).

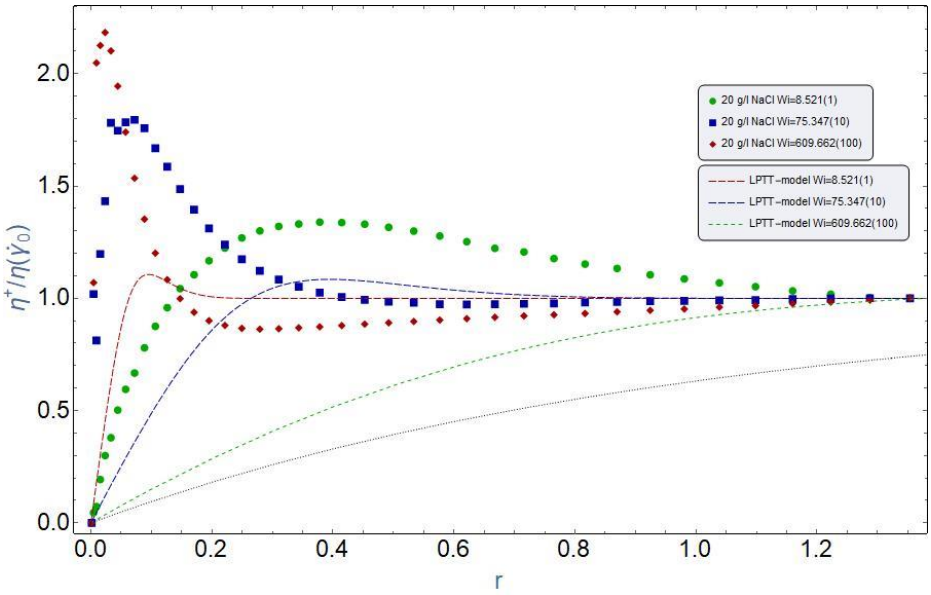

Figure 98 Normalized shear stress growth and LPTT-model prediction versus dimensionless time, r, for FLOPAAM 3630-S 20 g/l NaCl. Dots representing measured data and dashed lines representing model predictions for step rates (s^{-1}) 1 $(green)$, 10 $(blue)$ and 100 s^{-1}(red).

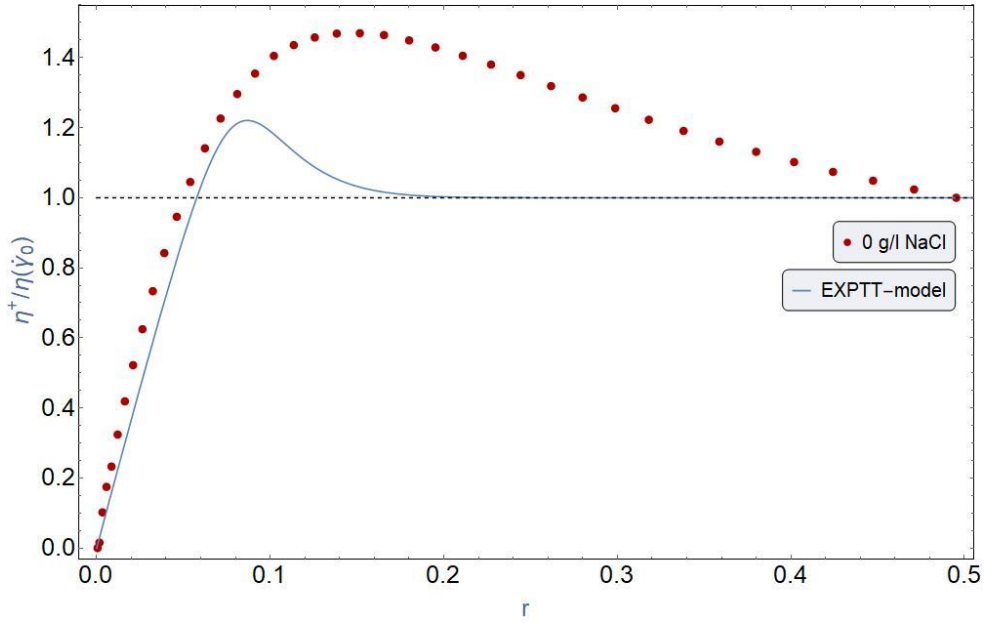

Figure 99 Normalized shear stress growth and EPTT-model prediction versus dimensionless time, r, for FLOPAAM 3630-S 0 g/l NaCl. Dots (red) representing measured data and dashed line (blue) representing model predictions for step shear rates 1 s^{-1}.

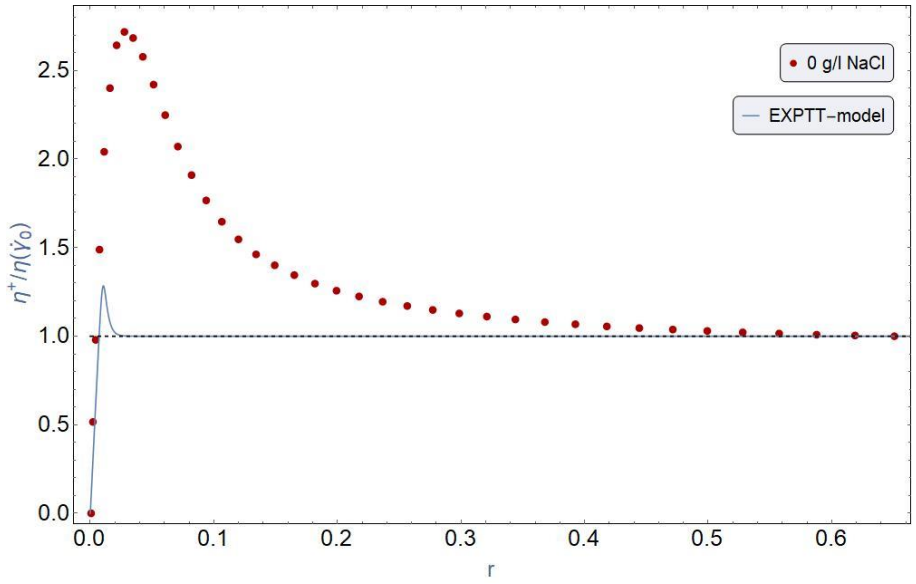

Figure 100 Normalized shear stress growth and EPTT-model prediction versus dimensionless time, r, for FLOPAAM 3630-S 0 g/l NaCl. Dots (red) representing measured data and dashed line (blue) representing model predictions for step shear rates 10 s^{-1}.

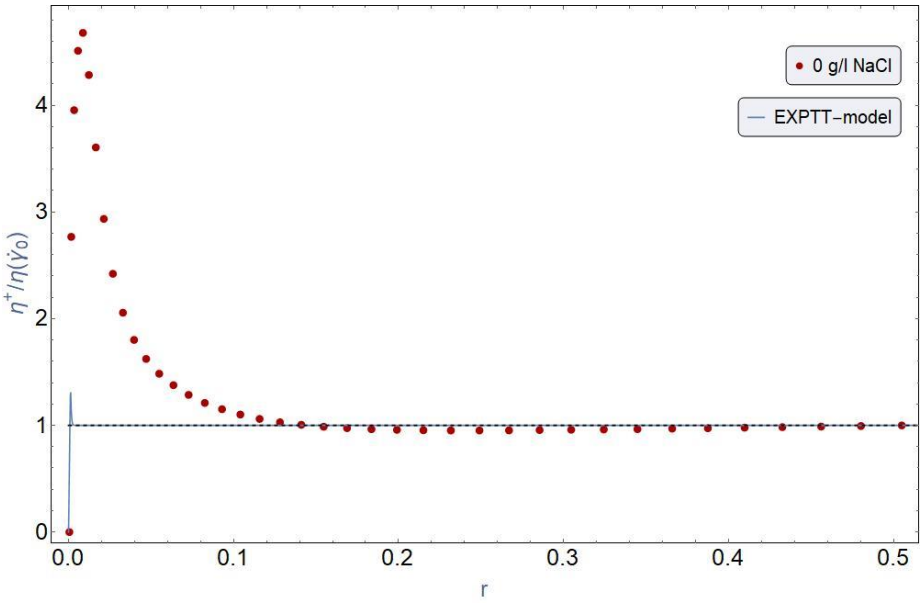

Figure 101 Normalized shear stress growth and EPTT-model prediction versus dimensionless time, r, for FLOPAAM 3630-S 0 g/l NaCl. Dots (red) representing measured data and dashed line (blue) representing model predictions for step shear rates 100 s^{-1}.

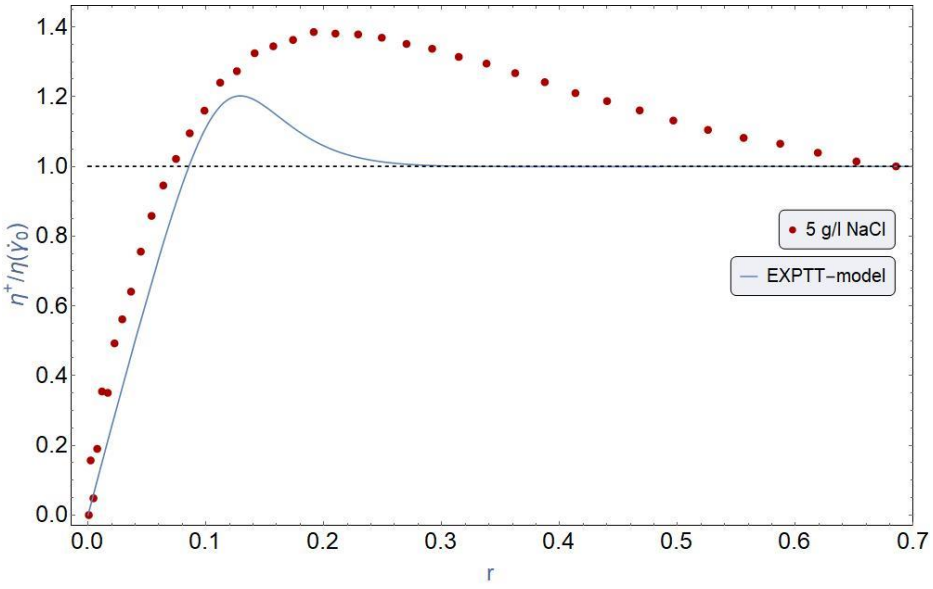

Figure 102 Normalized shear stress growth and EPTT-model prediction versus dimensionless time, r, for FLOPAAM 3630-S 5 g/l NaCl. Dots (red) representing measured data and dashed line (blue) representing model predictions for step shear rates 1 s^{-1}.

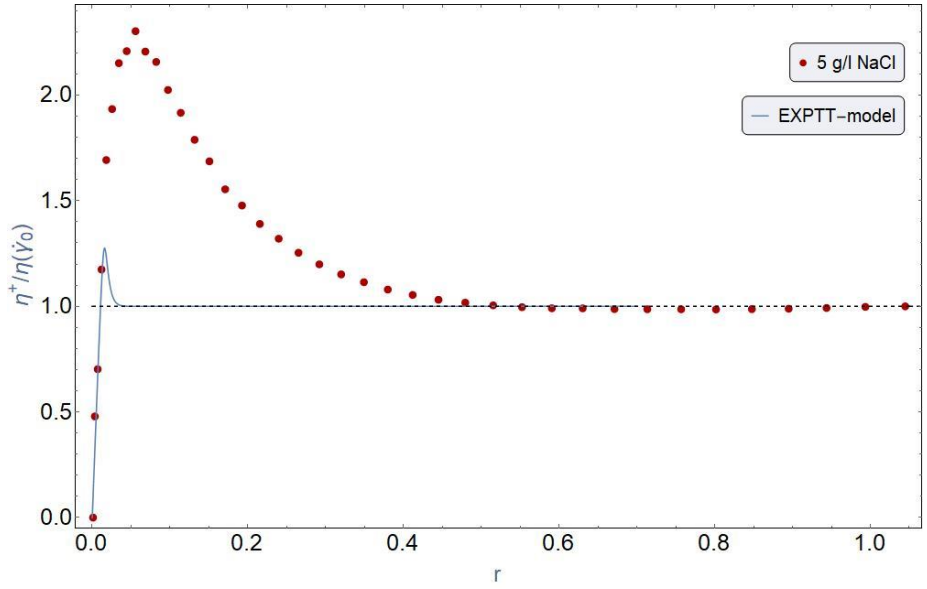

Figure 103 Normalized shear stress growth and EPTT-model prediction versus dimensionless time, r, for FLOPAAM 3630-S 5 g/l NaCl. Dots (red) representing measured data and dashed line (blue) representing model predictions for step shear rates 10 s^{-1}.

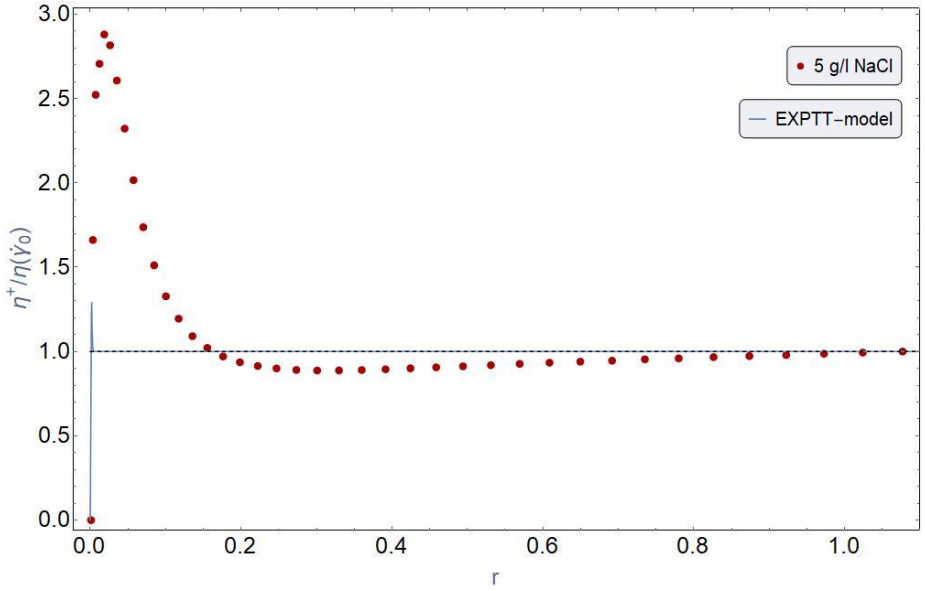

Figure 104 Normalized shear stress growth and EPTT-model prediction versus dimensionless time, r, for FLOPAAM 3630-S 5 g/l NaCl. Dots (red) representing measured data and dashed line (blue) representing model predictions for step shear rates 100 s^{-1}.

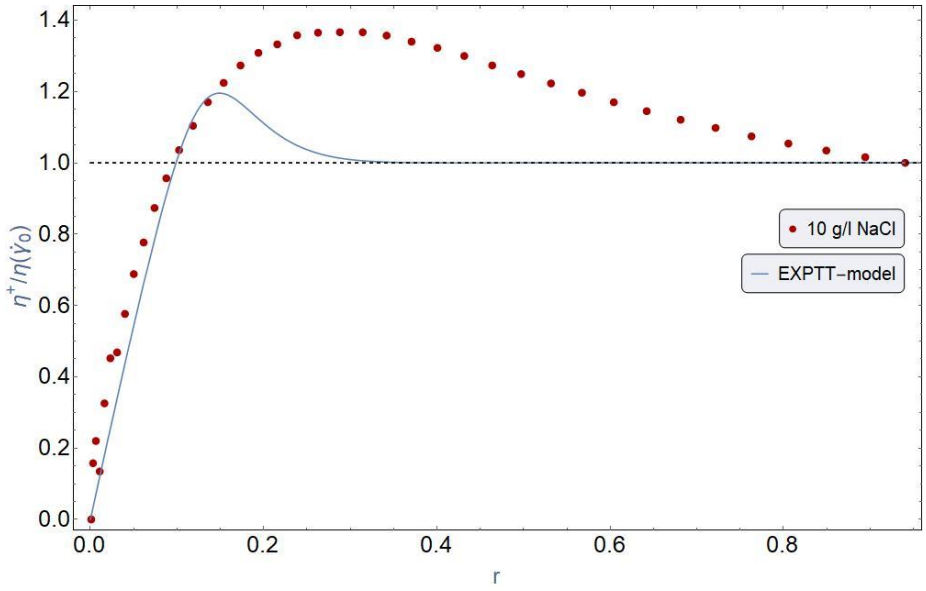

Figure 105 Normalized shear stress growth and EPTT-model prediction versus dimensionless time, r, for FLOPAAM 3630-S 10 g/l NaCl. Dots (red) representing measured data and dashed line (blue) representing model predictions for step shear rates 1 s^{-1}.

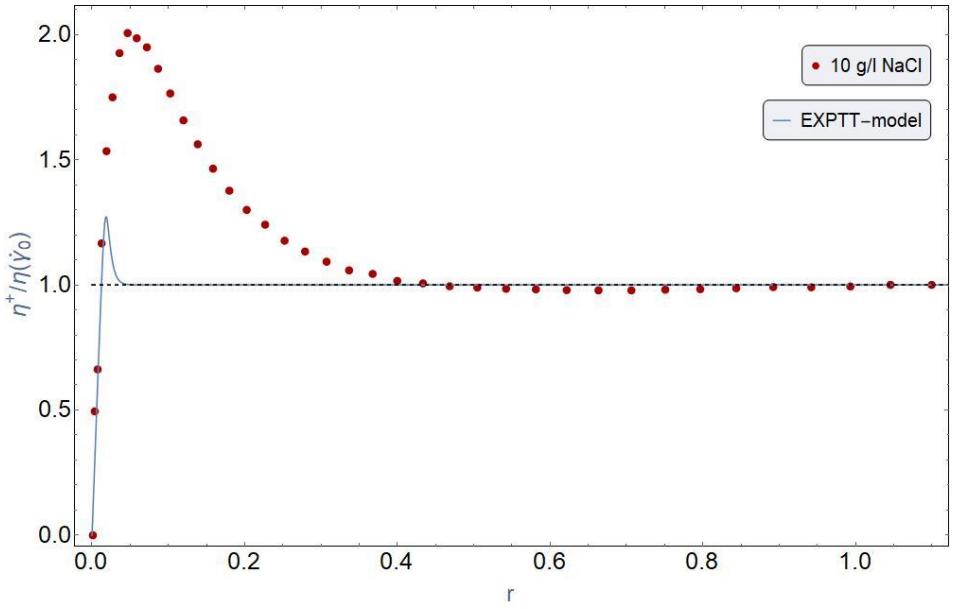

Figure 106 Normalized shear stress growth and EPTT-model prediction versus dimensionless time, r, for FLOPAAM 3630-S 10 g/l NaCl. Dots (red) representing measured data and dashed line (blue) representing model predictions for step shear rates 10 s^{-1}.

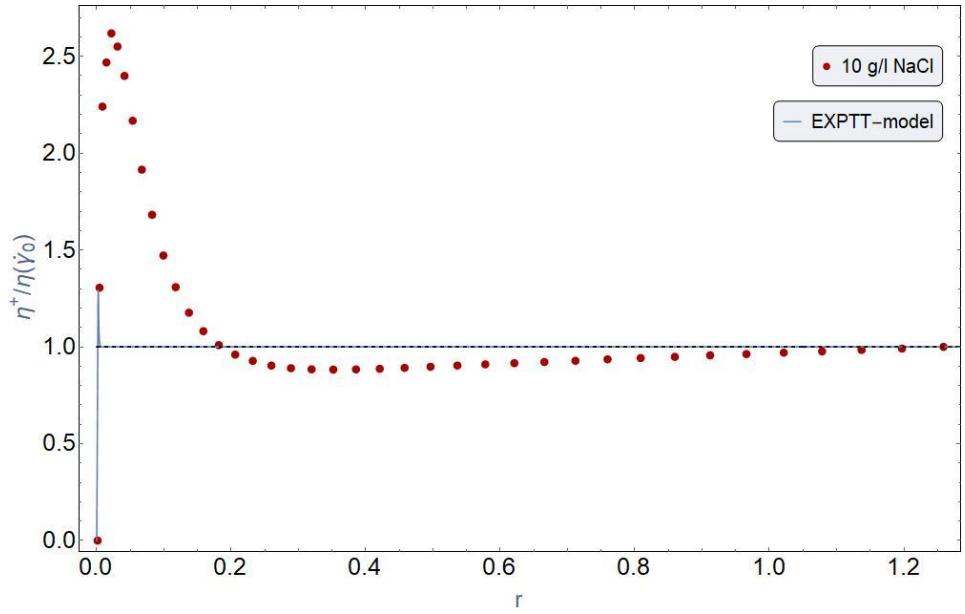

Figure 107 Normalized shear stress growth and EPTT-model prediction versus dimensionless time, r, for FLOPAAM 3630-S 10 g/l NaCl. Dots (red) representing measured data and dashed line (blue) representing model predictions for step shear rates 100 s^{-1}.

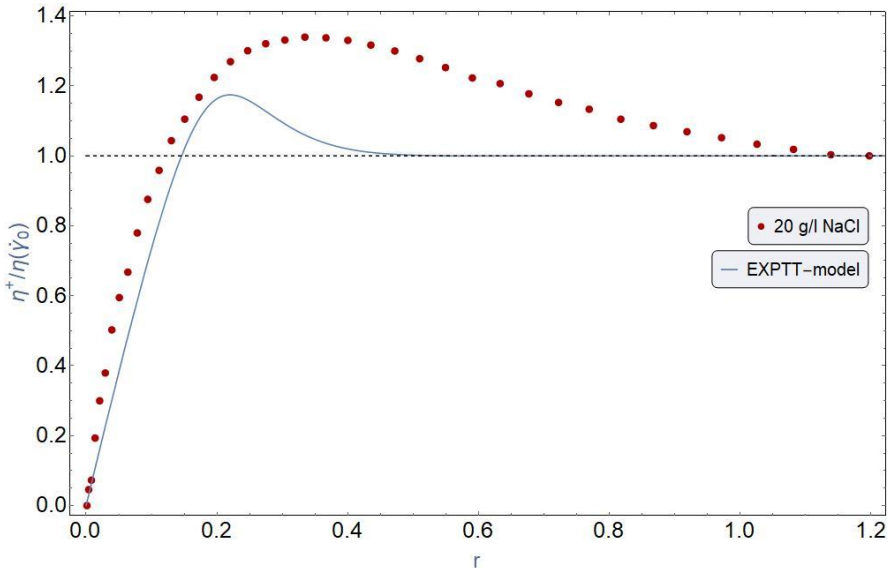

Figure 108 Normalized shear stress growth and EPTT-model prediction versus dimensionless time, r, for FLOPAAM 3630-S 20 g/l NaCl. Dots (red) representing measured data and dashed line (blue) representing model predictions for step shear rates 1 s^{-1}.

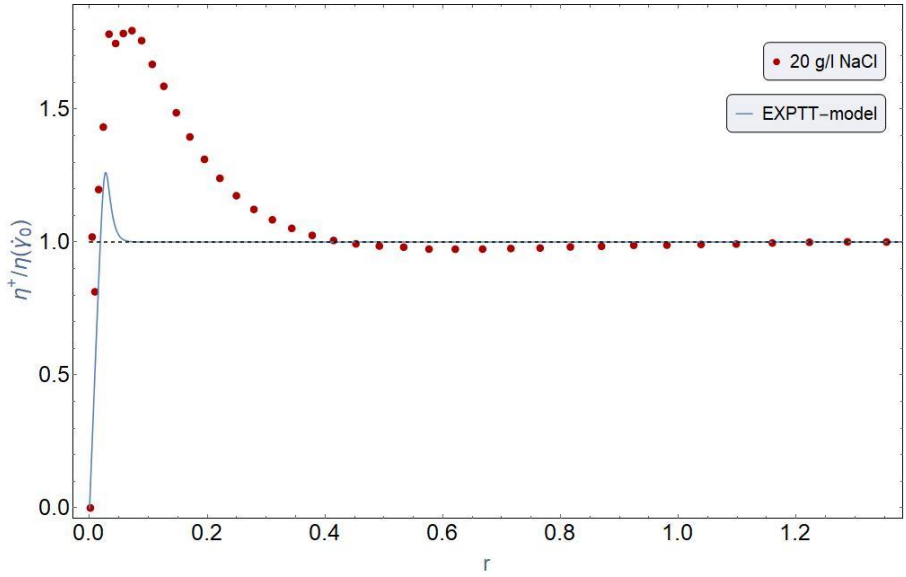

Figure 109 Normalized shear stress growth and EPTT-model prediction versus dimensionless time, r, for FLOPAAM 3630-S 20 g/l NaCl. Dots (red) representing measured data and dashed line (blue) representing model predictions for step shear rates 10 s^{-1}.

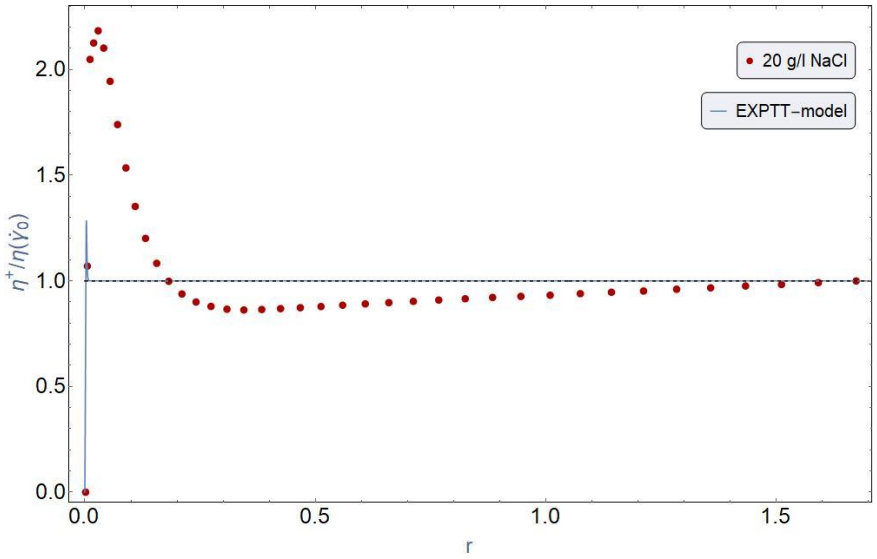

Figure 110 Normalized shear stress growth and EPTT-model prediction versus dimensionless time, r, for FLOPAAM 3630-S 20 g/l NaCl. Dots (red) representing measured data and dashed line (blue) representing model predictions for step shear rates 100 s^{-1}.

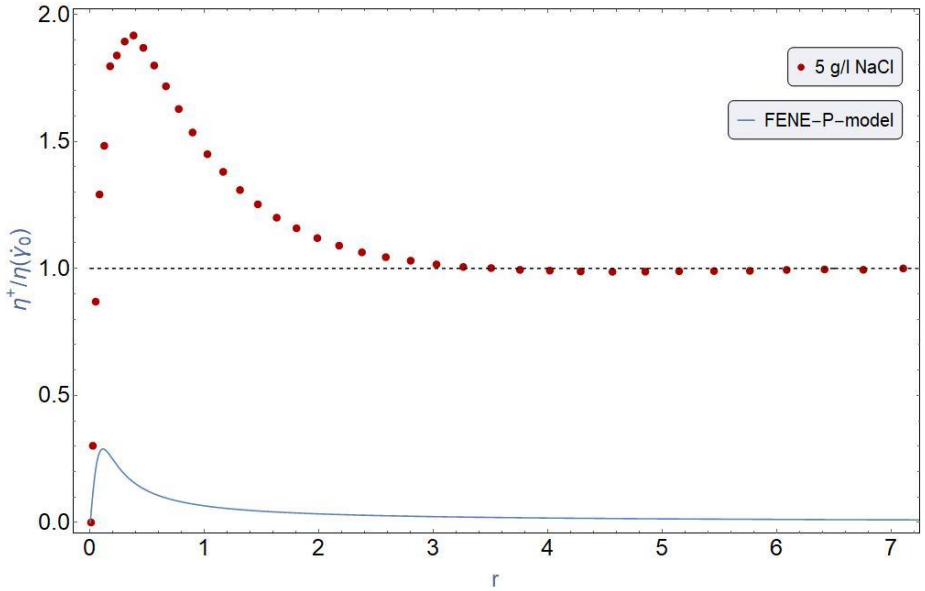

Figure 111 Normalized shear stress growth (red dots) and FENE-P-model prediction (blue line) versus dimensionless time, r, for FLOPAAM 5115 VHM 5 g/l NaCl. Dotted points representing measured data and dashed lines representing model predictions for step rate 10 s^{-1}.

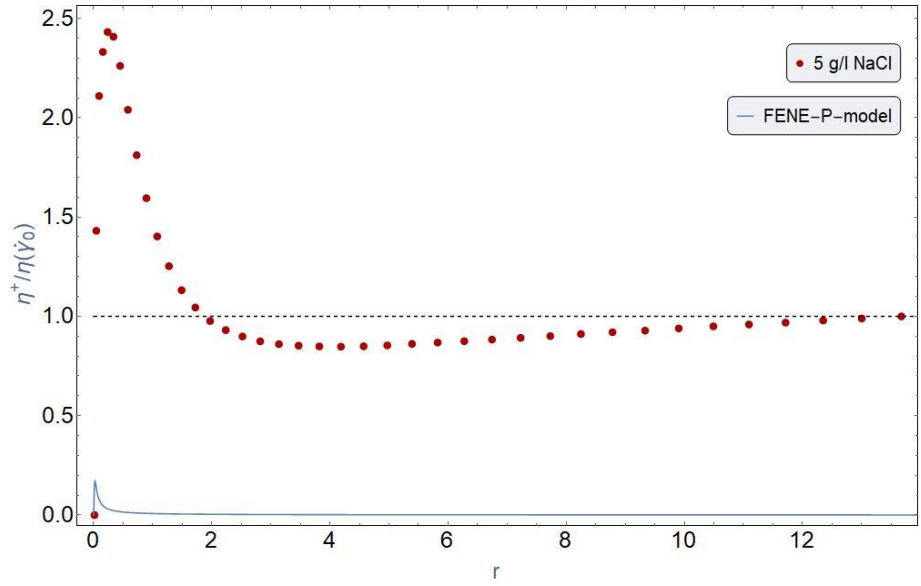

Figure 112 Normalized shear stress growth (red dots) and FENE-P-model prediction (blue line) versus dimensionless time, r, for FLOPAAM 5115 VHM 5 5 g/l NaCl. Dotted points representing measured data and dashed lines representing model predictions for step rate 100 s^{-1}.

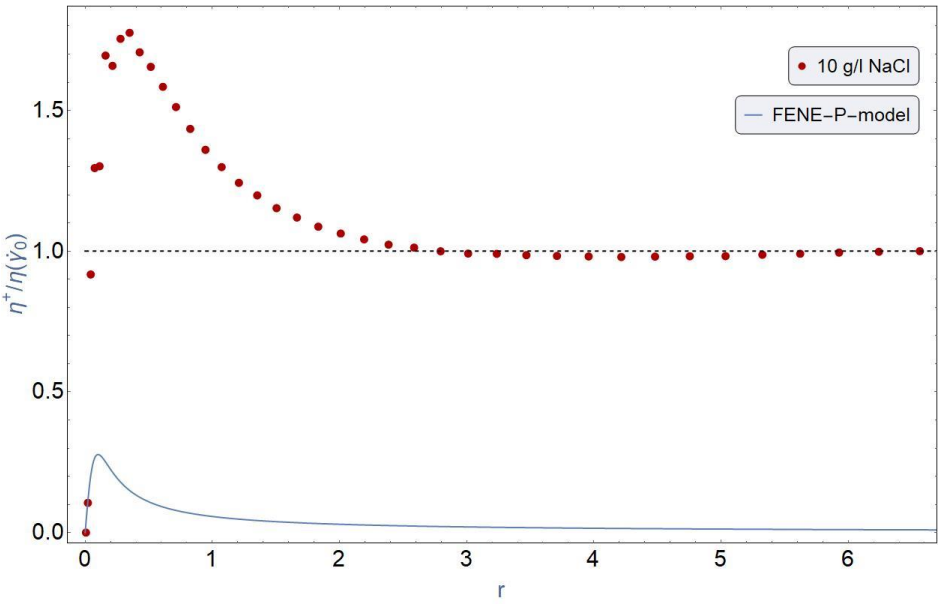

Figure 113 Normalized shear stress growth (red dots) and FENE-P-model prediction (blue line) versus dimensionless time, r, for FLOPAAM 5115 VHM 10 g/l NaCl. Dotted points representing measured data and dashed lines representing model predictions for step rate 10 s^{-1}.

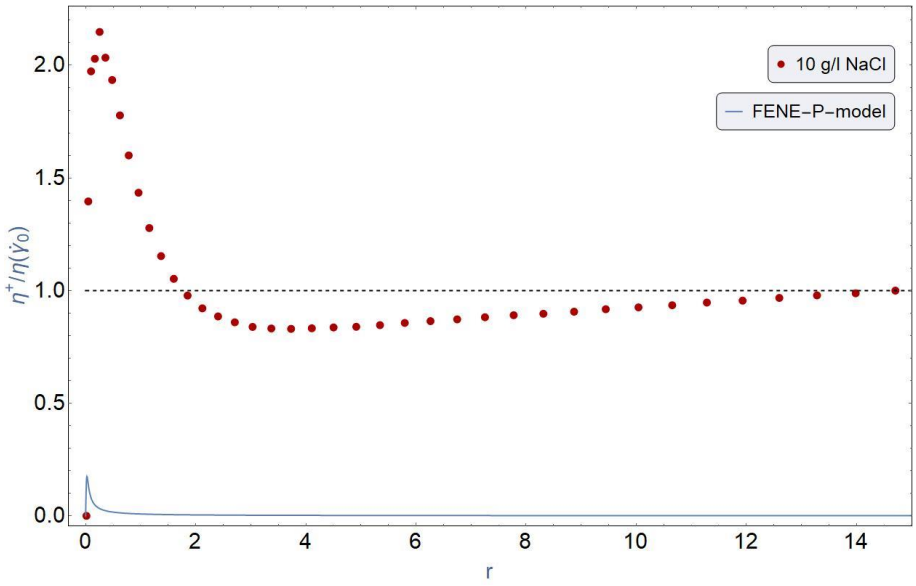

Figure 114 Normalized shear stress growth (red dots) and FENE-P-model prediction (blue line) versus dimensionless time, r, for FLOPAAM 5115 VHM 10 g/l NaCl. Dotted points representing measured data and dashed lines representing model predictions for step rate 100 s^{-1}.

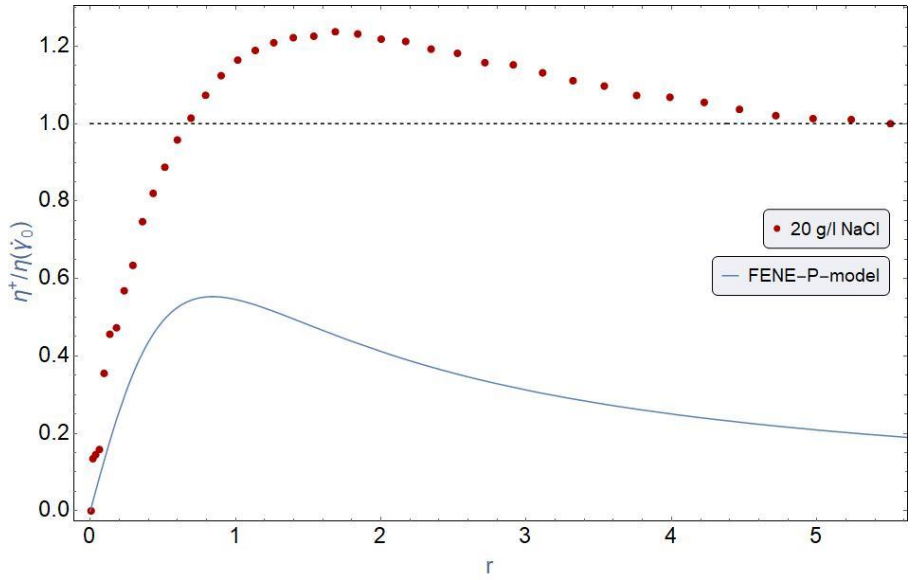

Figure 115 Normalized shear stress growth (red dots) and FENE-P-model prediction (blue line) versus dimensionless time, r, for FLOPAAM 5115 VHM 20 g/l NaCl. Dotted points representing measured data and dashed lines representing model predictions for step rate 1 s^{-1}.

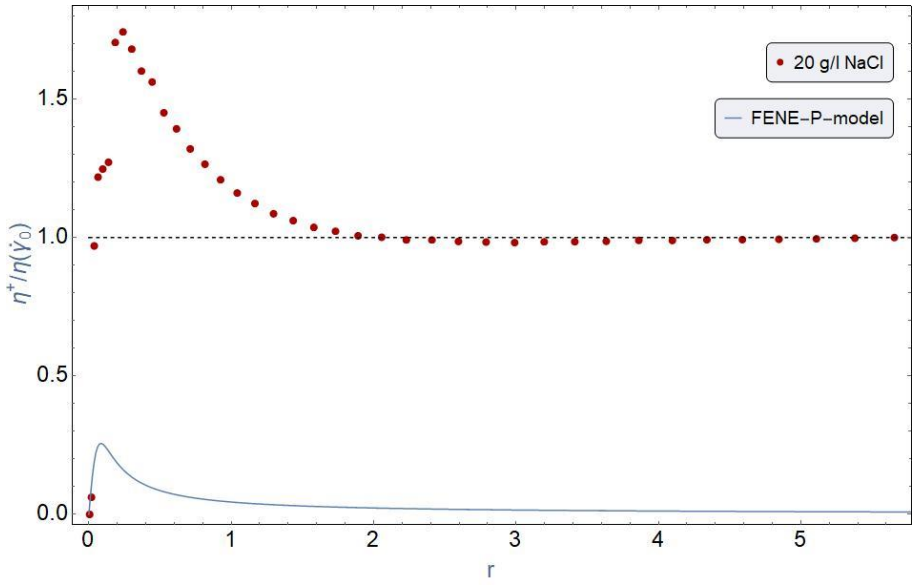

Figure 116 Normalized shear stress growth (red dots) and FENE-P-model prediction (blue line) versus dimensionless time, r, for FLOPAAM 5115 VHM 20 g/l NaCl. Dotted points representing measured data and dashed lines representing model predictions for step rate 10 s^{-1}.

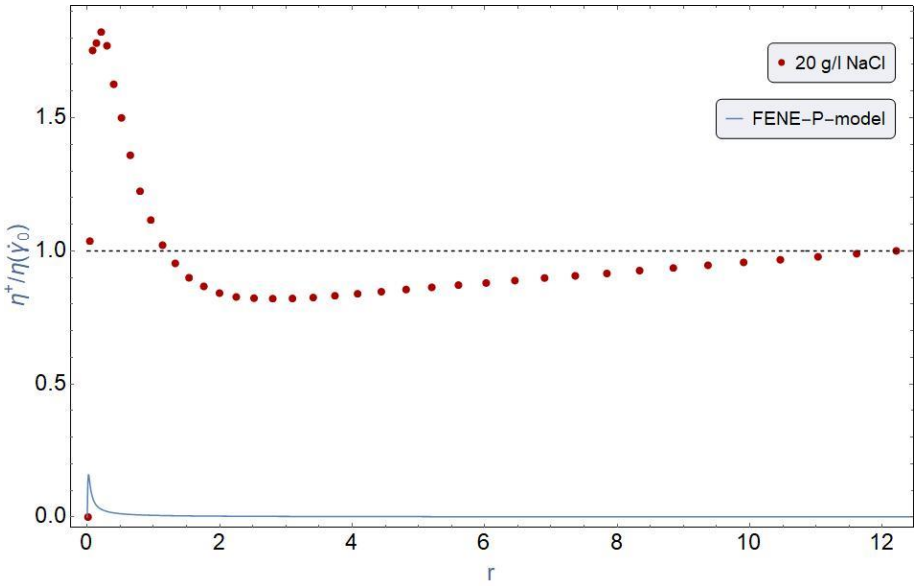

Figure 117 Normalized shear stress growth (red dots) and FENE-P-model prediction (blue line) versus dimensionless time, r, for FLOPAAM 5115 VHM 20 g/l NaCl. Dotted points representing measured data and dashed lines representing model predictions for step rate 100 s^{-1}.

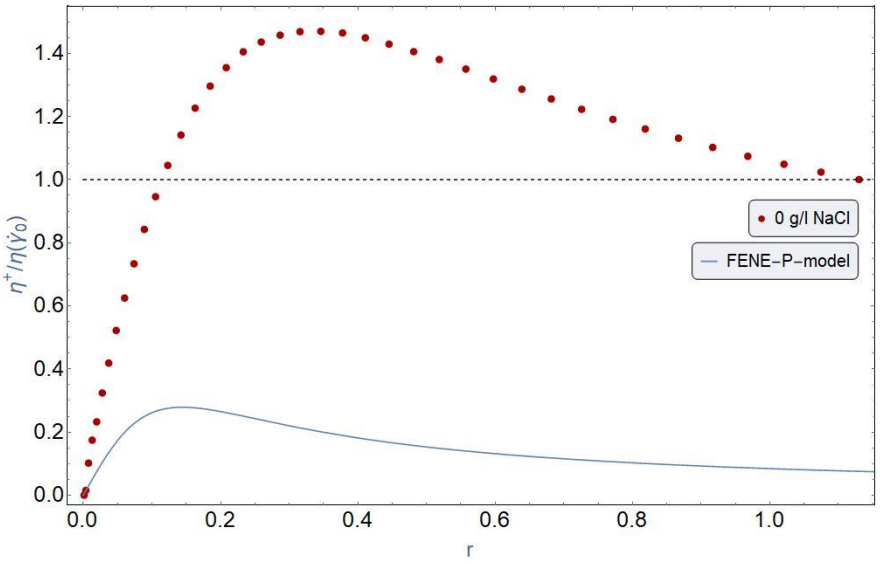

Figure 118 Normalized shear stress growth (red dots) and FENE-P-model prediction (blue line) versus dimensionless time, r, for FLOPAAM 3630-S 0 g/l NaCl. Dotted points representing measured data and dashed lines representing model predictions for step rate 1 s^{-1}.

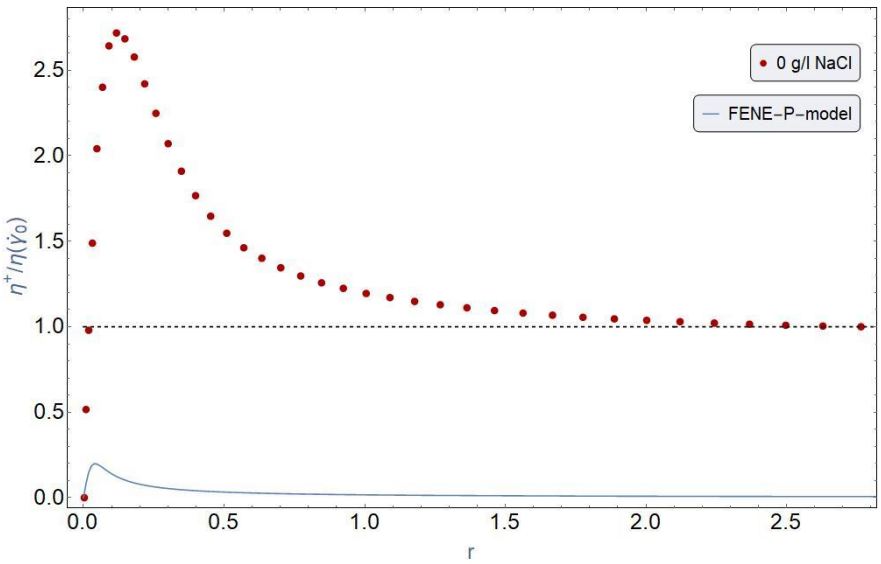

Figure 119 Normalized shear stress growth (red dots) and FENE-P-model prediction (blue line) versus dimensionless time, r, for FLOPAAM 3630-S 0 g/l NaCl. Dotted points representing measured data and dashed lines representing model predictions for step rate 10 s^{-1}.

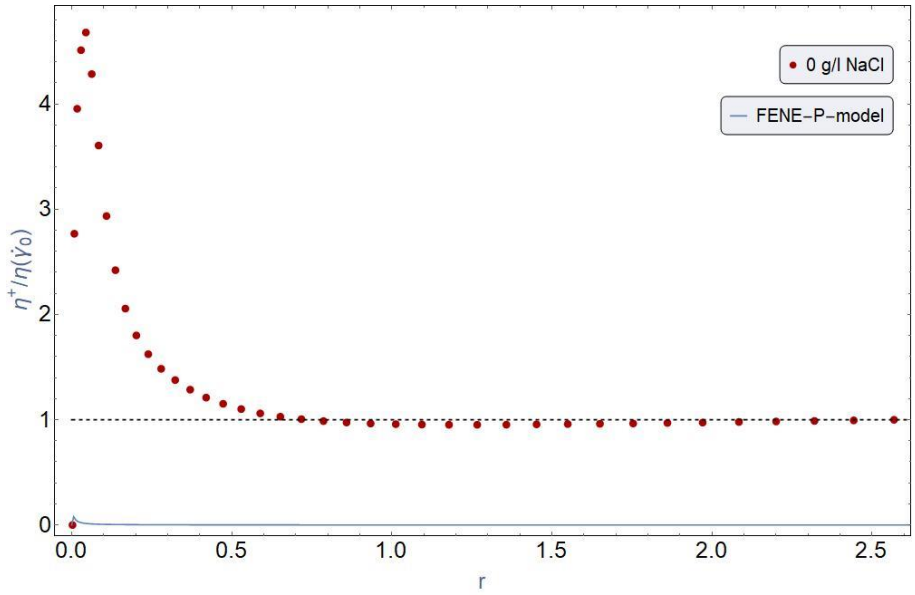

Figure 120 Normalized shear stress growth (red dots) and FENE-P-model prediction (blue line) versus dimensionless time, r, for FLOPAAM 3630-S 0 g/l NaCl. Dotted points representing measured data and dashed lines representing model predictions for step rate 100 s^{-1}.

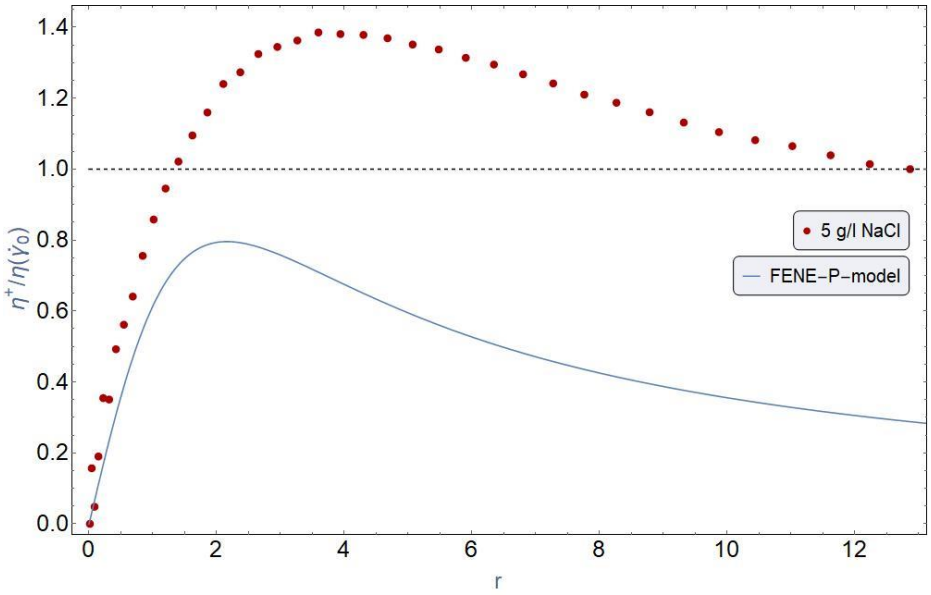

Figure 121 Normalized shear stress growth (red dots) and FENE-P-model prediction (blue line) versus dimensionless time, r, for FLOPAAM 3630-S 5 g/l NaCl. Dotted points representing measured data and dashed lines representing model predictions for step rate 1 s^{-1}.

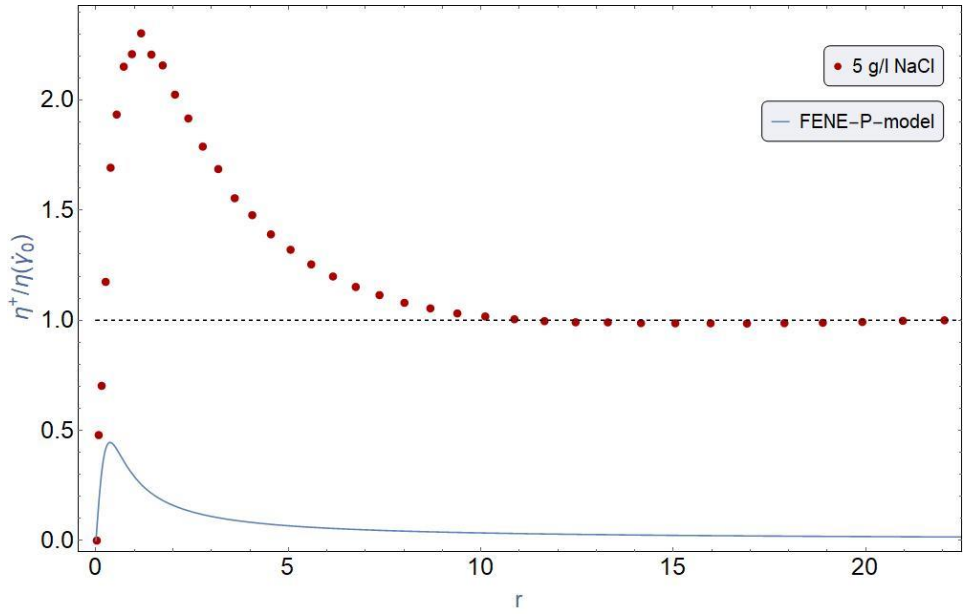

Figure 122 Normalized shear stress growth (red dots) and FENE-P-model prediction (blue line) versus dimensionless time, r, for FLOPAAM 3630-S 5 g/l NaCl. Dotted points representing measured data and dashed lines representing model predictions for step rate 10 s^{-1}.

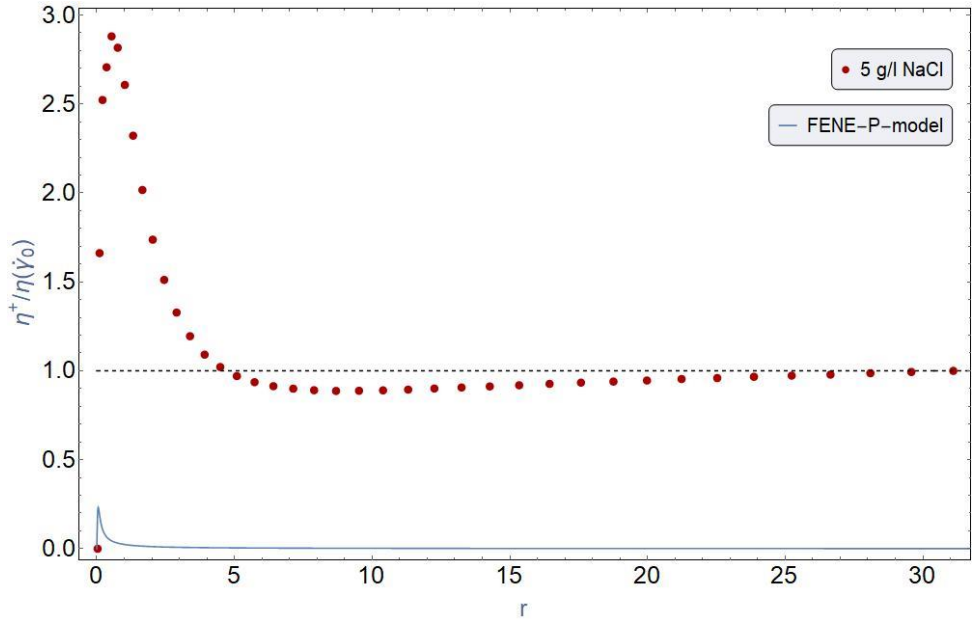

Figure 123 Normalized shear stress growth (red dots) and FENE-P-model prediction (blue line) versus dimensionless time, r, for FLOPAAM 3630-S 5 g/l NaCl. Dotted points representing measured data and dashed lines representing model predictions for step rate 100 s^{-1}.

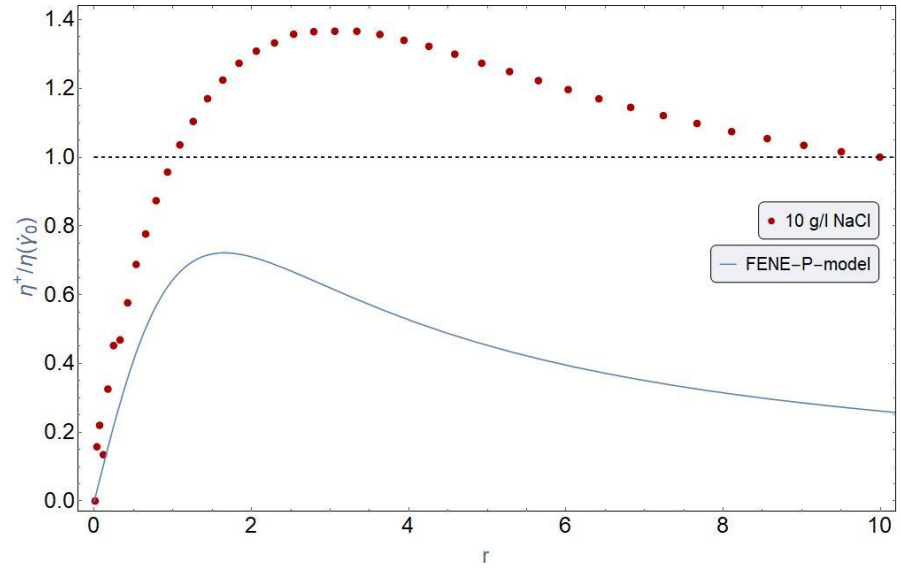

Figure 124 Normalized shear stress growth (red dots) and FENE-P-model prediction (blue line) versus dimensionless time, r, for FLOPAAM 3630-S 10 g/l NaCl. Dotted points representing measured data and dashed lines representing model predictions for step rate 1 s^{-1}.

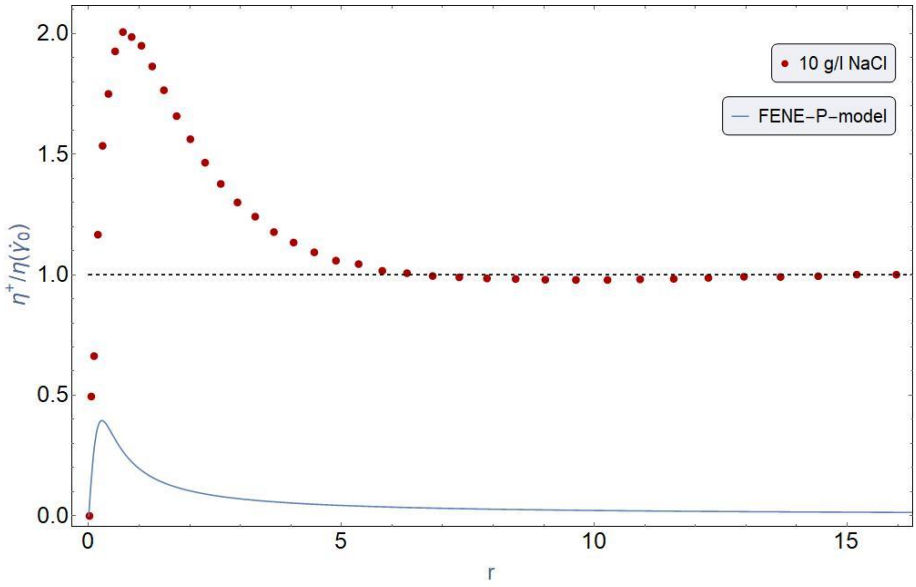

Figure 125 Normalized shear stress growth (red dots) and FENE-P-model prediction (blue line) versus dimensionless time, r, for FLOPAAM 3630-S 10 g/l NaCl. Dotted points representing measured data and dashed lines representing model predictions for step rate 10 s^{-1}.

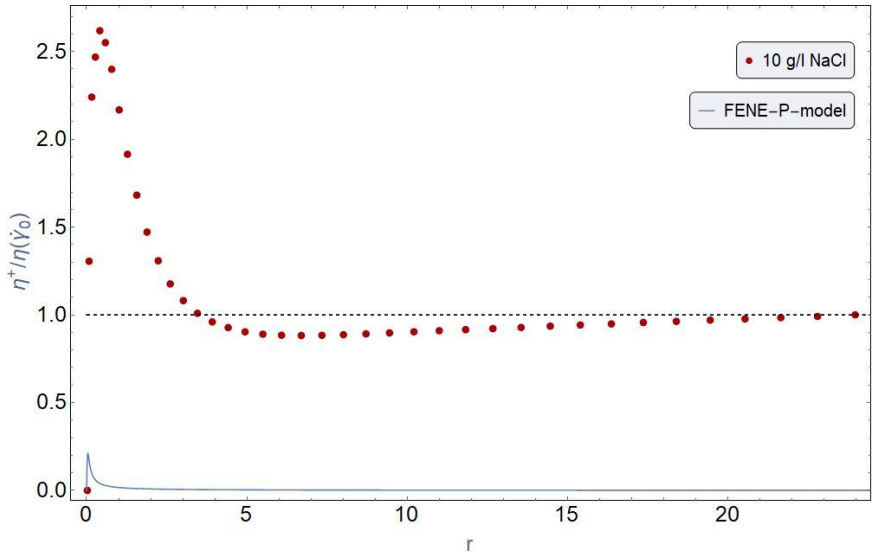

Figure 126 Normalized shear stress growth (red dots) and FENE-P-model prediction (blue line) versus dimensionless time, r, for FLOPAAM 3630-S 10 g/l NaCl. Dotted points representing measured data and dashed lines representing model predictions for step rate 100 s^{-1}.

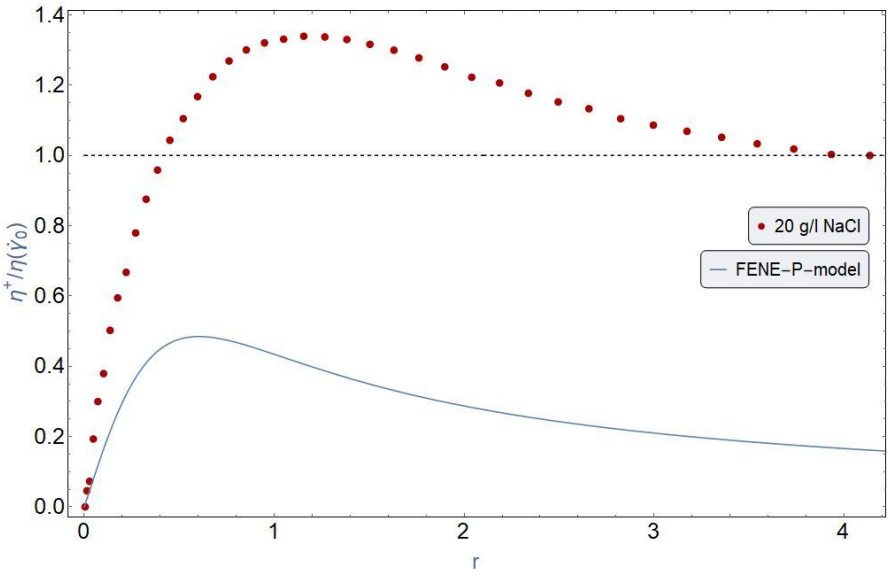

Figure 127 Normalized shear stress growth (red dots) and FENE-P-model prediction (blue line) versus dimensionless time, r, for FLOPAAM 3630-S 20 g/l NaCl. Dotted points representing measured data and dashed lines representing model predictions for step rate 1 s^{-1}.

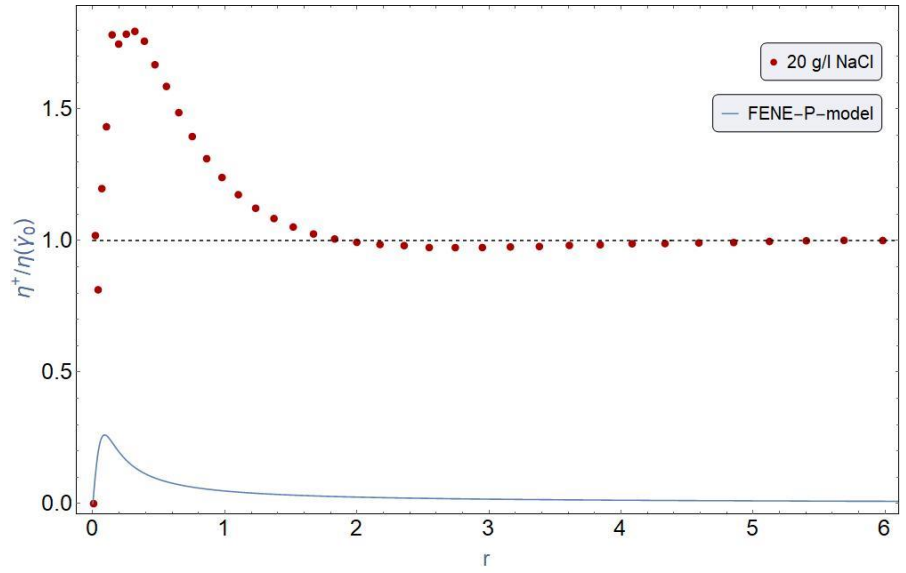

Figure 128 Normalized shear stress growth (red dots) and FENE-P-model prediction (blue line) versus dimensionless time, r, for FLOPAAM 3630-S 20 g/l NaCl. Dotted points representing measured data and dashed lines representing model predictions for step rate 10 s^{-1}.

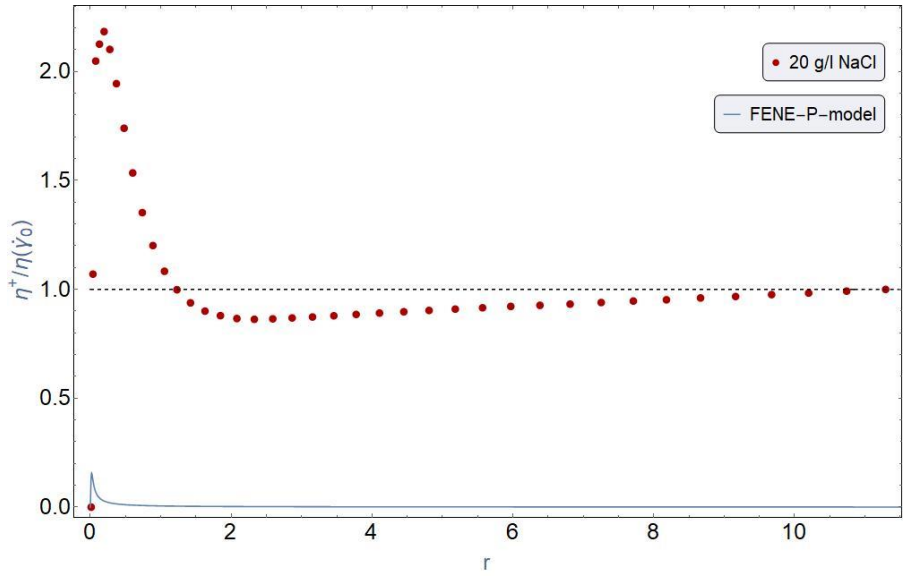

Figure 129 Normalized shear stress growth (red dots) and FENE-P-model prediction (blue line) versus dimensionless time, r, for FLOPAAM 3630-S 20 g/l NaCl. Dotted points representing measured data and dashed lines representing model predictions for step rate 100 s^{-1}.

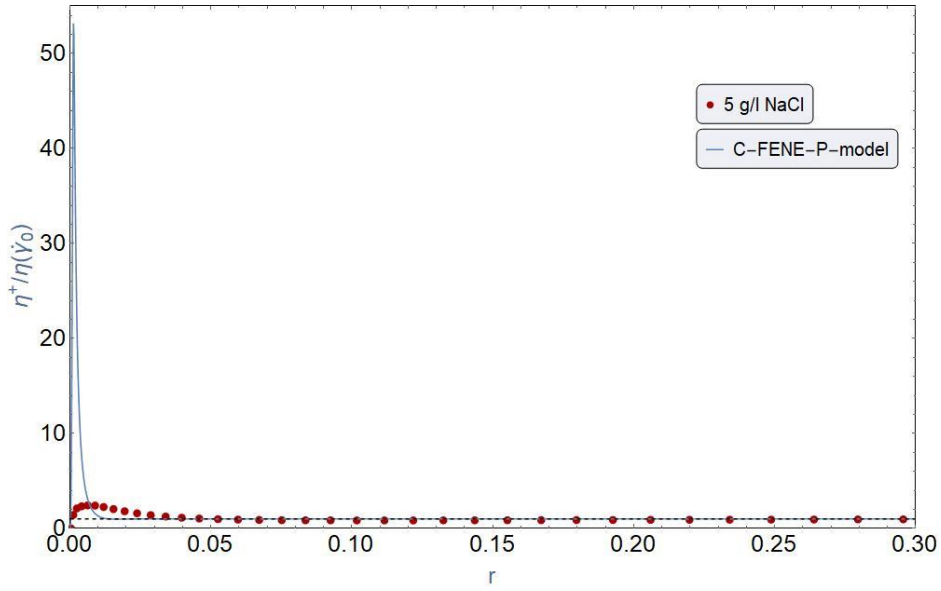

Figure 130 Normalized shear stress growth (red dots) and FENE-P-model prediction (blue line) versus dimensionless time, r, for FLOPAAM 5115 VHM 5 g/l NaCl. Dotted points representing measured data and dashed lines representing model predictions for step rate 100 s^{-1}.

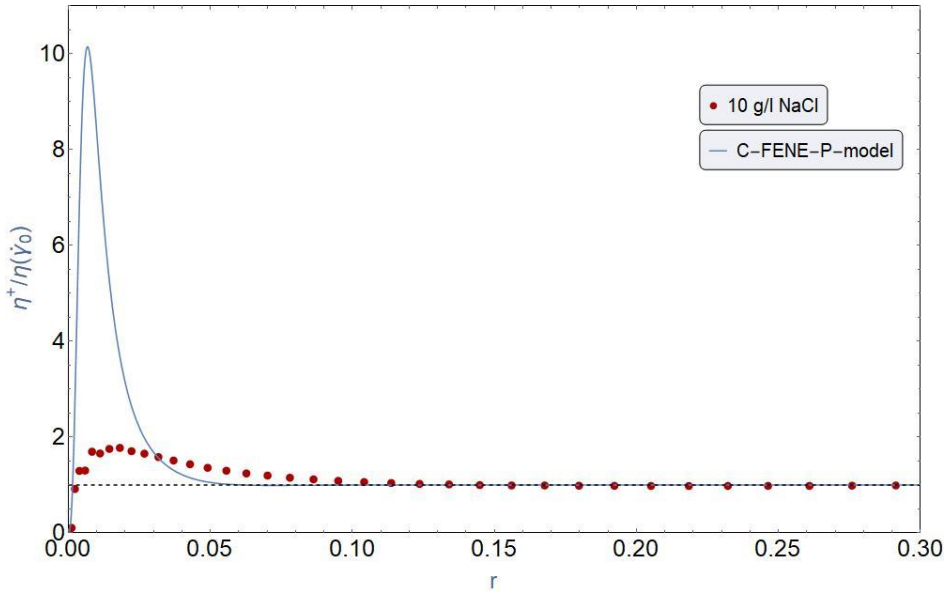

Figure 131 Normalized shear stress growth (red dots) and FENE-P-model prediction (blue line) versus dimensionless time, r, for FLOPAAM 5115 VHM 10 g/l NaCl. Dotted points representing measured data and dashed lines representing model predictions for step rate 10 s^{-1}.

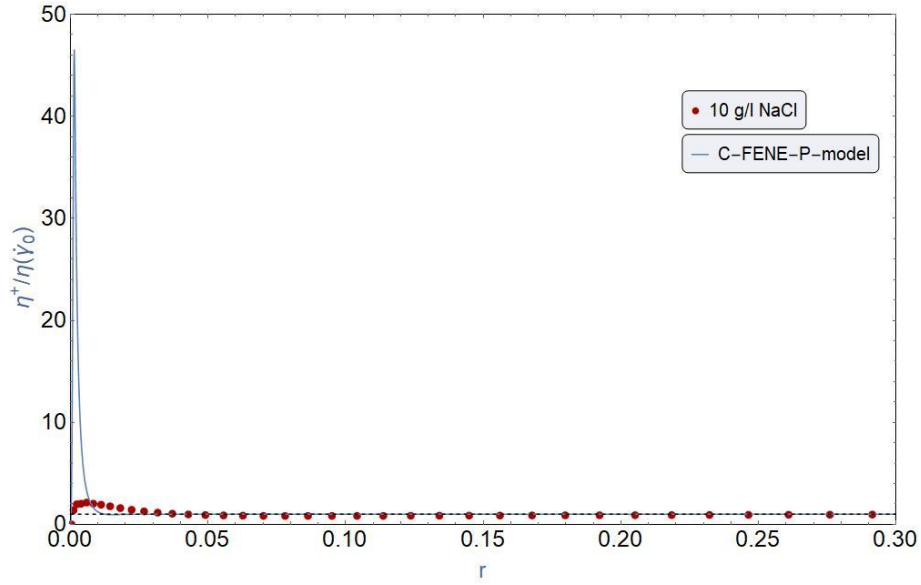

Figure 132 Normalized shear stress growth (red dots) and FENE-P-model prediction (blue line) versus dimensionless time, r, for FLOPAAM 5115 VHM 10 g/l NaCl. Dotted points representing measured data and dashed lines representing model predictions for step rate 100 s^{-1}.

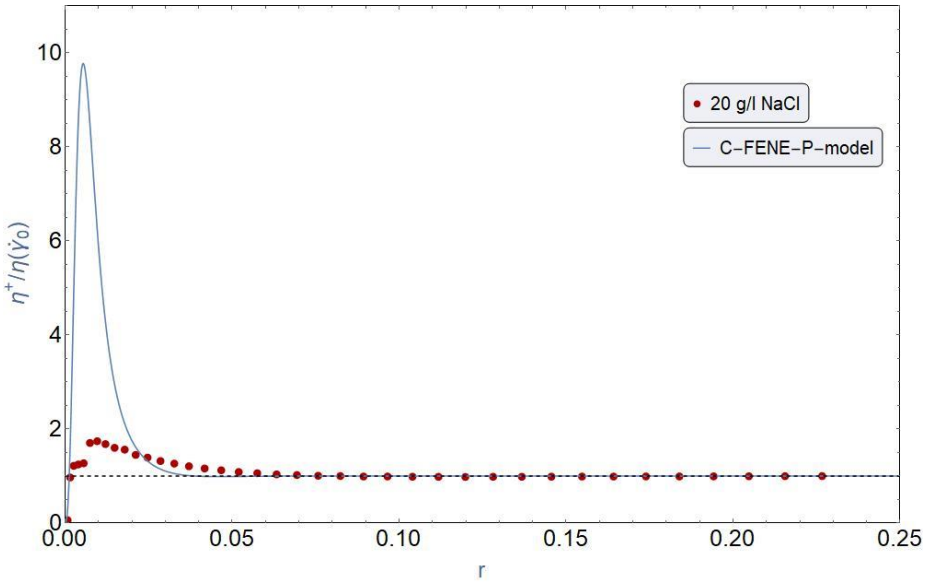

Figure 133 Normalized shear stress growth (red dots) and FENE-P-model prediction (blue line) versus dimensionless time, r, for FLOPAAM 5115 VHM 20 g/l NaCl. Dotted points representing measured data and dashed lines representing model predictions for step rate 10 s^{-1}.

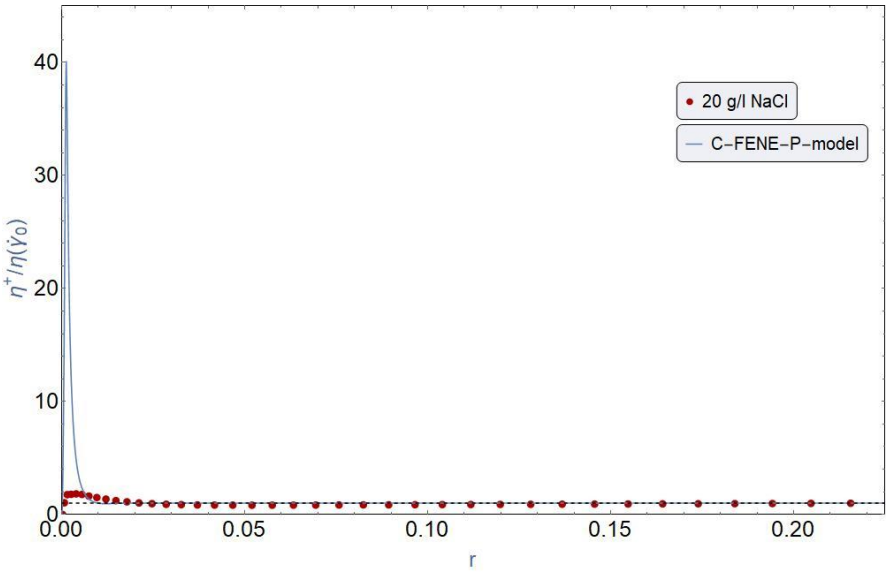

Figure 134 Normalized shear stress growth (red dots) and FENE-P-model prediction (blue line) versus dimensionless time, r, for FLOPAAM 5115 VHM 20 g/l NaCl. Dotted points representing measured data and dashed lines representing model predictions for step rate 100 s^{-1}.

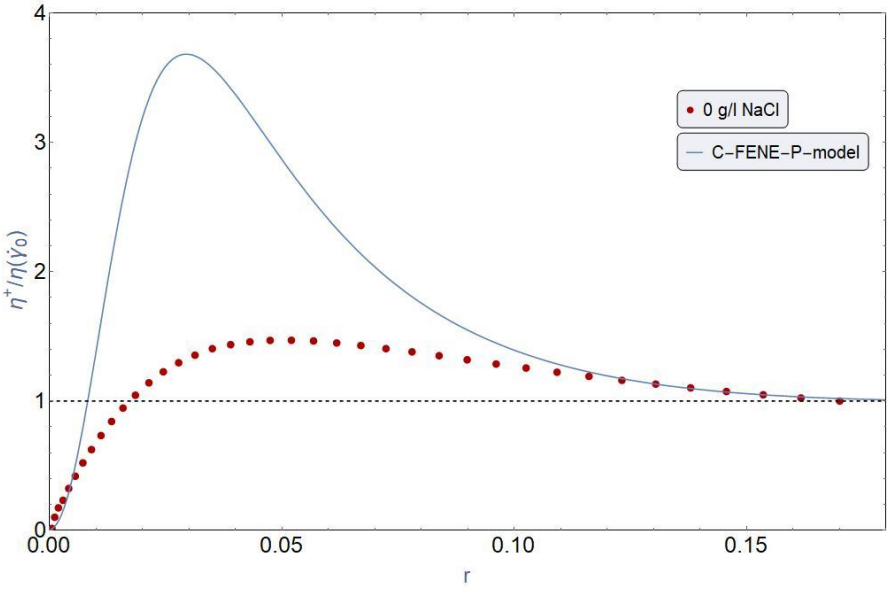

Figure 135 Normalized shear stress growth (red dots) and FENE-P-model prediction (blue line) versus dimensionless time, r, for FLOPAAM 3630-S 0 g/l NaCl. Dotted points representing measured data and dashed lines representing model predictions for step rate 1 s^{-1}.

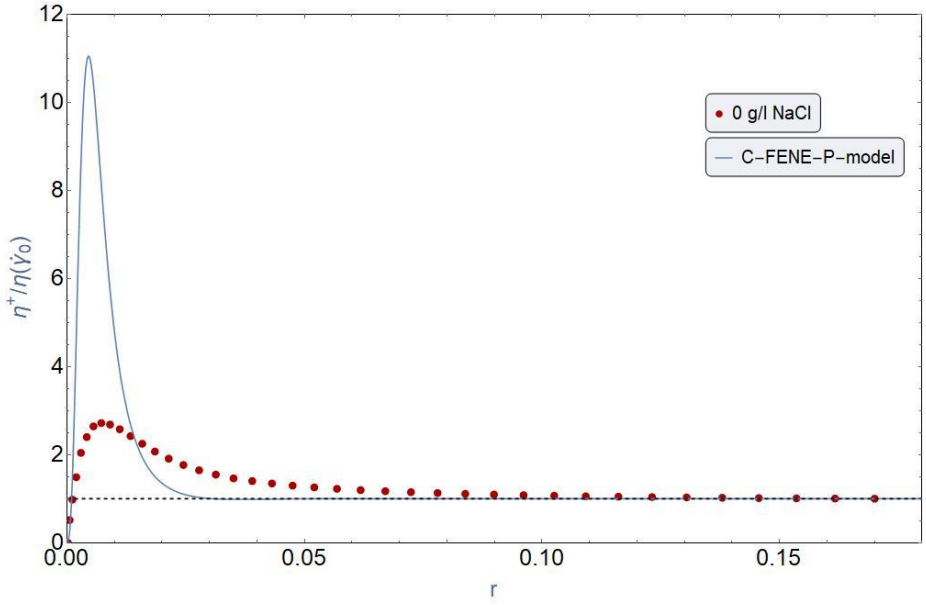

Figure 136 Normalized shear stress growth (red dots) and FENE-P-model prediction (blue line) versus dimensionless time, r, for FLOPAAM 3630-S 0 g/l NaCl. Dotted points representing measured data and dashed lines representing model predictions for step rate 10 s^{-1}.

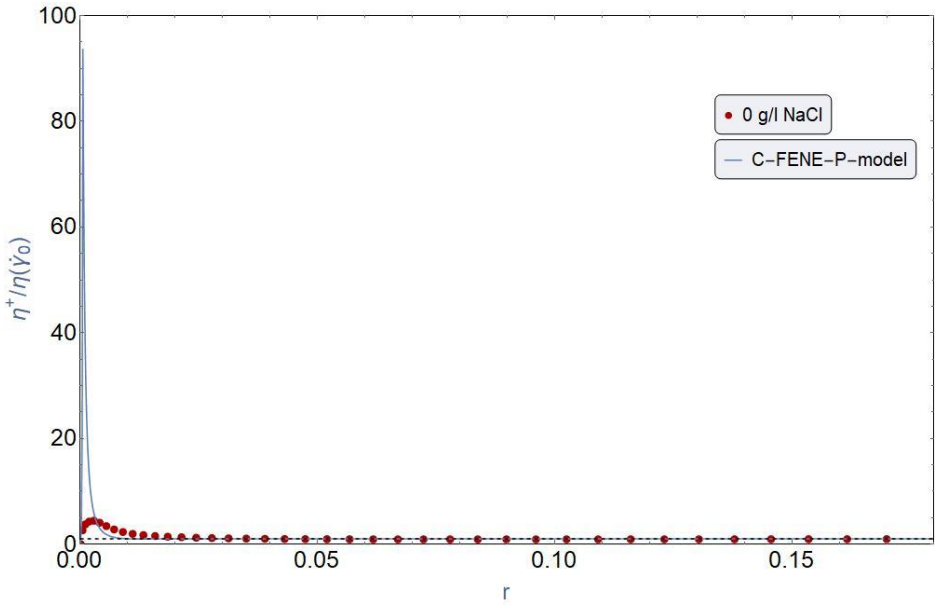

Figure 137 Normalized shear stress growth (red dots) and FENE-P-model prediction (blue line) versus dimensionless time, r, for FLOPAAM 3630-S 0 g/l NaCl. Dotted points representing measured data and dashed lines representing model predictions for step rate 100 s^{-1}.

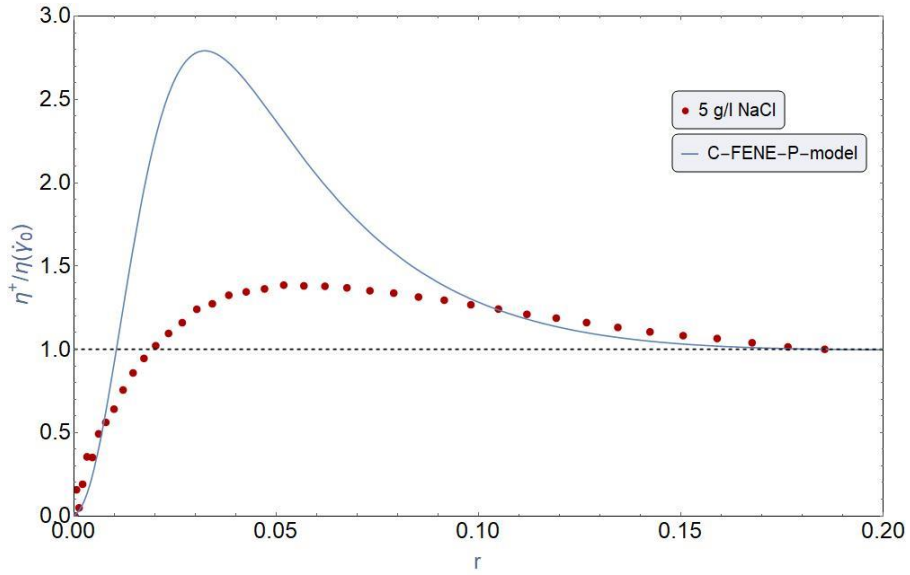

Figure 138 Normalized shear stress growth (red dots) and FENE-P-model prediction (blue line) versus dimensionless time, r, for FLOPAAM 3630-S 5 g/l NaCl. Dotted points representing measured data and dashed lines representing model predictions for step rate 1 s^{-1}.

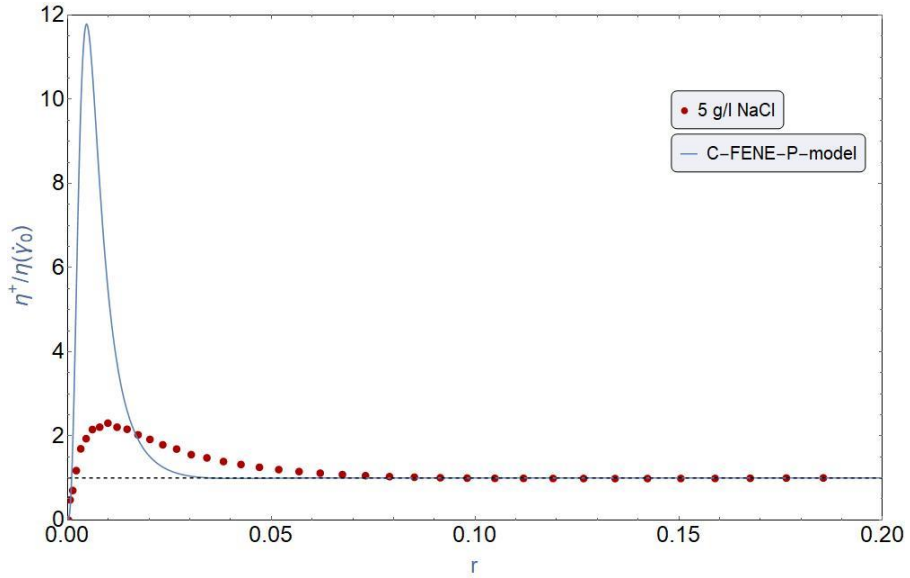

Figure 139 Normalized shear stress growth (red dots) and FENE-P-model prediction (blue line) versus dimensionless time, r, for FLOPAAM 3630-S 5 g/l NaCl. Dotted points representing measured data and dashed lines representing model predictions for step rate 10 s^{-1}.

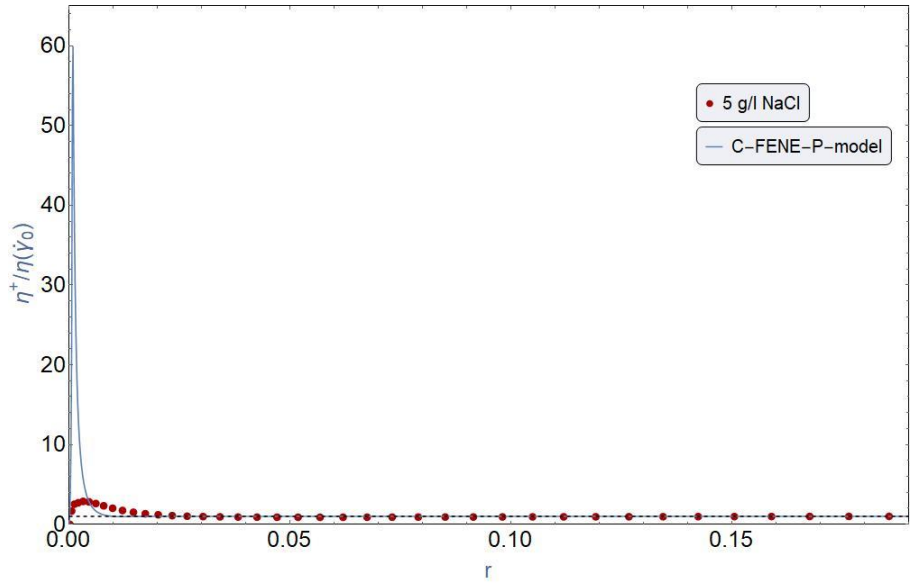

Figure 140 Normalized shear stress growth (red dots) and FENE-P-model prediction (blue line) versus dimensionless time, r, for FLOPAAM 3630-S 5 g/l NaCl. Dotted points representing measured data and dashed lines representing model predictions for step rate 100 s^{-1}.

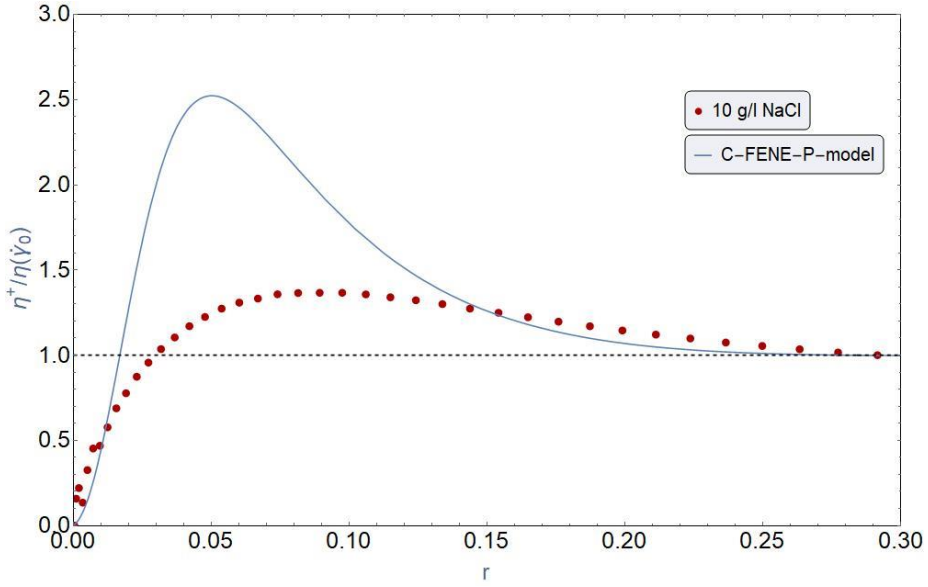

Figure 141 Normalized shear stress growth (red dots) and FENE-P-model prediction (blue line) versus dimensionless time, r, for FLOPAAM 3630-S 10 g/l NaCl. Dotted points representing measured data and dashed lines representing model predictions for step rate 1 s^{-1}.

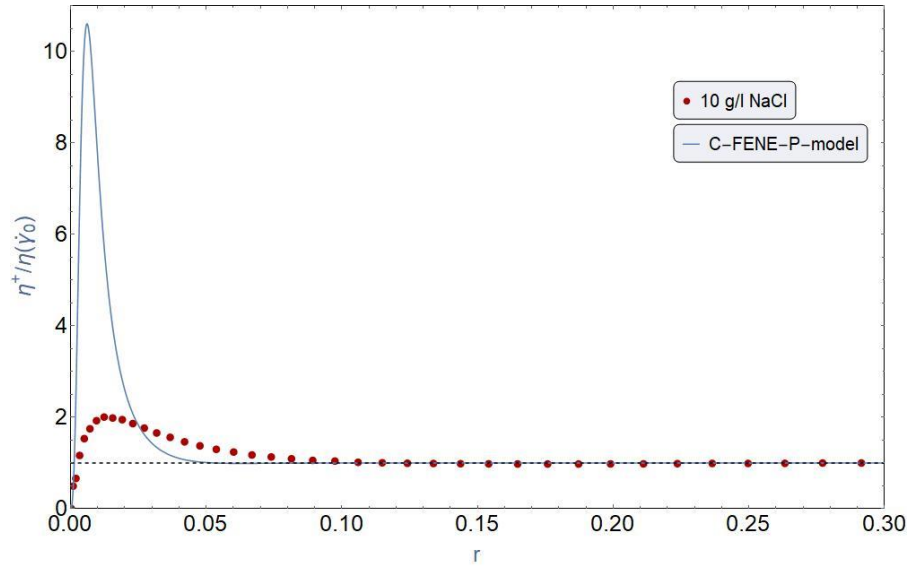

Figure 142 Normalized shear stress growth (red dots) and FENE-P-model prediction (blue line) versus dimensionless time, r, for FLOPAAM 3630-S 10 g/l NaCl. Dotted points representing measured data and dashed lines representing model predictions for step rate 10 s^{-1}.

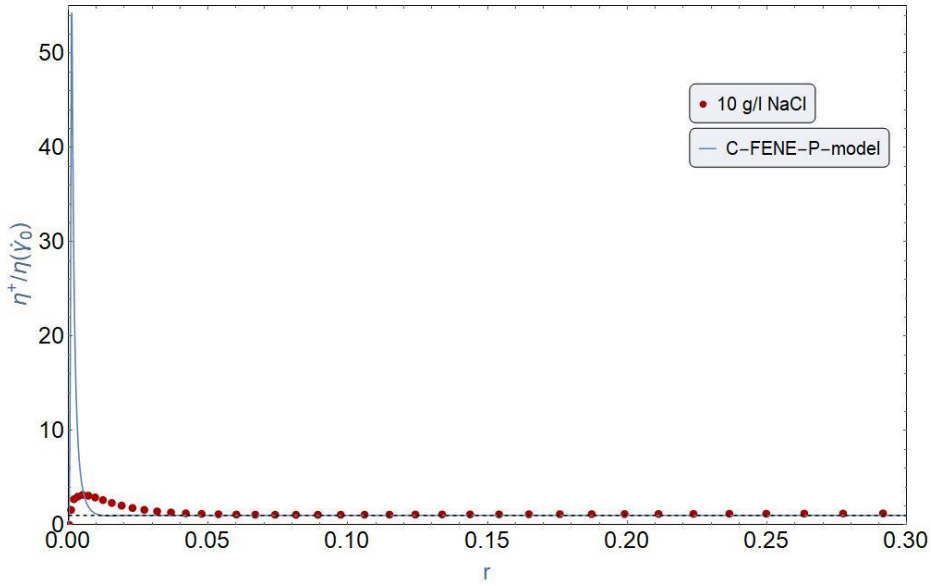

Figure 143 Normalized shear stress growth (red dots) and FENE-P-model prediction (blue line) versus dimensionless time, r, for FLOPAAM 3630-S 10 g/l NaCl. Dotted points representing measured data and dashed lines representing model predictions for step rate 100 s^{-1}.

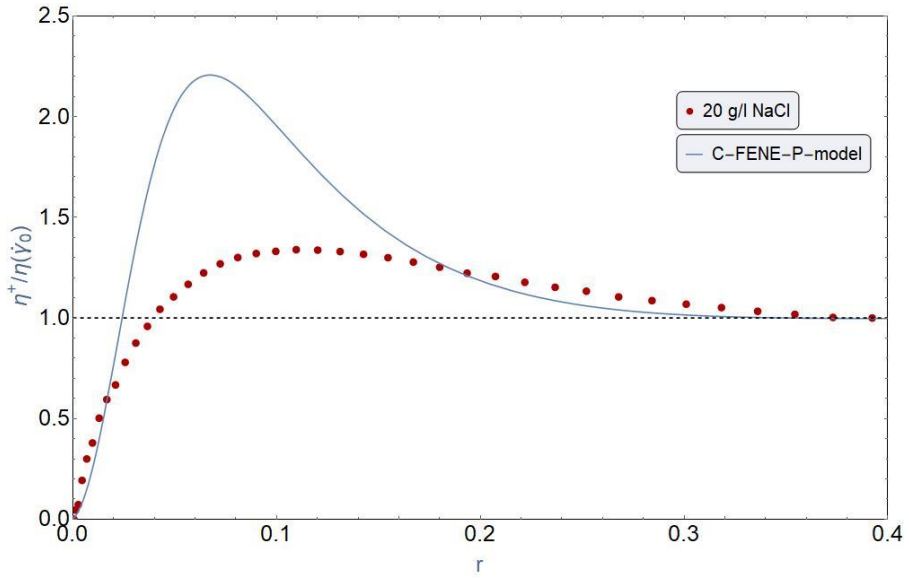

Figure 144 Normalized shear stress growth (red dots) and FENE-P-model prediction (blue line) versus dimensionless time, r, for FLOPAAM 3630-S 20 g/l NaCl. Dotted points representing measured data and dashed lines representing model predictions for step rate 1 s^{-1}.

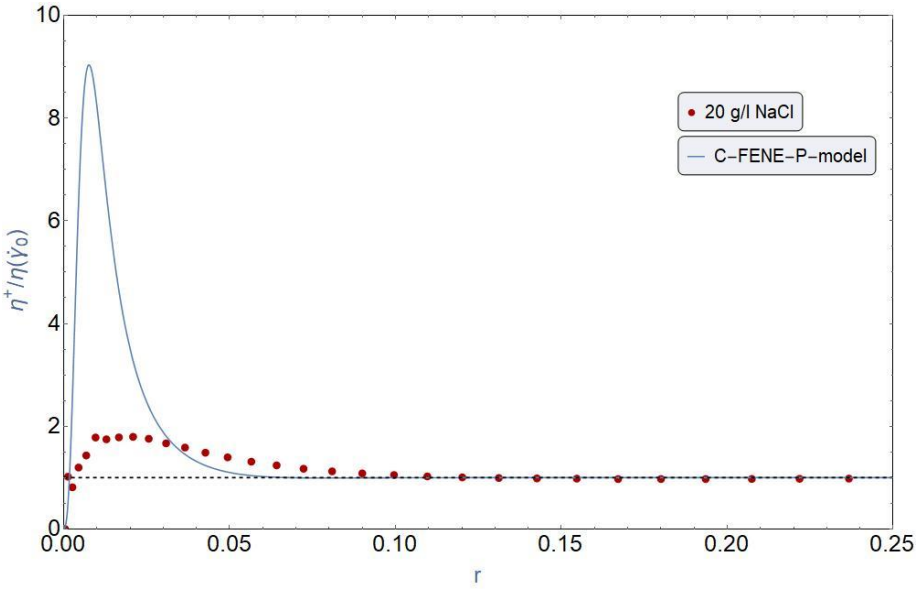

Figure 145 Normalized shear stress growth (red dots) and FENE-P-model prediction (blue line) versus dimensionless time, r, for FLOPAAM 3630-S 20 g/l NaCl. Dotted points representing measured data and dashed lines representing model predictions for step rate 10 s^{-1}.

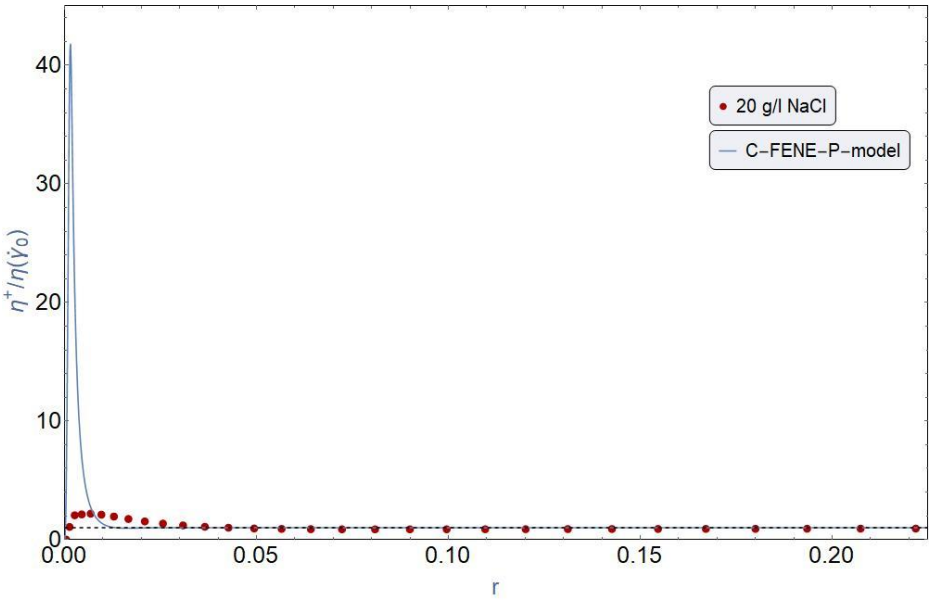

Figure 146 Normalized shear stress growth (red dots) and FENE-P-model prediction (blue line) versus dimensionless time, r, for FLOPAAM 3630-S 20 g/l NaCl. Dotted points representing measured data and dashed lines representing model predictions for step rate 100 s^{-1}.

Appendix. C

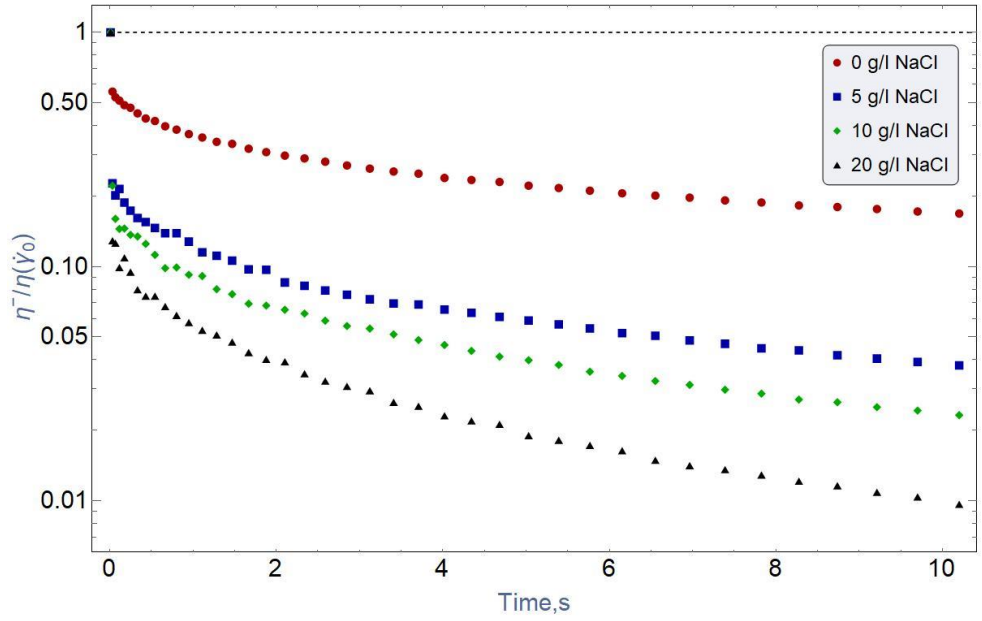

Figure 147 Normalized shear stress decay versus time for FLOPAAM 3630-S with various NaCl concentrations at step shear rate 1 s^{-1}.

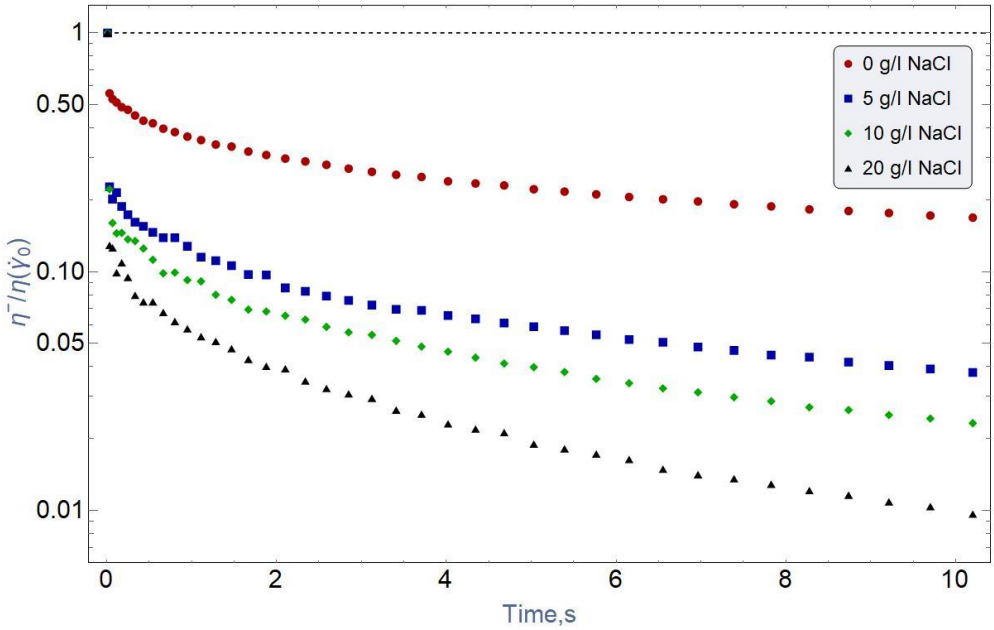

Figure 148 Normalized shear stress decay versus time for FLOPAAM 3630-S with various NaCl concentrations at step shear rate 10 s^{-1}.

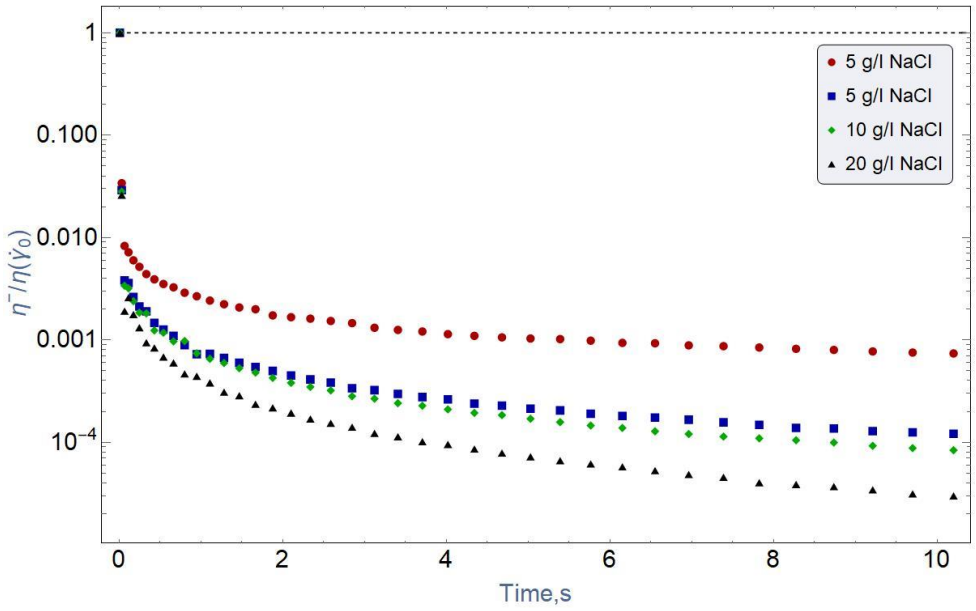

Figure 149 Normalized shear stress decay versus time for FLOPAAM 3630-S with various NaCl concentrations at step shear rate $100\ s^{-1}$.

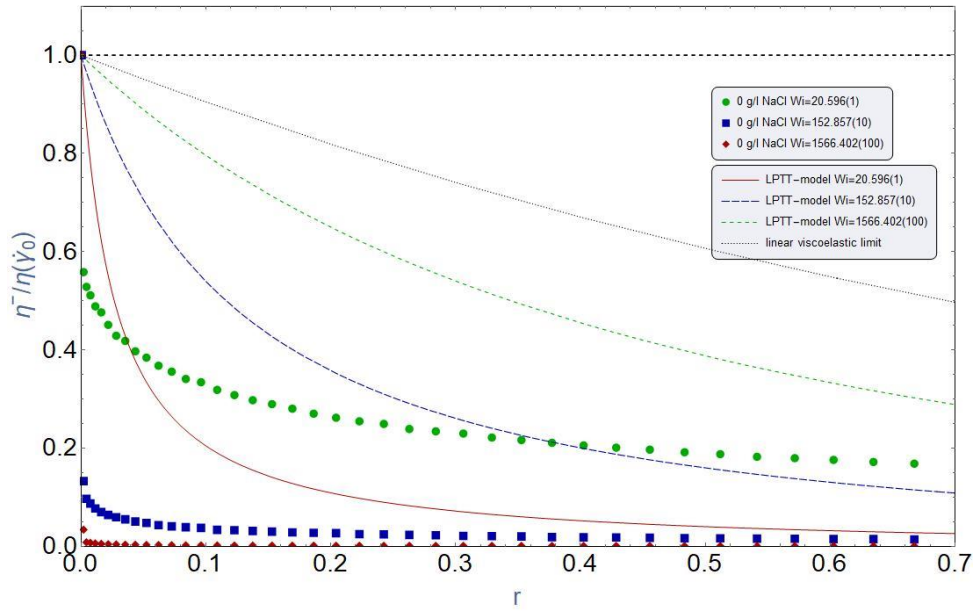

Figure 150 Normalized shear stress growth and LPTT-model prediction versus dimensionless time, r, for FLOPAAM 3630-S 0 g/l NaCl. Dots representing measured data and dashed lines representing model predictions for step shear rates 1 $(green)$, 10 $(blue)$ and $100\ s^{-1}$(red).

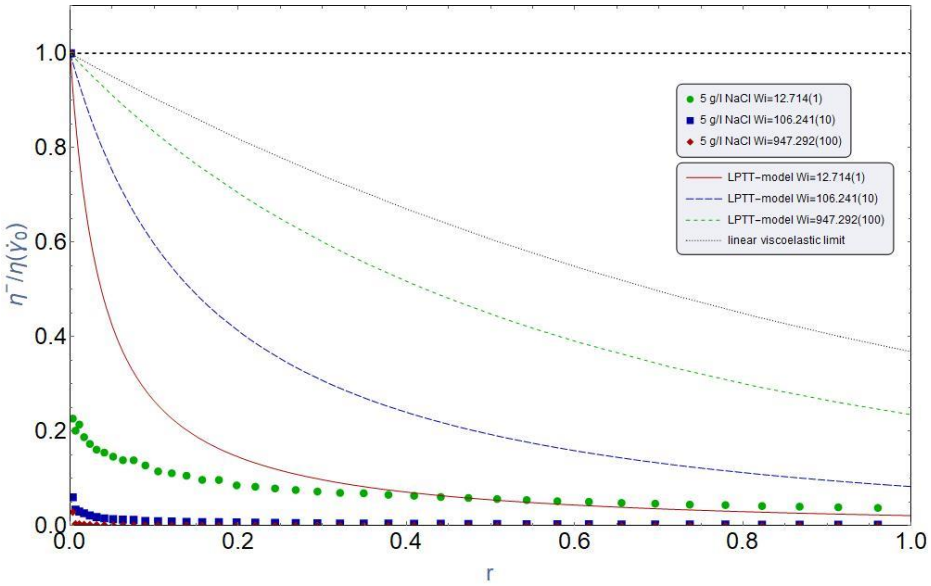

Figure 151 Normalized shear stress growth and LPTT-model prediction versus dimensionless time, r, for FLOPAAM 3630-S 5 g/l NaCl. Dots representing measured data and dashed lines representing model predictions for step shear rates 1 $(green)$, 10 $(blue)$ and 100 s^{-1}(red).

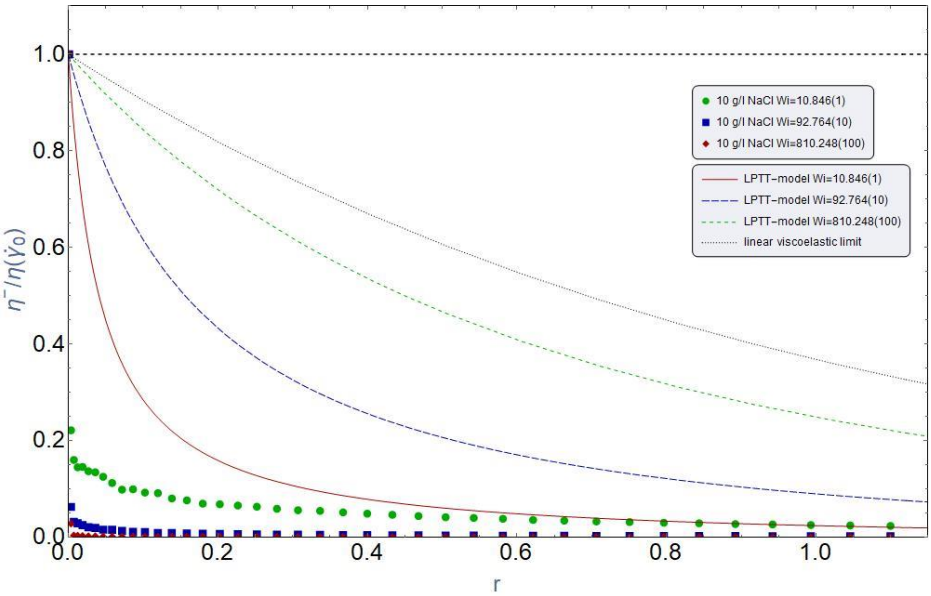

Figure 152 Normalized shear stress growth and LPTT-model prediction versus dimensionless time, r, for FLOPAAM 3630-S 10 g/l NaCl. Dots representing measured data and dashed lines representing model predictions for step shear rates 1 $(green)$, 10 $(blue)$ and 100 s^{-1}(red).

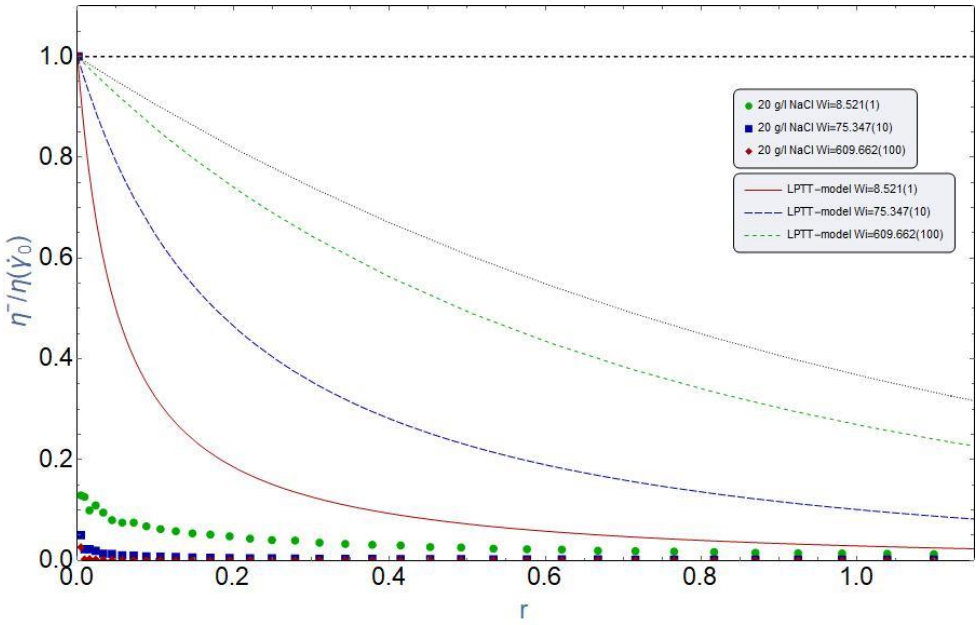

Figure 153 Normalized shear stress growth and LPTT-model prediction versus dimensionless time, r, for FLOPAAM 3630-S 20 g/l NaCl. Dots representing measured data and dashed lines representing model predictions for step shear rates 1 $(green)$, 10 $(blue)$ and 100 s^{-1}(red).

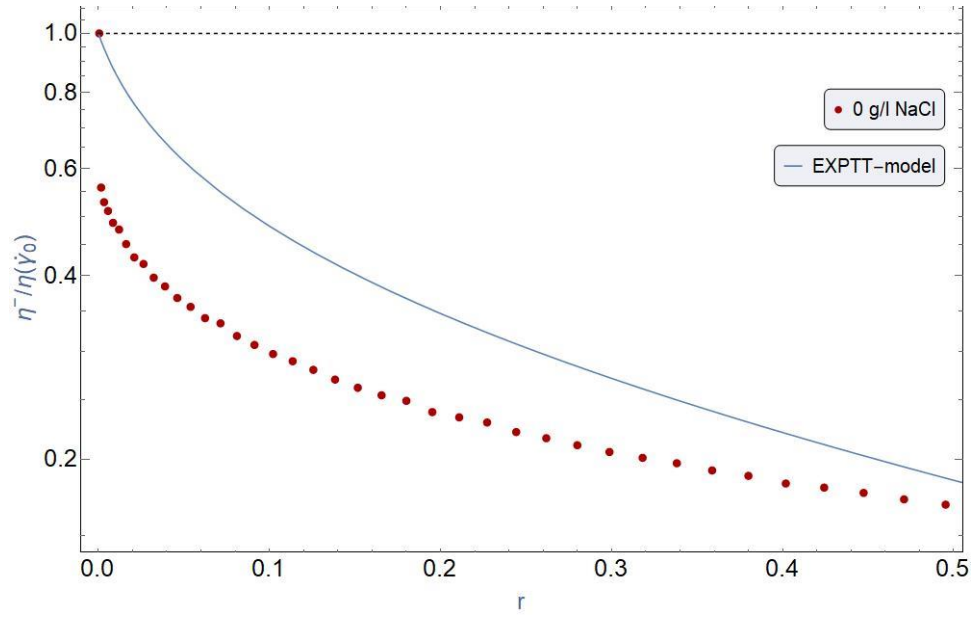

Figure 154 Normalized shear stress growth and EPTT-model prediction versus dimensionless time, r, for FLOPAAM 3630-S 0 g/l NaCl. Dots representing measured data and dashed lines representing model predictions for step rates 1 s^{-1}.

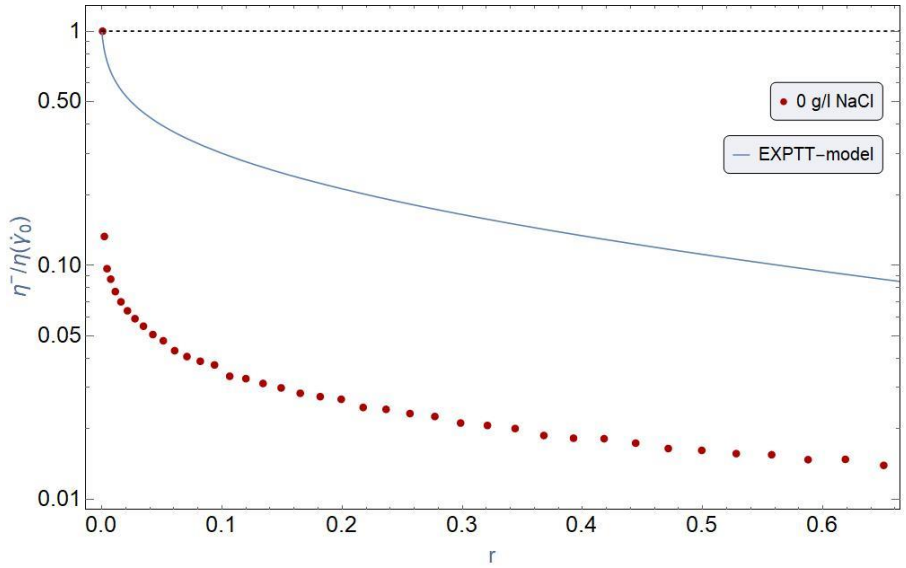

Figure 155 Normalized shear stress growth and EPTT-model prediction versus dimensionless time, r, for FLOPAAM 3630-S 0 g/l NaCl. Dots representing measured data and dashed lines representing model predictions for step rates 10 s^{-1}.

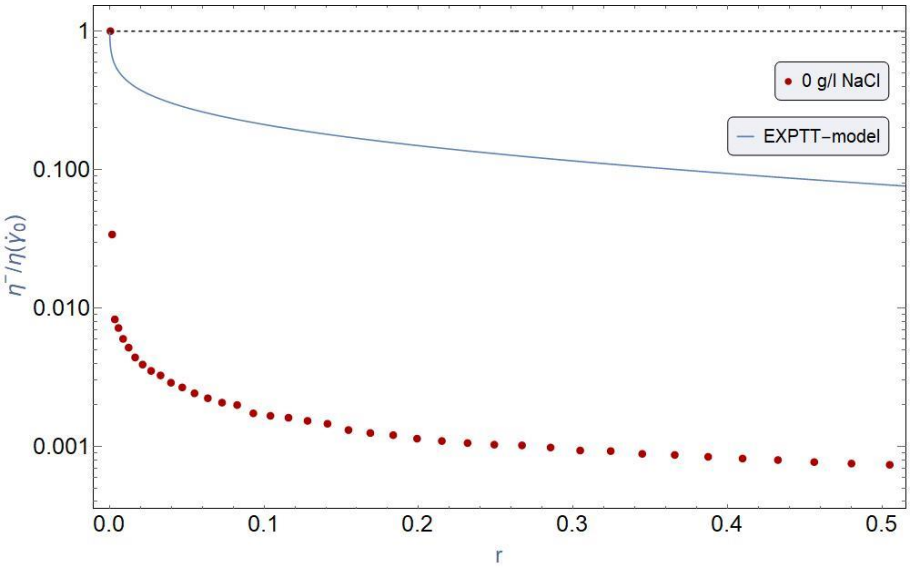

Figure 156 Normalized shear stress growth and EPTT-model prediction versus dimensionless time, r, for FLOPAAM 3630-S 0 g/l NaCl. Dots representing measured data and dashed lines representing model predictions for step rates 100 s^{-1}.

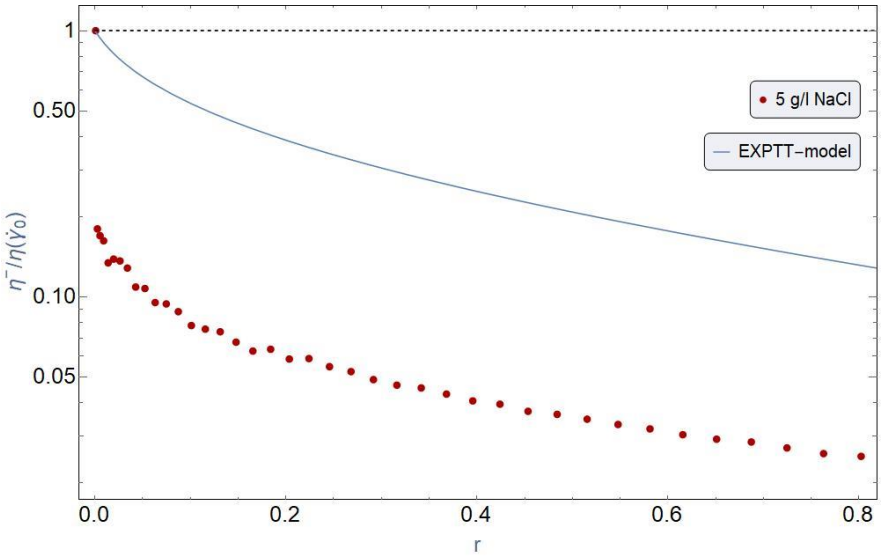

Figure 157 Normalized shear stress growth and EPTT-model prediction versus dimensionless time, r, for FLOPAAM 3630-S 5 g/l NaCl. Dots representing measured data and dashed lines representing model predictions for step rates 1 s^{-1}.

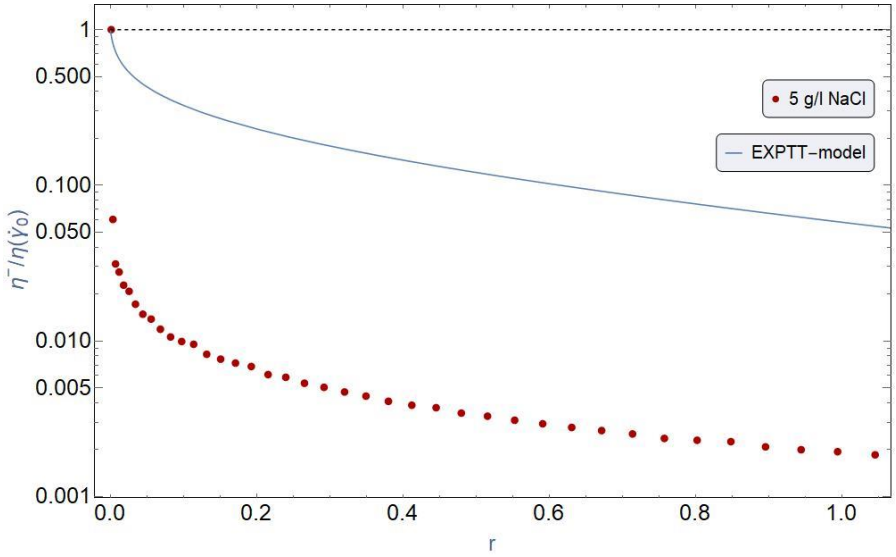

Figure 158 Normalized shear stress growth and EPTT-model prediction versus dimensionless time, r, for FLOPAAM 3630-S 5 g/l NaCl. Dots representing measured data and dashed lines representing model predictions for step rates 10 s^{-1}.

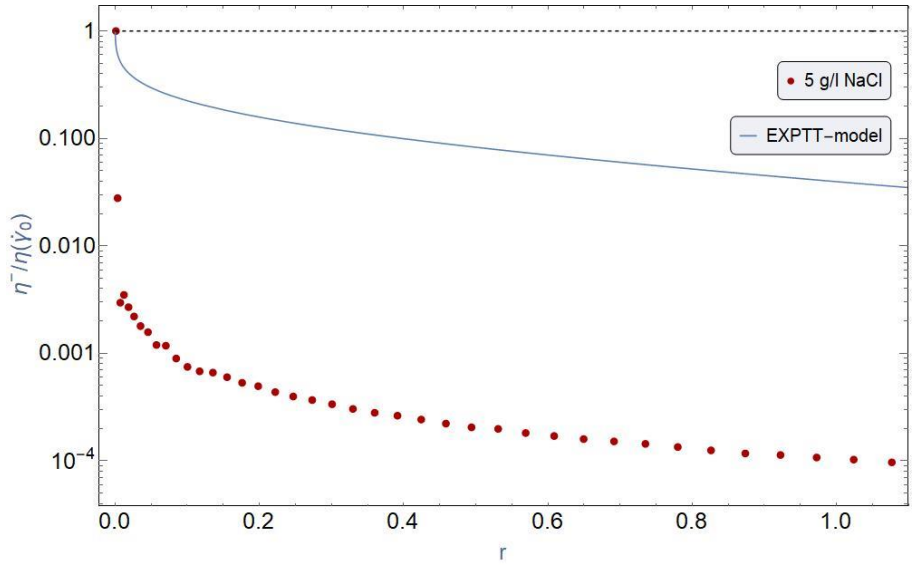

Figure 159 Normalized shear stress growth and EPTT-model prediction versus dimensionless time, r, for FLOPAAM 3630-S 5 g/l NaCl. Dots representing measured data and dashed lines representing model predictions for step rates 100 s^{-1}.

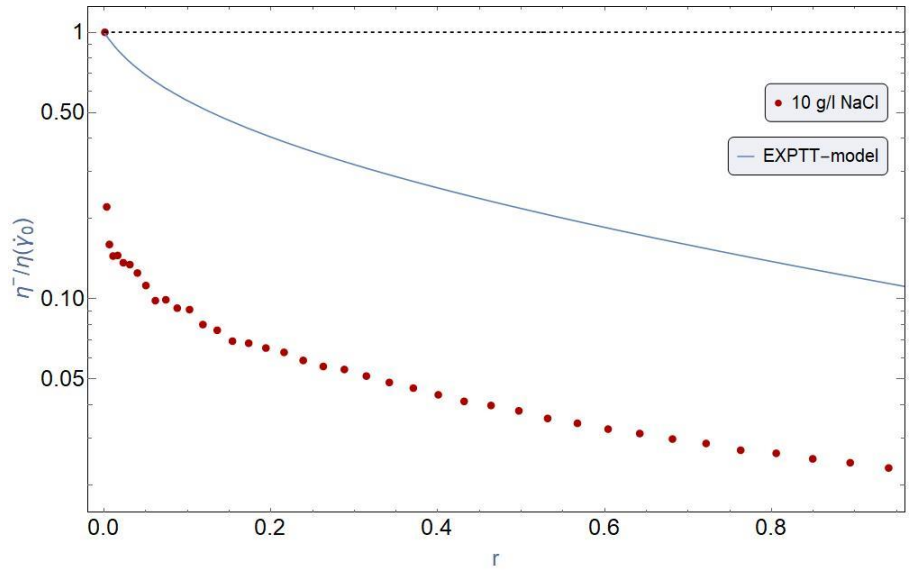

Figure 160 Normalized shear stress growth and EPTT-model prediction versus dimensionless time, r, for FLOPAAM 3630-S 10 g/l NaCl. Dots representing measured data and dashed lines representing model predictions for step rates 1 s^{-1}.

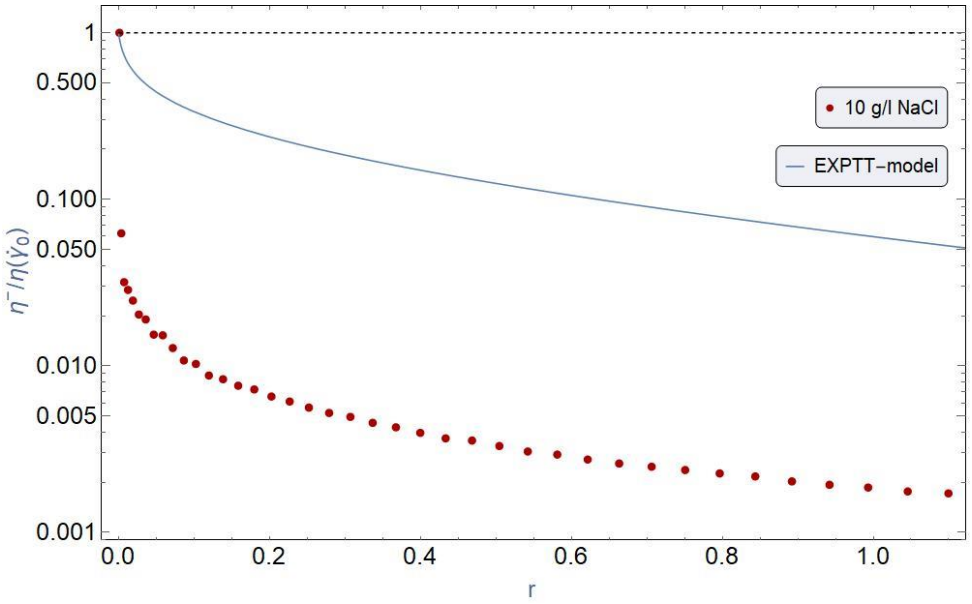

Figure 161 Normalized shear stress growth and EPTT-model prediction versus dimensionless time, r, for FLOPAAM 3630-S 10 g/l NaCl. Dots representing measured data and dashed lines representing model predictions for step rates 10 s^{-1}.

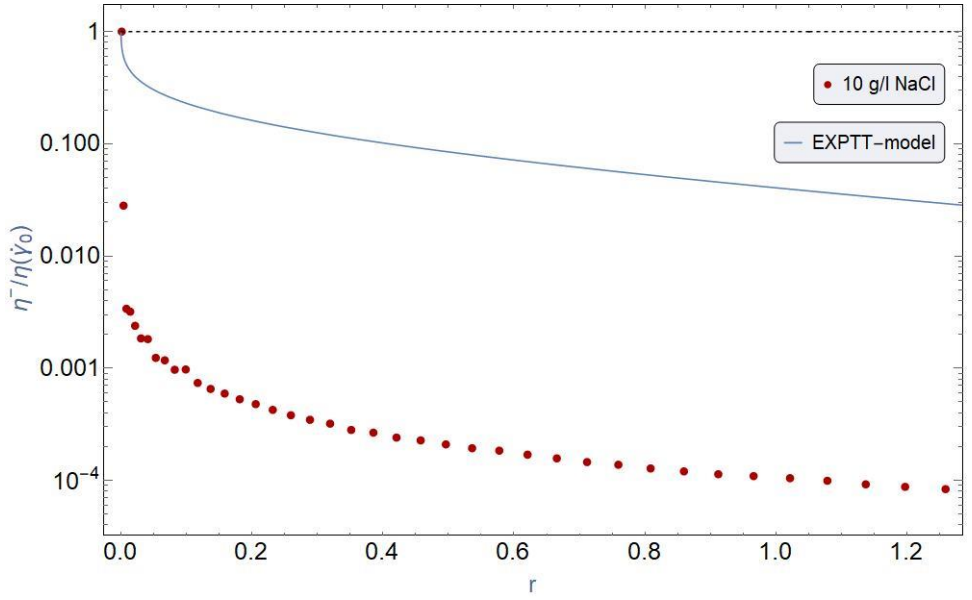

Figure 162 Normalized shear stress growth and EPTT-model prediction versus dimensionless time, r, for FLOPAAM 3630-S 10 g/l NaCl. Dots representing measured data and dashed lines representing model predictions for step rates 100 s^{-1}.

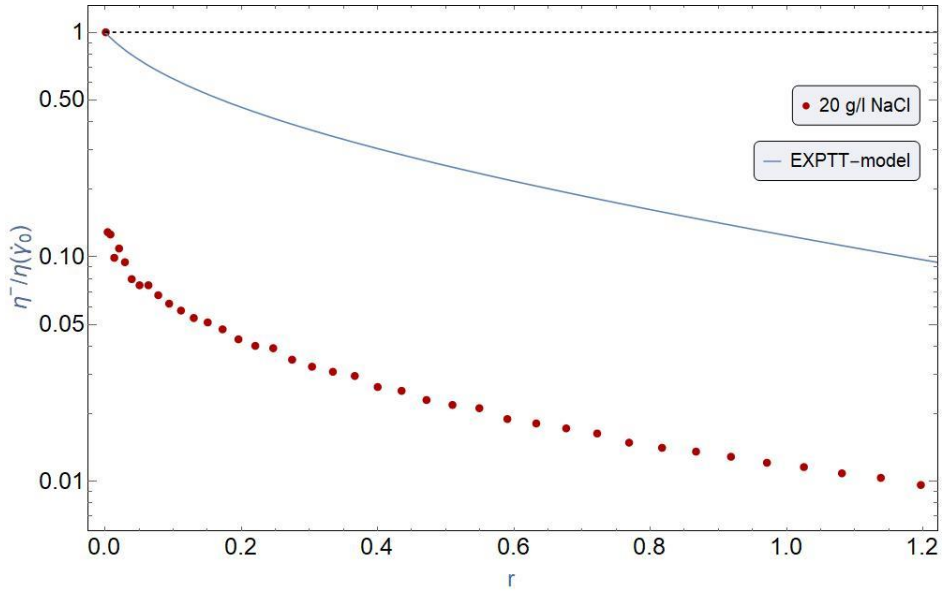

Figure 163 Normalized shear stress growth and EPTT-model prediction versus dimensionless time, r, for FLOPAAM 3630-S 20 g/l NaCl. Dots representing measured data and dashed lines representing model predictions for step rates 1 s^{-1}.

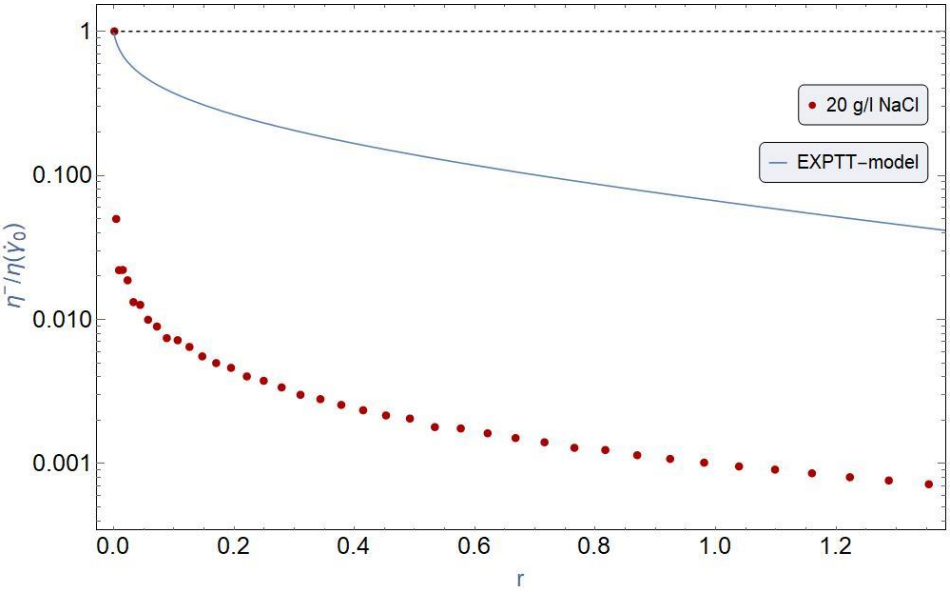

Figure 164 Normalized shear stress growth and EPTT-model prediction versus dimensionless time, r, for FLOPAAM 3630-S 20 g/l NaCl. Dots representing measured data and dashed lines representing model predictions for step rates 10 s^{-1}.

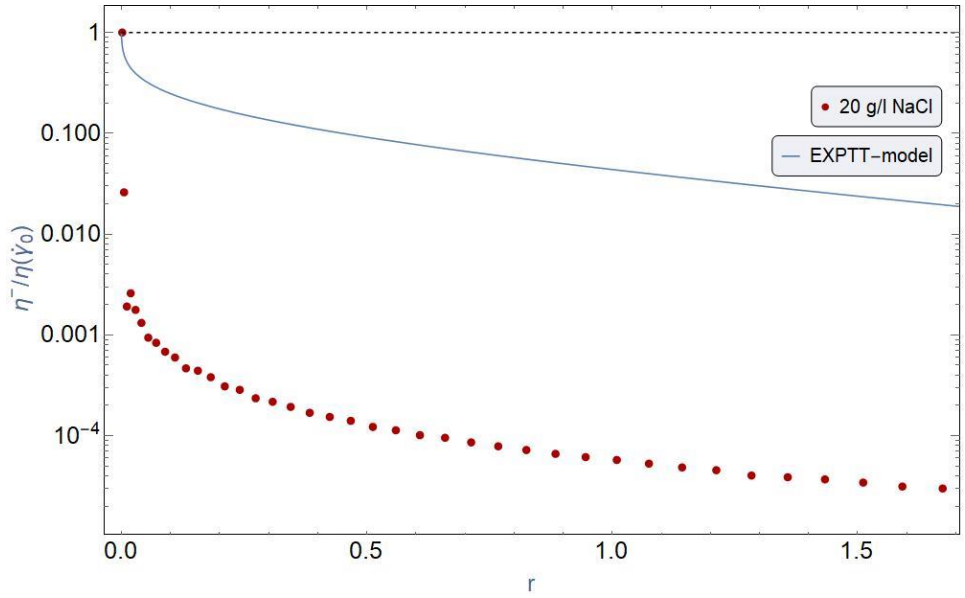

Figure 165 Normalized shear stress growth and EPTT-model prediction versus dimensionless time, r, for FLOPAAM 3630-S 20 g/l NaCl. Dots representing measured data and dashed lines representing model predictions for step rates 100 s^{-1}.